INVESTIGATION AND IMPROVEMENT OF A PCM-AIR HEAT EXCHANGER TO REDUCE ENERGY USE IN BUILDINGS

A thesis submitted for the degree of

Doctor of Philosophy (PhD)

By

Thiago Victor de Oliveira Santos

Department of Mechanical and Aerospace Engineering

College of Engineering Design and Physical Sciences

Brunel University London

Supervisor: Professor Maria Kolokotroni
Second-supervisor: Professor Luiz Wrobel
RDA: Dr Valentina Stojceska
London, UK
September 18

ABSTRACT

Energy demand for cooling buildings has risen in recent years due to increased external temperatures and occupants' demands for perceived increased comfort provided by air-conditioning systems. An alternative method to provide cooling without using energy is by ventilation in locations where ambient conditions are favourable. This thesis investigated one ventilative cooling (VC) system. The investigated system is a mechanical ventilation system which uses PCM thermal storage in the ventilation path and utilise night cool air for solidifying the PCM which in turn cools recirculated or external air during its melting phase. The project has analysed in detail the operational performance of the system and proposed improvements in the control system and heat transfer of the PCM encapsulation panel.

The methodology used for the investigation was (a) collection of system and field data from an operational system and their analysis to understand its performance using simple statistical methods as well as Dynamic Thermal Modelling (DTM) and Computational Fluid Dynamics (CFD). Based on the operational performance analysis, proposals for improvements were formulated for the control system and the PCM encapsulation panel and were investigated using DTM, CFD and a purposely built experimental rig.

Analysis of the detailed monitoring of the operational space with the system installed in retrofit and thermal/CFD analysis indicates that the system can provide acceptable thermal comfort throughout at seating occupant level (0.7 m from the floor) in the moderate weather summer conditions of south and west England using adaptive thermal comfort limits. They also indicate that indoor air quality is maintained.

Proposed improvements in the control system by changing the airflow set points can increase the permanence of temperatures within the set point range by 10%. This was implemented in the DTM model so that designers can model the system more accurately and it is easy to implement in existing systems. Improvements for the PCM panel proposed a new design of its encapsulation and variations of its packing in the thermal battery which offers double the heat transfer between the panel's surface and the air and is capable of holding 30% more PCM material for the same space requirement. With more material more energy can be stored allowing longer duration (up to 9 hrs during laboratory tests) until complete melting was reached.

The results obtained from this research using a combination of research methods (analysis of operational performance, computational models and laboratory test) indicate that mechanical ventilation systems with PCM integrated in the air path can provide the cooling demand required in non-domestic buildings in temperate climates reducing drastically operational energy environmental impacts and costs.

ACKNOWLEDGEMENTS

CONTENTS

LIST OF FIGURES

LIST OF TABLES

NOMENCLATURE

Symbols

$\dot{m}_{air}$	Air mass flow	kg/s
A	Area	m^2
E_x	Associated error for addition/subtraction	-
E_y	Associated error for multiplication/division	-
k	Conductivity	W/mK
ρ	density	kg/m^3
ρ_0	Density of the flow (constant)	kg/m^3
D	Diameter	m
Δ	Difference	-
y^+	Dimensionless wall distance	-
Nu_{DB}	Dittus-Boelter correlation	-
H	Duct height	m
μ	Dynamic fluid viscosity	N s/m^2
X,Y	External forces	N
f	Friction factor	-
μ_τ	Friction velocity	m/s
Nu_G	Gnielinski's correlation	-
∇	Gradient	-
g	Gravity	m/s^2
h	Heat of convection	W/m^{2}K
Q	Heat transfer	W
D_h	Hydraulic diameter	m
D_h	Hydraulic diameter	m
$T_{m,i}$	Inlet fluid temperature	ºC
ΔT_{LMDT}	Logarithmic mean temperature difference	K
θ_{max}	Maximum acceptable operative temperature	ºC
U_c	Mean velocity magnitude when	m/s
y_i and $\hat{y}_i$	Measured and simulated data at instant i	ºC
M	Metabolic heat production	W/m^2
Nu	Nusselt number	-
T_0	Operating temperature	ºC
$T_{m,o}$	Outlet fluid temperature	ºC
L_{panel}	Panel length	m
l	Panel length	m
T_t	Panel thickness	m
W_{panel}	Panel width	m
w	Panel width	m
∂	Partial derivative	-

Pr	Prandtl number	-
p	Pressure	Pa
r	Ratio of depth	-
Re	Reynolds number	-
Re	Reynolds number	-
e	Ridge height	m
s	Ridge pitch length	m
r	Ridge radius	m
w_r	Ridge width	m
$\overline{Y_s}$	Sample mean of the measured data	-
τ_w	Shear stress at the wall	Pa
c_p	Specific heat at constant pressure	J/kgK
σ	Standard deviation	-
$\tilde{T}_s$	Surface temperature average of all thermocouples	ºC
T	Temperature	ºC
T_b	Temperature average from inlet and outlet	ºC
y_T^+	Thermal boundary layer	m
η	Thermal Enhancement Factor (TEF)	-
β	Thermal expansion coefficient	1/K
L	Thermal load on the body	W/m²
θ_{upp}	Threshold/Upper Limit Temperature	ºC
t	Time	s
ω	Turbulent frequency	1/s
K	Turbulent kinetic energy	m²/s²
Pr_t	Turbulent Prandtl number	-
E_a, E_b, E_c	Uncertainties associated to each individual number	-
u, v	Velocity	m/s
$\dot{q}$	Volumetric rate of thermal energy generation	W/m²

Subscriptions

i,j	Axis directions
$comf$	Comfort
$conv$	Convection
c	Cooling
D	Diameter
o	Smooth surface
od	Daily mean
h	Heating
in	Inlet
max	Maximum
min	Minimum
out	Outlet
p	Point p
w	Wall
rm	Weighted running mean

Acronyms

Acronyms	Definition
AC	Air Conditioning
AIVC	Air Infiltration and Ventilation Centre
ANSI	American National Standards Institute
ASHRAE	American Society of Heating, Refrigerating and Air-Conditioning Engineers
ASME	American Society of Mechanical Engineers
BREEAM	Building Research Establishment Environmental Assessment Method
BB	Building Bulletin
BS	British Standard
CCA	Climate Change Act
CCC	Committee on Climate Change
CCD	Charged Coupled Device
CFD	Computational Fluid Dynamics
CIBSE	Chartered Institution of Building Services Engineers
COP	Coefficient of Performance
CPD	Continuing Professional Development
CPU	Central Processing Unit
CSEF	Centre for Sustainable Energy Use in Food Chains
CVRSME	Coefficient of Variation of the Root Mean Square Error
DNS	Direct Numerical Simulation
DSC	Differential Scanning Calorimetry
DSY	Design Summer Year
DTM	Dynamic Thermal Modelling
EBC	Energy in Buildings and Communities Programme
ECCP	European Climate Change Programme
EP	Existing Panel
EPC	Energy Performance Certificate
EPP	Expanded Polypropylene
EWT	Enhanced Wall Treatment
EWY	Example Weather Year
HCPV	High-Concentration Photovoltaics
HTM	Hybrid Thermal Mixing
HVAC	Heating, ventilation, and air conditioning
IAQ	Indoor Air Quality
IEO	International Energy Outlook
IESU	Indirect Evaporative and Storage Unit
IESVE	Integrated Environmental Solutions Virtual Environment
ISO	International Organization for Standardization
LEED	Leadership in Energy and Environmental Design
LES	Large-Eddy Simulation
LHTS	Latent Heat Thermal Storage
LTES	Latent Thermal Energy Storage
LTHW	Low Temperature Hot Water
MBE	Mean Bias Error
MVS	Mechanical Ventilation System
MWh	Mega Watt hour
NP	New Panel
OECD	Organisation for Economic Co-operation and Development
PCM	Phase Change Material
PMV	Predicted Mean Vote
PPD	Predicted Percentage Dissatisfied
RANS	Reynolds-Averaged Navier-Stokes
REHVA	Federation of European Heating, Ventilation and Air Conditioning Associations
RMSE	Root Mean Square Error

Acronyms	Definition
AC	Air Conditioning
RNG	Re-Normalisation Group
RSM	Reynolds Stress Model
SIMPLE	Semi-Implicit Method for Pressure-Linked Equations
SST	Shear Stress Transport
TB	Thermal Battery
TEF	Thermal Enhancement Factor
TES	Thermal Energy Storage
TRNSYS	TRaNsient SYstems Simulation Program
UK	United Kingdom
USA	United States of America
UWE	University of the West of England
VS	Ventilation System

CHAPTER 1 - INTRODUCTION

1.1 Research context

A growing number of countries have put policies to improve energy performance in buildings as energy use in buildings are responsible for 20.1% of the total world energy demand (U.S. Energy Information Administration, 2016). In the commercial sector, the International Energy Outlook (IEO) 2016 reports that the worldwide energy consumption is growing 1.6 % and will continue in this rate until 2040 (U.S. Energy Information Administration, 2016). This percentage tends to increase as global warming, population growth, growing needs for buildings and indoor occupation, affordability and increase in standards of life are demanding more needs for cooling (Santamouris and Kolokotsa, 2013; Zeinelabdein et al., 2018). As an example, the energy demand for heating and cooling in office buildings can respond for 33 % in countries such as the USA but can reach 51 % in tropical countries like Singapore (Prieto et al., 2017). This study demonstrates that refrigeration and air conditioning are responsible for about 15 % of the global energy demand.

In Europe, the final energy consumption had different trends between 1990 and 2015 depending on the activity sector (Figure 1.1). While sectors such as agriculture and forestry and industry fell by 26.6 and 25.8 % respectively, sectors such as residential remained stable. However, services and transport increased by 35.2 and 26.3 %, respectively. This can show a move from an energy-intensive industry to a service based economy as global temperature is continuously increasing ('Europe 2020 indicators - climate change and energy - Statistics Explained', n.d.). Nevertheless, this stabilization in energy consumption in Europe can also be explained by policies focused to reduce greenhouse gases emissions.
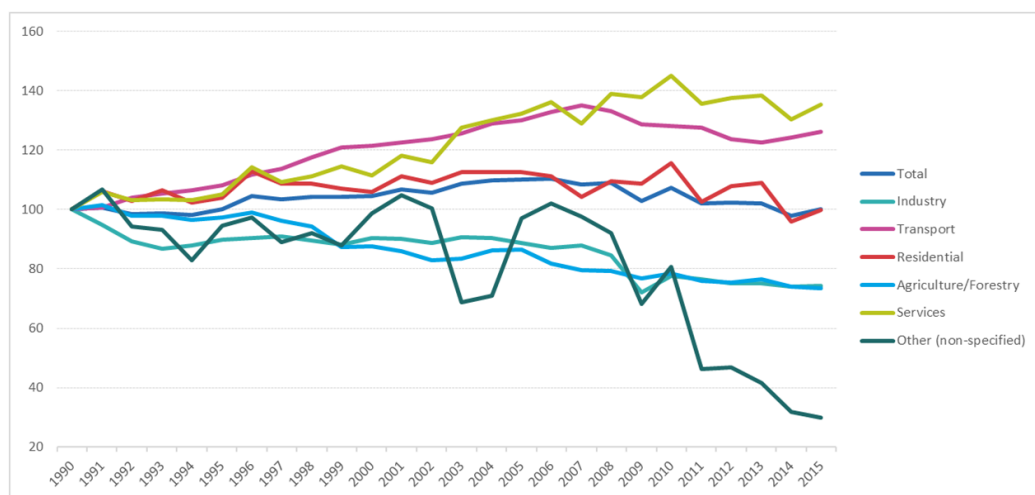
Figure 1.1 – Final energy consumption by sector in Europe ('Europe 2020 indicators - climate change and energy - Statistics Explained', n.d.).

The main milestone for such policies focused on greenhouse gases emission reduction was the Kyoto protocol, an international treaty implemented in 1997. Since then, incentives and agreements are in constant development in order to reduce CO_2 emissions and energy consumption (e.g. the European Climate Change Programme (ECCP) launched in 2000, ECCP II launched in 2005 and the Paris agreement in 2015.

In the UK, the Climate Change Act 2008 (CCA) is considered one of the most important standards and targets. This Act mandates a reduction of CO_2 levels in 80 % until 2050 by using the levels in 1990 as a baseline. To follow CCA, annual reports to the parliament have been published by the Committee on Climate Change (CCC). CCC is an Independent advice to government on building a low-carbon economy and preparing for climate change. In the 2018 progress report, UK emissions were reduced by 43 % when compared to 1990 levels (Committee on Climate Change, 2018). However, most of this excellent progress came from electricity generation as it can be seen in the infographic below (Figure 1.2). This made this committee deliver four key messages to Government:

1. Support the simple, low-cost options
2. Commit to effective regulation and strict enforcement
3. End the chopping and changing of policy
4. Act now to keep long-term options open
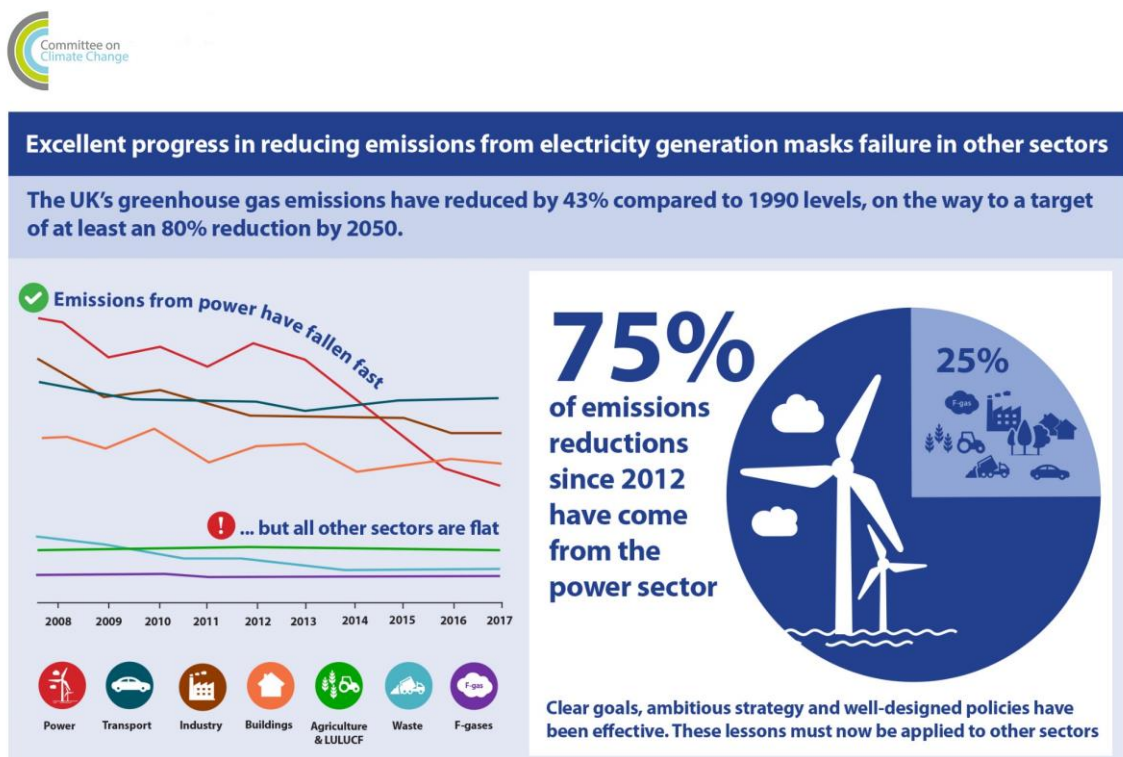
Figure 1.2 – Infographic presenting the reduction in emissions (CCC, 2018).

One possible solution to reduce energy use in buildings is to adopt natural or passive cooling strategies. Natural cooling is a strategy to remove heat using natural forces combined with the architectural design of the building; while passive cooling is understood as a cooling method focused on thermal comfort improvement with low or no energy consumption by controlling heat gain and heat dissipation (Santamouris and Asimakopoulos, 1996).

The use of ventilative cooling can also be an efficient solution for some climates and type of buildings. This technique uses the cooling capacity of the outdoor air flow by ventilation to reduce or eliminate cooling loads and/or energy use by mechanical cooling in buildings (Kolokotroni and Heiselberg, 2015). The most common technique used in ventilative cooling is to increase the ventilation airflow and night ventilation ('Venticool, http://venticool.eu/. Acessed in', 2018).In November 2013 an international project focussing on Ventilative Cooling (http://venticool.eu/annex-62-home/) was approved IEA EBC (Executive Committee of the IEA Energy in Buildings and Communities programme): The Annex 62 was completed in 2017, it included partners from research centres, universities and manufacturers and suppliers of ventilation equipment of 14 countries. Annex 62 is divided into 3 main subtasks (Kolokotroni and Heiselberg, 2015):

Subtask A "Methods and Tools": This subtask analysed, developed and evaluated design methods to predict cooling demand, ventilative cooling performance and risk of overheating including analysis and evaluation of their performance and inter-method functionality comparison. Furthermore, it provides strategies to integrate ventilative cooling in energy performance methods and regulation including specification and verification of key performance indicators with a special focus on performance indicators for high-temperature conditions. It offers recommendations for integration of ventilative cooling in legislation, standards, design briefs and energy performance calculation and verification methods (Heiselberg, 2018);

Subtask B "Solutions": With the knowledge in mechanical, natural and hybrid ventilation systems and technology, thermal comfort solutions and other involved technologies, this subtask developed solutions to integer all knowledge to improve comfort in any climatic condition (Holzer and Psomas, 2018). This subtask analysed from the perspective of utilization, the performance of existing ventilation systems and technologies in terms of cooling capacity as well as the ability to reduce energy use and support high-quality indoor environment.

Subtask C "Case studies": This subtask analysed 15 case study buildings by presenting the key characteristics and information about the design, simulation and operational performance of the case study. It also compares the use of different

ventilative cooling solutions in different climates and buildings (O'Sullivan and Adam O'Donovan, 2018).

This research project contributed to Subtask B and C of Annex 62 on the topic of PCM-Air heat exchanger to provide Ventilative Cooling. A PCM-Air heat exchanger is a phase change material thermal storage usually integrated into a mechanical ventilation system; to be referred to as MVS in this thesis. The MVS use the principle of thermal storage through latent heat in areas where night temperatures are cold enough to store the energy necessary to cool the environment during the day. It has a low energy consumption as only a fan is used and is suitable for areas where the outdoor ambient air temperature is not enough to cool the building environment during the day but cool enough to charge the thermal batteries during the night. This technology has been extensively studied but recent reviews also highlight that limited analysis has been carried out from operational buildings with commercially installed PCM-Air heat exchangers. Such results are important to accelerate inclusion in designs for new and refurbished buildings. In addition, studies focused on improving the system is necessary to reduce costs and make it more affordable.

Based on the above and as a part of subtask C of Annex 62, this project focused on the case study of a seminar room which is ventilated and cooled by a PCM-Air heat exchanger and analysed its performance. For subtask B, this project improved the design of the panel used to encapsulate the PCM. The new design focused on the reduction of costs and improvements in heat transfer efficiency.

1.2 Research Aims and Objectives

The aim of the thesis is to investigate and improve the performance of PCM-Air heat exchangers used in small mechanical ventilation systems to provide cooling. This research was carried out in collaboration with Monodraught Ltd who have commercialised such a ventilation system. The methods of investigation included analysis of operational data of the system, computational investigation to improve its performance and laboratory tests to verify proposed improvements.

To achieve the main aim, the following objectives were set:

Objective 1:

Conduct a literature review on (a) thermal comfort in non-domestic buildings, (b) use of PCMs as thermal storage in small (room size) ventilation systems (MVS), and (c) strategies to improve the ventilation system (MVS) cooling efficiency.

Objective 2:

Understand and describe in detail the operational performance of a PCM-Air heat exchanger integrated into a MVS together with an analysis of indicators of thermal comfort provision.

Objective 3:

Improve the cooling efficiency of the MVS by focussing on (a) control strategies and (b) the design of the PCM panel to increase heat transfer without additional (or even reduced) costs.

Objective 4:

Fabricate and validate the performance of the new design.

1.3   Research Methods

The methods used to achieve the aim and objectives are:

- Analysis of data from an operational MVS with PCM-air heat exchanger and field measurements in the space it is operating;
- Computational analysis using dynamic thermal modelling and CFD;
- Laboratory testing to confirm design performance.

Data from an operational MVS installed in a seminar room was used to analyse the performance of the system in detail. Field measurements were used to analyse thermal comfort and overheating in the space. The analysis show that the MVS was capable to maintain the room thermally comfortable according to the BS EN 15251. Monitoring, analysing and publishing studies of such systems in real operation will help researchers to understand their operation in detail and use it as a guide for future studies. It will also help designers to understand the benefits of this technology and opt for this low energy cooling system in new designs.

In order to increase MVS performance, computational tools were used to propose improvements in the control system and panel design. A correct representation of the MVS with PCM heat exchangers is important to correctly design the system and essential to decide what cooling system is appropriate. This will essentially help designers. Furthermore, simulations showing more reliable results can avoid future claims about system performance.

With a new panel design fabricated, laboratory tests confirmed improvements in the MVS. As researchers have focused their attention to develop new PCM's or assess existing PCM encapsulations in different climates and environmental conditions. The development of a new encapsulation panel for MVS opens a field of investigation where researchers are able to develop new tools to improve the MVS. The new PCM

panel will also contribute to the industry as it provides a new option of encapsulation for cooling purposes. The flexibility of providing different thicknesses is also positive characteristic of this panel.

Table 1.1 summarizes the steps of the research and methods used to achieve the objectives and Figure 1.3 presents the map of the thesis, A summary of the methods used to achieve the objectives follows.

Table 1.1 – Research objectives linked to methods

Obj.	Method	Technique	Study/Research
1	Literature review	Books, journal papers and CIBSE & ASHRAE guidelines	- Ventilation systems with thermal energy storage - Evaluate strategies to improve VS efficiency
2	Numerical & operational data	Data analysis and Energy Balance modelling	- Describe the operation of a PCM-Air heat exchanger through system data and CFD simulations
2	Field Measurements	Thermal comfort indices	- Overheating and thermal Comfort performance
3	Numerical	Dynamic Thermal Modelling	- Improve the control system
3	Numerical & laboratory testing	Energy Balance modelling	- Design of a PCM panel for a PCM-Air heat exchanger
4	Laboratory testing	Energy Balance modelling	- Evaluate the manufactured PCM panel evaluation
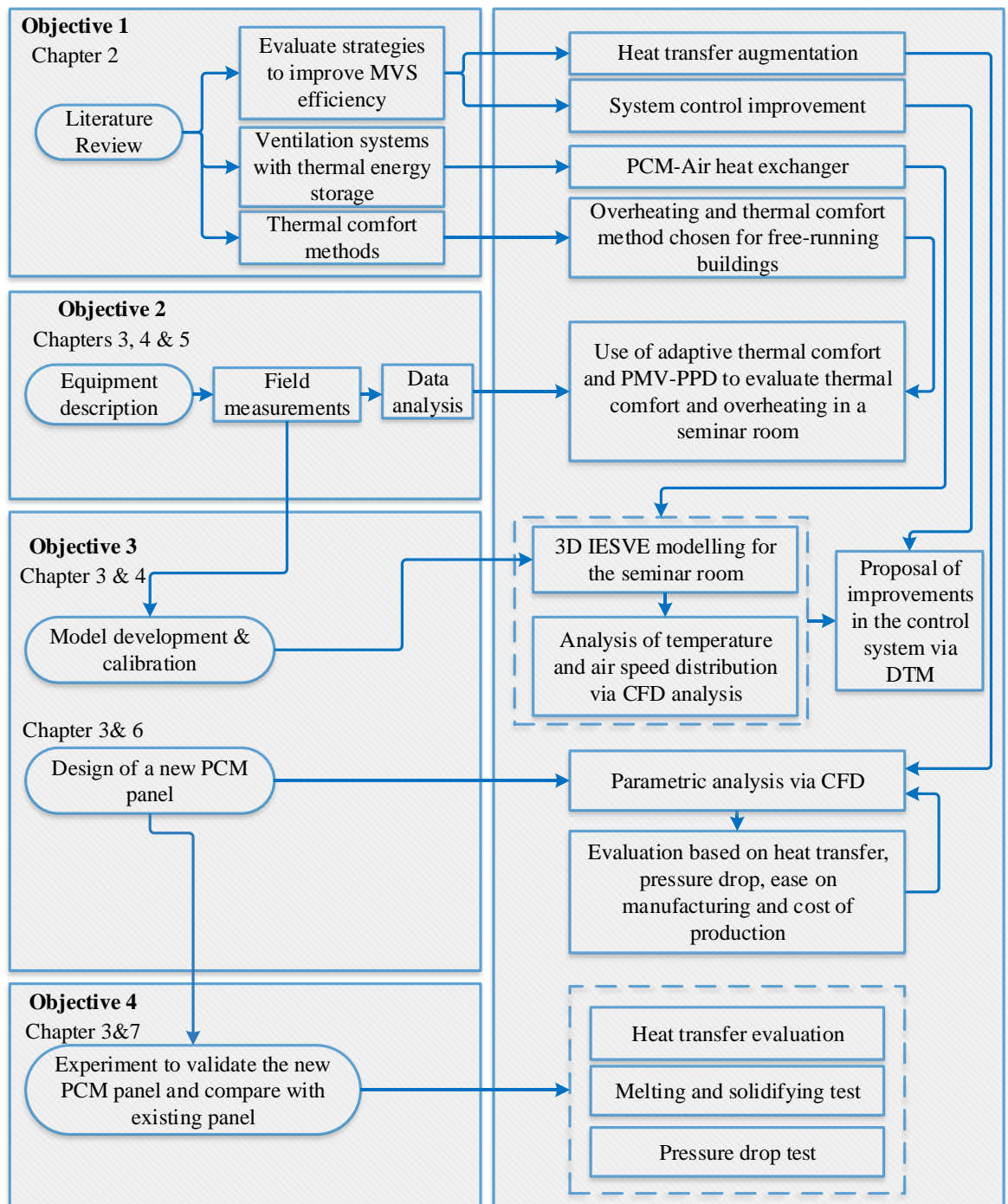
Figure 1.3 – Map of the thesis informing the structure of the thesis, objectives and how each chapter is linked.

1.3.1 Thermal Comfort and overheating performance

In 2013 a commercial PCM-Air heat exchanger (Cool-phase®) was installed in a seminar room at UWE (University of West England). The MVS has a control system able to maintain the indoor environment thermally comfortable and satisfactory indoor air quality. The data used for the control system is logged every minute and include (a) outdoor and indoor air temperature; (b) air temperature from different parts of the system; (c) outdoor and indoor CO_2; (d) outdoor and indoor Relative humidity; (e) system operation settings and (f) fan airflow. Data for one year was sourced and used to describe the performance of the system in detail.

In order to evaluate thermal comfort and avoidance of overheating, the methodology as outlined in BS EN 15251 (Ds/En, 2007) and CIBSE TM 52 (CIBSE, 2013) was adopted. For the cooling period, the analysis was based on the adaptive thermal comfort indices suited to naturally ventilated buildings or buildings using free-cooling systems. Free-cooling takes the advantage of weather conditions to offset the load on mechanical refrigeration system. Moreover, the thermal comfort during the heating period was also evaluated according to the static thermal comfort model (PMV-PPD) as recommended by current standards (BS EN 15251). Both cooling and heating season thermal comfort were evaluated by using monitored data from sensors installed in the room at seating level over one year (19/08/2015 – 25/08/2016).

1.3.2 MVS improvement

To propose improvements in the control system, system data was used to calibrate a model of the operational room using the dynamic thermal simulation program IESVE. This software has the plugin of the commercial PCM-Air heat exchanger used in this thesis (Cool-phase®). An iterative process was adopted to investigate the model predictions against system data and room measurements until prediction were within certain limits [18].

With the system calibrated, the control system was investigated by altering set-points and air flow rates until an improved performance was achieved.

One of the major considerations to not install a PCM-Air heat exchanger is the initial cost. Due to that, clients and contractors prefer to use other passive cooling techniques or install air conditioners. Improvements in the control system will enhance the MVS efficiency but will not reduce the cost of production.

The core and expensive components of a PCM-Air heat exchanger are the PCM and the panels used to encapsulate them. Improvement of these components such as the

increase in heat transfer between panel and air will increase the overall system performance and reduce the cost of manufacturing.

To achieve that, a new panel surface was designed. The whole design process was conducted via parametric CFD analysis. It started by simulating 3D designs and comparing with the existing panel in use. The mesh was generated as coarse and adapted through ANSYS Fluent, using realizable $K - \varepsilon$ turbulence model with scalable near wall treatment function. To validate the numerical model, a smooth panel was simulated and compared with Gnielinski's correlation (Gnielinski and V., 1976) for smooth channels. Moreover, a test rig analysed and validated the pressure drop of the existing panel. Based on the optimum design which considers rigidity, cost of production, ease of manufacture, heat transfer and pressure drop found on the 3D simulations, surface geometries were generated in 2D as the selected 3D design is uniform along its width. After that, the optimum design selected from 2D simulations was used for refinements. With surface dimensions unchanged, different designs evaluated the gap between panels, panel thickness and number of panels. Thus, the optimum design was selected to be fabricated.

1.3.3 Manufactured PCM panel evaluation

The selected panel was fabricated to be tested experimentally (pressure drop and heat transfer tests) and compared with the existing panel. This was achieved through three experiments carried out on purpose constructed experimental rigs.

i.   The first experiment analysed and compared three different gaps between panels at three different airflows. Resistance wires were added in half of the panel and filled with a heating compound. With a constant heat flux provided by a power supply, thermocouples logged surface panel and air temperature and were used to evaluate the heat transfer in terms of Nusselt number. To validate the experiment, a smooth panel was tested and compared with Gnielinski's Correlation.

ii. The second test analysed the pressure drop with one, two and three existing and new thermal batteries. To achieve that, a test rig with the MVS fan and ducts was constructed. A digital manometer registered the pressure drop for airflows ranging from 50 to 150 l/s. The airflow is represented as a volume flux because is the same representation used by the commercial equipment during its operation.

iii. The last test dealt with the melting and solidifying process. A test to verify the melting and solidifying time is necessary to analyse if this new configuration allows the panels to be fully solidified during night time and compare the performance of the new thermal battery against the existing. The test rig was

mounted by using MVS components (fan and ducts). As the new thermal batteries have 7 stacked panels instead of 9, a 3D carving machine was used to carve a support for the panels and to ensure the panels have the same spacing. The cycle of melting and solidifying take one day to be concluded. One, two and three thermal batteries were tested and the results of melting and solidifying between existing and new panel compared. Thermocouples measuring inlet and outlet air temperature as well as attached on panel surface confirmed the completion of melting and solidifying cycle.

1.4   Structure of the Thesis

The thesis is divided into 8 chapters. Figure 1.3 shows the structure of the thesis and each chapter is summarized as follows:

Chapter 1 presents the motivation of this research and its contribution to IEA EBC Annex 62. It presents the aims and objectives as well as a summary of the research methods used. Finally, the thesis structure is outlined.

Chapter 2 provides a literature review of thermal comfort theories and indices, ventilation systems with thermal energy storage, strategies to enhance heat transfer in channels, a numerical approach for CFD (Computational Fluid Dynamics) and Dynamic Thermal Modelling (DTM) simulations and laboratory tests commonly used to assess heat transfer augmentation in channels.

Chapter 3 describes the methods necessary to achieve the objectives. Starting with a description of the seminar room location, climate and room characteristics, it is followed by the description of how the room was monitored. Following that, it explains the plugin used to design MVS systems in IESVE, the tools necessary to calibrate the seminar room model and propose possible improvements in the control system. In order to analyse the seminar room airflow and air distribution as well as to design of the new panel, a section is dedicated to describe the boundary conditions and how the mesh was generated. The new panel design was achieved via parametric analyses and the steps of this study are also presented in this chapter. It is followed by an explanation of the experimental setup to validate the panel in three tests: (a) investigation of heat transfer and pressure drop of one panel with different gaps, (b) pressure drop and (c) melting and solidifying comparison between existing and new panel. It the end, the procedure to estimate the experimental uncertainties and the values obtained are presented.

Chapter 4 provides a description of the PCM-Air heat exchanger investigated in this thesis. Supported by system operational data, the chapter explains how the system

works and performs according to the season. An analysis via CFD simulation shows how the MVS distributes temperature and airflow within the ventilated space.

Chapter 5 presents the analysis of the operating the system in depth. The room was monitored and adaptive thermal comfort approach was applied to analyse if the room overheated or not during the cooling period. During the heating period, PMV-PPD was used. CFD simulations were also used to understand temperature and air distribution within the room. Improvements in the system are suggested through Dynamic Thermal Modelling (IESVE) which includes a plug-in of the system. In the end, a section is dedicated to present the energy consumption and performance of the MVS installed in the seminar room.

Chapter 6 presents a solution to improve the PCM-Air heat exchanger by improving the air-side heat exchange. A new surface design to encapsulate the PCM is proposed and developed via CFD simulations with the numerical model validated by correlations and a purpose designed experiment rig.

Chapter 7 presents the experimental work of the new panel that encapsulates the PCM. The design proposed in chapter 6 was fabricated and an experimental rig constructed to test it. Three laboratory tests were carried out to assess its performance and the results are presented.

Chapter 8 presents the conclusions of the research work together with recommendations for future works.

1.5   Publications

The following publications are a direct outcome of the research presented in this thesis:

<u>Peer review Journals</u>

1. T. Santos, C. Wines, N. Hopper, M. Kolokotroni, Analysis of operational performance of a mechanical ventilation cooling system with latent thermal energy storage, Energy Build. 159 (2018) 529–541. doi:10.1016/j.enbuild.2017.11.067.

<u>Peer review conferences</u>

2. T. Santos, M. Kolokotroni, N. Hopper, K. Yearley, A study of panel ridges effect on heat transfer and pressure drop in a ventilation duct, in: 38th AIVC - 6th TightVent 4th Vent. Conf., 2017.
3. T. Santos, N. Hopper, M. Kolokotroni, Performance in practice of a ventilation system with thermal storage in a computer seminar room, in: CLIMA 2016, 12th CLIMA REHVA World Congr., Aalborg, Denmark, 2016. http://vbn.aau.dk/files/233719310/paper_142.pdf.

<u>Professional Journals</u>
4. M. Kolokotroni, T. Santos, N. Hopper, Ventilative cooling of a seminar room using active PCM thermal storage, REHVA. 53 (2016) 36–40. http://www.rehva.eu/publications-and-resources/hvac-journal/2016/012016/ventilative-cooling-of-a-seminar-room-using-active-pcm-thermal-storage/.

<u>CPD article</u>

5. T. Dwyer, Operating and enhancing PCM-cooled ventilation systems in office applications, CIBSE. (2018) 55–58.

The work carried out contributed to the following official deliverables of IEA EBC Annex 62 on Ventilative Cooling:

1. Holzer, P., & Psomas, T. (2018). *Ventilative Cooling Sourcebook Energy in Buildings and Communities Programme*. Retrieved from http://venticool.eu/wp-content/uploads/2016/11/VC-Sourcebook-EBC-Annex-62-March-2018.pdf
   a. Passive cooling ventilation components, p. 66

2. O'Sullivan, P., & Adam O'Donovan. (2018). *Ventilative Cooling Case Studies Energy in Buildings and Communities Programme*. Retrieved from http://venticool.eu/wp-content/uploads/2016/11/VC-Case-Studies-EBC-Annex-62-May-2018-Final.pdf.
   a. Case study brochure, p. 170.

3. Heiselberg, P. (2018). *Ventilative Cooling Design Guide Energy in Buildings and Communities Programme*. Retrieved from http://iea-ebc.org/Data/publications/EBC_Annex_62_Design_Guide.pdf
   a. Conceptual design phase: application example of a seminar room, p. 51

In order to learn different energy efficient methods for buildings during the PhD studies, I contributed to another three projects related to the main topic of this PhD; SMART GEMS, Cool Roofs and CSEF:

- The SMART GEMS project ('SMART GEMS project', n.d.) aims to analyse all aspects of 'smart grids targeting at improving consistency, reduce security risks, load shaping and energy efficiency, optimal integration and generation-consumption matching with smart monitoring and control'. As a part of this project, I had the opportunity to do two secondments in two companies in Italy. I spent one month at AEA Ltd and one month at IDEA Ltd where a mixture of research and training was blended. Apart from the knowledge from training, it was important to my knowledge the understanding of how the industry works in conjunction with academia to develop, improve and disseminate technologies. As a contribution to SMART GEMS, I worked on the design process of a PCM tank to reduce the weight and size of a reservoir used in an HCPV (High-Concentration Photovoltaics) at IDEA Ltd.
- The Coolroofs project used the knowledge acquired during my MSc studies and was focused on the use of Cool Materials as a solution to improve energy efficiency

and thermal comfort of low-income houses in high solar radiation countries (Brazil, Jamaica and Ghana).

- CSEF (Centre for Sustainable Energy in Food chains) brings a multidisciplinary team from the universities of Brunel, Manchester and Birmingham to investigate and develop new approaches and technologies on the food chain. My studies were conducted within this Centre (Brunel University London) and along the period of the PhD, I contributed in different activities such as a working group about energy consumption in professional kitchens. This work involved researchers from all three universities.

The following papers were published as part of this work:

1. Kolokotroni, M. *et al.* (2018) 'Cool Roofs: High Tech Low Cost solution for energy efficiency and thermal comfort in low rise low income houses in high solar radiation countries', *Energy and Buildings*. Elsevier. doi: 10.1016/J.ENBUILD.2018.07.005.
2. C. Amaris, T.V.O. Santos, B.L. Gowreesunker, S.A. Tassou, M. Kolokotroni, Environmental impacts, energy and emissions reductions from food catering in the UK, in: 29th EFFoST Int. Conf. Proc., Athens, 2015.

CHAPTER 2 - LITERATURE REVIEW

Introduction to the chapter

This chapter starts with an introductory section on energy storage systems and how they can be used to reduce cooling demand in buildings. After that, it focuses on MVS with PCM-Air heat exchangers and how these have been used to provide thermal comfort in buildings with minimum energy use. As the system is used to provide thermal comfort in the conditioned space a review on thermal comfort criteria is presented. An important component of the heat exchanger is the encapsulation of the PCM because it enables the heat transfer between the PCM and air. A literature review on how this can be improved is presented. Finally, an overview of the computational tools used in this study to enable the assessment of the MVS is presented.

2.1 Ventilation systems with thermal energy storage

Energy storage is a very active area of research in recent years as it provides a sustainable solution to energy demand fluctuations and increases energy efficiency. Different energy storage methods such as electrical storage (e.g. batteries); thermal storage (sensible, latent) and thermochemical heat storage (Sharma et al., 2009) can be used. Thermal energy storage (TES) is particularly suited to buildings because a high percentage of their energy demand relates to heating and cooling needs. Sensible TES utilizes the heat capacity properties of materials while latent TES uses heat exchanges via the phase change of materials, usually between solid and liquid for building applications. Latent thermal energy storage (LTES) can provide more energy per volume than a sensible thermal storage system, making LTES a promising solution for buildings either integrated into building envelope (passive LTES) or in ventilation systems (active LTES) to reduce cooling demand (Aneke and Wang, 2016) or reduce heating demand (Labat et al., 2014).

Active LTES integrated into a mechanical ventilation system (PCM-Air heat exchangers) received attention during the last two decades. PCM-air heat exchangers use the principle of thermal storage through latent heat in areas where night temperatures are cold enough to charge (solidify) the PCM and use it to cool the environment during the day. However, it performs better in places where diurnal temperatures range is higher than 15 °C (Raj and Velraj, 2010).

A room ventilation system incorporating heat pipes embedded in the PCM thermal battery was tested experimentally and numerically for applications in the UK 20 years ago (Turnpenny et al., 2000). In this test, a low powered fan was responsible to charge the PCM (Figure 2.1) allowing the night coolness be stored and used for cooling on the following day. The same system was then improved by Turnpenny et al.

(Turnpenny et al., 2001) where a series of heat pipes were arranged in a 1.20 m wide ceiling fan (Figure 2.2). Heat transfer rates of up to 200 W were measured under simulated UK summer conditions comparing the system favourably to conventional air conditioning and other technologies such as chilled beams. Since then, many investigations through experiments and simulations followed.
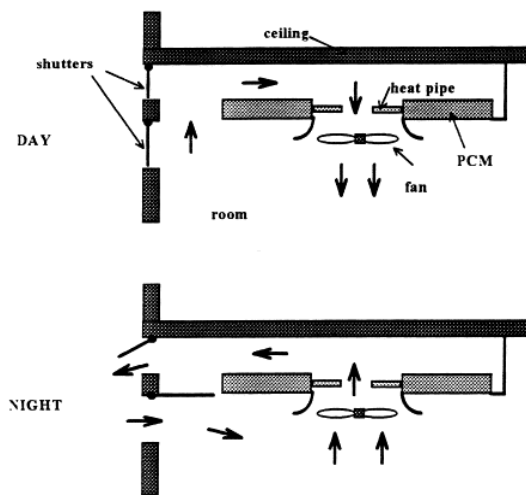
| Figure 2.1 – Schematic of proposed cooling system (Turnpenny et al., 2000) | Figure 2.2 – Heat pipe/PCM unit with fan (Turnpenny et al., 2001). |
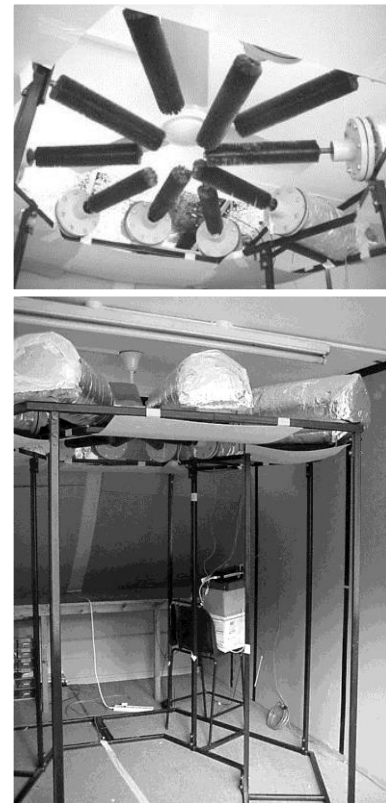
A study performed in China proposed to use PCM packed bed as a storage system (Yanbing et al., 2003). The experimental part of this work carried out for 10 days and used 150 kg of PCM with a latent heat of 190 kJ/kg and melting range of 22-26 °C. As a result, the system was capable to maintain the room thermally comfortable.

In order to investigate the thermal behaviour of a free cooling system installed in four cities in France, Borderon et al. (Borderon et al., 2015) performed a numerical analysis via TRNSYS and MATLAB with results showing that the system is not optimally designed. Recommendations to increase the airflow was recommended to achieve better results, however, pressure drop and sizing of the fans need to be taken into consideration. 6 PCM's with different melting points and configurations were simulated. The result shows that even in cities located in the same country such as France, different PCM configurations (melting point, airflow and number of PCM units) should be used.
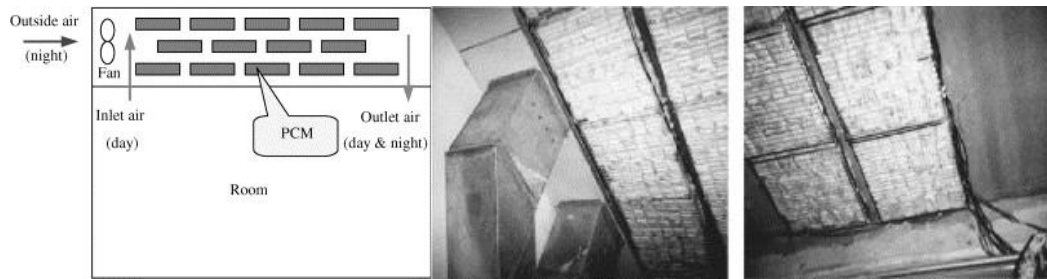
Figure 2.3 – packed bed storage proposed by Yanbing (Yanbing et al., 2003)

Zalba et al. (Zalba et al., 2004) performed a parametric analysis to investigate a prototype where commercially flat panels were used. His findings show the dominance of inlet temperature over other parameters such as encapsulation thickness and airflow rate. The study also confirmed the feasibility (both technical and economical) of the system when compared with conventional cooling systems.

A direct heat exchanger with granules including PCM in a porous media of 1-3 mm and paraffin wax was proposed by Nagano (Nagano et al., 2004). The system was improved by Takeda (Takeda et al., 2004) with results showing a decrease in ventilation load between 42.8 % to 62.8 %. The authors also pointed out that the system depends on diurnal temperature variation instead of average temperature. Nagano also proposed an underfloor cooling system with PCM (Nagano et al., 2006) (Figure 2.4). Granules of PCM with a melting point of 20 °C were directly embedded in the floor. A scale model was constructed and results measurements indicated that 89 % of the cooling load for an office building can be stored each night.
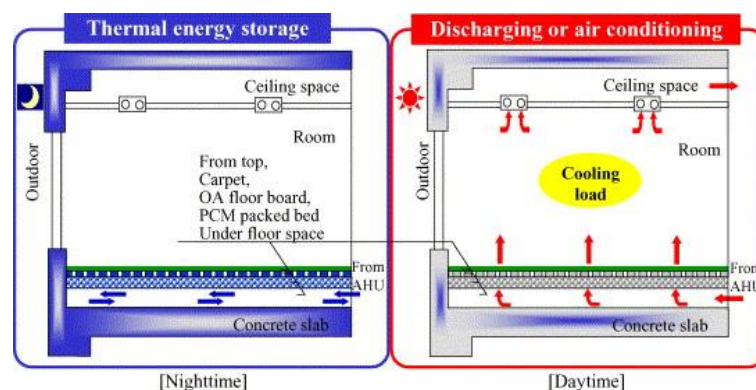
Figure 2.4 – Schematic underfloor cooling system model by Nagano (Nagano et al., 2006)

Stritih and Butala (Butala and Stritih, 2009) designed a metallic PCM cold storage container capable to be installed into the ceiling. Internal and external fins were attached to the metal box intended to increase the heat transfer (Figure 2.5).

Laboratory and modelling results presented a good agreement with the system being capable to reduce temperatures from 27 to 24 °C for more the 2.5 h when a flow rate of 7.8 l/s was used. This represented savings up to 87 %.
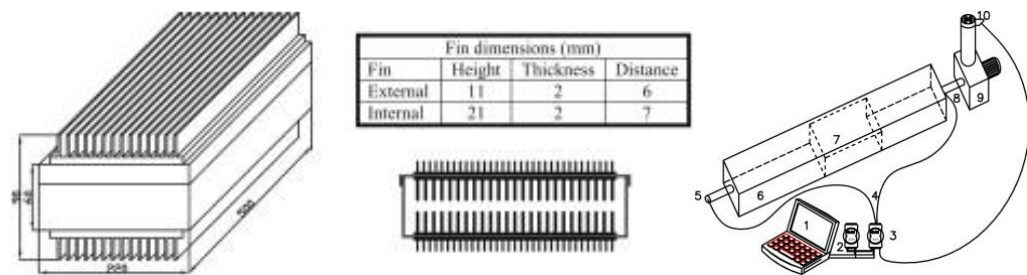
Figure 2.5 – Metallic box design and test rig for measuring cold storage efficiency (Butala and Stritih, 2009)

Lazaro et al. (Lazaro, Dolado, Marin, et al., 2009) designed two real-scale PCM-Air heat exchanger prototypes for free cooling based on the results obtained by Zalba et al. (Zalba et al., 2004) (one utilizing commercial aluminium pouches and the other commercial aluminium panels, Figure 2.6). The author proved through his laboratory tests that is better to enhance the heat exchanger design rather than increase PCM conductivity levels. Based on that, Lazaro proposed a model (Lazaro, Dolado, Marín, et al., 2009) consisting of 18 commercial PCM panels. With this, it was possible to design the number of modules based on the cooling power needed and the duration of time required to maintain the temperature.

Figure 2.6 –Pouch and PCM panel used by Lazaro et al. (Lazaro, Dolado, Marín, et al., 2009; Lazaro, Dolado, Marin, et al., 2009)

Good results of free cooling application were presented through simulations in Athens summer where the city has a daily mean temperature up to 26.4 °C and varies slightly during the day ± 4.87 K (Medved and Arkar, 2008). Satisfactory results were also achieved in Spain (Macias et al., 2006). In hot climates with a lower daily temperature amplitude, Waqas & Kumar (Waqas and Kumar, 2011) analysed different charging PCM's conditions and suggested the possibility to use free cooling. His prototype used a commercialized PCM salt hydrate (SP29 by Rubytherm GmbH) with a phase change temperature of 28-29 °C. The PCM was enclosed in a flat galvanized

steel (0.5m x 0.5m x 0.01m) and tested through three different inlet airflows for charging (20, 22 and 24 °C) and three for discharging (36, 38 and 40 °C). It was found that changing the inlet temperature leads to considerable increase in time for a complete solidification. When temperatures increase from 22 to 24 °C, 55 % more time is required to solidify and when temperatures decrease from 22 to 20°C, 33 % less time is necessary. The authors also noticed an increase of 16 % when the airflow was augmented from 4.0 to 5.0 m^3/h. In another study, Waqas and Kumar (Waqas and Kumar, 2011) numerically analysed a free cooling system in Islamabad, Pakistan. They maximized the system by selecting a PCM melting point equal to the comfort temperature of the hottest summer month, which seems to be the most influential parameter on that system.

Antony Aroul Raj and Velraj (Antony Aroul Raj and Velraj, 2011) developed a thermal storage for free cooling consisting in a shell of 750 mm in diameter with several tubes where the air can pass (Figure 2.7). With CFD results validated by laboratory experiments, a steady state analysis was performed to determine the pressure drop across the modules and spacers as well as the flow and the heat transfer in the model. With this, the geometry and the flow parameters were properly selected for a given inlet condition. Furthermore, a transient analysis determined the suitability of the selected geometry and PCM features. The authors noticed that the DSC (Differential Scanning Calorimetry) analysis should be made according to the cooling/heating rate of the application for more reliable results between theoretical and practical applications.
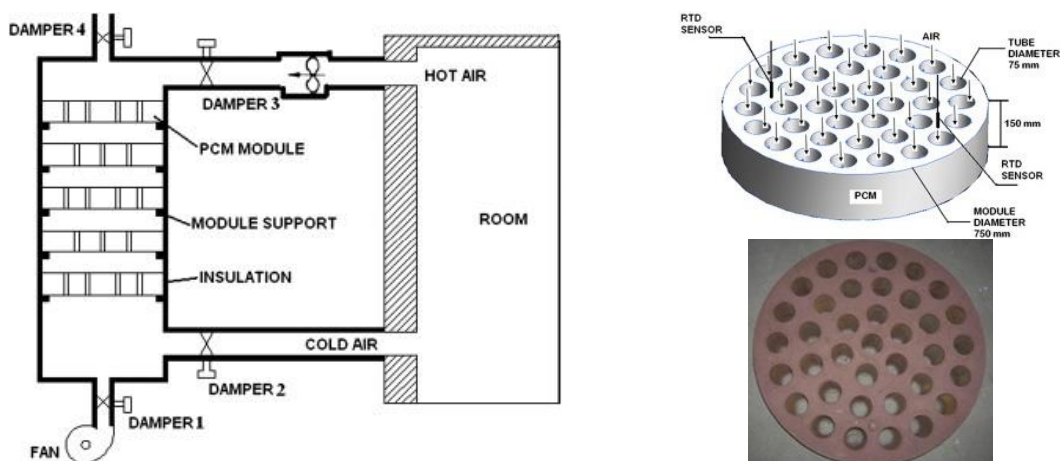
Figure 2.7 – Test rig and shell to encapsulate the PCM (Antony Aroul Raj and Velraj, 2011)

An innovative system was designed by Jaber and Ajib (Jaber and Ajib, 2012). As it can be seen from Figure 2.8, it is an Indirect Evaporative and Storage Unit (IESU) for domestic applications. It consists of a heat exchanger made of corrugated flat tubes with PCM layers and constant air flow in one direction. Perpendicular to its direction,

the air can vary according to the period of the year every 6 min. A parametric analysis investigated parameters related to the PCM storage configuration and operating conditions. The results showed that an increase in length rather than in width is more influential for the heat transfer. Furthermore, an optimised design was found and able to provide savings up to 80 % of the annual cooling demand for a payback period of 7.87 years.
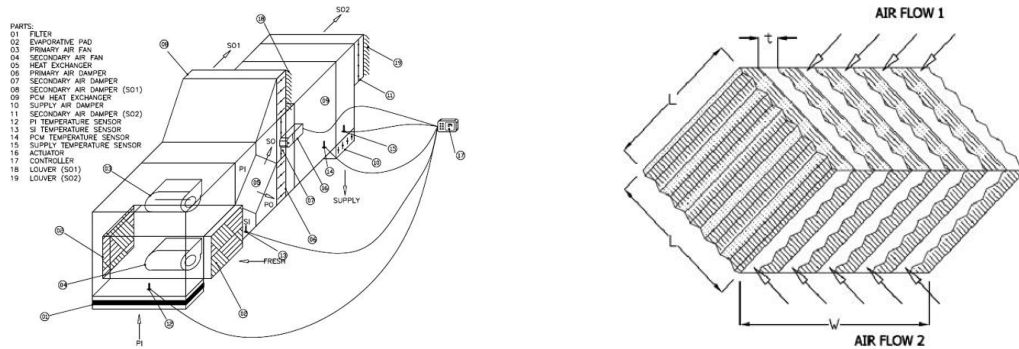
Figure 2.8 – Test rig and IESU proposed by Jaber and Ajib (Jaber and Ajib, 2012).

Rouault et al. (Rouault et al., 2013) developed a numerical model of a Latent Heat Thermal Storage (LHTS) to be used in lightweight buildings during summer time. The model was able to simulate the thermal behaviour of different energy storage systems made up with different rectangular tubes (as seen in Figure 2.9). The results showed that rectangular tubes positioned vertically present slightly better results than the horizontal tubes. Moreover, the authors suggest that improvements in heat exchange are needed to increase the system cooling power.
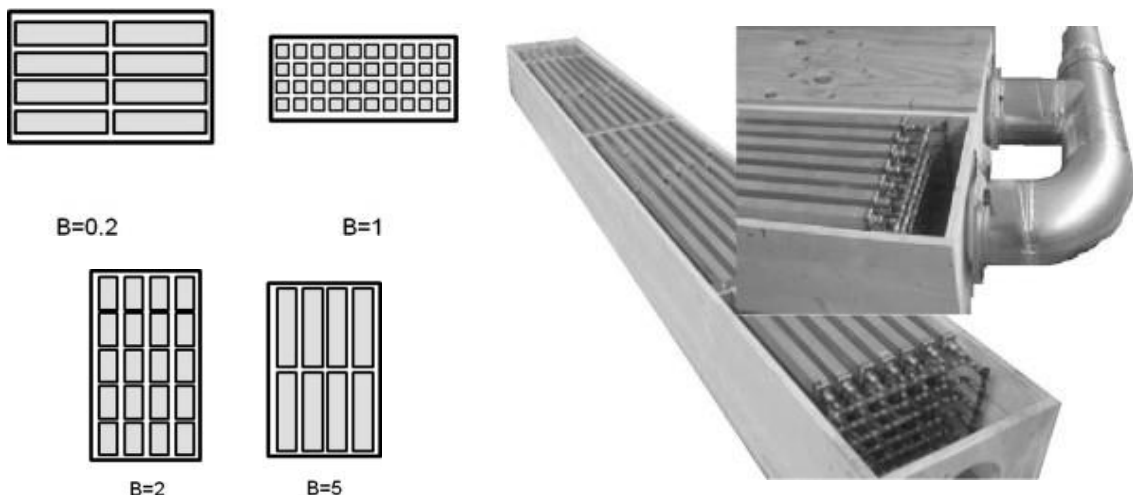
Figure 2.9 – Test rig and shell to encapsulate the PCM (Rouault et al., 2013)

Using solar and night ambient temperature, Waqas et al. (Waqas et al., 2017) used a PCM-Air heat exchanger to keep a building within thermal comfort temperatures in

a dry-cold and dry-hot climate in Islamabad, Pakistan. By adding a solar air collector, the equipment can now be used for both winter (from 00:00–8:00) and summer (from 08:00–00:00). The authors found that a PCM with a melting point of 27.5 °C represent the best solution for the whole year considering building location. When only the summer is taken into consideration, the optimum melting point is 29 °C. This allows a reduction of 15 % in the cooling load during summer and reduces the heating load by 3 % during winter time. The system was maximized during the winter period when the melting point of 21 °C was used. However, this melting point is not suitable for summer cooling.
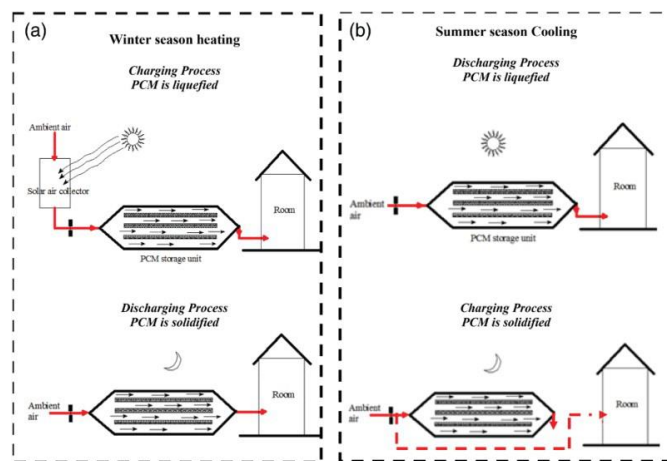
Figure 2.10 – Schematic PCM heat-Air heat exchanger operation for winter season heating and summer season cooling (Waqas et al., 2017).

Osterman et al. (Osterman et al., 2015) performed a parametric analysis (inlet air temperature, airflow and air gap) in order to evaluate the heat transfer of a thermal battery for heating and cooling purposes. Using an aluminium panel (Figure 2.6, right) with a paraffin (RT 22HC) PCM. Depending on panels' orientation (vertical or horizontal, Figure 2.11), the thermal battery can hold 15 (with an air gap of 8mm) or 30 (with an air gap of 10mm) panels where each panel hold 1003g of paraffin. For the melting test, three different inlet temperatures were tested (30, 35 and 45 °C) for an initial temperature of 16 °C. The results show melting times of 8, 12.5 and 18.5h respectively for 45, 35 and 30 °C. During freezing period, an initial temperature of 26 °C reflected in a solidification time of 13.5 and 11h for inlet temperatures of 9 and 4 °C, respectively. The authors found that when the airflow is increased two times, the thermal power also increases by the same factor. The distance between panels was also a point of interest where a smaller distance will allow more panels to be stacked. By testing four distances for melting and keeping the airflow constant, the distance varies between either 8 or 16mm with results showing that the bigger air gap represents approximately 80 % of the smaller air gap thermal power.

In an experimental study performed by Iten and Liu (Iten and Liu, 2015), the results showed that the air velocity had a higher impact for both charging and discharging period. Higher air velocities achieved higher cooling and heating loads but rapidly drops as the phase change ceased. Conversely, lower air velocities can maintain cooling and heating loads for a longer time.
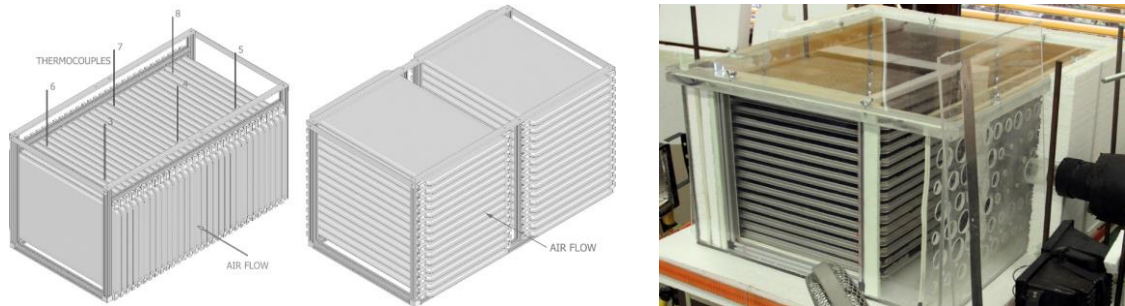
Figure 2.11 – Orientation of the panels (Osterman et al., 2015)

A review (Kasaeian et al., 2017) critically discusses experimental studies of PCM applications in buildings dividing them into free cooling passive and active methods, active and passive heating methods and hybrid applications. It describes developments in ventilation and air-conditioning systems based on PCMs as well as nano-enhanced PCMs. The extensive literature review has revealed that active LTES incorporated within the ventilation system can overcome heat exchange limitations of passive systems because of the increased heat transfer by convection and LTES is an appropriate solution to increase energy efficiency of cooling systems in buildings.

Another review (Souayfane et al., 2016) focusing on cooling LTES applications summarises the experimental results of PCM-Air heat exchangers and discusses the importance of PCM selection according to cooling needs due to internal heat gains and climatic conditions. The work points out that PCM melting temperature is one of the most influencing parameters for the success of the application. Such recent reviews have also highlighted that limited analysis has been published from operational buildings with commercially installed PCM-Air heat exchangers; such results are important to accelerate inclusion in designs for new and refurbished buildings.

A recent review (Zeinelabdein et al., 2018) updated the discussions of latent storage systems for free cooling in buildings and highlight that climate conditions, phase change temperature, encapsulation of the PCM, heat transfer problems (due to low thermal conductivity, incongruent melting, and supercooling of PCMs) and the stability of the PCM are the major issues that affect thermal performance and application of free cooling technologies.

The literature discussed above revealed that few commercial PCM-Air heat exchangers are available in the market as well as few studies on its performance during real operation. Thus, this study carried out a comprehensive analysis of an operational MVS with PCM-Air heat exchanger through a case-study of a seminar room in the UK. To correctly assess the provision of thermal comfort of the PCM-Air heat exchanger, it is important to understand what thermal comfort is and how to estimate if a space is thermally comfortable or suffering from overheating. Current criteria and indices are presented in section 2.2. In this study, the DTM software IESVE was used to evaluate the performance of the MVS examined in terms of provision of required environmental conditions and thermal comfort and show how the system can be improved when the control system is better tuned. A description of IESVE and how PCM-Air heat exchange is simulated is included in section 2.4.1.

Improvements in tuning are restricted as PCM-Air heat exchanger performance is limited by the cooling capacity of the PCM. The literature review revealed that a critical component in the PCM-Air heat exchanger is the design of the encapsulation panel and in particular, the heat transfer channels. One solution is to increase the PCM material but this will result in larger space requirements or develop a material with higher conductivity but this will increase the final cost of the MVS. Another solution is to increase the heat transfer rate of the existing encapsulation as PCM materials have a lower thermal conductivity. A literature review on how channels can be used to enhance heat transfer is presented in section 2.3 while the CFD tool used for their study is presented in section 2.5.

2.2   Thermal comfort

Thermal comfort is a condition where the mind feels satisfied with the thermal environment (ASHRAE, 2013c). As defined, thermal comfort is a subjective concept as it depends on both environment and occupant sensation. In terms of health, thermal discomfort is a body warning because our human body is regulated to maintain a constant internal temperature. If the surrounding temperatures are too high or too low, the body will have difficulties to regulate. This can lead to a thermal stress when the body is not able to regulate the temperature and occurs mainly during the summer where the average temperature is high (Oliveira Santos T.V., 2011). As an example, during the summer of 1995 in Chicago (Rosenzweig et al., 2005), a prolonged heat wave elevated the mortality rate of mainly elderly people living in apartments with poor air circulation or lack of cooling. In 2003, Europe faced a heat wave causing more than 70,000 deaths in which France was the most affected (Robine et al., 2008; Dhainaut et al., 2004). In another heat wave, in 2006, about 2065 excess deaths were identified in France. This is approximately 4,400 fewer deaths than the heat wave registered in 2003. This reduction may be interpreted as a

decrease in vulnerability of heat and increased awareness of the risk related to extreme temperatures (Fouillet et al., 2008). Policies such as this should continue and in addition, strategies to improve the thermal comfort must be tackled.

To assess thermal comfort, two models are commonly used and in accordance with ISO standards: the heat balance model (also called static model) and the adaptive thermal comfort model (de Dear and Brager, 1998; ISO, 2005). The heat balance model is based on laboratory experiments at steady state where six factors are taken into consideration; four related to environmental conditions and two behavioural. These are air temperature, mean radiant temperature, relative air velocity and air humidity, clothing insulation and metabolic rate. Heat balance equations were then used to evaluate the thermal comfort of the subjects and to derive indices. These are PMV-PPD (Predicted Mean Vote – Predicted Percentage Dissatisfied), (Fanger, 1972) which were adopted by professional bodies and ISO standard (ISO, 2005). PMV is a thermal scale index used to predict the average thermal sensation experienced by a group of occupants in a certain space for a given insulation and metabolic rate (ASHRAE, 2017). This psychological strain is defined as 'the difference between the internal heat production and the heat loss to the actual environment for a person kept at the comfort values for skin temperature and sweat production at the actual activity level' (Fanger, 1972). The scale (Table 2.1) varies from Cold (-3) to Hot (+3) or according to Bedford, from 1 (Much too cold) to 7 (Much too hot).

Table 2.1 – Two PMV scales commonly used for thermal comfort

ASHRAE scale		Bedford scale	
Hot	3	Much too warm	7
Warm	2	Too warm	6
Slightly warm	1	Comfortably warm	5
Neutral	0	Comfortable neither warm nor cool	4
Slightly cool	-1	Comfortably cool T	3
Cool	-2	Too cool	2
Cold	-3	Much too cool	1

To predict the percentage of dissatisfied occupants, the PMV was extended to PPD (Predict Percentage Dissatisfied). It is a function of PMV and varies from 0 (or neutral) to 100 %. BS EN 15251 (Ds/En, 2007) recommends that an interior space is acceptable if less than 6, 10 or 15 % respectively for categories I, II and III are dissatisfied. For values above 15 %, the building is considered category IV.

To estimate PMV and PPD eq. (2.1) is used. '*M*' is the metabolic rate which is the rate of energy per unit of time needed to keep the body functioning and '*L*' is the thermal load on the body established by Rohles and Nevins (Rohles and Nevins, 1971) and is

the difference between internal heat production and loss to the environment (ASHRAE, 2017).

$$PMV = [0.303\,exp\,(-0.036M) + 0.028]L$$
$$PPD = 100 - 95[-(0.03353\,PMV^4 + 0.2179\,PMV^2)]$$

(2.1)

For designers, it is necessary to know what clothing the occupants will wear as well as their activities. This might be a problem if different activities are taken place in the same environment.

The method above is recommended for mechanically conditioned spaces ((Ds/En, 2007)).

For buildings without mechanical cooling (also termed free-running buildings), the adaptive thermal comfort model is more suitable as occupants' satisfaction occurs through adaptation to the indoor environment.

This interaction can be distinguished into three categories of thermal adaptation (de Dear and Brager, 1998):

i. Behavioural adjustment – Modifications that a person might consciously or unconsciously make to feel more comfortable. These adjustments are also subdivided into personal adjustment (e.g. remove or add clothes, carrying umbrellas etc.); technological responses (e.g. turn on/off an air conditioner) and cultural modifications such as dress code.

ii. Physiological adjustment – Involves the body adjustment to the environment and leads to a gradual reduction in thermal strain. Physiological adaptation can be subdivided into generic adaptation and acclimatization.

iii. Psychological adjustment – Refers to previous sensorial experience and expectation related to a particular environment (e.g. fear of heat and sun exposure, expectation etc.).

Following previous studies, de Dear (de Dear and Schiller Brager, 2001) and many others confirmed that PMV is not an appropriate model for naturally ventilated buildings which led to the adoption of adaptive thermal comfort in current standards ((CIBSE, 2013)). The expression that describes thermal comfort temperature is:

$$T_{comf} = 0.33T_{rm} + 18.8$$

[ºC]   (2.2)

Where T_{rm} is the exponentially weighted running mean of the daily mean outdoor air temperature, given by:

$$T_{rm} = (1 - \alpha)(T_{od-1} + \alpha\,T_{od-2} + \alpha^2\,T_{od-3}\,...)$$

[ºC]   (2.3)

Where α is a constant (< 1) and T_{od-1}, T_{od-2}, etc. are the daily mean temperatures from yesterday, the day before yesterday and so on.

By using data from comfort surveys around Europe, the best value to estimate the thermal comfort temperature is when $\alpha = 0.8$ (CIBSE, 2013). Due to the weight of α, as it can be seen from eq. (2.3), the temperature lose its influence when days are moving away. When a whole range of days are not available, BS EN 15251 (Ds/En, 2007) gives an estimated calculation by using the last seven days:

$$T_{rm} = \frac{T_{od-1}+0.8T_{od-2}+0.6T_{od-3}+0.5T_{od-4}+0.4T_{od-5}+0.3T_{od-6}+0.2T_{od-7}}{3.8} \qquad [°C] \quad (2.4)$$

BS EN 15251 also points out that the comfort temperature established by eq. (2.2) can vary based on the type of building, categorized as Category I, II, III and IV with explanation and acceptable range presented in Table 2.2:

Table 2.2 – Acceptable temperature ranges for free-running buildings and suggested applicability according to BS EN 5251 (Ds/En, 2007)

Category	Explanation	Suggested acceptable range (K)
I	High level of expectation only used for spaces occupied by very sensitive and fragile persons	±2
II	Normal expectation (for new buildings and renovations)	±3
III	A moderate expectation (used for existing buildings)	±4
IV	Values outside the criteria for the above categories (only acceptable for a limited period)	>4

Temperatures can exceed the acceptable range shown in Table 2.2, however, if high temperature persists, the indoor space could be suffering from overheating. This condition was defined by CIBSE Overheating Task Force ((CIBSE, 2013)) for both new and existing buildings. For new designs, the use of dynamic thermal modelling (DTM) is recommended where DSY (Design Summer Year) weather files are recommended. For existing buildings, thermal comfort can be assessed by monitoring the operative temperature in a number of representative spaces.

Simulation or monitoring results, make it possible to determine if a building overheats or not. For the summer period, two out of three criteria must be met (CIBSE, 2013):

1. Hours of Exceedance: The number of hours operative temperature exceeds the maximum acceptable operative temperature (θ_{max}) by 1K, must not exceed 3 % of the total occupied hours or 40 hours, during the five summer months.
2. Weighted Exceedance: The sum of the weighted exceedance for each degree K above θ_{max} (1 K, 2 K and 3 K) is ≤ 10.0.

3. Threshold/Upper Limit Temperature (θ_{upp}): The measured/predicted operative temperature should not exceed the θ_{max} by 4K or more at any time.

As this study focussed on the MVS with PCM-Air heat exchanger in a seminar room, thermal comfort and indoor air quality requirements in schools are outlined. Until recently in the UK, overheating criteria for schools were based on fixed air temperature and applied for the cooling season and occupied period from 1st May to 30th September as follows:

a) There should be no more than 120 hours when the air temperature in the classroom rises above 28°C;
b) The average internal to external temperature difference should not exceed 5°C (i.e. the internal air temperature should be no more than 5°C above the external air temperature on average);
c) The internal air temperature when the space is occupied should not exceed 32°C.

This criterion was updated and now the current guidance for schools is provided by the Education Funding Agency (Education Funding Agency, 2014a). It includes guidelines on ventilation, thermal comfort and indoor air quality, including the Services Output Specification (Education Funding Agency, 2013), the Baseline Design Environmental Services and Ventilation Strategy (Education Funding Agency, 2014b) and the Building Bulletin 101 (Regulations Standards Design Guidance, 2006). These documents are now aligned with CIBSE's guidance on prevention of summertime overheating (CIBSE, 2015b, 2013, 2015c, 2010) which refer to calculations according to European Standard BS EN 15251 and UK Building Regulations Parts L (Conservation of Fuel and Power) and F (Ventilation) (Ministry of Housing, 2010).

In terms of IAQ based on CO_2 concentration, the guidance states that the average concentration of carbon dioxide should not exceed 1500 parts per million (ppm) when measured at seated head height, during the continuous period between the start and finish of teaching on any day.

This criterion was updated to the following criteria (Education Funding Agency, 2014b):

1. Ventilation should be provided to limit the concentration measured at seated head height in all teaching and learning spaces.
2. Where mechanical ventilation is used or when hybrid systems are operating in mechanical mode, i.e. the driving force is provided by a fan, sufficient fresh air should be provided to achieve a daily average concentration of carbon dioxide during the occupied period of less than 1000ppm and so that the maximum

concentration does not exceed 1,500ppm for more than 20 consecutive minutes each day.

2.3 Heat transfer augmentation in PCM encapsulation channels

The introduction of ridges, fins, dimples and grooves are techniques commonly used to increase the heat transfer over a channel. These turbulators are widely applied and studied in engine turbine blades to protect them from exceeding the maximum allowable temperature (Figure 2.12).

In PCM-air heat exchangers, turbulators are used to increase cooling performance. However, if the turbulence increases the pressure drop, an oversized fan will be demanded and energy consumption will rise. Therefore, a design with higher thermal efficiency and small pressure drop is desired and motivational for researchers.
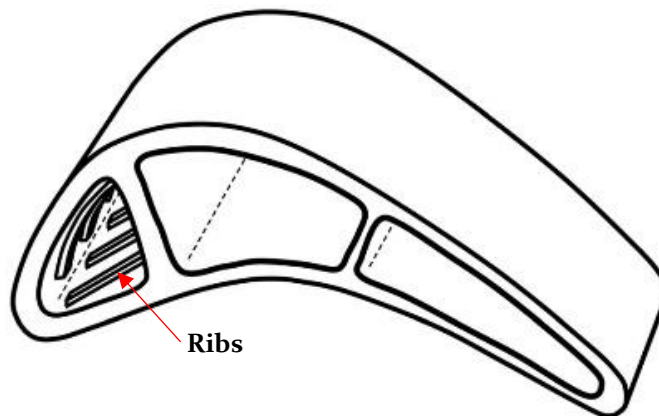
Figure 2.12 – Ribbed channel in a gas turbine blade (Domaschke et al., 2012)

Moon (Moon et al., 2014) analysed sixteen ridge shapes (with different geometries) by varying pitch ratio through CFD simulations. Results show that boot-shaped ridge presented the best results in terms of heat transfer with a pressure drop similar to a square ridge for a Reynolds number between 5000 and 50,000.

The inclusion of dimples, protrusions or both dimples and protrusions also show good results in heat transfer augmentation. Liu et al. (Liu et al., 2015) found, via ANSYS Fluent, that secondary protrusions cause downward flow, reducing recirculation in the adjacent primary dimple and improving the reattachment. In all cases studied, the area-averaged Nu/Nu_o enhanced between 1.8 and 1.5 in average for Reynolds ranging from 5000 to 27,500. Hwang et al. (Hwang et al., 2010) experimentally analysed at low Reynold numbers ($1{,}000 < Re_{Dh} < 10{,}000$) via CCD camera that dimple-protrusion periodically patterned had Nu/Nu_o of 6.0 (in average for a single-side wall and $Re = 1000$) and 10.4 (in average for a double-side staggered

wall) and an overall average of Nu/Nu_o=2.5 for $Re = 10,000$. The result was compared with a previous experimental study (Hwang et al., 2008) where dimples or protrusions were patterned in a single and doubled wall. Significant differences were found in the doubled protrusion wall in comparison with other walls studied (Nu/Nu_o of 14 against ~6.5 for Re=1000 and 8 against ~3 for $Re = 3,000$). However, a double protrusion wall presents a friction factor 4 times higher. This was confirmed by Yang et al. (Yang et al., 2017) by introducing symmetric and staggered squared high ribs in channels after validating the model via experiment. These results show that a larger blockage ratio corresponds to a higher friction factor and heat transfer. The symmetric arrangement and higher blockage increased Nu/Nu_o in the range of 6-7 and the staggered arrangement and higher blockage 3.5.

As described above, dimpled surfaces significantly enhance the heat transfer with a minimum cost in pressure drop. However, depth ratios (the ratio of depth r to diameter D) higher than 30 %, results in a reduced heat transfer (Park et al., 2004; Chen et al., 2012). Chen et al. (Chen et al., 2012) identified a significant increase in terms of heat transfer when an asymmetric dimple (teardrop) was used in comparison to a dimpled surface (4 % when $h/D = 10$ % and 23 % when $r/D = 15$ %). For both cases, the pressure drop decrease 1 and 8 % in comparison to a dimpled surface.

Moreover, Liou et al. (Liou et al., 2016) analysed the Nusselt number of a 90° ribbed opposite walls with two static two-pass parallelogram channel for Reynolds number between $5,000 - 20,000$. An atomizer introduced filtered compressed air and salt water to the system and a speed camera (Photron FASTCAM SA3 120 K M2, mounted with a Nikon Nikkor 50 mm lens) recorded the particle images. The images were then processed via modified Matlab-based package PIVlab to obtain the raw vector fields. At the end, the Thermal Enhancement Factor (TEF) were about 66 % and 28 % higher than a parallelogram smooth channel (Liou et al., 2014) for respectively Re = 5,000 and 20,000. The increase in pressure drop in a higher rate than the Nusselt number explains the reduction in performance for high Reynolds number.

The addition of turbulators in pipes is also being studied. Bile et al. (Bilen et al., 2009) tested three different grooved tubes shapes (circular, trapezoidal and rectangular) from $Re = 10,000 - 38,000$ for a length to diameter ratio of 33. The circular groove obtained the highest increase in heat transfer (63 %), followed by trapezoidal (58 %) and rectangular (47 %). Interestingly, the friction factor has nearly the same values for all three grooves.

Instead of attaching one integer rib along the width of the channel, ribs can be broken down to reduce pressure loss and also be positioned in a different orientation. Tanda (Tanda, 2004) studied a transverse integer and broken ribs and also a V-shaped

broken rib (at 45° and 60°) with different 3 different pitch-to-height ratios (Figure 2.13).

The results show the highest Nu/Nu_o for transverse broken ribs with pitch-to-height $4 \left(\frac{Nu}{Nu_o} = 3.2 - 2.4 \right)$ and followed by a transverse pitch-to-height of 8 and a V shaped rib for a $Re = 8,900 - 36,000$. Kim et al. (Kim et al., 2009) studied the effect of angled rib turbulators in a double-side wall cooling channel at $Re = 10,000$. Results through simulations found an optimized value of Nusselt ratio of 2.9 at 53.41° for a simulated range from 30° to 80°.

When ribs are detached as the 60°-broken shape (Figure 2.14) experimented by SriHarsha et al. (SriHarsha et al., 2009), ribs did not help to enhance heat transfer.
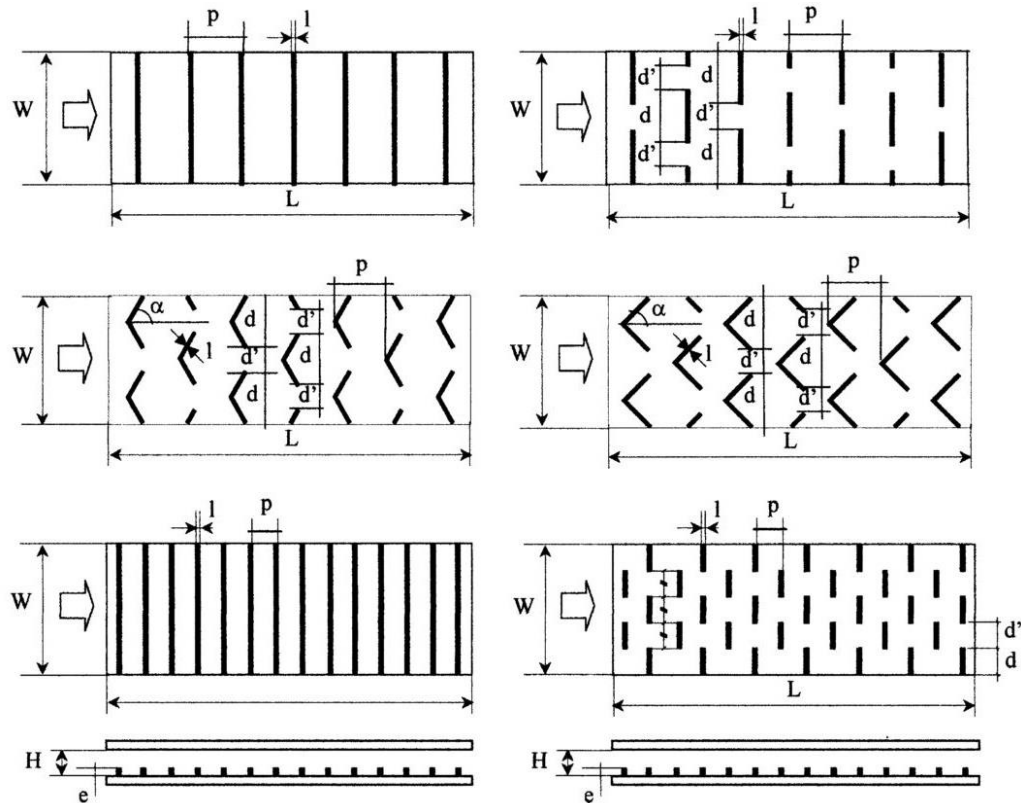
Figure 2.13 – Example of ribs studied by Tanda (Tanda, 2004)
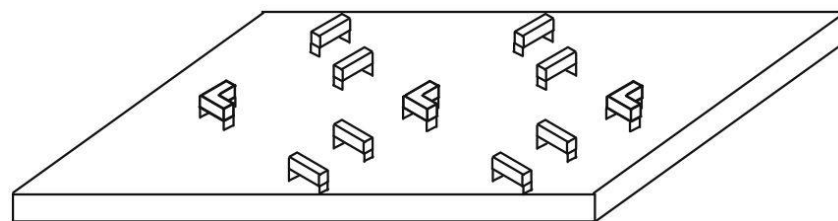
Figure 2.14 – Detached broken shape experimented by SriHarsha et al.

Alternatively, protrusions and grooves can be combined. Zhang et al. (Zhang et al., 2017) compared the heat transfer in a channel with a single-wall composed by one upstream rib and one downstream groove with one upstream protrusion in three different positions in a channel and one downstream groove and three upstream protrusions in parallel followed by one groove. The result shows that parallel protrusions upstream to grooves perform better $\left(Re = 5000, \frac{Nu}{No_o} = 1.40; Re = 20,000, \frac{Nu}{No_o} \cong 1.44\right)$ than other cases $\left(Re = 5000, \frac{Nu}{No_o} \cong 1.35; Re = 20,000, \frac{Nu}{Nu_o} \cong 1.3 - 1.32\right)$ with an increase in the average Nusselt number ratio when the Reynolds number increases.

Promvonge and Thianpong (Promvonge and Thianpong, 2008) tested four different shaped ridges (Figure 2.15): wedge pointing upstream, wedge pointing downstream, triangular and rectangular ridge staggered and in-line over a turbulent channel ($Re = 4000 - 16,000$).
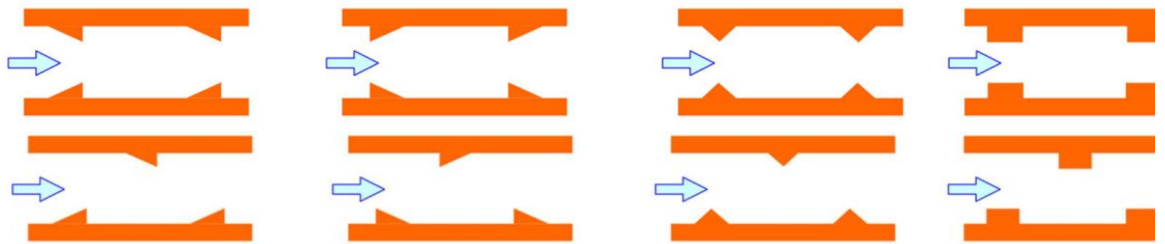
Figure 2.15 – Inline and staggered ridges used in Promvonge and Thianpong experiment (Promvonge and Thianpong, 2008)

The result shows improvements in heat transfer when compared to a smooth channel. The wedge pointing downstream in-line presents best performance in terms of Nusselt number ratio ($Nu/Nu_o \cong 4.4$) and the rectangular in-line ($Nu/Nu_o \cong 3.7$), the worst. When pressure drop is taken into account to estimate the Thermal Enhancement Factor $\left(\eta = \left(\frac{Nu}{Nu_o}\right)/\left(\frac{\Delta p}{\Delta p_o}\right)^{1/3}\right)$, the triangular staggered was the best ($\eta \cong 1 - 1.1$) followed by triangular in line and staggered upstream wedge. After that, Thianpong et al. (Thianpong et al., 2009) experimentally studied different heights of triangular ridges staggered and in-line through a constant heated-flux channel for Reynolds from 5,000 to 22,000. Results show an increase of $\frac{Nu}{Nu_o}$ of approximately 1.8 – 4 and a variation of thermal performance (η) up to 1.3.

As a conclusion, the studies presented above confirmed that the inclusion of ridges over a channel is an efficient solution to enhance the heat transfer. To design a new

PCM panel for a PCM-Air heat exchanger, rounded ridges are more likely due to the small increase in pressure drop when compared to other ridges as well as the reduced cost of production. Moreover, longitudinal ridges drive the air uniformly along its width and ensure a uniform melting and solidifying process. This configuration will help to avoid panel leaking due to unbalanced pressure and non-uniform stress due to panel expansion and contraction. The design method in this thesis used a CFD software (ANSYS Fluent) to design the panel surface. As this software was the main tool during the design process, the selection of the correct turbulence model is important to ensure reliable results. Section 2.5.3 presents a summary of the main turbulence models available in ANSYS Fluent and points out the best option for the purpose of this thesis.

2.4 Building energy performance modelling

Building performance modelling has an important role for building and plant design and as mentioned before can be used for the assessment of overheating in buildings. In addition, current building regulations demand the use of building simulation tools to meet specific CO_2 emission targets for compliance. This section describes DTM and explains why IESVE was selected and address the MVS component in IESVE.

2.4.1 **Dynamic Thermal Modelling**

DTM uses the concept of multizone or network models to address airflow, heat transfer, contaminant transport or a combination of them. Each zone is characterized as a node and provides the average value of the zone (ASHRAE, 2017). Unlike CFD simulation, network models do not prescribe airflows or temperature gradients in zones.

Furthermore, it is possible to include the location of specific weather files to represent the climatic conditions of the building. For overheating assessment, CIBSE (CIBSE, 2013) recommends to use DSY (Design Summer Year) weather files. Additionally, DTM offers the possibility to design and renovate buildings via parametric analysis through simulations. There is a number of DTM software available in the market. For this study, IESVE was chosen because it has a plug-in that allows the simulation of PCM-Air heat exchangers as a cooling option. Due to that, the main characteristics of this software are detailed below.

IESVE and Cool-phase® component

IESVE is an integrated suite of applications with a friendly interface. This software englobes compliance evaluation and assessment tools, and tools to design energy efficient buildings (CIBSE, 2015a). It offers the possibility to design or renovate

buildings and test different passive solutions, compare low carbon technologies, CO_2 emissions, occupant comfort (also via adaptive thermal comfort), light levels, airflow, Part L, LEED, BREEAM, EPC ratings and so on.

Within IESVE Pro 2013 the low energy cooling and ventilation system (Cool-Phase®) developed by Monodraught is available. With this plugin it is possible to use the component for design or retrofit. In IESVE, a navigator toolbar gives access to the component modelling procedure (Figure 2.16). This is the preferred method as it provides a step-by-step for applying Cool-Phase® systems into the building and serves as a guide where the user can add notes for future reference (Figure 2.16).
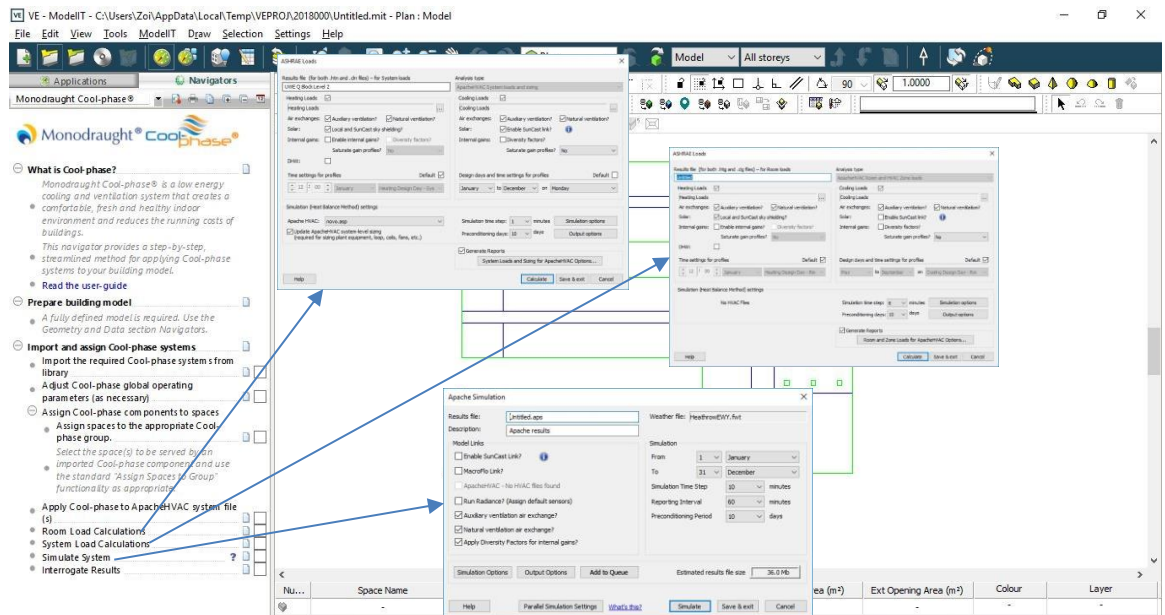
Figure 2.16 – Navigation toolbar with Monodraught component and room, system load calculation and Apache Simulation window

After the building is constructed and all thermal gains are added, the Cool-phase® should be imported. After choosing the model and size from the option: "import the required Cool-Phase® from library" the user should assign the equipment and choose the number of units necessary for each room.

Before running the dynamic thermal simulation, it is necessary to calculate the room loads. Once completed, the option '*Update ApacheHVAC system sizes?*' is selected to ensure that the radiator and boilers are resized before running the system loads (Figure 2.16).

Once completed, the dynamic thermal simulation can be performed by selecting '*Simulate System*' on the navigator menu. After that, VistaPro should be used to analyse the results (Figure 2.17).
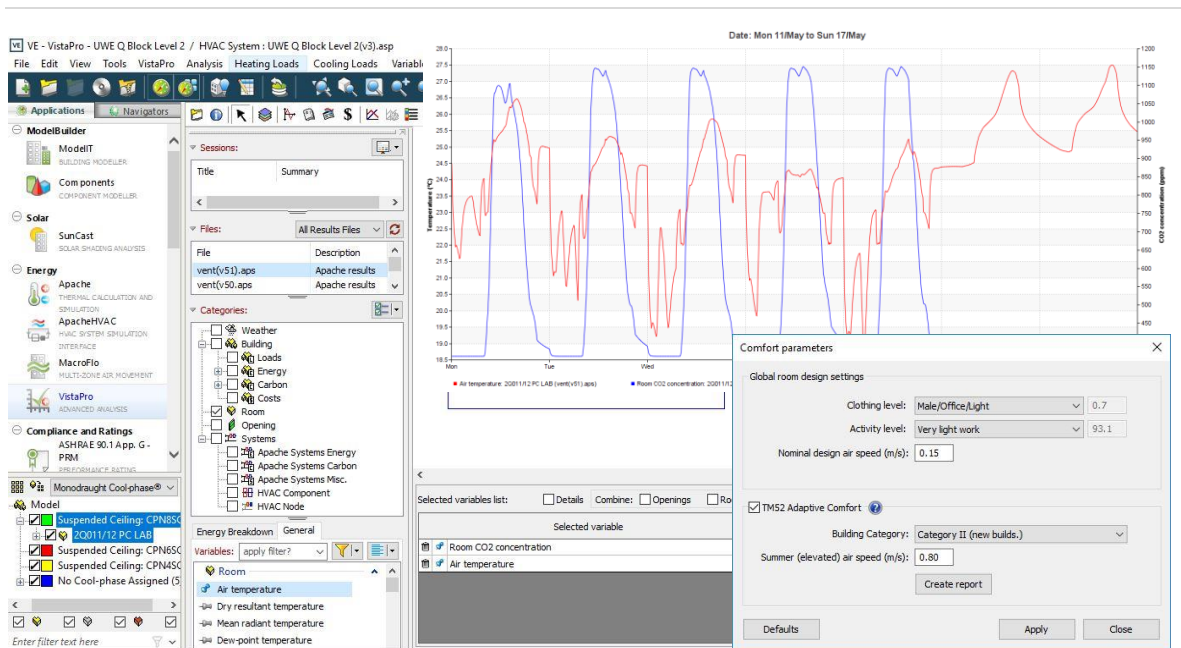
Figure 2.17 – VistaPro and option to evaluate if the room is suffering overheating according to TM52.

2.5 Computational Fluid Dynamics (CFD)

CFD tools are increasingly used to study environmental conditions within buildings spaces. Complex geometries can increase costs as it demands more processing power to generate the mesh and run simulations. To decrease that, simplifications in the model are allowed as long as the final results are not altered (e.g. dimensions can be reduced, reduce dimensionality from 3D to 2D or 2D to 1D; geometry simplified, periodicity applied, etc.).

To achieve satisfactory results in CFD simulations, Lomax et al. (Lomax et al., 2001) stated in his book that independent of the application under study, a sequence of steps must be followed:

1. Specify the problem, including geometry, flow conditions and simulation requirements. An existing geometry may be needed as a starting point or when no geometry is supplied, aims and constraints must be specified. Flow conditions could be the Reynolds number or Mach number used and requirement includes the definition of the level of accuracy and parameters of interest;

2. With the problem being specified, governing equations and boundary conditions must be set.

3. After that, the mesh is generated and the numerical method chosen. Different meshes exist nowadays, including structured, unstructured, hybrid, etc. with the possibility to make local refinements by adapting the mesh based on the expected solution;

4. With solution being converged, results should be interpreted by flow visualization tools, extraction of the data and error estimation techniques. Solutions can also be compared with correlations to estimate if the model is correctly addressed.

Furthermore, Lomax et al. (Lomax et al., 2001) also mentioned that the model equation can simplify the Navier-Stokes equation, this reduction in complexity make numerical solutions able to solve complex systems. An understanding of what happens when numerical approximations are applied to the model equations is a major first step for reliable and competent results. Due to that, this section is dedicated to present the governing equations used followed by Boussinesq and turbulence models.

2.5.1 Governing equations

Software such as ANSYS Fluent, ANSYS CFX, STAR, COMSOL, FloVENT, SimFlow, OpenFOAM etc. analyse and solve fluid problems in a particular domain by using the finite volume method to solve the Navier-Stokes equations. Navier-Stokes is the equation of momentum supplemented by mass conservation (continuity equation) and energy equations. Simulations in 2D and 3D were used in this thesis but to simplify, the following equations describing the above phenomenon will be presented in 2D. The fluid is considered as viscous, steady and incompressible with constant properties in the x and y directions. Differential equations are used to predict velocity and temperature fields within the fluid.

Conservation of mass

The conservation law states that the viscous fluid flow can be neither created nor destroyed. For steady flow problems, the net between the inflow and outflow must be zero. Applying this law to a differential control volume:

$$\frac{\partial u}{\partial x} + \frac{\partial v}{\partial y} = 0 \tag{2.5}$$

where *u* and *v* are the mass average velocity components of x and y. The equation applies for a single fluid where the density is considered constant.

Newton's Second Law of Motion

This law states that *the sum of all forces acting on the control volume must equal the net rate at which momentum leaves the control volume* (outflow - inflow). Body and surface forces are the forces that may act on the fluid where the first can be gravitational, centrifugal, magnetic and/or electric and the second (surface forces) are

due to the static pressure and viscous stress. Applying Newton's second law to a 2D differential control volume:

$$\rho\left(u\frac{\partial u}{\partial x} + v\frac{\partial u}{\partial y}\right) = -\frac{\partial p}{\partial x} + \mu\left(\frac{\partial^2 u}{\partial x^2} + \frac{\partial^2 u}{\partial y^2}\right) + X$$

$$\rho\left(u\frac{\partial v}{\partial x} + v\frac{\partial v}{\partial y}\right) = -\frac{\partial p}{\partial y} + \mu\left(\frac{\partial^2 v}{\partial x^2} + \frac{\partial^2 v}{\partial y^2}\right) + Y$$

(2.6)

where p is pressure, μ the fluid viscosity and X and Y are the external forces applied on the control volume.

Conservation of energy

The conservation of energy applied in a differential control volume over a moving fluid under steady state conditions expresses the net rate where energy enters the control volume, the heat rate added minus the rate which work is done by the fluid in the control volume is equal to zero. This can be rewritten as a thermal energy equation. For a steady, two dimensional incompressible flow fluid, the resulting equation is

$$\rho c_p\left(u\frac{\partial T}{\partial x} + v\frac{\partial T}{\partial y}\right) = k\left(\frac{\partial^2 T}{\partial x^2} + \frac{\partial^2 T}{\partial y^2}\right) + \dot{q}$$

(2.7)

where T is temperature, c_p the specific heat at constant pressure, $\dot{q}$ is the volumetric rate of thermal energy generation, k is the thermal conductivity.

In Equation 2.7, the left side term accounts for the net term which the thermal leaves the control volume due to advection while the right-hand side account for net inflow of conduction and thermal energy generation. The generation term signifies the conversion from other forms of energy (nuclear, electromagnetic chemical etc.) to thermal energy.

2.5.2 **The Boussinesq Approximation**

For non-isothermal flows such as natural convection problems where density variations are small, the Boussinesq approximation $[\beta(T - T_0) \ll 1]$ can be applied. It assumes that density variations have no effect on the flow field apart from the rise of buoyance forces. This model is ideal for fluids at room temperature or natural ventilation in buildings (ANSYS, 2017).

The Boussinesq approximation states that the continuity equation $\left(\frac{1}{\rho}\frac{\partial \rho}{Dt} + \nabla \cdot u = 0\right)$ is reduced to the incompressible form ($\nabla \cdot u = 0$) because $\frac{1}{\rho}\frac{\partial \rho}{Dt}$ have a smaller magnitude when compared to velocity gradients. The viscosity term is also assumed to be constant. The only non-constant term is the buoyancy force in the momentum equation:

$$(\rho - \rho_0)g \approx \rho_0 \beta (T - T_0)g \tag{2.8}$$

where ρ_0 is the constant density, T_0 the operating temperature and β the thermal expansion coefficient. Eq. (2.8) is approximated by $\rho = \rho_0(1 - \beta \Delta T)$ to eliminate the density (ρ) from the buoyancy term (ANSYS, 2017; COMSOL, 2018).

2.5.3 Turbulence Modelling

Turbulence modelling is a construction of a model able to predict the turbulence phenomenon. An ideal model should be able to represent the relevance of the physics with the minimum of complexity. For simple applications, skin friction and heat transfer coefficients are enough but more complex applications require detailed knowledge of turbulence fluctuation magnitudes, scales and energy of spectrum.

Turbulence modelling started with Boussinesq (Boussinesq, 2016) in 1877 with the hypothesis that *turbulent stresses are linearly proportional to mean strain rates*. Osborne Reynolds experiments (Reynolds, 1895) proved the hypothesis above and his paper is one of the most significant on turbulence. Reynolds concluded that turbulence is far complicated to permit a detailed understanding and proposed the use of statistics to describe turbulent flows. In 1925 Prandtl added significant credibility to the statistical approach to predict the eddy viscosity. Despite the fact that this model was never successful at true turbulent flow predictions, for certain simple flows it makes good "postdictions". In 1935 Taylor (Taylor, 1935) presented the assumption that turbulence is a random phenomenon and introduced statistical methods to analyse homogeneous and isotropic turbulence.

By 1960s experimental instrumentation improved considerably but the digital computer changes the treatment of turbulence. In 1963 the meteorologist E. Lorenz presented a deterministic solution to a simple model of the Navier-Stokes equations via computer that could not be distinguished from random (Lorenz, 1963).

Advances on computational power during the 1970s and 80s was probably the most important achievement and helped the use of Large-Eddy Simulation (LES) by Deardorff (Deardorff, 1970) in 1972, Direct Numerical Simulation (DNS) by Orzag and Patterson (Orszag and Patterson, 1972) and the Reynolds-Averaged Navier-

Stokes (RANS) (Launder and Spalding, 1973; Launder et al., 1975). This last one is the most successful model up-to-date due to successful results while the other models were not computationally feasible at that time. RANS is the model used for all simulations on the present thesis where equations are time-averaged and primarily used to describe turbulent flows. For a stationary and incompressible Newtonian fluid, these equations can be written in Einstein notation as:

$$\rho \frac{\partial \bar{u}_i}{\partial x_j} = \rho \bar{f}_i + \frac{\partial}{\partial x_j}\left[-\bar{p}\delta_{ij} + \mu\left(\frac{\partial \bar{u}_i}{\partial x_j} + \frac{\partial \bar{u}_j}{\partial x_i}\right) - \rho\overline{u'_i u'_j}\right] \tag{2.9}$$

where the left side term is the change in mean momentum of the fluid due to unsteadiness in the mean flow and convection by mean flow, which is equal to the balance of the mean body force, mean pressure field isotropic stress viscous stress and apparent stress $\left(-\rho\overline{u'_i u'_j}\right)$ due to velocity field fluctuation (Reynolds stress). This last term represents the rate of momentum transported or diffused due to turbulent fluctuations and requires additional modelling to solve the RANS equation. To solve this last term, many different turbulent models were developed where the most common are as follows:

1. One equation model: Spallart-Almaras;
2. Two equation model: $K - \varepsilon$ models (Standard, RNG and relizable) and $K - \omega$ model;
3. Seven equation model: Reynolds stress model.

Spallart-Almaras has been proved to be an accurate and robust model for aerodynamic application (Bardina et al., 1997) where adverse pressure gradients are observed. It was calibrated using results of 2D mixing layers, wakes and flat-plate boundary layers. It is capable to provide a smooth transition between laminar to turbulent flow at user specific locations. Spalart-Allmaras equation at one point does not depend on the solution of other points, the grid could be multi-block structured or unstructured, it converges fast to steady-state and requires only moderate grid resolution in the near-wall region (Blazek, 2005). In ANSYS Fluent this model provides crude simulations on coarse meshes where turbulence is not critical (ANSYS, 2017).

$K - \varepsilon$ is the most widely employed two-equation turbulence model used and is based on turbulent kinetic energy and turbulent dissipation rate equations. It requires the damping functions (also called low Reynolds number models) to stay valid at the viscous sublayer to the wall. $K - \varepsilon$ turbulence model is more difficult to solve numerically due to the damping functions and requires a higher grid resolution near the walls to solve the viscous sublayer. Conversely, it is important to notice that the

accuracy of the $K - \varepsilon$ standard model degrades for flows with adverse pressure gradient (Blazek, 2005; Wilcox, 2006; Patel et al., 1985). Improvements have been made to achieve better solutions than the standard model. In ANSYS Fluent two of these are available: the RNG $K - \varepsilon$ model and the realizable $K - \varepsilon$ model. The first is derived using a rigorous statistical technique and includes an additional term in the ε equation that improves significantly the accuracy for strained flows; enhances accuracy for swirling flows; provides an analytical formal for turbulent Prandtl numbers while the standard model uses constant values and RNG theory accounts the low-Reynolds number effect, however, if an appropriate treatment is given to the near-wall region.

The realizable $K - \varepsilon$ model differentiates from the standard because it contains a new formulation for turbulent viscosity and a new transport equation for dissipation rate derived from an exact transport equation of the mean-square vorticity fluctuation. This model predicts more accurately the spreading rate of planar and round jets, provides a superior performance on flows involving rotation, boundary layers suffering strong adverse pressure gradients, separation and recirculation. Conversely, the realizable $K - \varepsilon$ model contains the effects of mean rotation in turbulent viscosity formulation. This produces non-physical turbulent viscosities where the computational domain comprehends rotating and stationary fluid zones.

In ANSYS Fluent, the standard $K - \omega$ model is based on the Wilcox $K - \omega$ model (Wilcox, 2006) and includes modifications for low Reynolds number effects, shear flow spreading and compressibility. This model predicts free shear flow spreading rates in close agreement with measurements for mixing layers, far wakes and plane, round and radial jets and is therefore valid to free shear flows and wall-bounded flows. To effectively join the robust and accuracy formulation of the $K - \omega$ model in the near-wall region with a free-stream independence of the $K - \varepsilon$ model in the far field Menter (Menter, 1994) developed the shear stress transport (SST) $K - \omega$ model. As a highlight, this model combines the standard $K - \omega$ model in the near wall region with the $K - \varepsilon$ away from the surface.

The Reynolds Stress Model (RSM) is the most elaborated turbulence model in ANSYS Fluent. It comprises five transport equations in 2D and seven in 3D. This model is recommended when flow features are a result of anisotropy in the Reynolds stresses, for example: cyclone flows, highly swirling flows in combustors, rotating flow paths and stress-induced secondary flow in ducts. However, RSM predictions are limited by closed assumptions in the exact transport equations and need 50-60 % more CPU time and 15-20 % more memory when compared with $K - \varepsilon$ and $K - \omega$ models (ANSYS, 2017).

2.5.4   Near-wall treatment

The presence of walls affect considerably turbulent flows and therefore, near wall modelling has a significant impact on the reliability of numerical solutions. Closer to the wall, viscous damping reduces tangential velocity fluctuations while normal fluctuations are reduced by kinematic blocking. However, turbulence is rapidly increased outside the near-wall region due to kinetic energy production. Consequently, near wall modelling impacts considerably on the predictions of wall-bounded turbulent flows, making the selection of the appropriate model extremely important (ANSYS, 2017).

The so-called near wall region can be subdivided into three layers as observed in Figure 2.18. In the viscous sublayer, the flow is almost laminar and molecular viscosity plays an important role in momentum and heat or mass transfer.
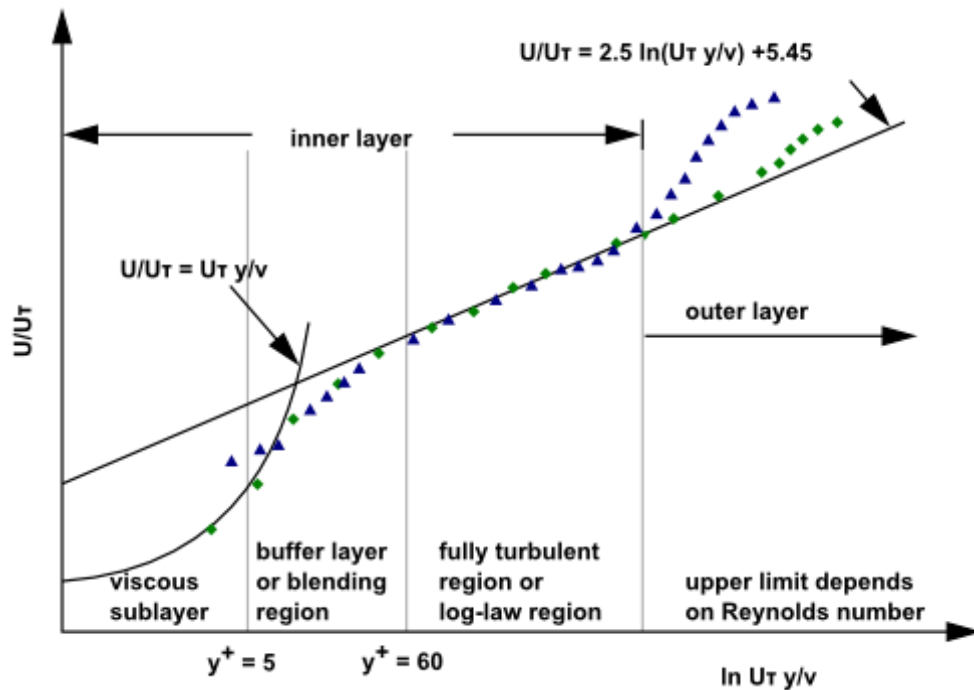
Figure 2.18 – Subdivisions of the near wall region. (ANSYS, 2017)

In the above figure, $y^+ \equiv \rho \mu_\tau / \mu$, where μ_τ is the friction velocity ($\sqrt{\tau_w / \rho}$). In the log-law region the turbulence is the protagonist and between these two regions, the buffer layer have influence from the viscous sublayer and log-law region.

To achieve confident results, ANSYS Fluent offers more advanced wall formulations as the standard wall function gradually provides unbounded errors in wall shear stress and wall heat transfer when y^+ is less the 15. This can be schematically seen in Figure 2.19. These formulations are default for ω-equation–based turbulence models and for ε-equation–based Menter-Lechner and Enhanced Wall Treatment (EWT) are able to

solve within the subviscous layer. Furthermore, with the Spalart-Allmaras model, it is possible to run independent of the near wall y^+ resolution.

Wall Function Approach

Direct duct

?

turbulent
core

buffer
&
sublayer

wall

- The viscosity-affected region is not resolved, instead is bridged by the wall functions.

- High-Re turbulence models can be used.

Near-Wall Model Approach

- The near-wall region is resolved all the way down to the wall.

- The turbulence models ought to be vali throughout the near-wall region
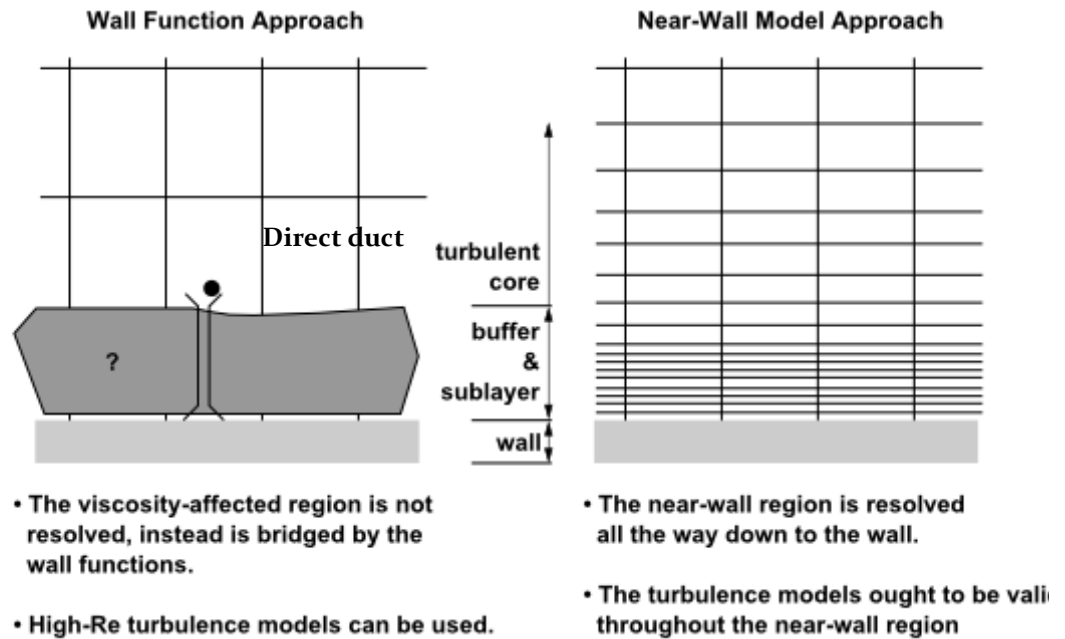
Figure 2.19 – Subdivisions of the near wall region. On the left, the boundary layer mesh lies entirely with the log-law region. On the right, the mesh covers all regions in the inner layer. (ANSYS, 2017)

It is important for high-quality numerical results that the boundary layer has a minimum of 10 cells (20 are desirable). For standard or non-equilibrium wall functions, y^+ between 30 and 300 is suggested but $y^+ \approx 30$ is desirable.

However, it is important to note that ANSYS Fluent uses y^* rather than y^+ to estimate mean velocity and temperature. The function y^* is defined as:

$$y^* = \frac{\rho C_\mu^{\frac{1}{4}} K_P^{\frac{1}{2}} y_P}{\mu} \tag{2.10}$$

Where ρ is the density of the fluid; C_μ is a constant; K_P the turbulent kinetic energy at point P; y_P the distance from point P to the wall and μ the dynamic viscosity of the fluid.

The mean velocity for the law of the wall yields

$$U^* = \frac{1}{\kappa} ln(Ey^*) \tag{2.11}$$

where E is an empirical constant equal to 9.793.

In ANSYS Fluent the log-law is employed when $y^* > 11.225$. When y^* is below 11.225 Fluent consider $U^* = y^*$.

To estimate the mean temperature at the log-law region, two different laws could be applied: The linear law when conduction is important and the logarithmic law when turbulent effects prevail on turbulent regions. Additionally, the contribution from viscous heating is included in the temperature wall function by ANSYS Fluent for high compressible flow simulations. In this situation, the temperature in the near wall region can be very different from low subsonic flows. Therefore, the mean temperature through the law of the wall is:

$$
T^* = \frac{(T_w - T_P)\rho c_P C_\mu^{\frac{1}{4}} K_P^{\frac{1}{2}}}{\dot{q}}
$$

$$
= \begin{cases}
\Pr y^* + \dfrac{1}{2}\dfrac{\rho \Pr C_\mu^{\frac{1}{4}} \kappa_P^{\frac{1}{2}}}{\dot{q}} U_P^2 & (\boldsymbol{y^* < y_T^*}) \quad (2.12) \\[2em]
\Pr_t\left[\dfrac{1}{\kappa}ln(Ey^*) + P\right] + \dfrac{1}{2}\dfrac{\rho \Pr C_\mu^{\frac{1}{4}} K_P^{\frac{1}{2}}}{\dot{q}}\{\Pr_t U_P^2 + (Pr - \Pr_t)U_c^2\} & (\boldsymbol{y^* > y_T^*})
\end{cases}
$$

where P is computed by Jayatilleke formula:

$$
P = 9.24\left[\left(\frac{\Pr}{\Pr_t}\right)^{\frac{3}{4}} - 1\right]\left[1 + 0.28e^{-\frac{0.007\Pr}{\Pr_t}}\right] \tag{2.13}
$$

where K_P is the turbulent kinetic energy point at P; ρ is the density of the fluid; c_P the specific heat; $\dot{q}$ the wall heat flux; T_P the temperature at the cell adjacent to the wall; T_w is the wall temperature; Pr is the molecular Prandtl number; $\Pr_t$ is the turbulent Prandtl number (0.85 at the wall) and U_c the mean velocity magnitude when $y^* = y_T^*$ where y_T^* is the non-dimensional thermal sublayer thickness.

Scalable wall functions avoid deterioration of standard wall functions when $y^* < 11$. These wall functions force the use of the log-law in conjunction with the standard law of the wall and produce consistent results for grids with arbitrary refinement. For industrial applications, it might be difficult to achieve such requirements and for that, scalable functions are recommended. The wall function virtually generates the mesh at the transition to the log-law layer ($y^+ \approx 11.225$). It is important to mind that in regions where $y^+ > 11.225$, the scalable functions provide identical results to the standard wall functions (ANSYS, 2017).

The design of the new panel surface was not focused on the behaviour of attachment and detachments at the boundary layer. Instead, the overall heat transfer was the interesting point and due to that, $K - \varepsilon$ turbulence model with scalable wall function was the best and economical option to be used. Moreover, experiments and correlations were used to ensure that the results obtained thorough simulations are reliable.

2.6 Laboratory testing

Experimental studies are imperative to validate numerical simulation and also understand the impact of simplifications made during the simulation process. Section 2.3 raised the importance of turbulators to increase cooling performance. This section reveals the experiments commonly used by researchers to evaluate heat transfer due to heat transfer augmentation and the melting/solidifying process of a PCM-air heat exchanger.

2.6.1 **Heat transfer augmentation**

Section 2.3 of the literature review presented the benefits when rib, fin or baffle turbulators are attached on channel surfaces to increase convective heat transfer. In the literature, two main tests were found: One measure the surface temperature by thermocouples attached to its surface and the other use infrared cameras.

Thermocouple test rig

Promvonge (Promvonge et al., 2010; Promvonge and Thianpong, 2008) assessed a turbulent forced convection test with different shaped ribs (wedge pointing upstream, wedge pointing downstream, triangular and rectangular). A 1.45 kW high-pressure blower was used to analyse heat transfer and pressure drop with flow rate measured by an orifice plate. Twelve thermocouples were fitted to the wall with holes drilled from the rear face to measure temperature surface distribution. The temperature surface was averaged and the heat of convection was calculated by eq. (2.14):

$$h = \frac{Q_{conv}}{A(\widetilde{T}_s - T_b)} \tag{2.14}$$

Where A is the panel surface area, T_{in} and T_{out} is the air inlet and outlet temperature acquired by thermocouples.

$$T_b = (T_{\text{out}} + T_{in})/2 \tag{2.15}$$

and $\widetilde{T}_s$ is the surface temperature average of all thermocouples and is given by eq. (2.16):

$$\widetilde{T}_s = \sum_{i=1}^{N} T_{s_i}/N \tag{2.16}$$

where N is the number of thermocouples.

Q_{conv} is the heat transfer between panels and air will be calculated by the energy balance through the air crossing the volume control and is given by:

$$Q_{air} = Q_{conv} = \dot{m}_{air}\left(c_{p_{air_{(out)}}}T_{out} - c_{p_{air_{(in)}}}T_{in}\right) \tag{2.17}$$

where: $\dot{m}_{air}$ is the air mass flow rate in $\frac{kg}{s}$; $c_{p_{air}}$ in $\frac{J}{kgK}$ and will depend on inlet and outlet air temperature.

With the heat of convection evaluated, it is possible to estimate the averaged Nusselt, which is a dimensionless term equal to the temperature gradient on the surface and provides the ratio between convective and conductive heat transfer (Incropera, 2007). It is given by:

$$Nu = \frac{hD_h}{k_{air}} \tag{2.18}$$

Where D_h is the hydraulic diameter, k_{air} is the thermal air conductivity and h is the heat transfer coefficient.

The heat transfer increase comes with the cost of pressure drop augmentation. The thermal enhancement factor evaluates the convective heat transfer of the augmented surface over a smooth surface (eq. (2.19)):

$$\eta = \frac{\left(\frac{Nu}{Nu_o}\right)}{\left(\frac{\Delta p}{\Delta p_o}\right)^{1/3}} \tag{2.19}$$

To estimate Nu_o and Δp_o, Promvonge (Promvonge et al., 2010) tested a smooth surface and Dittus-Boelter (eq. (2.20)) correlation to validate the Nusselt number results, which is:

$$Nu_{DB} = 0.023\, Re_D^{4/5}Pr^n \tag{2.20}$$

Where $n = 0.4$ for the fluid being heated and $n = 0.3$ when the fluid being cooled.

Similarly to Promvonge, experimental studies of inclusions in channels follow the same procedure to analyse heat transfer and pressure drop (Promvonge, 2010; Bilen et al., 2009; Tanda, 2004; Singh et al., 2017; Yang et al., 2017; Chang et al., 2008;

Bhuiya et al., 2012; SriHarsha et al., 2009; Eiamsa-ard and Promvonge, 2009; Promvonge and Thianpong, 2008; Hwang et al., 2010).

Infrared camera test rig

When local Nusselt number field is important, a thermal camera allows a better understanding of the heat exchange along the panel and have been widely used (Tanda, 2004; Domaschke et al., 2012; Ligrani et al., 2001; Singh et al., 2017; Tyagi et al., 2015; Choi et al., 2013). Yang *et al.* (Yang et al., 2017) used a thermal camera to analyse the thermal temperature distribution along the channel surface. Ribs of 3 mm x 3 mm x 60 mm were glued on the heating foil and infrared glass. Three thermocouples were used as a reference for the infrared camera to generate a relationship between corrected infrared temperature and thermocouple data. Validated by experiment, CFD simulation showed the importance of the separation and reattachment region and also shown a higher increase of heat transfer effectiveness at laminar flow rate and a larger blockage ration in the ribbed channel correspond a larger heat transfer coefficient. The optimum pitch to height ration in this experiment was 10.

SriHarsha (SriHarsha et al., 2009) analysed the local heat transfer and pressure drop in a square channel with 90 ^{o} continuous and 60° V-broken ribs. An air compressor supplied the air measured by a calibrated orifice flow meter with airflow being controlled by two needle valves (one each side of the orifice flow meter). The temperature distribution of the ribbed wall was measured by a Thermal camera ('Thermoteknix' Ti200) and MATLAB was used to analyse the captured images. The back surface was painted in black, providing an emissivity of 0.99 and surface temperature was calibrated using a tank filled with water and heated with 500 W heater and two thermocouples attached at its surface. After achieving 70°C, the heater was switched off and the emissivity was adjusted until the temperature measured in the camera was the same as that read by the thermocouples.

Equipment used in both thermocouple and infrared camera tests

In both experiments, the pressure drop is evaluated by two static pressure taps placed on inlet and outlet and can be measured by a transducer or inclined U tube. To specify the airflow, inverters are commonly used to vary speed rotation and orifice meter or Pitot tube measure the air velocity.

2.6.2 Melting and solidifying test

Section 2.1 revealed the importance of ventilation systems with thermal energy storage to reduce energy consumption and how it can provide enough cooling to

maintain the environment thermally comfortable. To experimentally assess the performance of a PCM-air heat exchanger, key parameters need to be studied:

1. Study the effect of inlet temperature on melting and solidification stages;
2. The effect of airflow on charging and discharging;
3. The effects on the distance between panels
4. Evaluate the energy exchanged between air and panel during charging and discharging;
5. Evaluate the charging and discharging time.

To experimentally achieve the results described above, there is a consensus among researchers that test rigs should have a fixed temperature for both charging and discharging process to evaluate different configurations and designs. It also needs to have thermocouples attached to its surface in order to guarantee when the charging and discharging cycle is completed. Due to that, test rigs found in the literature (Iten and Liu, 2015; Iten et al., 2016; Dolado et al., 2011; Osterman et al., 2015; Turnpenny et al., 2001; Stritih and Butala, 2010) follow the same principle as the ones proposed by Madyira et al. (Dolado et al., 2011) and Iten (Iten and Liu, 2015) (Figure 2.20) where temperature sensors measured the temperature before and after the thermal battery (labelled storage box in Figure 2.20).
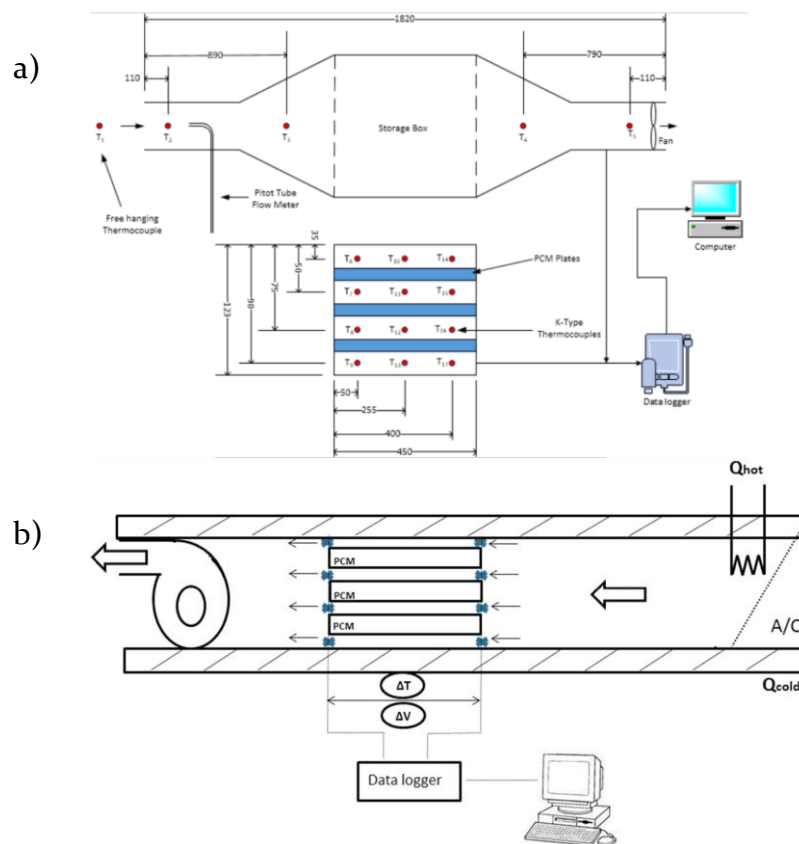
Figure 2.20 – Test rig used by (a) Madyira (Dolado et al., 2011) and (b) Iten (Iten and Liu, 2015).

The thermocouples attached on the panel surface are distributed close to the edge and in the middle of the panel to guarantee that the PCM is fully melted or solidified. One example can be seen in Dolado et al. work (Figure 2.21).
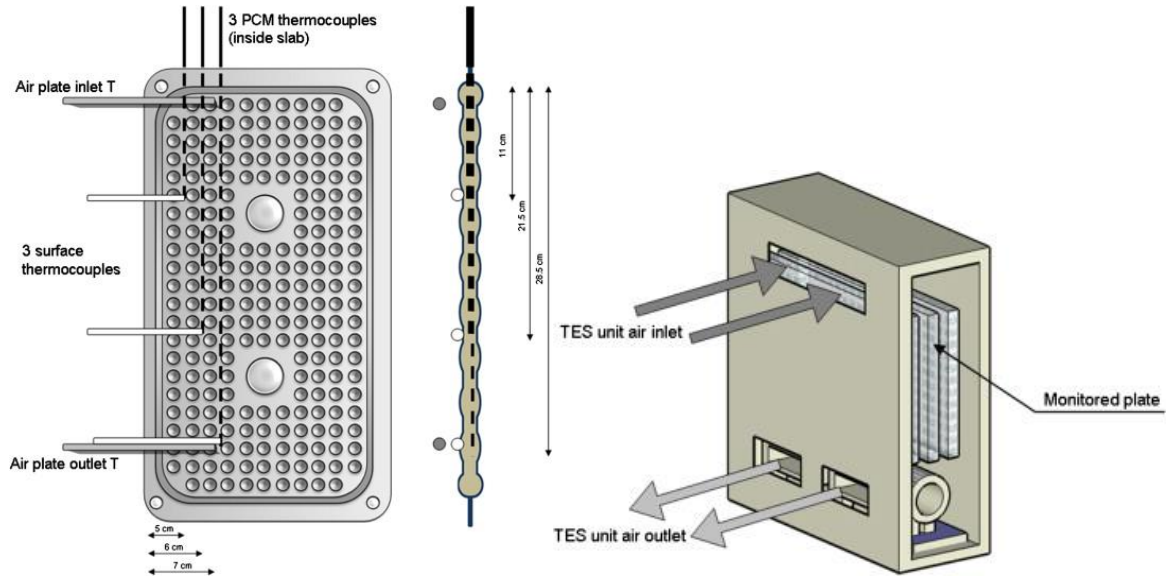
Figure 2.21 – Thermocouples distribution in the PCM-air heat exchanger proposed by Dolado et al. (Dolado et al., 2011) and the test section

To investigate the influence of inlet temperature and inlet velocity in the cooling/heating load, a test rig was mounted by Iten and Liu (Iten and Liu, 2015). The experiment consisted of a duct of 2.2 x 0.25 x 0.218m (L x W x H) with a heating/cooling unit and an exhaust fan of 0.11 kW able to provide 147 m³/h. Three flat panels stacked with the dimensions of 0.5 x 0.25 x 0.02 m was filled with a 23-25 °C melting point PCM. The heating consisted in four electrical heating coils (three of 2 kW and one of 2.5 kW). Air velocity was measured in 25 points according to ASHRAE (HANDBOOK, 2012) via Tchebycheff's method (ASHRAE, 2013b). 15 thermocouples were attached at its surface to capture melting and solidifying temperature and ensure that the PCM is fully melted or solidified. All thermocouples were located at the centre of the panel and connected to a digital temperature recorder model 3470A by Agilent Technologies with 10s of time step.

The first test consisted to vary the air velocity (0.6, 1.6 and 2.5 m/s) at a constant charge and discharge temperature (38 and 12 °C, respectively). The second test varied the inlet temperature for the charging (12, 16 and 18 °C) and discharging (30, 34 and 38 °C) period while the inlet velocity was kept constant (1.6 m/s). In the end, the equations (2.21) and (2.22) were used to evaluate the PCM-air heat exchanger performance.

$$Q_c = \int_0^t \dot{m}_{air}\, c_{p,air}\, (T_{out} - T_{in})_{air}\, dt \qquad \text{[Wh]} \quad (2.21)$$

$$Q_h = \int_0^t \dot{m}_{air}\, c_{p,air}\, (T_{out} - T_{in})_{air}\, dt \qquad \text{[Wh]} \quad (2.22)$$

2.7 Chapter's summary

This chapter started by describing energy storage systems with a focus on Thermal Energy Storage (TES) and the suitability of Latent Thermal Storage System for building applications. The literature review shows the benefit of having a ventilation system with thermal energy storage and points out that few researchers have focused on improving the heat transfer on the air-side of the PCM-air heat exchanger. To cover that, a review on mechanisms to increase heat transfer in channels was presented. Furthermore, few commercial MVS with PCM-air heat exchangers are available on the market as well as few studies on its performance and the evaluation of thermal comfort provision.

The Dynamic Thermal Modelling software which has incorporated a commercial MVS (IESVE) to design and retrofit buildings is described in details. The software will be used to improve the control system.

To design the encapsulation surface and analyse the MVS performance via air temperature and air speed distribution along a room, a Volume Finite software (ANSYS Fluent) was used. To form a base and correctly assess the models during the simulations, a section in this chapter was dedicated to present the governing equations and turbulence models.

The chapter concludes by presenting how recent studies experimentally test PCM-air heat exchangers, which was used to assess the fabricated panel.

CHAPTER 3 - RESEARCH METHODS

Introduction to the chapter

This chapter presents the necessary tools to analyse the MVS via a case-study and improve the controls and components. This was achieved by four methods:

1. Case-study of an operational MVS through which system data and field measurements were obtained to describe its performance and calibrate the computational models;
2. Dynamic thermal modelling to model the MVS and the conditioned space;
3. CFD modelling to analyse air temperature and airflow distribution within the conditioned space and design the panel;
4. Laboratory testing to validate the proposed panel design.

3.1 Description of the case-study MVS and conditioned space

There are few MVS available on the market; one is Cool-Phase® by Monodraught Ltd. Figure 3.1 shows the system investigated in this study indicating its components consisting of a G4 filter, recirculation damper, fan, LTES and diffusers. A diagram of the system is shown in Figure 3.2.
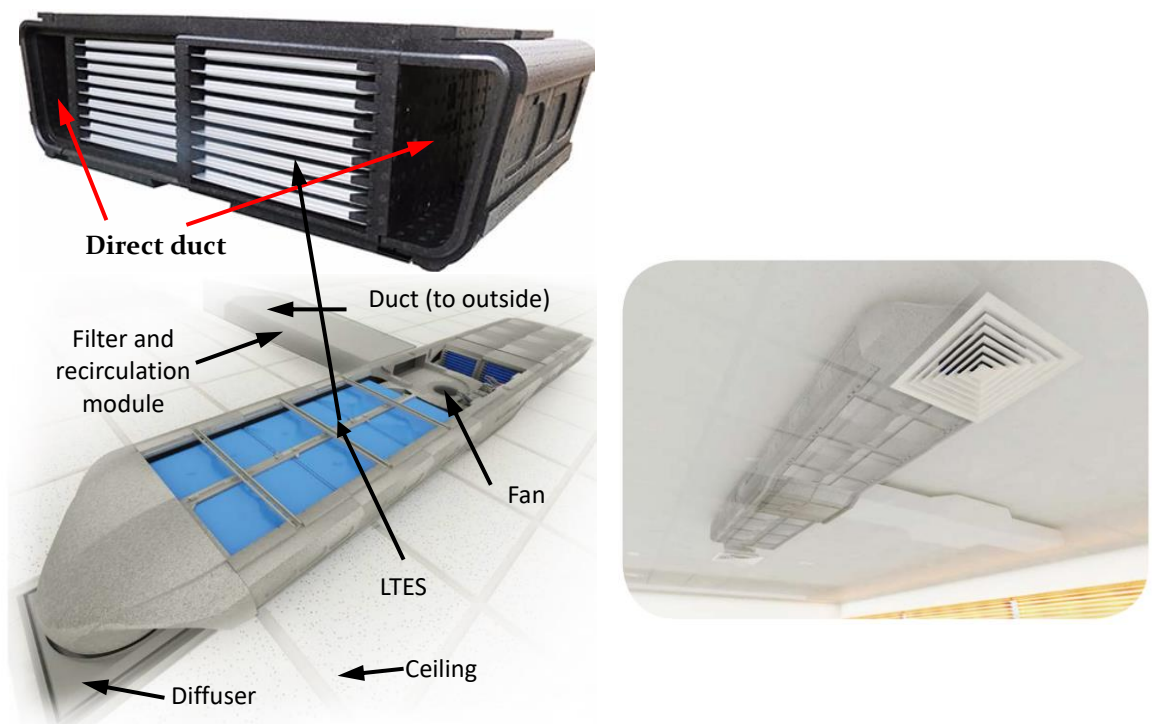
Figure 3.1 - Cool-Phase® Unit [source: Monodraught Ltd]
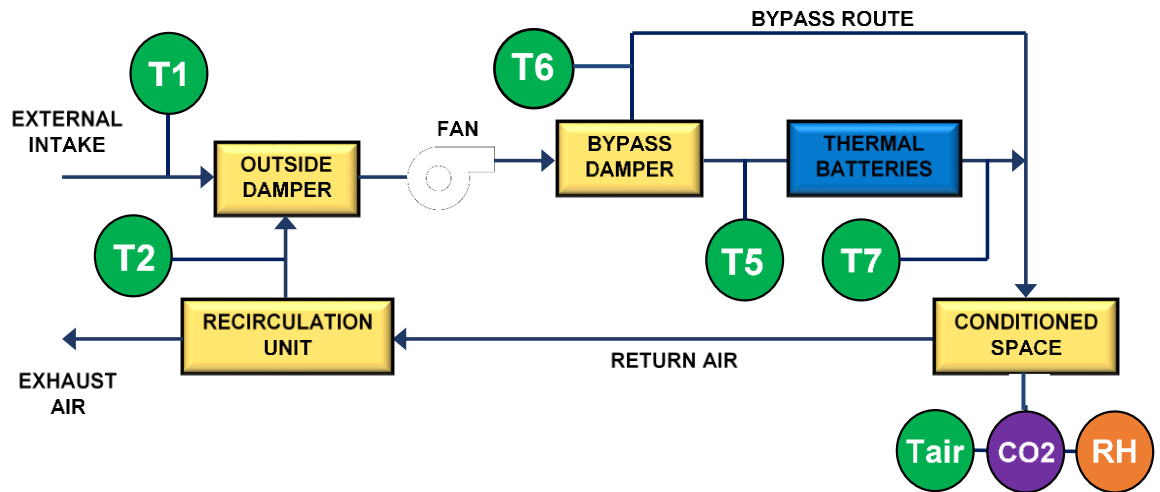
Figure 3.2 - Diagram of the PCM-Air heat exchanger indicating the location of the sensors and below the description of each sensor.

Sensor	Description
T1	External temperature located outside of the intake damper recirculation box
T2	Internal temperature located outside of the recirculation damper of the recirculation box
T5	Temperature before crossing the LTES
T6	Temperature located at the bypass duct
T7	Temperature after crossing the LTES
RH	Humidity inside the room
CO_2	CO_2 concentration (ppm) inside the room
T_{air}	Room temperature

The MVS physical size varies according to capacity (6, 8 and 10 kW) and model; 3995mm to 5805 mm width, 966mm depth and 400mm height. The PCM is encapsulated in an aluminium panel available commercially (Figure 3.3, [8]).

Figure 3.3 – Existing panel [8].

Each panel holds 2 kg of PCM able to provide 88 Wh (317 kJ); each module of the MVS studied has 18 panels. Modules are put together depending on the required capacity; for the 10 kW model, the unit consists of 18 panels x 6 modules (3 modules per side) which is equals to 9.5 kWh (34.2 MJ); the 8 kW model consists of 18 panels

x 4 modules (2 modules per side) which is equal to 6.37 kWh (22.8 MJ). The supply diffusers have a squared shape and are divided into four triangles where the air is directed with an angle of 45°. The exhaust grille has a square and uniform shape. An electronic system controls the damper and directs the airflow through the thermal battery or bypasses it through an EPP (Expanded Polypropylene) duct (see Figure 3.2). The fan provides 260 l/s maximum during cooling mode and 300 l/s during charging mode.

The PCM's solidifying temperature used in this MVS is limited by the temperature used to charge the material (night outside air temperature). This selection is also based on the cooling demand (lower melting point for high demand and higher melting point for lower demand) (Lazaro, Dolado, Marín, et al., 2009). Due to this, the Salt-hydrated PCM SP 21E by Rubitherm (melting: 22-23°C; solidifying: 21-19°C; heat capacity: 170 kJ/kg for a temperature range of 13-28 °C; heat conductivity 0.6 W/mK) suits the studied system and its applications. Salt hydrates work by arranging and breaking the reaction salt-water (hydrate-dehydrate). They have high latent heat per unit volume, high conductivity (double of paraffin) and little volume change during melting. However, salts have a density higher than water and stay at the bottom of the container, making the freezing process more complicated (Sharma et al., 2009). Due to that, new releases of this MVS are now using a water-insoluble organic phase change material (CrodaTherm™ 21, melting: 21°C; solidifying: 19°C; heat capacity: 212 kJ/kg for a temperature range of 13-28 °C; heat conductivity: ~0.165 W/mK) derived from plant-based feedstocks and has the form of a crystalline wax or oily liquid (depending on temperature).

3.1.1   Location, climate and room characteristics

The case-study with the system installed is a seminar room in a University Campus in West England (Figure 3.4 and Figure 3.5). Similar units have been installed in many rooms (typical classrooms and offices) of the building but a seminar room (computer laboratory) was chosen because of its higher internal heat gains.

The climate in the location (Bristol, UK) is temperate maritime with 2684 Heating Degree Days and 196 Cooling Degree Days (base 15.5°C) (Vesma, 2014) indicating low cooling requirements due to external conditions so the cooling load is mainly determined by internal heat gains.

The case-study was renovated into a seminar room by joining three pre-existing rooms. The existence of a plenum favoured the installation of the suspended ceiling system model of the system. The refurbished seminar room floor plan can be seen in Figure 3.6 where the position of space monitoring sensors (for the purpose of this study) are shown. The room has a floor area of 117 m² and includes 29 desktop

computers, peak occupancy of 29 students, and artificial lighting comprising of 24 luminaires each equipped with one 48 W lamp. The total maximum internal heat gain in the room is 60 W/m². The room has one external wall facing west with U-value of 0.56 W/m² K while 23 % is glazing (overall U-value 1.82 W/m²K) with internal blinds. Ventilation and cooling are provided via the 10kW MVS which is positioned in the middle of the room above the suspended ceiling. Heating is provided through perimeter hot water radiators and windows are openable. More information regarding the building fabric and the climatic conditions can be found in Appendix I.
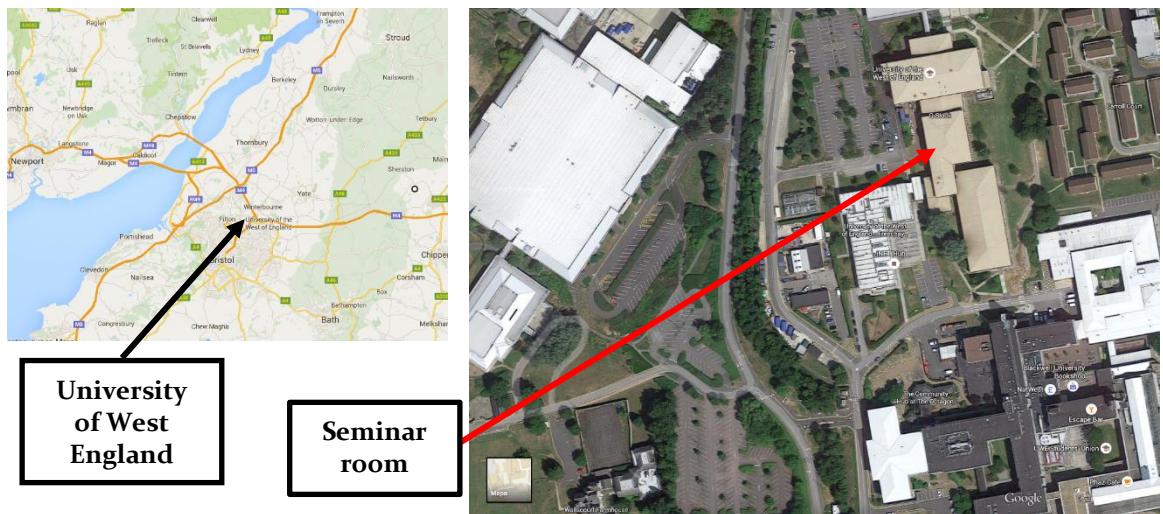
Figure 3.4 – Maps indicating the University and the seminar room (from Google maps)

Figure 3.5 – External building façade and seminar room view

3.2   System data and field monitoring

The MVS includes monitoring of key parameters to control its operation according to required indoor air quality and thermal comfort in the conditioned space. The data

from the system were available for the period from 16/05/2013 to 31/12/2015 and were measured every 1 min to include the following:

- Air temperature, relative humidity and CO_2 at one location in the conditioned space (Cool-Phase® mounted wall control, Figure 3.6);
- Air Temperature at different parts of the system (T1, T2, T5, T6, T7 in Figure 3.2);
- Airflow provided by the fan;
- System operation settings;
- The position of the damper (Table 3.1).

Table 3.1 – Conditions of volume flow through Cool-Phase®

Conditions	Air intake (Outside damper)		Flow through thermal batteries		Recirculation unit (inside damper)	
	open	closed	on	off	open	closed
Direct outside air ventilation	X			X	X	
Outside ventilation and cooling	X		X		X	
Recirculation and cooling		X	X			X
Heat recovery cycle	X			X		X
CO_2 control	X		On or off			X
Charging mode	X		X		X	

However, within the conditioned space only one sensor is placed as part of the MVS installation. In order to examine the variation of conditions within the space and understand the conditions of air flow before and after the LTES, additional monitoring was carried out in the room as part of this study. The monitoring was carried out for the period of 19/08/2015 - 18/08/2016 as follows:

- Air temperature and relative humidity was measured at 5 minutes intervals using 8 HOBO (HOBO UX100-003) loggers;
- Sensors H1, H2, H3 and H4 were installed at 0.70 m from the floor, H5 and H6 at 1.80 m, H7 at the same level as the system's wall-mounted user control (1.5m) and H8 was placed close to exhaust grille (located on the ceiling).
- Air temperature of the supply diffuser was measured with four ibutton (ibutton DS1922L) loggers placed at the four faces of the logging at 5 mins interval.
- CO_2 measurements were taken using two Telaire sensors for two days (25-26/11/2015) to analyse the CO_2 distribution and compare with system data.

The location of the sensors mentioned above can be found in Figure 3.6. Sensors' specifications and photographs showing the location of four of them are presented in Appendix II.

8.7m

13.5m

Cool-phase® wall mounted control

windows

Filter

Cool-phase® air intake

Cool-phase® fan

LTES

N

H1
H2
H3
H4
H5
H6
H7
H8
CO₂-1
CO₂-2
i1-4

57
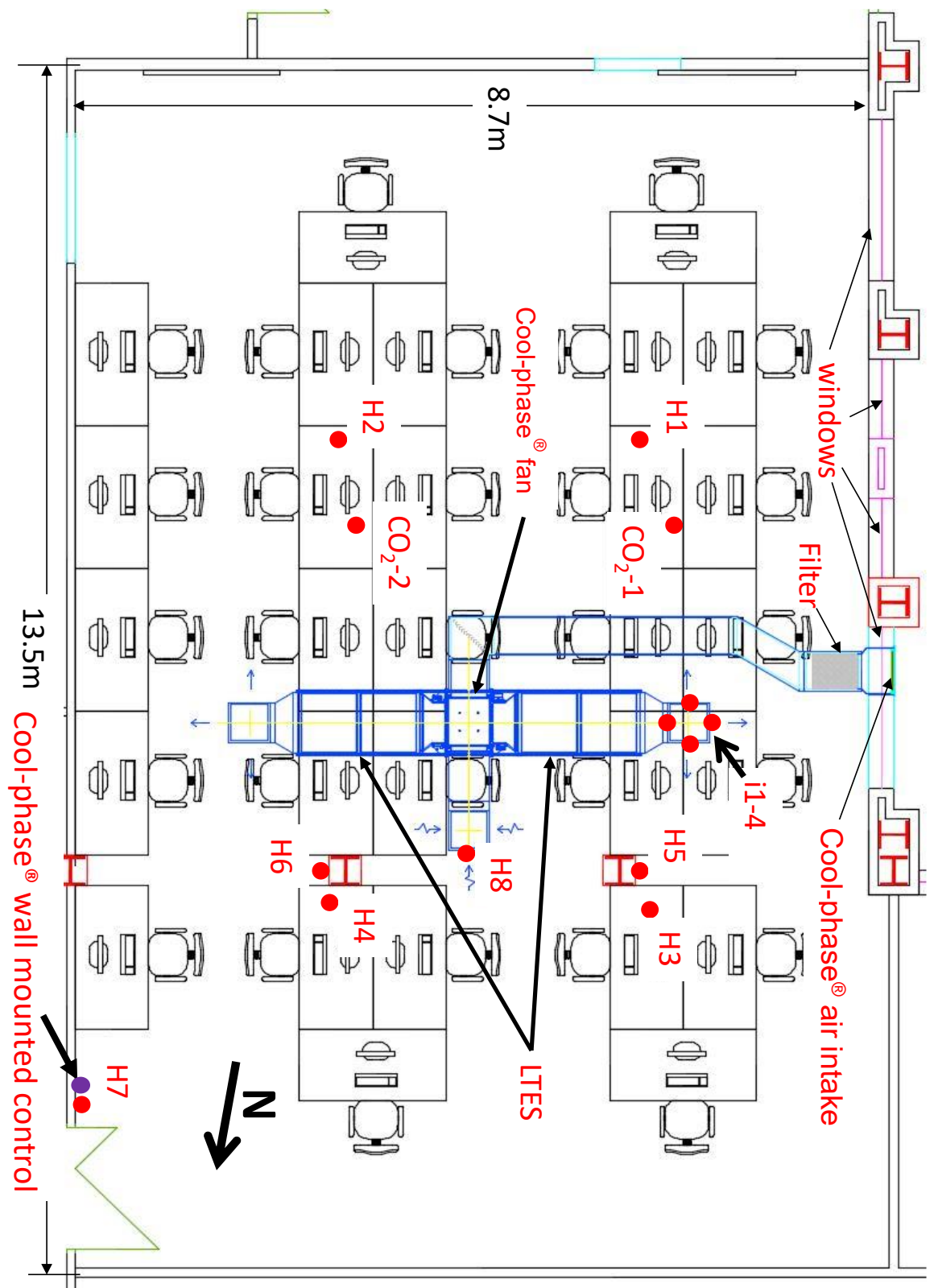
Figure 3.6 – Seminar room floor plan with sensors location.

3.3 Dynamic Thermal Modelling (DTM)

The DTM software IESVE (IESVE, 2016) was used to carry out energy and environmental predictions in the seminar room, evaluate the system's performance details and propose improvements. Mentioned in the section 2.4.1, IESVE was chosen because it has a plug-in that enables the user to design the Cool-Phase® MVS by changing parameters such as system type, size and number of units required. To perform this analysis, a geometrical and thermal model of the seminar room was created. Geometry and construction details of the room were provided by the owner of the building and MVS system details by Monodraught Ltd. Internal heat gains and scheduling was estimated by data provided by the energy manager of the building as well as a number of visits to the location; system data were also used to estimate occupancy schedule and intensity (number of students). The accuracy of the predictions was checked by comparing IESVE predictions with measured air temperature for one year. The Mean Bias Error (MBE) and the Coefficient of variation of the Root-Mean-Square Error CV(RMSE) were calculated using equations 3.1 to 3.3 (ANSI/ASHRAE, 2002):

$$\boldsymbol{MBE} = \frac{\sum_{i=1}^{N}(y_i - \widehat{y_i})}{\sum_{i=1}^{N} y_i} \ (3.1) \qquad \boldsymbol{CV(RMSE)} = \frac{\sqrt{\sum_{i=1}^{N}(y_i - \widehat{y_i})^2 / N}}{\overline{Y_s}} \ (3.2) \qquad \overline{Y_s} = \frac{\sum_{i=1}^{N} y_i}{N} \ (3.3)$$

where y_i and $\hat{y}_i$ are measured and simulated data at instant i, respectively; $\overline{Y_s}$ is the sample mean of the measured data and N is the sample size (8760 for hourly based validation analysis or 12 for monthly based validation analysis).

The use of MBE and CV(RMSE) for calibration purposes are recommended by ASHRAE Guideline 14 (ANSI/ASHRAE, 2002) where a difference of less than 5 % in MBE and less than 15 % in CV(RMSE) between monthly prediction and measurements is recommended. When hourly data is used, a difference of 10 % in MBE and 30 % in CV(RMSE) is recommended as a good agreement between predictions and measurements. The MVS plugin on IESVE has a simplified representation of the control system, which may reflect in a system under or overdesigned. To better design a MVS, improvements in the plugin were proposed before the calibration takes place. With model being calibrated according to MBE and CV(RMSE), parameters in IESVE plug-in can be adjusted and improvements on system performance can be tested with confidence. To evaluate the performance of the system in more detail and propose improvements, the analysis follows the schematic below (Figure 3.7).
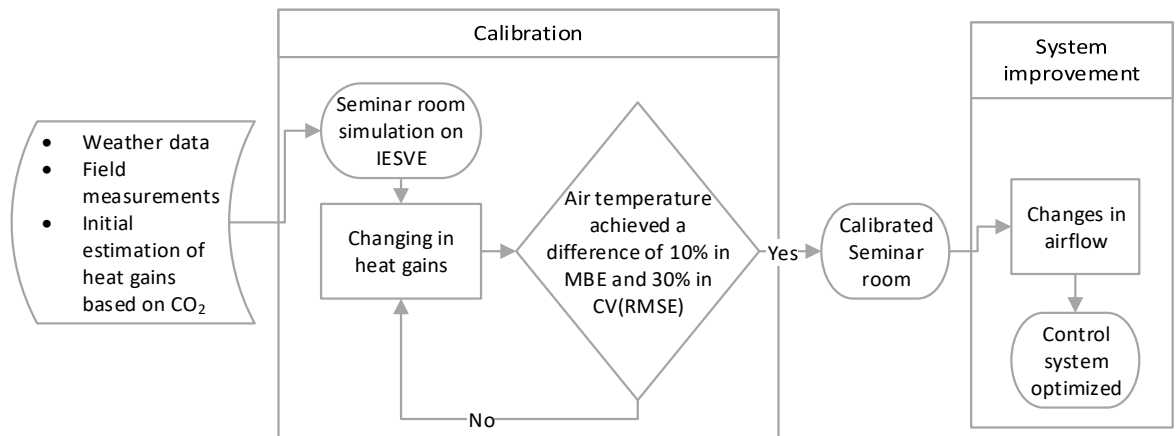
Figure 3.7 – Schematic of calibration procedure followed by system improvement.

3.4 CFD modelling

ANSYS Fluent (version 16.2 and later 17.1) was used to investigate air temperature and air flow distribution within the seminar room, and to design a new panel for the MVS. To achieve time effective results, simplifications in the model have to be made. Those simplifications save computer power, time and memory while most relevant aspects of the physics are preserved. For both studies, steady state was considered because the indoor conditions for the seminar room are stable for the selected day and time. For the panel design, the literature review indicated that studies focused on heat transfer enhancement are performed in steady state for both numerical (section 2.3) and experimental (section 2.6). Furthermore, the results used to evaluate the panel heat transfer (first laboratory test, section 3.5.1) were gathered after steady state achievement. The air flow is not subjected to an elevated pressure difference or high velocities and therefore is considered incompressible. Therefore, the Boussinesq hypothesis was adopted for the seminar room analysis. Moreover, the air temperature does not vary considerably and therefore its properties do not have significant changes. Due to that, the air properties were considered constant at 300K. For both cases, the air supplied was perpendicular to the surface.

The procedure for generating the geometry until the results followed the workflow presented in Figure 3.8.
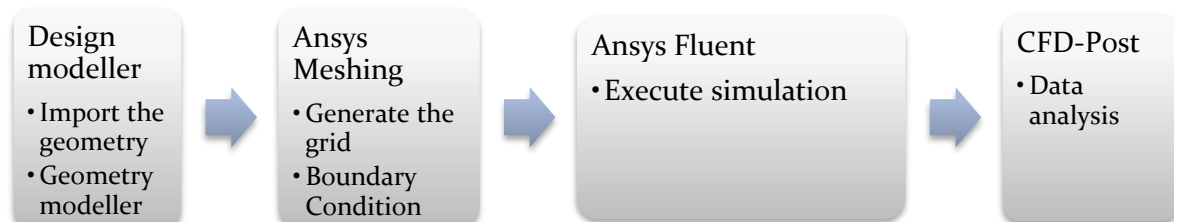
Figure 3.8 – workflow for the CFD modelling

In terms of convergence, there is no unique method to evaluate it. It depends on the size of the problem and initial assumptions of the boundary conditions. ANSYS Fluent user guide (ANSYS, 2017) suggests that convergence should be judged on value and behaviour. A residual lower than 10^{-6} for energy and 10^{-3} for other variables are is default in ANSYS Fluent and desirable for most cases. However, solutions can reach convergence when residuals do not reach the default values. To ensure that, a combination of key parameters for the desired simulation should converge (eg. temperature or velocity over the section of interest). ASHRAE fundamentals (ASHRAE, 2017) pointed that convergence is most likely to be reached if no change in the fourth digit is found in the major dependent variables (eg. temperature and velocities) within the last 100 iterations. Furthermore, a small total heat transfer rate and mass flow net are desired. Based on this, it is important to understand the physics of what is being studied and track the correct parameters to ensure convergence.

Seminar room air temperature and airflow distribution

A model of the room was created aimed to understand how the MVS distributes the air within the conditioned space. The MVS was represented by two supply inlets and one exhaust grille. Figure 3.9 shows the modelled room (13.5 x 8.5 x 2.7 m) drawn in ANSYS Workbench design modeller.
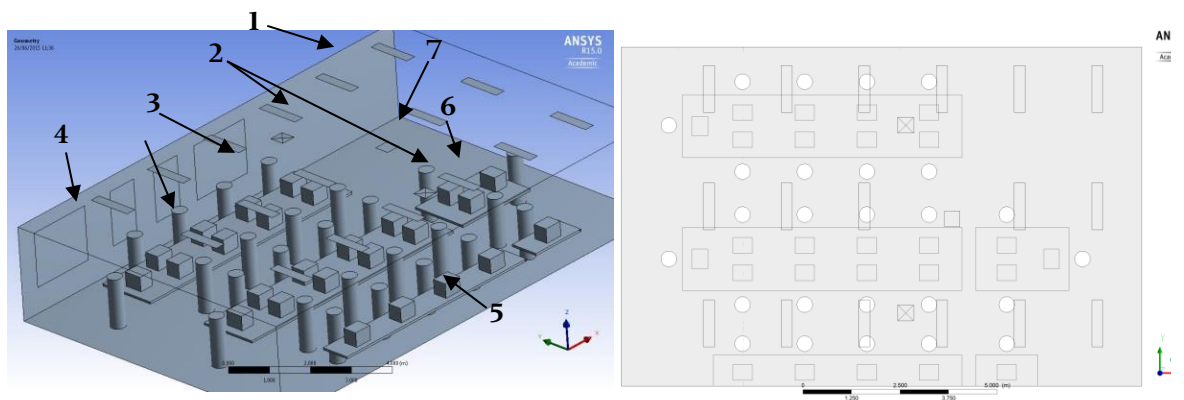
Figure 3.9 – Seminar room model (isometric and top view) and mesh generated {1 – Lamp; 2 – inlet airflow (supply air); 3 – Occupants; 4 – Window; 5 – table; 6 – Computer; 7 – outlet (exhaust grille)}

The room wall, ceiling and floor temperature were assumed to have the same temperature as the outer rooms and because of this, the heat flux is zero. The fourth wall and windows to outside have convection as a boundary condition and the heat transfer coefficient was calculated using McAdams correlation (McAdams, 1954). The properties for the wall and window are presented in Table 3.2. Computers and lights have a temperature of 40 °C (Lei et al., 2014), tables are made of wood with zero heat flux. It was assumed an average skin temperature of 33.7 °C as a boundary condition

for the students with skin properties being presented in Table 3.3 (Zolfaghari and Maerefat, 2010).

Table 3.2 – Wall and window properties (IESVE, 2016)

	Location	Thickness (m)	Density (kg/m3)	Specific heat (J/kgK)	Thermal conductivity (W/mK)
			Properties		
Wall	Gypsum-plastering	0.015	1200	837	0.420
	Concrete	0.1	2400	750	1.500
	Dense-eps-slab	0.0585	30	1400	0.025
	Brick	0.1	1700	800	0.840
Window		0.024	2500	800	0.0123

Table 3.3 – Thermal skin properties (Zolfaghari and Maerefat, 2010)

Location	Thickness (m)	Density (kg/m3)	Specific heat (J/kgK)	Thermal conductivity (W/mK)
		Properties		
Epidermis	80 x 10-6	1200	3578 – 3600	0.24
Dermis	0.002	1200	3200 – 3400	0.45
Subcutaneous	0.01	1000	2280 – 3060	0.19

For all cases studied, students remain seated during class. Their body was represented as a cylinder with a diameter of 0.4m and 1.36m of height. The body surface area of approximately 1.83 m² corresponds, according to DuBois (Nicol and Humphreys, 2002), to a man with 1.70 height and approximately 73 kg.

Boussinesq approximation was used because density does not vary significantly. Radiation model was not considered in this analysis and Realizable $k - \varepsilon$ with scalable wall function was chosen. The solution methods were selected based on ANSYS Fluent manual (ANSYS, 2017) and are presented in Table 3.4.

Table 3.4 – Solution Methods implement in ANSYS Fluent based on ANSYS Fluent manual

Pressure-Velocity coupling	SIMPLE
Spatial Discretization	Green-Gauss Node Based
Pressure	Body Force Weighted
Momentum	Second Order Upwind
Turbulent Kinetic Energy	Second Order Upwind
Turbulent Dissipation Rate	Second Order Upwind
Energy	Second Order Upwind

SIMPLE is a Semi-Implicit Method for Pressure Linked Equations algorithm. The value of pressure and velocity are initially guessed and an under-relaxation factor helps to improve the stability and convergence of the iterative process. This factor limits the change in a variable from one iteration to the next. Second-Order Upwind is essential for tri/tet mesh or when the flow is not aligned with the mesh but it might take more time to converge. According to ANSYS Fluent theory guide (ANSYS, 2017), Green-Gauss Node-Based is recommended for tri/tet meshes and Body Force Weighted when body forces are large, e.g., high Ra natural convection or highly swirling flows.

To compare the simulation with the measured indoor temperature, it is necessary to use same day and time environmental parameters (temperature, wind velocity and humidity). These values were taken from Weather Underground ('Weather Underground', n.d.).

Meshes of 580,094, 801,471, 920,117 nodes were generated and simulations performed. The minimal variation on average temperature (between the last two meshes on the z plane located at 1.2 m above the floor) was encountered (28.77 against 28.78 ^{o}C). The mesh with 920,117 nodes was chosen because the increase in the computational time was acceptable. Figure 3.12 shows a 3D view generated mesh and the temperature difference between the last two meshes in two sections and on the occupant's body, while Table 3.5 shows the main mesh parameters used to generate the mesh with 920,117 nodes in ANSYS Mesh Generator. In addition, Figure 3.11 presents the y^+ of the walls on the x-direction where the different values of y^+ justifies the use of the scalable wall function.

Table 3.5 – Main mesh parameters

Relevance	100
Size function	Proximity and curvature
Relevance	Fine
Span Angle Center	Fine
Transition	Slow
Curvature Normal Angle	12
Proximity Size Functions Sources	Faces and Edges
Min Size	Default (1.6173 e-003 m)
Proximity Min Size	Default (1.6173 e-003 m)
Max Face Size	0.180 m
Max Tet Size	0.180 m
Growth Rate	1.13
Mesh Metric	Skewness
Min	7,90E-05
Max	0,89983

Average	0,2274
Standard Deviation (σ)	± 0.124

The study comprised two analysis of air temperature and airflow distribution (Figure 3.10):

- The first dealt with the MVS performance over the seasons (summer, winter and spring/autumn) in order to understand the MVS behaviour. The results are presented in Chapter 4;
- The second used the calibrated data obtained in IESVE to extract heat gains and establish the boundary conditions. The results from this simulation validated the CFD model and are presented in Chapter 5.
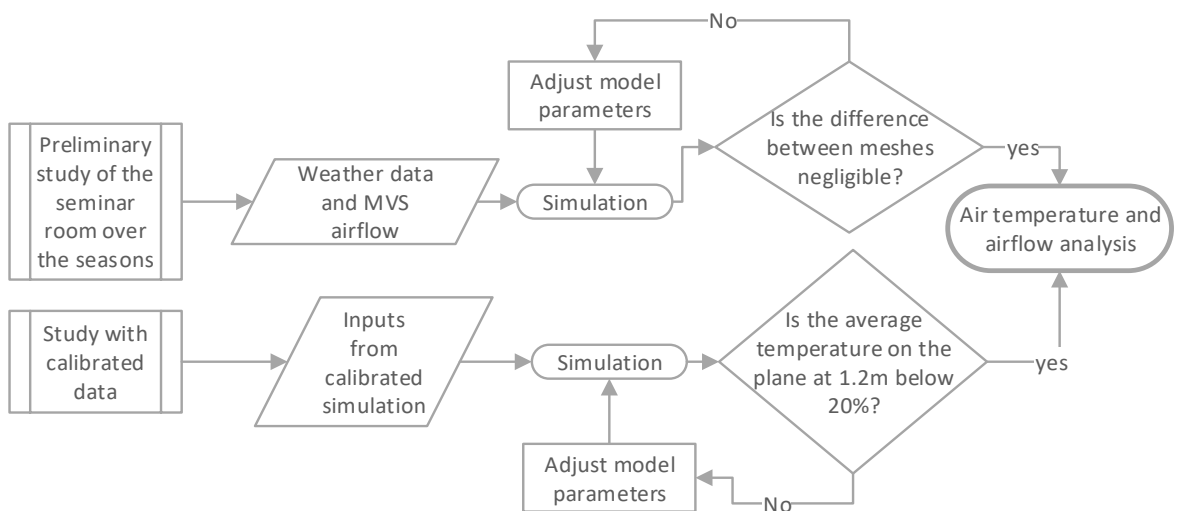
Figure 3.10 –Air temperature and airflow distribution methodology.
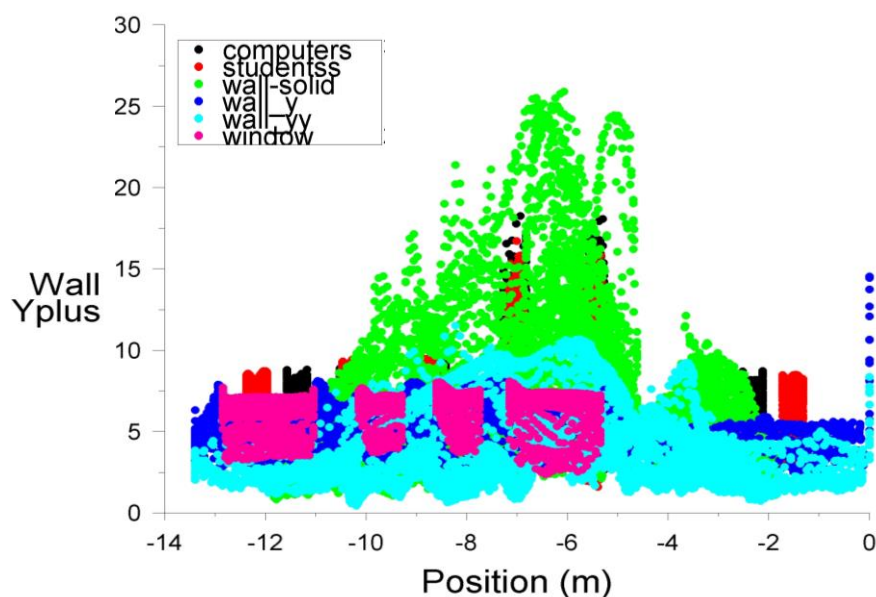
Figure 3.11 – y⁺ of the walls over the x direction
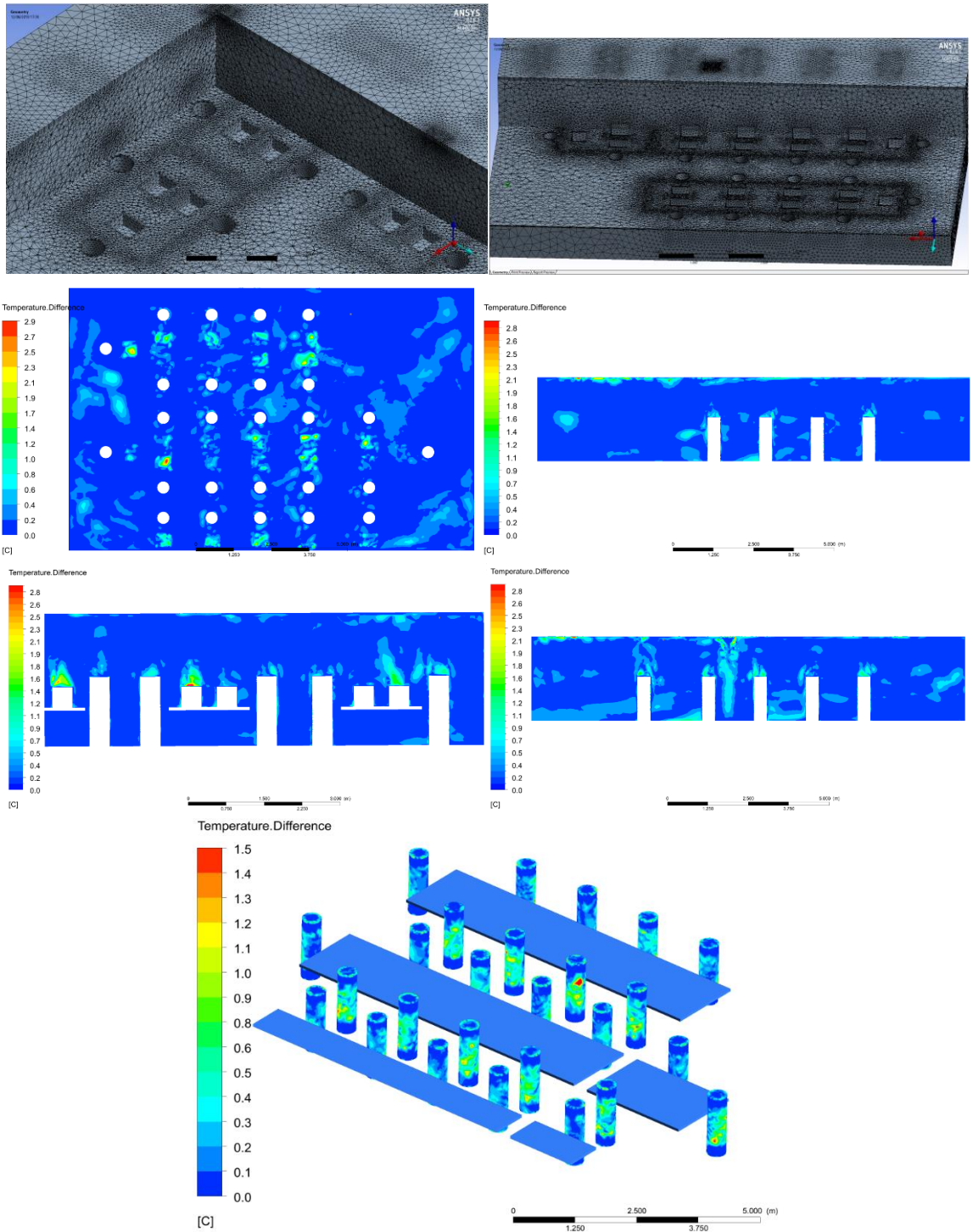
Figure 3.12 – Seminar room generated mesh and temperature difference between two meshes (801,471 and 920,117 nodes)

3.4.1 PCM panel design

ANSYS Fluent was also used to investigate the PCM panel design. The investigation focussed on the PCM encapsulation panel. A number of designs have been investigated and compared with the existing panel. Based on the literature review as presented in section 2.3, the following parameters are important for the performance of the panel and its fabrication.

Table 3.6 – Criteria for selecting optimum design

1.	**Heat transfer using the Nusselt number (the method of evaluation is presented in more detail in section 3.4.3)**
2.	**Rigidity**
3.	**Pressure drop**
4.	**Cost of production**
5.	**Ease of manufacture**

The design process including 2D and 3D simulations are summarized below and illustrated in Figure 3.13.

I. Nine 3D designs of a section of one panel channel were simulated and compared with a hemispherical (dimpled), a teardrop and the existing panel in use. Both dimpled and teardrop were presented in the literature review as an efficient mechanism to enhance heat transfer at a lower cost in pressure drop. The mesh was generated as coarse and adapted through ANSYS Fluent, realizable $k - \varepsilon$ turbulence model was used with scalable near wall treatment function. Realizable. The surface temperature was fixed at 20°C because this is a typical melting point for PCMs used for this application, and the inlet channel temperature was set as 26°C because this is a typical value for the return air through recirculation or outside air during cooling periods. The inlet has a prescribed airflow of Re=18736 which is equivalent to 260 l/s in the MVS.

   i. A smooth panel was simulated with results being used to validate the numerical model by comparing with Gnielinski's correlation for smooth channels (see section 3.4.2).

   ii. An experiment using the existing panel in 1, 2 and 3 thermal batteries analysed the pressure drop over the channel of one Cool-Phase® unit. The results were used to validate the pressure drop of the CFD results. Based on the criteria presented in Table 3.6 for optimum design 13 surface geometries were generated in 2D as the selected 3D design is uniform along its width.

II. The optimum design (again based on the criteria presented in Table 3.6) selected from 2D simulations was used for refinements. With surface dimensions unchanged, 9 new designs evaluated the gap between panels, panel thickness and number of panels.

III. The final design selected was used to fabricate the panel which was evaluated using a laboratory rig (described in section 3.5)
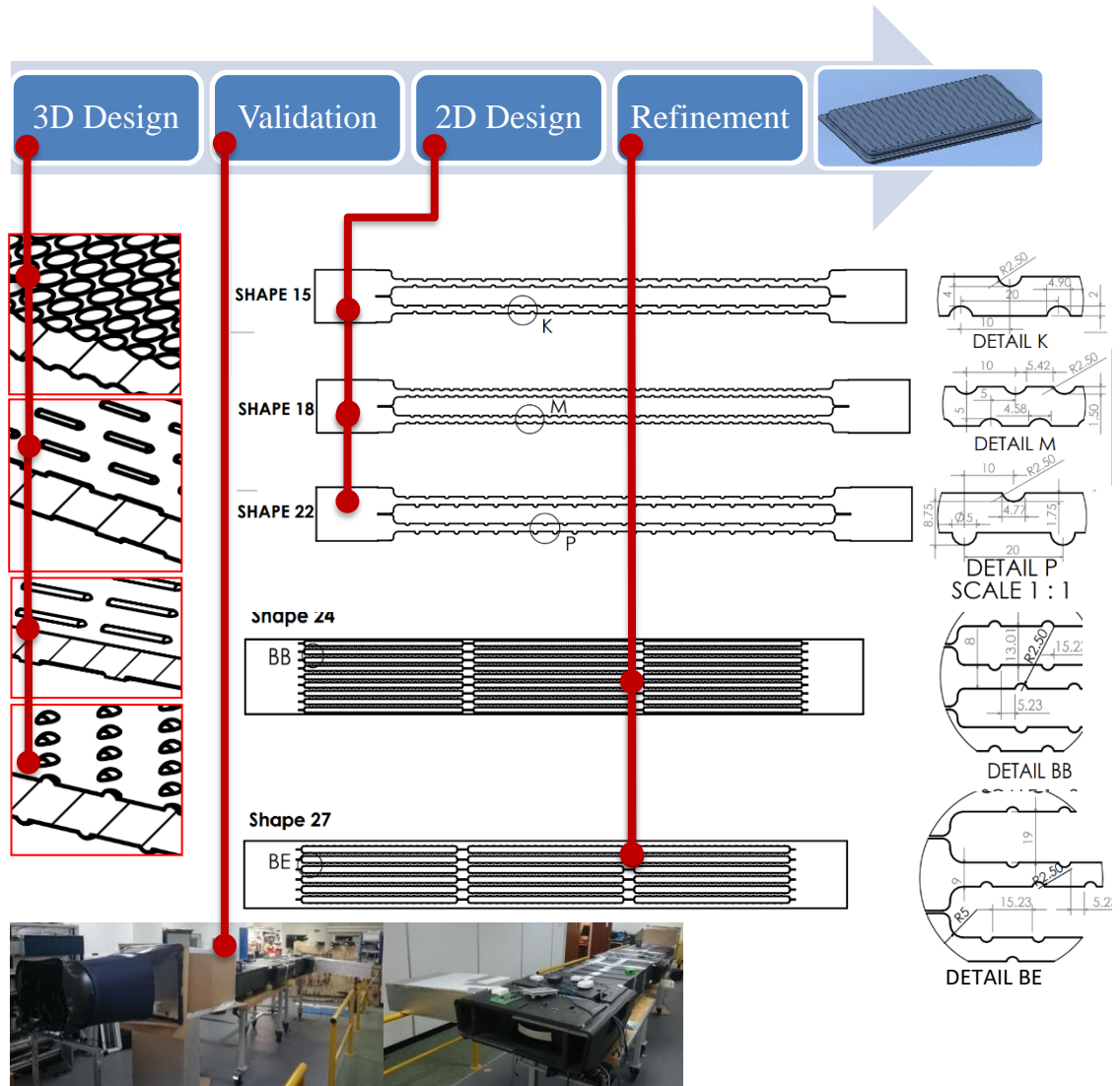
Figure 3.13 – Design Methodology

3.4.2 Methodology of optimum design selection

This section presents the methodology for the selection of the optimum design based on the criteria presented in Table 3.6.

As observed in the literature review, the Nusselt number is the term commonly used to evaluate heat transfer in channels with augmented surfaces. To estimate its value, it is necessary to calculate the convective heat transfer coefficient (h) with a control volume being applied on the gap between the panels (Figure 3.14):
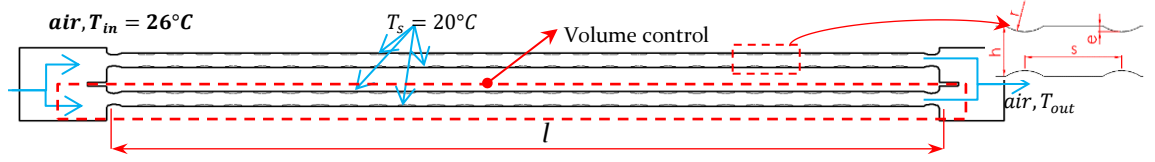
Figure 3.14 – PCM panel control volume

For this study, it is assumed that the outer region of the PCM panel is filled with PCM with a melting point of 20 °C and during the phase change, the temperature remains constant. Due to that, all energy released by the panel (Q_{conv}) is transferred by convection (first by diffusion and then by advection) to the air (Q_{air}), thus:

$$Q_{air} = Q_{conv}$$
$$\dot{m}_{air} C_{p(air)} \left(T_{m,o} - T_{m,i} \right) = h A_{panel} \Delta T \tag{3.4}$$

where $A_{panel} = L_{panel} \cdot W_{panel}$; $\dot{m}_{air}$ is the air mass flow rate in $\frac{kg}{s}$; $T_{m,o}$ is the outlet fluid temperature calculated by the CFD simulation; $T_{m,i}$ is the inlet fluid temperature and equal to 26 °C and Q_{air} in Watts. Air properties were fixed at 300K (specific heat ($C_{p(air)}$) of 1007 $\left[\frac{J}{kgK} \right]$, conductivity ($k_{air}$) of 0.0263 $\left[\frac{W}{m\,K} \right]$ and density (ρ_{air}) of 1.1614 $\left[\frac{kg}{m^3} \right]$) (Incropera, 2007).

The surface temperature of the panel was assumed constant at 20°C. For such situations, the difference between hot and cold (ΔT) is given by a logarithmic mean temperature difference ΔT_{LMDT} (Incropera, 2007):

$$\Delta T_{LMDT} = \frac{(\Delta T_{out} - \Delta T_{in})}{\ln \left(\frac{\Delta T_o}{\Delta T_i} \right)} = \frac{(T_s - T_{m,o}) - (T_s - T_{m,i})}{\ln[(T_s - T_{m,o})/(T_s - T_{m,i})]} \qquad [K] \quad (3.5)$$

where T_s is the surface temperature. Adding Eq. (3.5) in Eq. (3.4:

$$h = \frac{\dot{m}_{air} C_{p(air)} (T_{m,o} - T_{m,i})}{(L_{panel} \cdot W_{panel}) \left(\dfrac{(T_s - T_{m,o}) - (T_s - T_{m,i})}{\ln \left[\dfrac{T_s - T_{m,o}}{T_s - T_{m,i}} \right]} \right)} \qquad \left[\frac{W}{m^2 K} \right] \quad (3.6)$$

The introduction of ridges restricts the airflow and requires more pumping power from the fan. The thermal enhancement factor (η) (Tyagi et al., 2015) analyses the ratio of the convective heat transfer of the augmented surface over a smooth surface at a constant pumping power and is given by:

$$\eta = \frac{\left(\dfrac{Nu}{Nu_o} \right)}{\left(\dfrac{\Delta p}{\Delta p_o} \right)^{1/3}} \tag{3.7}$$

where Nu_o and Δp_o are the Nusselt number and the pressure drop in a smooth panel. Values higher than 1 suggest an increase in heat transfer or reduction on pressure drop when compared to a smooth panel, and values lower than 1 suggest the opposite. Therefore, it is an expression of efficiency.

To ensure that the correct numerical model was selected, a 3D smooth panel was designed (0.0422 x 0.027 x 0.575 m) to evaluate the Nusselt number and compare with Gnielinski's correlation for smooth channels. The mesh was generated as coarse and adapted through ANSYS Fluent until no changes on the fourth digit were found on inlet pressure and outlet temperature within the last 100 iterations. Table 3.7 shows the adaptation methods used. Added to that, under-relaxation factors were adjusted to allow convergence and the simulation stopped when the minimum residual of 10^{-5} is achieved for turbulence, energy and continuity (see Table 3.8).

Table 3.7 – Adaptation methods used for validation

Adaptation method	Variables
Gradient of	Static pressure, total pressure, static temperature, turbulent intensity, velocity magnitude
Iso-Value	Velocity magnitude, cell Reynolds number, turbulent intensity, cell equiangle skew

Table 3.8 – Under-relaxation factors used on the 2D design procedure.

Pressure	0.3
Density	1
Body Forces	1
Momentum	0.85
Turbulent Kinetic Energy	0.82
Turbulent Dissipation Rate	0.82
Turbulent Viscosity	1

The model applied to all simulations are Realizable $k - \varepsilon$ turbulence with scalable near wall treatment function and the solution methods are SIMPLE method for pressure-velocity coupling was used with second-order upwind scheme for pressure, momentum, turbulence and energy were the solution methods applied to all simulations.

The results of Nusselt number obtained from the CFD simulation were compared with Gnielinski's correlation (eq.(3.8)) in order to validate the simulation in terms of heat transfer.

$$Nu_G = \frac{\left(\frac{f}{8}\right)(Re_D - 1000)Pr}{1 + 12.7\left(\frac{f}{8}\right)^{\frac{1}{2}}\left(Pr^{\frac{2}{3}} - 1\right)} \tag{3.8}$$

where Re is the Reynolds number, Pr is the Prandtl number of the air and f is the friction factor calculated by Petukhov correlation (eq.)

$$f = (0.79\ln(Re_{Dh}) - 1.64)^{-2} \tag{3.9}$$

After several iterations, the final mesh of the panel section had 2,389,901 nodes and presented consistent result with a difference of 5.41 % between Gnielinski's correlation and CFD simulation for the simulated Reynolds number (Re=18736).

Moreover, an experiment (Figure 3.15) using the existing panel with 1, 2 and 3 thermal batteries measured the pressure drop along the channel to validate the CFD model. A duct with the length of 5 times the size of the hydraulic diameter was created before and after the thermal battery to ensure uniformity of the airflow. Measurements were made upstream and downstream of the thermal batteries using Tchebycheff's method (ASHRAE, 2013b) with the Pitot tube TSI TA465-P ('Airflow Instruments Micromanometer PVM610', n.d.) (Accuracy of ±1 Pa and resolution of 0.1 Pa; and an accuracy of 10.16 m/s with 0.01 m/s resolution). This method provides the greatest accuracy because measurement point locations account for the wall friction effect and fall-off velocity near wall ducts (Zhang, 2005).
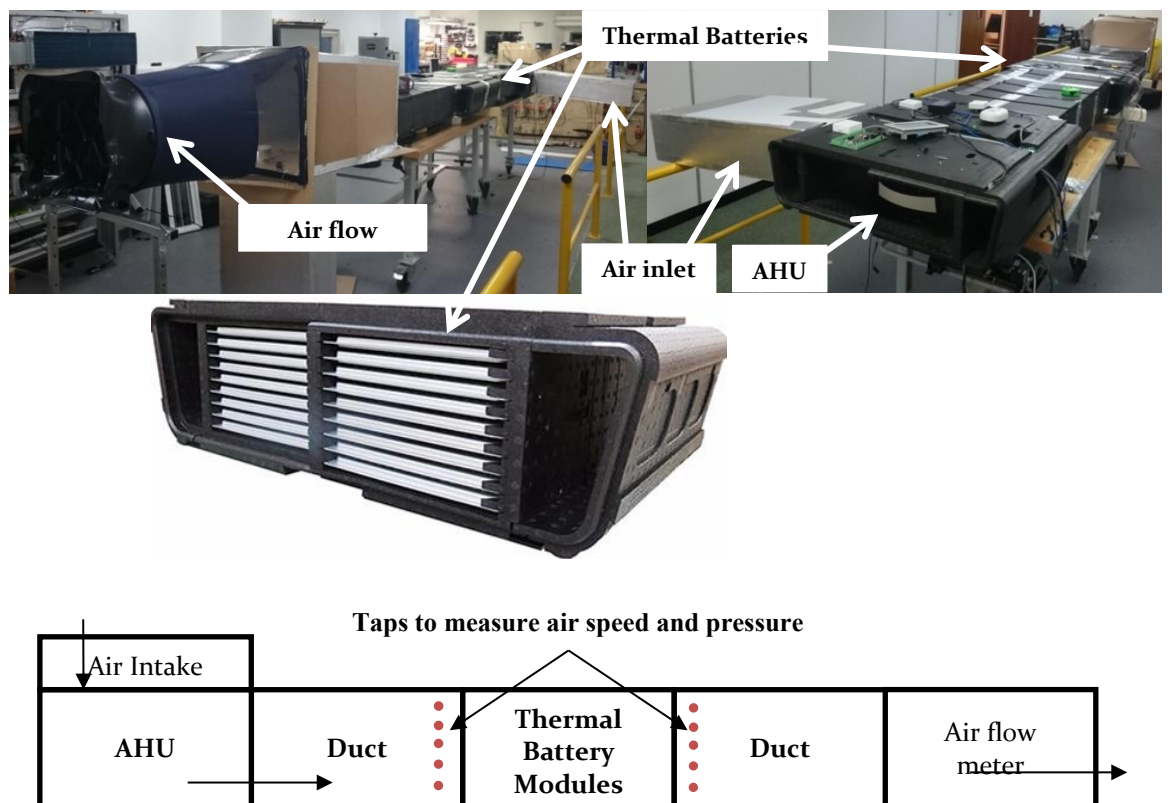
Figure 3.15 – Test rig with two thermal batteries and a schematic

The process of validating the pressure drop in 3D can be time-consuming as it requires a large number of nodes due to MVS dimensions. For this reason, a 2D analysis was performed as the geometry of the systems allows it. A section located at the top of the bulges was selected as the existing panel is not uniform along its width. The mesh generated followed the same criteria developed for the smooth panel in 3D. Figure 3.16 shows the mesh before and after the last adaptation and Table 3.9 the number of nodes and elements.
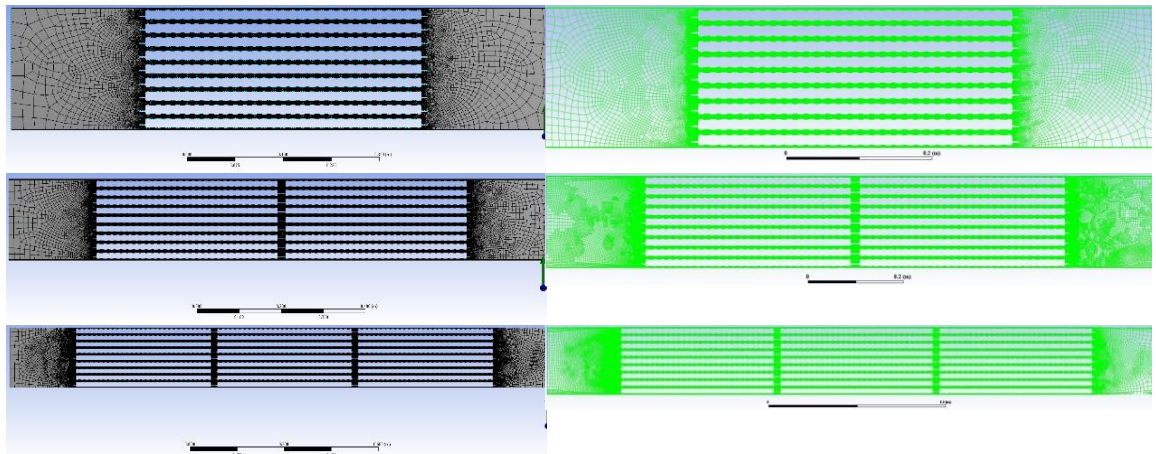
Figure 3.16 – 1, 2 and 3 modules generated for validation with meshes before and after adaptive cells.

Table 3.9 – Number of nodes and elements before and after adaptive meshing

Shapes	First Mesh		Adapted Mesh	
	Nodes	Elements	Nodes	Elements
1 module	168,489	158,948	371,043	330,158
2 modules	265,665	248,554	1,083,181	982,672
3 modules	272,987	252,044	1,395,533	1,202,846

The results of experiments and simulations presented in Table 3.10 show that even if the existing panel is not uniform along its width, 2D simulations present acceptable results compared to experimental measurements with a maximum difference of 16.05 Pa (or -23.85 %) for 3 modules at Re = 21,600 and a minimum of 0.77 Pa (or -6.96 %) for Re = 10,089 and 2 modules. This higher pressure drop compared to the experimental values was expected because the existing panel has bulges distributed along its surface (as it can be seen on Figure 3.3) and 2D simulations used a cross-section plane along the top of the bulges. Furthermore, air leakages in the experiment can reduce the pressure drop. Even though, Zhang et al. (Zhang et al., 2007) suggest that differences close to 20 % are considered acceptable.

Table 3.10 – Experiment and simulation pressure drop and the difference between them.

Experiment pressure drop (Pa)			Pressure drop simulation in 2D (Pa)			Difference between experiment and simulation (Pa)		
Air flow (l/s)	1 TB	2 TB	3 TB	1 TB	2 TB	3 TB	1 TB	2 TB	3 TB
10,089	5.24	10.30	14.23	6.11	11.07	15.37	0.87	0.77	1.14
18,736	15.38	28.58	40.98	19.80	37.77	52.69	4.42	9.19	11.71
21,600	20.20	43.47	51.24	25.51	45.92	67.29	5.32	2.44	16.05

With simulation presenting good results when compared to Gnielinski's correlation and experiment, this method of generating the grid was applied to all 32 simulated cases.

3D simulations

First, nine 3D designs were generated (four of them are presented in Figure 3.13 and the rest in Appendix III) to analyse heat transfer and pressure drop via CFD simulations over a channel. Each design was drawn with different rounded lozenges, protrusion and groove radius. All geometries vary by

  a) Ridge height per airgap $[0.125 < e/h < 0.313]$,
  b) Ridge pitch length $[0.033 < s/l < 0.078]$,
  c) Ridge pitch width $[0 < w_r/w < 0.233]$,
  d) Ridge radius $[1.5 < r < 6]$.

The ratios of the nine designs are presented in Table 3.14. The designs were compared with a flat, a hemispherical, a teardrop and the existing panel. For all 3D simulations, an air gap of 8mm was considered. Due to periodicity, panels were sectioned as shown in Figure 3.17.
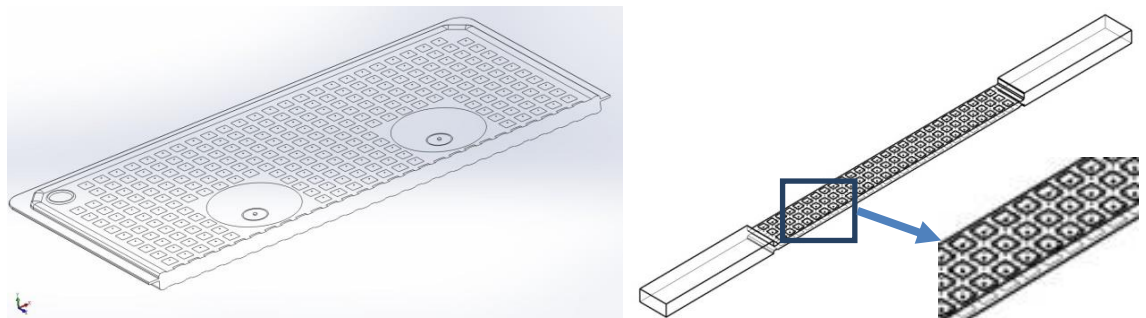
Figure 3.17 – Existing Cool-Phase® panel sectioned and the section used for 3D simulation.

A Reynolds number of 18736 for all cases was used as it represents the average airflow during the charging period. Inlet and surface temperature were the same used to validate the CFD model. Figure 3.14 presents the control volume, the boundary

conditions and the dimensions used. Table 3.11 the number of nodes and elements of each 3D model simulated.

Table 3.11 – Number of nodes and elements per shape

Shapes	Nodes	Elements
Existing	3,265,690	8,810,678
Dimpled	2,075,661	8,590,584
Shape 1	2,699,169	9,303,927
Shape 2	2,207,470	7,111,393
Shape 3	2,704,645	9,404,379
Shape 4	2,097,016	7,218,422
Shape 5	3,724,710	12,111,020
Shape 6	1,673,820	5,896,861
Shape 7	2,248,649	8,342,824
Teardrop	2,932,058	10,981,344
Shape 9	9,914,91	3,004,446
Shape 10	2,877,668	10,304,636

2D simulations

Based on the optimum design which considers rigidity, cost of production, ease of manufacture, heat transfer and pressure drop calculated with the 3D simulations, 13 surface geometries were generated in 2D as the selected 3D design is uniform along its width. A parametric analysis varying ridge height [$0.063 < e/h < 0.281$], ridge pitch [$0.022 < s/l < 0.056$] and ridge radius [$2.5 < r < 7.5$] evaluated pressure drop and heat transfer. These dimensions are represented in Table 3.14 and the drawings on Appendix IV. The flow rate in terms of Reynolds number used for all 2D simulations were based on the inlet hydraulic diameter of the channel and ranged from 7,200 to 21,600 which is equivalent to an airflow from 100 to 300 l/s. The mesh generation followed the same procedure for the 3D simulations. Table 3.12 presents first and last number of nodes and elements for each shape. The optimum design considering cost of production, ease of manufacture, heat transfer and pressure drop was then selected for refinements.

Table 3.12 – Number of nodes and elements before and after adaptive meshing

Shapes	First Mesh		Adapted Mesh	
	Number of Nodes	Number of Elements	Number of Nodes	Number of Elements
11	261,455	242,096	758,254	674,120
12	211,956	200,092	2,849,541	2,804,017
13	180,965	165,381	909,846	821,961
14	391,529	369,633	1,073,442	968,622
15	397,073	371,870	1,138,497	1,048,130
Smooth	152,305	139,106	985,091	914,054
17	137,334	124,793	790,548	714,029
18	260,551	240,699	703,061	611,823
19	255,077	236,486	1,038,140	951,017
20	243,337	225,878	644,767	570,974
Existing	272,987	252,044	1,395,533	1,202,846
21	141,890	129,319	1,131,285	1,042,030
22	99,697	90,535	1,176,767	1,107,409
23	109,081	99,783	993,174	943,299

Refinement

The optimum design selected from 2D simulations was used for refinements. With surface dimensions unchanged, 9 new designs evaluated the gap between panels $[0.03 < h/H < 0.063]$, panel thickness $[0.069 < T_t/H < 0.151]$ and number of panels $[4 < p < 9]$ and presented in Table 3.14. The first and last mesh after adaptation of each shape is presented on Table 3.13. At the end, the final design was used to fabricate the panel. The drawings can be found in Appendix V.

Table 3.13 – Number of nodes and elements before and after adaptive meshing

Shapes	First Mesh		Adapted Mesh	
	Number of Nodes	Number of Elements	Number of Nodes	Number of Elements
24	127,267	116,047	944,848	865,159
25	85,866	75,574	1,047,050	1,001,788
26	56,648	48,540	700,175	671,499
27	70,922	63,937	926,525	898,627
28	87,258	79,504	476,101	442,951
29	60,937	54,544	859,450	837,787
30	56,650	51,288	570,794	543,423
31	80,006	69,812	756,021	695,969
32	77,489	66,576	858,862	799,566

Table 3.14 – Modelled geometrical variations of the panel

3D Simulations				
Shape	Ridge height/ Air gap (e/h)	Ridge pitch length/ Panel length (s/l)	Ridge width / Panel width (w_r/w)	Ridge Radius (r) (mm)
Existing	0.125	0.033	0.033	-
Teardrop	0.313	0.039	0.029	5
Dimpled	0.250	0.058	0.033	6
Shape 1	0.188	0.039	0.077	1.5
Shape 2	0.188	0.039	0.083	1.5
Shape 3	0.313	0.039	0.083	2.5
Shape 4	0.125	0.039	0.077	1.5
Shape 5	0.313	0.078	0.183	2.5
Shape 6	0.250	0.039	0.093	5
Shape 7	0.250	0.062	0.867	5
Shape 9	0.219	0.044	0.867	2.5
Shape 10	0.313	0.056	0.867	2.5

2D simulation of Shape 9			
Shape 9 variations	Ridge Height / Air gap (e/h)	Ridge Pitch / Panel length (s/l)	Ridge Radius (r) (mm)
Shape 11	0.219	0.044	2.5
Shape 12	0.063	0.022	7.5
Shape 13	0.063	0.022	7.5
Shape 14	0.188	0.044	2.5
Shape 15	0.250	0.044	2.5
Shape 17	0.188	0.033	2.5
Shape 18	0.188	0.022	2.5
Shape 19	0.219	0.044	2.5
Shape 20	0.219	0.056	2.5
Shape 21	0.281	0.044	3.0
Shape 22	0.219	0.044	2.5
Shape 23	0.281	0.044	2.5

2D simulation refinement			
Shape 9 in module	Gap between panels / Duct height (h/H)	Panel thickness / Duct height (T_t/H)	Number of panels (p)
Shape 24	0.042	0.069	9
Shape 25	0.042	0.079	8
Shape 26	0.042	0.124	6
Shape 27	0.048	0.101	6
Shape 28	0.053	0.101	6
Shape 29	0.051	0.121	5
Shape 30	0.063	0.151	4
Shape 31	0.034	0.080	8
Shape 32	0.030	0.070	9

3.5 Laboratory testing

The literature review presented in Chapter 2 reveals the importance of ridges to enhance heat transfer in the channel. Section 3.4.2 presented the design procedure of a new panel for the MVS based on criteria presented in Table 3.6. To assess the performance of the new design, this section describes three laboratory tests constructed to evaluate the new panel and compare with the existing panel, which are:

1. Investigation of heat transfer of one panel with different gaps between panels
2. Pressure drop along 1, 2 and 3 Thermal batteries
3. Melting and solidifying comparison between the existing and new panel

3.5.1 First laboratory test: Investigation of heat transfer of one panel with different gaps between panels

Test rig selection

Section 2.6.1 presented 2 main experiments commonly used to test ridges on duct channels as well as the methodology used to evaluate the heat transfer in terms of the Nusselt number. According to this, an experimental rig with thermocouples was selected; the laboratory test is intended to evaluate the overall heat transfer by comparing existing and new panel results instead of analysing the interaction between air and ridges at the boundary layer. Appendix VI explains how the thermocouples used in the laboratory tests were calibrated together with the specification of all instrumentation used for the measurements.

Construction of the rig

The experimental rig was constructed at Monodraught Ltd and it consists of fan and ducts from Cool-phase®. The test section is made of wood with a reduction to allow the air to pass through one single panel gap (Figure 3.18). The outlet consists of an expansion made of wood and another made of cardboard to allow the attachment of the airflow meter (Sensing Precision Balance Master 4250, (Precision, n.d.)). A heat pump was used to stabilize the temperature during all tests.
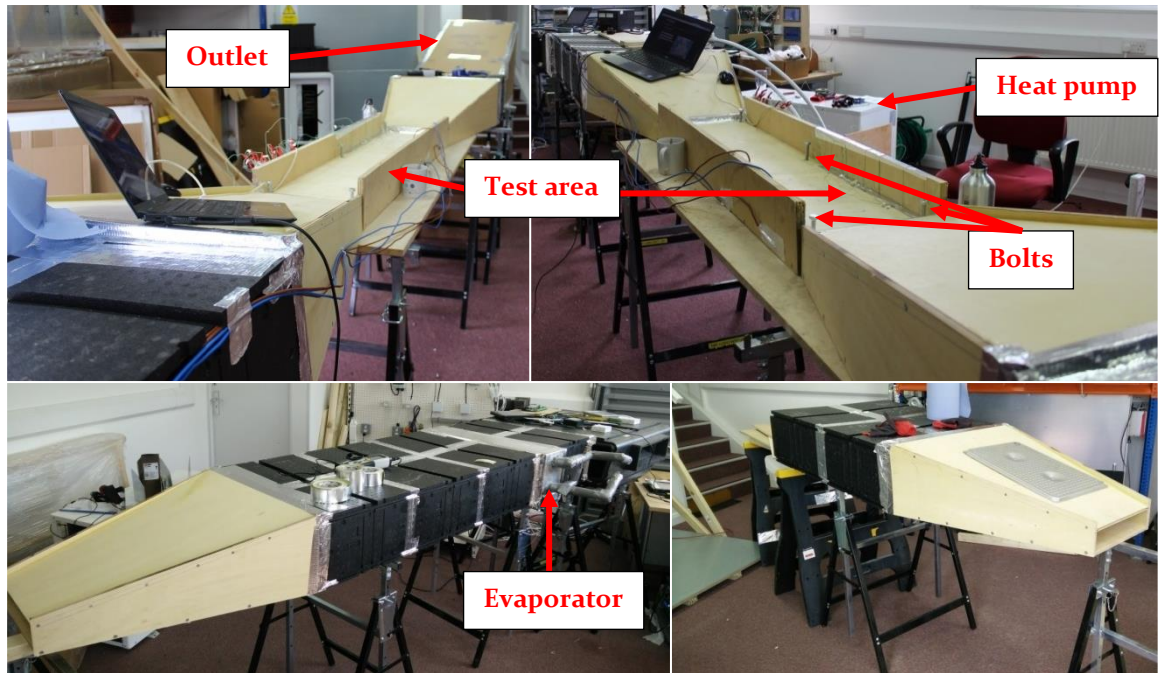
Figure 3.18 – Rig for the first experiment mounted at Monodraught

The panel was divided in two halves where thermocouples were attached on its surface and a 3m wire resistance (Block Resistance Wire, 0.01 mm² CSA 39m ('RD 100/0,6 | Block Resistance Wire, 0.01 mm² CSA 39m | Block', n.d.)) was introduced and filled with a potting compound (RS Pro White Chemical Resistance, Water Resistance Epoxy Potting Compound ('RS Pro White Chemical Resistance, Water Resistance Epoxy Potting Compound', n.d.)) (see step-by-step in Figure 3.19).
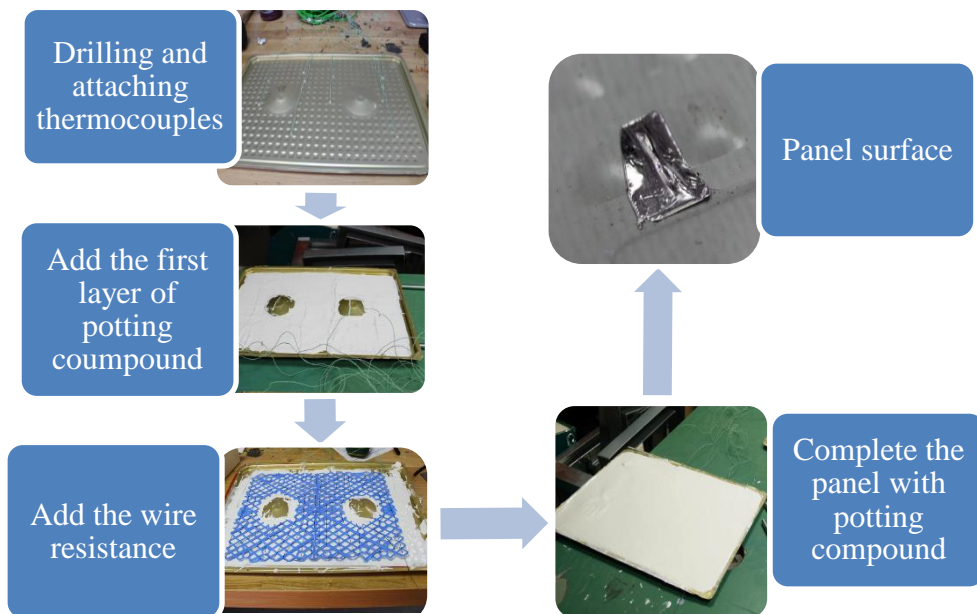
Figure 3.19 – Procedure of attaching thermocouples, resistance wire ('RD 100/0,6 | Block Resistance Wire, 0.01 mm² CSA 39m | Block', n.d.) and filling with potting compound ('RS Pro White Chemical Resistance, Water Resistance Epoxy Potting

14 thermocouples were attached on the panel surface with one sensor before and one after the panel (Figure 3.20). Holes were drilled before the panel to measure air speed through a pitot tube and one hole before and one after to measure the pressure drop using the micromanometer PVM610 from TSI ('Airflow Instruments Micromanometer PVM610', n.d.).
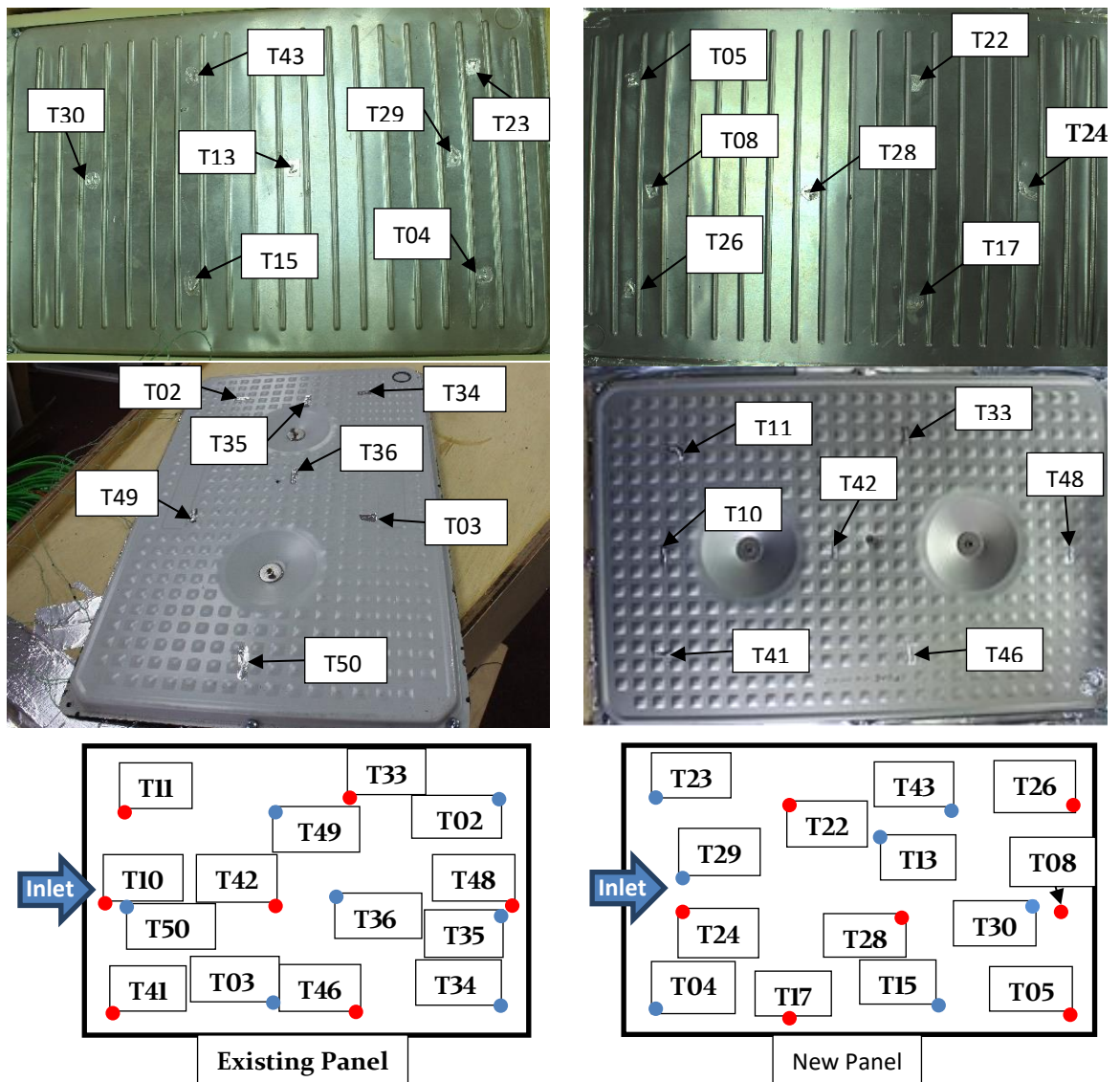
Figure 3.20 – Thermocouple location for the existing and new panel.
Red: thermocouples at the top panel, Blue: thermocouples at the bottom panel

First attempt

The experiment started by attaching the existing panel on the rig and adjusting the panel gap by the use of four rulers attached to the wall of the test channel (Figure 3.21).

Figure 3.21 – Existing and new panels on the test rig with rulers used to measure the gap between panels.

A pitot tube was used to measure the airspeed of 0.5, 1.0 and 1.5 m/s (Re = 2000, 4100 and 6061, respectively). The airspeed measurement with the pitot tube was uniform along the section but not stable (± 15 %). An average was taken and the airflow was confirmed by the use of the airflow meter (Sensing Precision BalanceMaster 4250, (Precision, n.d.)) installed at the end of the rig.

The system has an on/off control, leading to high fluctuations on inlet temperature and therefore, the test had difficulties to achieve steady state. As the interest of this test is to analyse and compare the temperature gain between existing and new panel due to the heat generated by the resistance wire, the heat pump was turned off and ambient air was used.

The first test started by setting a power input of 37 W per panel. At the end of the first test, the rig was opened and it was observed that the panel surface expanded due to the elevated heat generated by the resistance wire as it can be seen in Figure 3.22. This altered the gap distance between panels and due to that, the experiment needs to be repeated.

Figure 3.22 – panel expansion due to excessive heat supply

Second and final attempt

The second test was performed with some improvements in the rig. At first, the walls where the panels were located are now removable. This change made the panel gap visible and easily measured with a calliper. The top panel can move forward and backwards to ensure coincidence between panels. Thermocouples were recalibrated

and reattached at the panel with a screw fixed on the panel to reduce the expansion effect. A new potting compound was used (Pro power epoxy encapsulant – PPC186 (Farnel, n.d.)) and to ensure no deformation on the panel during cure time, doubled tapes were placed on the panel surface. Testo 410i vane anemometer (Testo, n.d.) was used instead of the Pitot Tube and airflow was now calculated using the cross-section area where the panel was installed instead of using the Sensing Precision Balance Master 4250 (Precision, n.d.). Three thermocouples (instead of one) were evenly distributed at the outlet and the temperature acquired was averaged. The heat provided by the power supply was now reduced to 17 W to avoid panel expansions. These alterations can be seen in Figure 3.23.

A smooth panel was also tested to validate the experimental results with existing correlations for heat transfer and friction factor. The experimental procedure for this panel followed the same method for the existing and new panel.
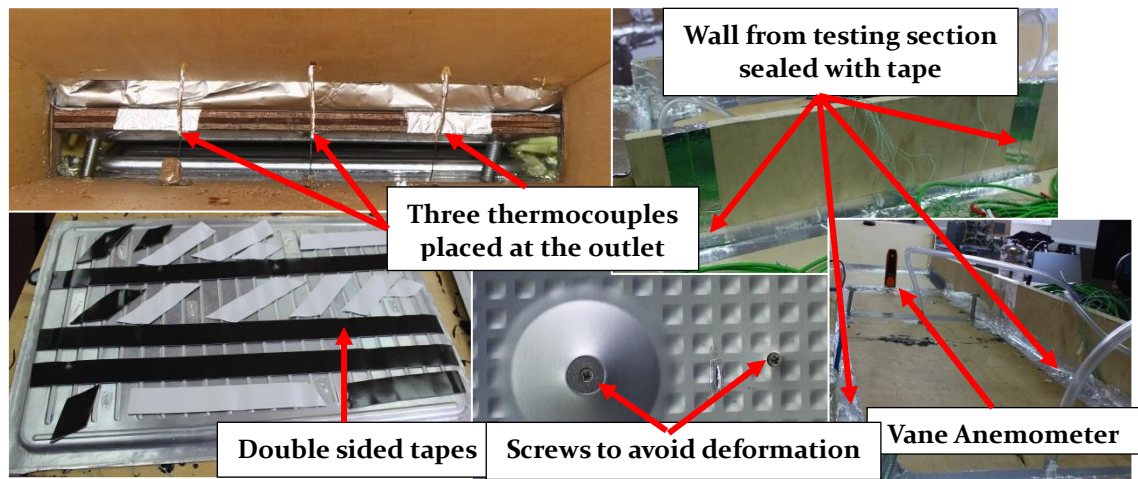
Figure 3.23 – Experimental rig improvements

Airflow and Airspeed

To replicate the airflow found in Cool-Phase®, a relationship between the areas from the MVS and the rig was established to measure the airflow:

Table 3.15 – Tests for the first experiment

	Test 1.1: Air flow (l/s) for 8 mm gap			Test 1.2: Air flow (l/s) for 9 mm gap			Test 1.3: Air flow (l/s) for 10 mm gap		
Existing panels:	7.8	15.7	23.5	8.1	16.3	24.4	8.4	16.8	25.3
New panel	7.8	15.7	23.5	8.1	16.3	24.4	8.4	16.8	25.3

Difficulties to measure the airflow using the airflow meter were encountered during the experiment due to the low airflow. This was bypassed by fixing the airspeed from 0.5 to 1.5 m/s which reflected an average airflow of 6.9, 13.7 and 20.6 l/s. In the real

scale MVS this airflow is equivalent of 66.2, 132.4 and 198.65 l/s, representing 33.8 % less than the maximum airflow.

Table 3.16 summarizes the inlet areas for all configurations with the corresponding ratio from the inlet Cool-Phase® area and Table 3.17 shows the airflow calculated based on the area and airspeed set on the experiment and the airflow in a real scale Cool-Phase®.

Table 3.16 – Inlet area for existing and new panel used in the experiment, the real scale inlet area and the ratio between the experiment and the Cool-Phase® inlet area.

	Existing panel (8 mm)	Existing panel (9 mm)	Existing panel 10 mm	New panel (8 mm)	New panel (9 mm)	New panel (10 mm)	Cool-Phase® area
Inlet area	0.0105	0.0109	0.0112	0.0112	0.0116	0.0119	0.1081
Ratio	9.7 %	10.0 %	10.4 %	10.4 %	10.7 %	11.0 %	100 %

Table 3.17 – Airflow (in l/s) for each panel gap and airspeed and the airflow for a real scale Cool-Phase®

	Panel gap	Airspeed		
		0.5 m/s	1.0 m/s	1.5 m/s
Airflow used in the experiment	Existing panel (8 mm)	6.4 l/s	12.9 l/s	19.3 l/s
	Existing panel (9 mm)	6.6 l/s	13.3 l/s	19.9 l/s
	Existing panel 10 mm	6.9 l/s	13.7 l/s	20.6 l/s
	New panel (8 mm)	6.9 l/s	13.7 l/s	20.6 l/s
	New panel (9 mm)	7.1 l/s	14.1 l/s	21.2 l/s
	New panel (10 mm)	7.3 l/s	14.6 l/s	21.9 l/s
	Average of all gaps	6.9 l/s	13.7 l/s	20.6 l/s
Airflow in real scale	Existing panel and New panel (for all gaps)	66.2 l/s	132.4 l/s	198.6 l/s

Experimental procedure

The experiment started by adjusting the gap between panels with a calliper, closing the walls and sealing the fenestration with sealing tape. After that, the fan was turned on and the airspeed adjusted with the Vane anemometer. The power supply provided 17 W per panel and measurements were logged every 10 seconds. The experiment was concluded when the surface and outlet temperature achieved constant temperature (± 0.25 °C) for at least 25 min. Subsequently, a new airspeed was set until the steady state was achieved. After testing all 3 airspeeds, the walls were removed, the new gap adjusted and another set of tests performed. The whole experiment finished when 0.5, 1.0 and 1.5 m/s were tested for 8, 9 and 10 mm gap for the existing and new panel.

3.5.2 Second laboratory test: Investigation of pressure drop for 1, 2 and 3 thermal batteries

The airflow provided by the MVS needs to be enough to charge the PCM during night time and provide an environment thermally comfortable within the requisites of indoor air quality (IAQ). For Cool-Phase®, this value varies from 100 – 300 l/s for the existing panel. With the development of new panels, it is necessary to ensure that the fan is capable to provide the same airflow range for 1, 2 and 3 thermal batteries.

To achieve this, a pressure drop test was designed to evaluate both existing and new thermal batteries. A test rig consisting of half of the MVS was constructed and 1, 2 and 3 thermal batteries were tested. As half of the system was mounted, the airflow was tested in steps of 20 l/s (from 50 until 150 l/s). The airflow was measured using an airflow meter (Sensing Precision Balance Master 4250, (Precision, n.d.)) and the micromanometer PVM610 by TSI ('Airflow Instruments Micromanometer PVM610', n.d.) measured the static pressure before and after the thermal batteries to estimate the pressure drop. Cool-Phase® components were used to evaluate the pressure drop on the existing panel (ducts and fan). For the new thermal battery, the number of panels is different and therefore, the duct from the MVS cannot be used to hold the panels. Due to that, the test section with the correct distance between panels was made of wood and carved using a 3D carving machine (X-CARVE® 1000mm by Inventables ('Inventables', n.d.)). The tests were concluded when 1, 2 and 3 existing and new thermal batteries were tested from 50 – 150 l/s.
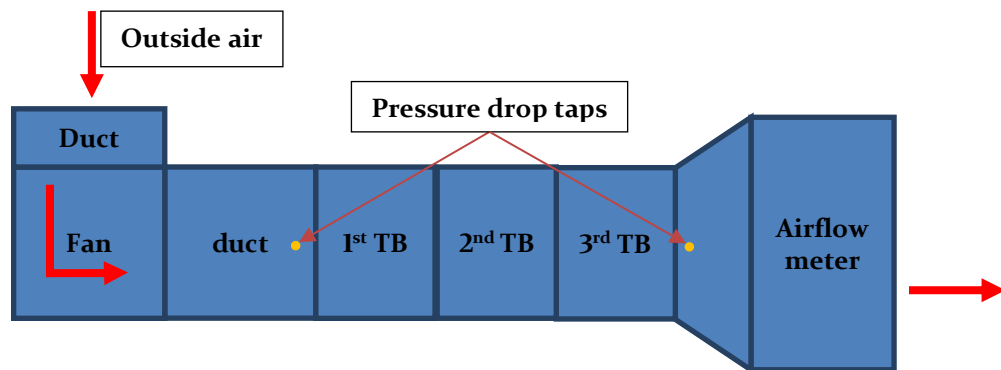
Figure 3.24 – Pressure drop test

3.5.3 Third laboratory test: Melting and solidifying analysis between the existing and new panel

To compare the existing and new panel in terms of cooling power and time of charging and discharging, a test rig was constructed at Monodraught Ltd using Cool-Phase® fan and ducts. This test rig follows the studies found in literature and discussed in section 2.1.

As discussed in section 3.5.1, the heat pump was unable to maintain stable conditions so a HTM LTHW (Hybrid Thermal Mixing Low Temperature Hot Water) was used as a heat source. HTM LTHW is a cooling system designed by Monodraught Ltd and able to provide hybrid ventilation by mixing air temperature for winter periods. In addition, three boilers and a control system are capable to rapidly increase and keep the temperature stable. During summer, the system has the ability to provide night cooling and boosted levels of ventilation. Due to that, the HTM was attached to the test rig and used to control inlet temperature and time of operation.

Air airflow of 75 l/s measured by the Sensing Balance Master was used for charging and discharging periods. This airflow was chosen because is the maximum airflow used by the MVS during its operational charging period. Datataker DT 80 with the extension CEM20 was used to log inlet, surface and outlet temperatures. Each cycle to charge or discharge demands 12 hours to be concluded.

The PCM used in this test was the CrodaTherm™ 24. This PCM is a water-insoluble organic phase change material with a form of crystalline wax or oil liquid (depending on temperature). The PCM was subjected to a DSC (differential scanning calorimetry) and a 3LC (three-layer calorimetry) test by the manufacturer. The results for both tests are presented in Table 3.18 and the datasheet containing more a detailed information about the PCM can be found in Appendix VII.

Table 3.18 – Typical properties of Crodatherm™ 24

	Typical value (3LC)	Units
Peak melting temperature	24	°C
Total stored heat, 15°C to 30°C (melting)	218	kJ/kg
Peak crystallization temperature	21	°C
Total stored heat, 30 °C to 15 °C (crystallisation)	221	kJ/kg

To estimate cooling and heating load and melting/solidifying time of the existing and new panel, thermocouples were attached on its surface with a logging interval of 15 seconds. The The cooling source was outside air and the charging period takes place from 00:00 (midnight) until 12:00 (noon). The discharging period was from 12:00 (noon) until 00:00 (midnight). Figure 3.25 shows the test rig with all components used and the configuration of 1, 2 and 3 thermal batteries used for both existing and new panel. Figure 3.26 presents the test rig mounted.
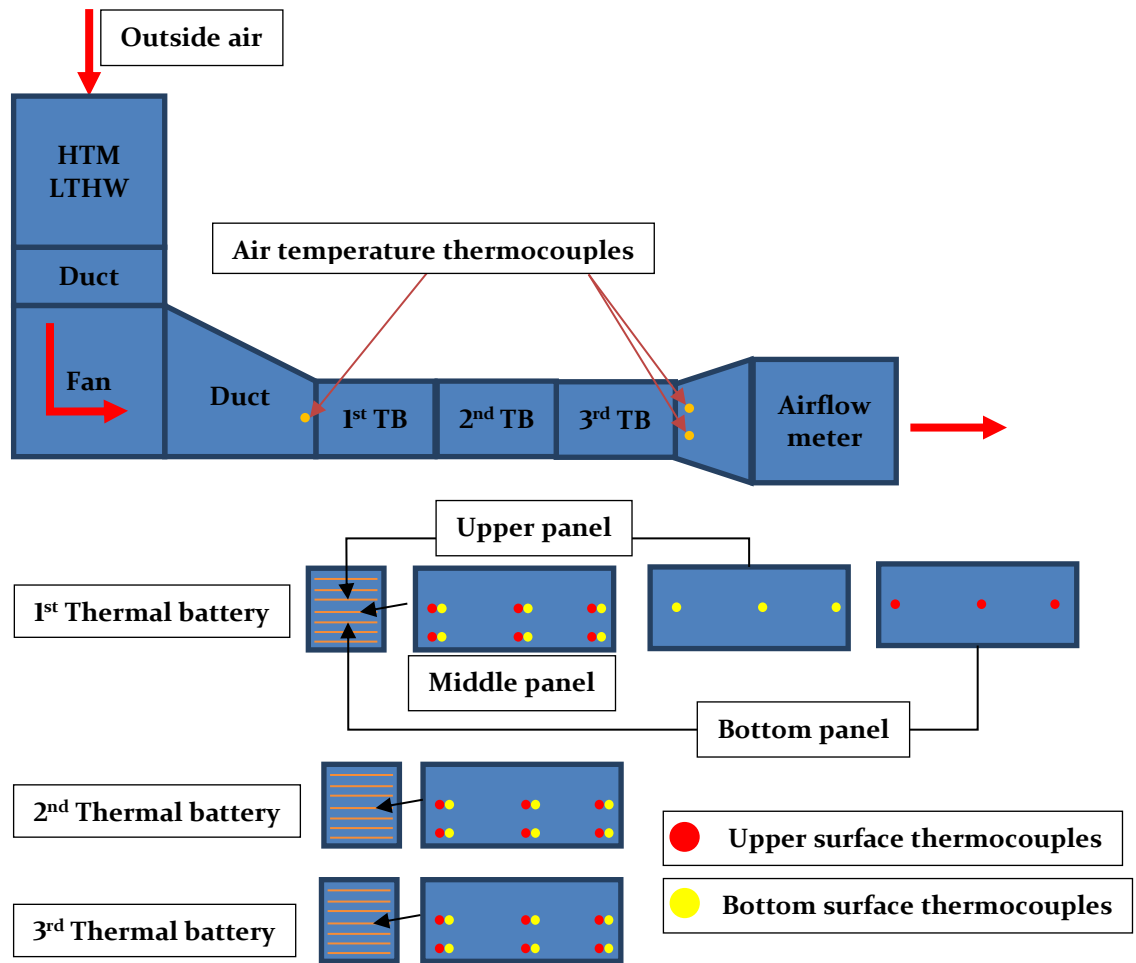
Figure 3.25 – Test configuration of 1, 2 and 3 thermal batteries for both existing and new panel

Thermocouples were attached on the panel's surface to guarantee that the PCM was fully charged or discharged. Due to that, 12 thermocouples were attached on the panel surface (six on the top and six on the bottom) located at the middle of the thermal battery. For the first thermal battery, the three thermocouples were also attached to the bottom and upper panel to analyse if the thermal battery is charging and discharging uniformly. The results of the first test for both new and existing panel confirmed the uniformity in temperature. Due to that, the second and third thermal battery have thermocouples attached only on the middle panel.
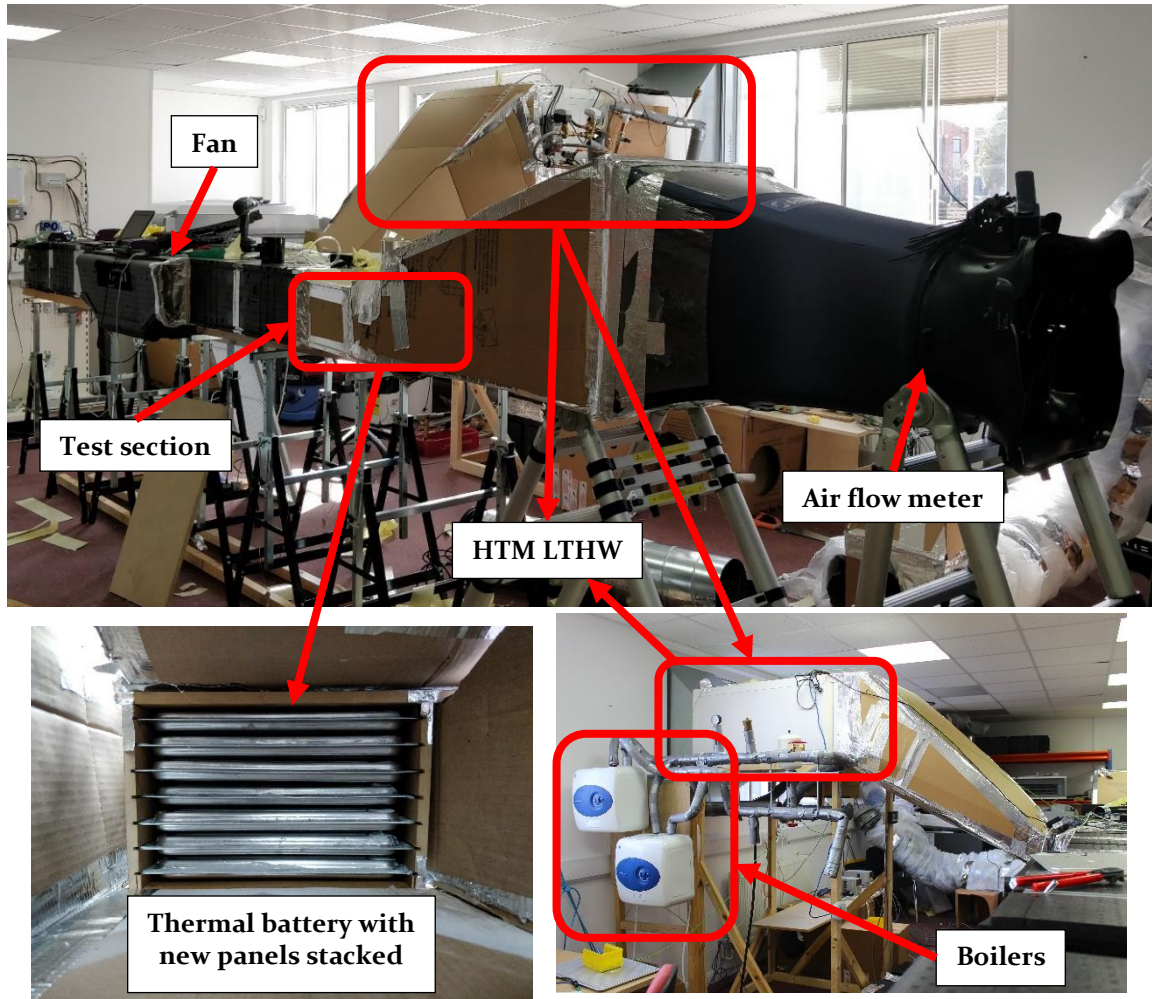
Figure 3.26 – Test rig for melting and solidifying tests

To analyse the cooling/heating load and the effectiveness of the phase change, a control volume was applied for the air (Figure 3.27), thus:
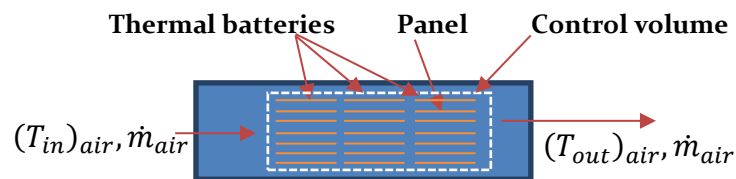
Figure 3.27 – control volume for cooling/heating load for 1,2 and 3 thermal batteries

$$Q_c = \int_0^t \dot{m}_{air}\, c_{p,air}\, (T_{out} - T_{in})_{air}\, dt \qquad \text{[Wh]} \quad (3.10)$$

$$Q_h = \int_0^t \dot{m}_{air}\, c_{p,air}\, (T_{out} - T_{in})_{air}\, dt \qquad \text{[Wh]} \quad (3.11)$$

Where Q_c is the cooling load provided by the thermal battery during the melting period (12:00 – 24:00) and Q_h is the heating load during the solidifying period (00:00 – 12:00). T_{in} and T_{out} is the inlet and outlet temperature for each time step dt (15

seconds); $\dot{m}_{air}$ is the airflow measured by the airflow meter (in kg/s) and $c_{p,air}$ the heat capacity of the air. The air properties used were the same as the one applied during the design process (300 K). For this test, losses were neglected. This procedure is in agreement with several studies in this field (Iten and Liu, 2015; Iten et al., 2016; Dolado et al., 2011; Osterman et al., 2015; Turnpenny et al., 2001; Stritih and Butala, 2010).

3.5.4 Summary of experimental procedure

The following summarises the experimental steps.

A. Laboratory test 1: Investigation of heat transfer and pressure drop of one panel with different gaps between panels.

    a. A test rig consisting in a variable fan, rectangular ducts and a test section was mounted to evaluate the heat transfer of new and the existing panel;

    b. Each half of panel was filled with a potting compound and a resistance wire;

    c. A power supply of 13.5 W heated each panel and 14 thermocouples measured the surface temperature of the panels every 10 seconds;

    d. One thermocouple before and 3 after the test section measured the increase in air temperature every 10 seconds;

    e. Three different airspeeds were tested (0.5, 1.0 and 1.5 m/s or Re $\cong$ 2000, 4100 and 6061, respectively) at three different gaps (8, 9 and 10mm gap). Each test finished after the steady state was achieved for at least 30 minutes;

    f. With panel surface and air temperature data acquired, the heat of convection was calculated through energy balance and Nusselt number estimated.

    g. To validate the results acquired on the rig, a smooth panel with the same gaps and airspeed was simulated with ANSYS Fluent. The Nusselt number estimated in the test was validated by Gnielinski's correlation;

    h. Results of pressure drop and heat transfer from the smooth panel were used to estimate the Thermal Enhancement Factor (TEF);

    i. The optimum configuration considering heat transfer and efficiency will be used in the second experiment.

B. Laboratory test 2: Pressure drop along 1, 2 and 3 Thermal batteries

    a. A test rig consisting in a fan and rectangular ducts was mounted to measure the pressure drop of 1, 2 and 3 thermal batteries for existing and new thermal batteries.

    b. The airflow of the tests varied between 50 l/s – 150 l/s with steps of 20 l/s;

    c. The test was concluded when the pressure drop for new and existing panels was tested for 1, 2 and 3 thermal batteries.

C. Laboratory test 3: Melting and solidifying process of 1, 2 and 3 thermal batteries to compare the efficiency between existing and new panel.

  a. A test rig consisting in a fan, rectangular ducts and a Cooling/heating source with a control system able to provide stable temperature during charging and discharging tests (Charging setpoint of 15 °C and heating setpoint of 30°C adjusted on the cooling/heating source (HTM LTHW ('HTM F Hybrid Ventilation', n.d.)));

  b. The existing and new panels were filled and sealed with the PCM CrodaTherm™ 24.

  c. One thermocouple before and 2 after the test section measured the air temperature every 15 seconds;

  d. 12 thermocouples were attached on the panel surface located at the middle of the thermal battery (6 on the upper and 6 on the bottom surface) plus 6 thermocouples were attached on the panel located below and above the middle panel;

  e. The fixed airflow of 75 l/s for all tests was measured using the airflow meter Sensing Precision Balance Master 4250, [19];

  f. The energy balance from the airside was applied to evaluate the charging and discharging process as well as the time necessary.

3.6 Experimental uncertainty

Thermocouples, flowmeters and air velocity sensors were used in the experiments where each of them is presented in appendix VI. However, no physical quantity can be measured with certainty and there is always an error associated. It can be propagated by many factors such as human reading error, equipment usage, inaccurate set-up etc. When the mathematical operation is performed, errors are propagated. To evaluate these errors the following expressions are used for multiplication/division and addition/subtraction (Moffat, 1988).

$$E_x = \sqrt{E_a^2 + E_b^2 + E_c^2 + \cdots} \tag{3.12}$$

$$E_y = y \sqrt{\left(\frac{E_a}{a}\right)^2 + \left(\frac{E_b}{b}\right)^2 + \left(\frac{E_c}{c}\right)^2 + \cdots} \tag{3.13}$$

Where x and y is the result of the calculation, E_x and E_y the respective associated error for addition/subtraction and multiplication/division; a, b and c are the individual numbers used in a certain calculation and E_a, E_b and E_c are the uncertainties associated to each individual number used in the calculation.

Table 3.19 presents these results. To facilitate, the table presents the uncertainty when a different number of sensors are averaged. Table 3.19 also presents the uncertainty of the Nusselt number and the thermal enhancement factor used in experiment 1 and the heat transfer uncertainty used in experiment 3. The highest percentage in value was used when the error in percentage was needed.

Table 3.19 – experimental uncertainty of thermocouples and main expressions

	Number of sensors		
ibutton	4	1.00	ºC
Hobo	4	0.42	ºC
	8	0.59	ºC
Thermocouples	2	0.51	ºC
	3	0.62	ºC
	6	0.88	ºC
	7	0.95	ºC
	14	1.35	ºC
Heat transfer		3.7	%
TEF		8.6	%
Nusselt number		5.6	%

3.7 Chapter's summary

This chapter described the tools and methods used in this study. It started by describing data acquired during the MVS operation in a case-study application of a seminar room as well as field monitoring in the room to obtain data for the evaluation of thermal comfort and airflow distribution within the room. These data were also used to validate computational models. The computational models were created using (a) the dynamic thermal simulation program IESVE which includes a plugin of the studied system and (b) the ANSYS Fluent CFD program. CFD models were used to simulate the distribution of air temperature and air flow within the conditioned space as well as for the design of the new panel for the MVS. This chapter also described three laboratory tests aimed to compare the efficiency of the existing and new panel. In the end, the method to calculate the uncertainty is described and the uncertainties of the laboratory tests are presented.

There follow four chapters presenting the results. Chapter 4 presents the operational MVS system performance in the case-study space of the seminar room, Chapter 5 presents thermal comfort and overheating analysis as well as proposed improvements in the control of MVS. Chapter 6 presents the design of the panel while Chapter 7 presents the results of the laboratory tests comparing the existing and new panel.

CHAPTER 4 - DESCRIPTION OF THE OPERATIONAL SYSTEM

Introduction to the chapter

This chapter describes the operation of the MVS in study. It includes:

- Description of the MVS according to operational modes and setpoints;
- A detailed explanation of the system over the seasons (summer, spring/autumn, winter). For each case, the MVS performance is described for one week and in more details for one day.

4.1 MVS operation

The studied system is essentially a demand control ventilation and cooling system, controlled by temperature, relative humidity and CO_2 concentration inside the conditioned space. To adjust the air temperature, the airflow can cross the LTES with air recirculated from the room or from outside. If the room exceeds CO_2 concentration limit, outside damper open and fresh air is introduced to reduce CO_2 concentration until the set point is achieved. A summary of the operation modes is presented in Table 4.1.

Table 4.1 – Brief Description of Operation Modes

Cooling modes	Description
Direct outside air ventilation	Used when the outside temperature is cooler than inside, the air is supplied into the room bypassing the LTES until it reaches a set point temperature.
Outside ventilation and cooling	Used when the outside temperature is lower than inside but is not low enough to cool the space; the air crosses the LTES before entering the room.
Recirculation and cooling	When the temperature outside is higher than inside, recirculating air passes over the LTES before entering the room.
Summer Charging	During unoccupied hours, the fan supply outside cold air to charge the LTES and release the build-up heat. When the LTES is fully charged, the system turns off automatically.
Heat recovery cycle	In winter times, when the room is unoccupied or warm, the air is re-circulated through the LTES to charge and use it to reduce the heating system load.
CO_2 control	When CO_2 concentration inside is higher than a specific set point, outside air is supplied.
Humidity control	When the room relative humidity is lower or higher of a pre-set set point, the system will change outside air supply until the set point range is achieved.
For all modes during occupied hours, an outside minimum volume flow is provided to ensure a minimum air flow rate according to regulations.	

Figure 4.1 presents a diagram of the system indicating the location of the sensors used to control its operation. Temperature is controlled by air either drawn from outside or recirculated from the room; depending on the temperature and relative humidity in the conditioned space, external air is used directly or mixed with recirculated air

by-passing the LTES. If cooling is needed the air is directed to the LTES. If the room exceeds the set point CO_2 concentration limit, fresh air from outside is introduced.

The control system has default set-points intended to comply with CIBSE and ASHRAE guidelines (de Dear and Brager, 1998; ISO, 2005) but the user is able to adapt them according to their needs. Additionally, a wall mounted control (Figure 4.2) gives flexibility to the user by changing the fan speed or turning the system off.
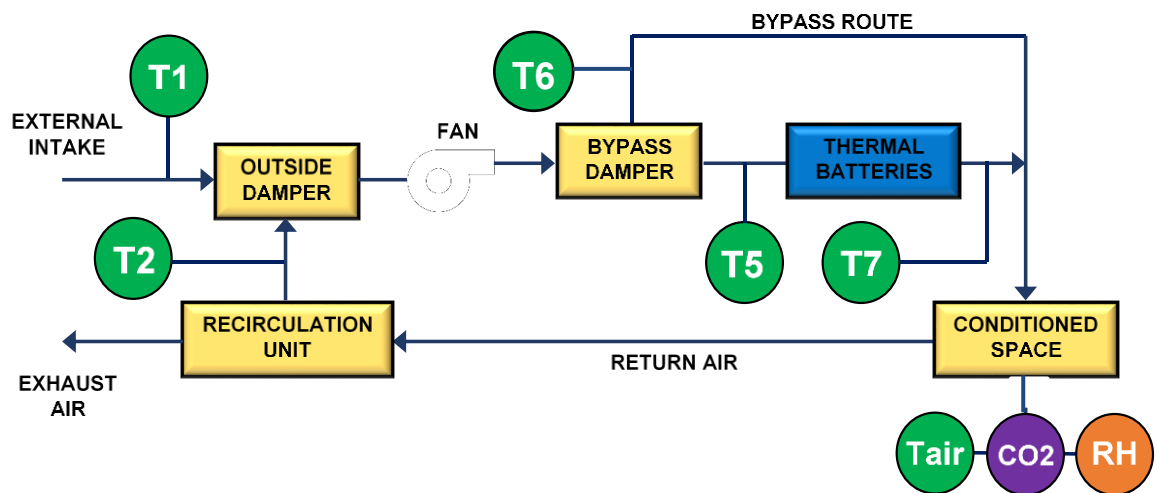
Figure 4.1 - Diagram of the PCM-Air heat exchanger indicating the location of the sensors and below the description of each sensor.

Sensor	Description
T1	External temperature located at the outside of the intake damper recirculation box
T2	Internal temperature located at the outside of the recirculation damper of the recirculation box
T5	Temperature before crossing the LTES
T6	Temperature at the bypass duct
T7	Temperature after crossing the LTES
RH	Humidity inside the room
CO_2	CO_2 concentration (ppm) inside the room
T_{air}	Room temperature

Figure 4.2 – Wall mounted control ('Monodraught; Natural Ventilation, Cooling and Lighting Specialists', n.d.)

Table 4.2 presents the default set-points of a Cool-phase® installed in a seminar room in the University of West England (UWE). Air temperature set-point varies according to the season and airflow rate according to metabolic CO_2 and air temperature. Additionally, the equipment maintains relative humidity within a range of 30-70 %.

Table 4.2 – Set points according to the seasons for the Seminar Room

Season	Autumn	Winter	Spring	Summer
Start day	01-Oct	01-Dec	01-Mar	01-May
Temperature	23	24	23	22
Minimum humidity	20			
Maximum humidity	80			
Desired CO_2 (ppm)	900			
High CO_2 (ppm)	1200			
Charging mode	1:00 to 6:59			
Cooling mode	8:00 to 20:59			
Boost Charge mode	00:00 to 00:59			

Considering Table 4.2, dampers open and close automatically to achieve the required set-points according to each operational modes. To achieve that, the air can get into the room in the ways described in Table 4.3. When Cool-Phase® controls CO_2 it is possible to choose air flowing through the LTES or not.

Table 4.3 – Conditions of volume flow through Cool-Phase®

Conditions	Air intake (Outside damper)		Flow through thermal batteries		Recirculation unit (inside damper)	
	open	closed	on	off	open	closed
Direct outside air ventilation	X			X	X	
Outside ventilation and cooling	X		X		X	
Recirculation and cooling		X	X			X
Heat recovery cycle	X			X		X
CO_2 control	X		On or off			X
Charging mode	X		X		X	

4.1.1 Cool-phase® operational modes

Cool-Phase® has 7 operational modes where each of them is explained below. To exemplify, data from a unit installed at the University of West England was used. Table 4.4 presents the fan range according to the operational mode as well as the operation time according to the season for this particular case. Figure 4.3 shows the operation for a typical day. It is important to mention that the period of each operation mode varies according to regulations, design and client needs. The room used to exemplify the operational system had system and set-points designed according to the Building Bulletin 101 (BB 101) (Regulations Standards Design Guidance, 2006).

Table 4.4 – Airflow range according to each operational mode and operational time according to the season

		Airflow (l/s)							Winter		Spring and Autumn		Summer	
		0	100	140	200	220	260	300	Start	Finish	Start	Finish	Start	Finish
Operational Mode	1	X	X	X	X	X	X	X					8:00	21:00
	2							X					0:00	1:00
	3			X	X	X	X						1:00	7:00
	4	X							23:00	8:00	21:00	8:00	7:00	8:00
	5	X	X	X	X	X	X	X			8:00	21:00		
	6	X	X	X	X	X	X	X	8:00	21:00				
	7	X							21:00	23:00				

Below the operation modes are explained chronologically, starting from midnight.

Operation Mode 2: Charging mode (Night Purge) – Midnight to 01:00 – the fan runs at the highest speed setting for 1 hour to flush the room of stale air. Figure 4.3 shows that all temperatures within this period decrease including the Internal Space Temperature, T_{air}. It should note that T1 (external intake duct) is the temperature of the sensor placed at the face of the intake duct. This sensor can be influenced by infiltration from the room if the plenum is not well sealed. This is what happened in this case and highlights the importance of sensor position for optimum operation of the system.

Operation mode 3: Summer night charge- 01:00 to 07:00 – During this period, the inlet and outlet temperatures of the LTES (T5 and T7, respectively) can be seen to decrease indicating that the LTES is being 'charged' as the external intake air is being passed through them.

Operation mode 4: System switched off - 07:00 to 08:00 – The system is turned off for 1 hour in the morning in a period before the occupancy schedule begins. A crucial observation, however, is that the internal space temperature (T_{air}) rises during this period which effectively negates some of the work done to cool the space during the night. The internal space temperature at 7:00 was well within the thermal comfort range and there was no risk of overcooling.

Operation mode 1: Summer day mode - 08:00-21:00 – In the beginning of the day (8:00 – ~12:00) the LTES is by-passed as the outside air is cooler and room temperature is below summer set-point (22 ºC). At ~12:00, the external temperature measured by the external intake duct (T1) reaches the summer set-point and the air is directed through the LTES maintaining air temperature in the room below external

temperature. Differences between T5 and T7 from 12:00 to 21:00 confirm LTES absorbing heat and delivering cool air into the room, although complete melting must have been reached towards the end of the cooling mode.

Operation mode 4: System switched off - 21:00 to 00:00 – At 21:00 the conditioned period in the space ends, the system switches off and all temperatures converge to the same value. The system remains switched off until midnight where the process starts again.

Operation mode 6: Winter cooling – 08:00-21:00 – the PCM-Air heat exchanger is off but in standby mode. The fan will provide external air when CO_2 concentration are high or temperature goes over the set-point.

Operation mode 7: System switched Off - 21:00 to 23:00 – The room is unoccupied and the system is turned off.
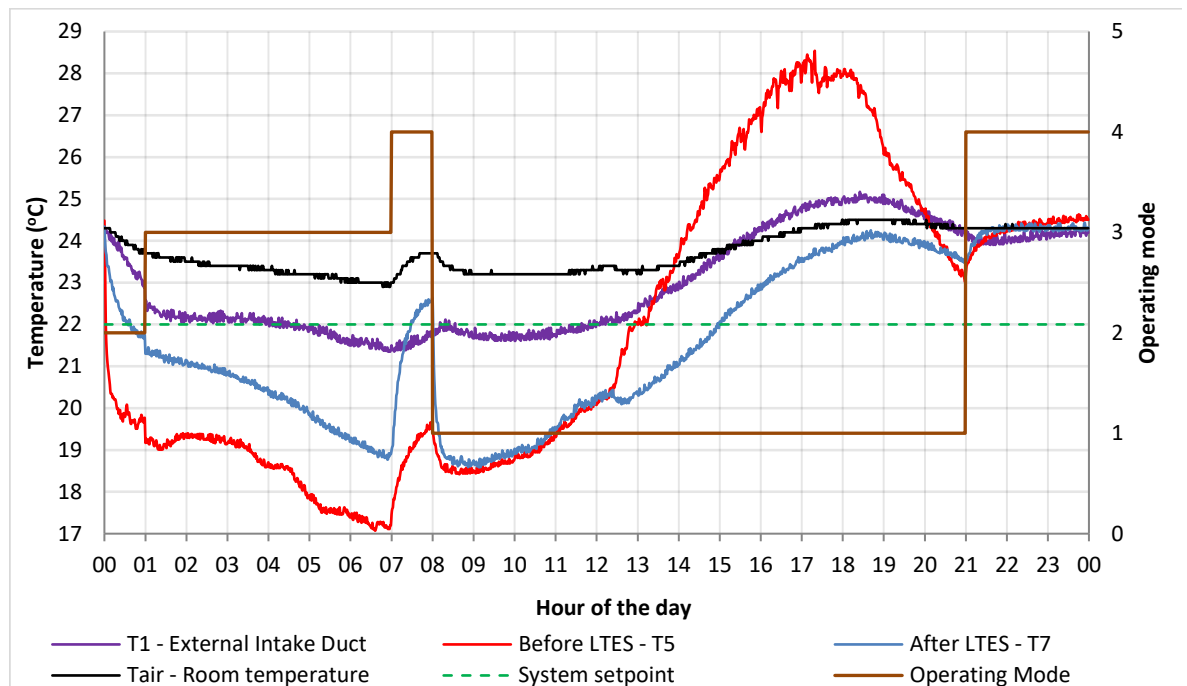
Figure 4.3 – Operation a PCM-Air air heat exchanger in the seminar room one day in August. (1 = cooling mode, 2 = purge mode, 3=charging mode, 4 = off)

The system is operated similarly in different building types according to their occupancy schedules. To maintain the parameters (temperature and CO_2 concentration) close to the setpoint designed and consequently keep the room within BB101 specification, a step control regulates Cool-Phase® airflow and actuators control the dampers based on indoor temperature and CO_2 room concentration. These set-points are presented in Table 4.5 and in Figure 4.4, the MVS control system flowchart.

Table 4.5 – Fan speed set-points.

Air flow (l/s)	Temperature (°C)	CO$_2$ concentration (ppm)	Notes
300			Predominantly during purge mode
260	26°C	1800 ppm	Maximum under normal conditions
220	25°C	1600 ppm	
200	24°C	1300 ppm	
140	23°C	1000 ppm	
100	22°C	900 ppm	Default Minimum set point
0	Off	Off	
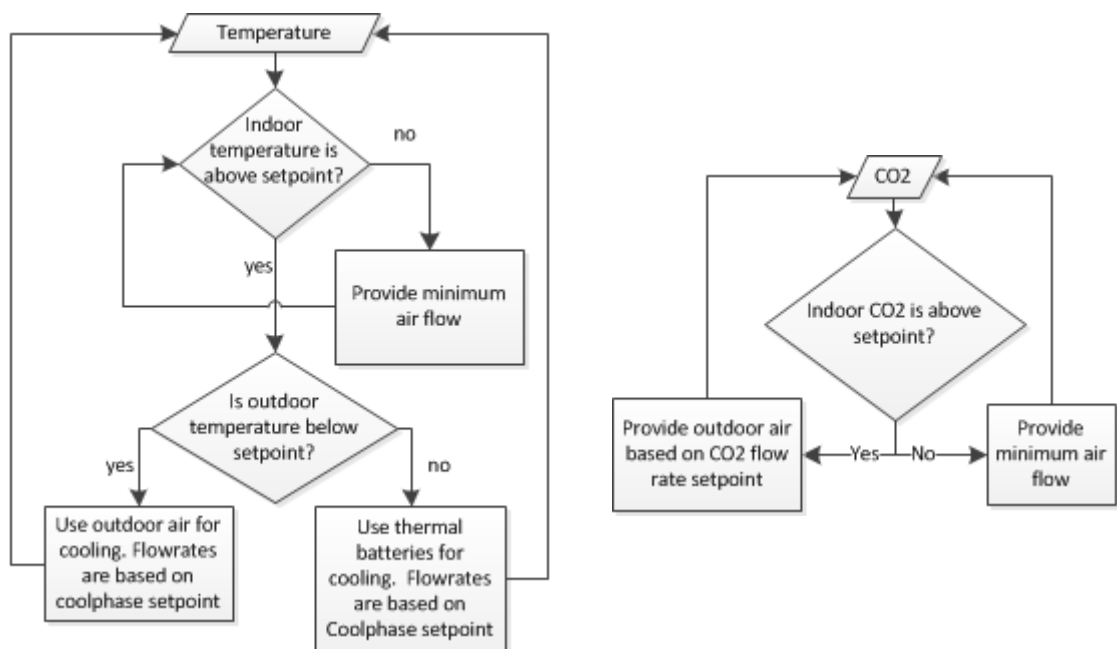
Figure 4.4 – Cool-Phase® control flowchart

From the set-points, cooling modes and operational modes, it is possible to have an overview of how the system works. To deeply comprehend how the system behaves and controls temperature and CO$_2$ during the occupied hours, a particular week for summer, winter and autumn were chosen and for each week, a day. Spring season was not used because Cool-Phase® has the same operational mode of the autumn season. All data was acquired from Cool-phase® system data.

4.2 Summer period (May – September)

Figure 4.5 shows the temperature distribution through a summer week (15/07/2013 to 21-07/2013). It can be seen that Cool-phase® kept room temperature below 28 °C and the temperature after the LTES is close to the temperature before LTES, showing that the batteries were discharged and the MVS cooling the room. From 1:00 to 8:00, T5 and T7 are decreasing and the gap between them proves that the battery is charging. During the weekend, when Cool-phase® is not working and there are no classes, the room temperature has an average of 27.3 °C.

The relative humidity varies considerably during the week and for 13.1 % of the time are lower than 30 %. It is important to notice that the relative humidity below 30 % is not acceptable by BB 101 (Regulations Standards Design Guidance, 2006). Dry air cause discomfort to students by enhancing chances to become ill, inflame the respiratory tract mucous membrane and dry skin and eyes (ASHRAE, 2013a).
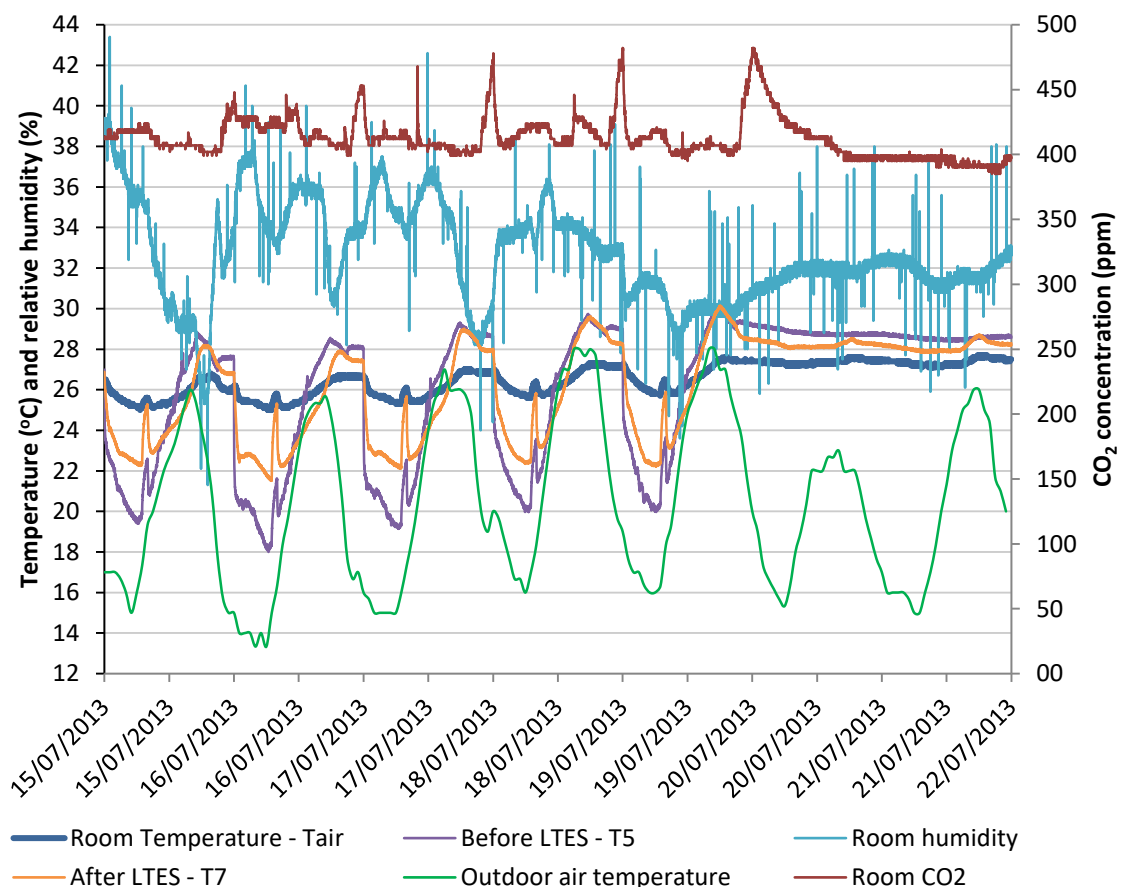
Figure 4.5 – Room temperature, Cool-Phase® T5, T7, humidity, CO_2 concentration and outdoor air temperature of a 2013 summer period (15/07 – 21/07/2013)

For a closer analysis, one day of the week (15/07/2013, Figure 4.6) was chosen. From midnight to 01:00, a deep drop due to the purge mode can be seen from T7. The charging mode continues until 7 AM. To avoid overcooling, between 7 AM and 8 AM the system was off. At 8 AM the cooling mode started and the system control worked to reach temperature and CO_2 concentration set-points. Around 11 AM, the temperature before the LTES (T5) started to become higher than T7 and in this case, the Cool-Phase® started to use the PCM to cool the system. Around 17:00, T7 started to increase more intensely which indicates that the PCM was fully melted and at 20:00 the T5 and T7 had nearly the same temperature and indicates that the LTES were completely discharged. Even if the PCM became fully discharged, the equipment was able to maintain the temperature within temperatures of 25-27 ºC by controlling the air that enters the room. CO_2 concentration were stable (with an average of 410 ppm) during the day which indicates low occupancy.
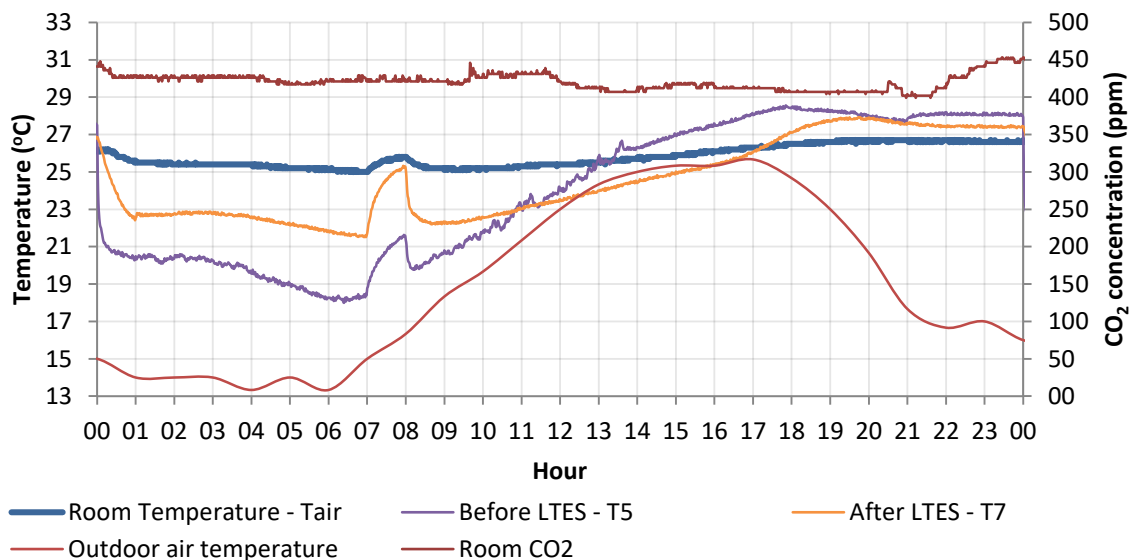
Figure 4.6 – Room temperature, Cool-Phase® T5 and T7, humidity, CO_2 concentration and outdoor temperature of 16/jul/2013

With the objective of regulating temperature and CO_2, dampers from recirculation or outside air open and close and the volume flow vary as can be seen in Figure 4.7. During this period, Cool-Phase® partially closed the outside air damper (43 % open) and turned on the recirculation mode (inside damper 100 % open). This allowed a minimum of fresh air to be introduced in the room. Airflow stays on 210 l/s and when the recirculation damper is open, the air flow increased to 240 l/s. During purge mode, the airflow was constant at 300 l/s to quickly cool down the fabric and boost the charging process.
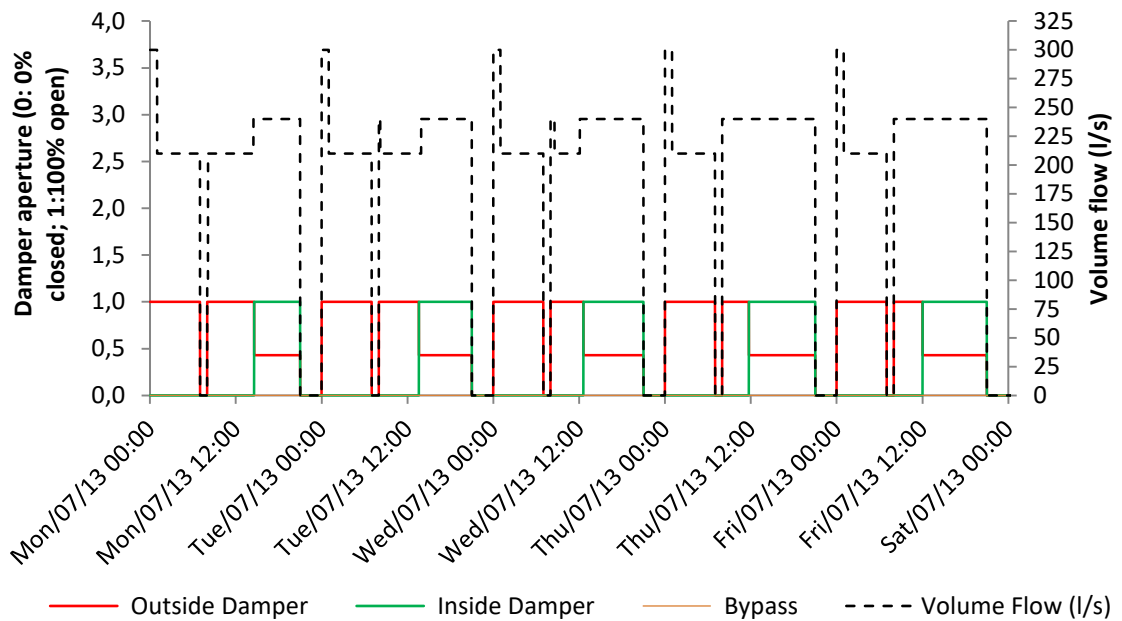
Figure 4.7 – **Damper operation and volume flow during the week**

Table 4.6 shows minimum, average and maximum room temperature values, temperatures before and after the thermal battery (Cool-Phase® T5 and T7), outside air temperature, humidity and CO_2 concentration during the occupied hours of a 2013 summer period (15/jul – 21/jul). It can be seen that the average temperature was 4 ºC above the set-point during occupied hours, which shows that the system is not performing well during this week. This can be seen by the temperature provided by the MVS. The average difference between T5 and T7 is lower than 1 ºC. Conversely, temperatures above the set point show equipment inefficiency but did not mean that the room is suffering overheating. The overheating analysis will be discussed in Chapter 5. However, it indicates that a possible improvement in the controls is needed.

Table 4.6 – Minimum, average, maximum and standard deviation of the average from Room temperature, Cool-Phase® T5 and T7, outside air temperature, humidity and CO_2 concentration during the occupied hours of a 2013 summer period (15/jul – 21/jul).

	Minimum	Average	Maximum	Standard deviation (σ)
Room Temperature (ºC)	25.1	26.2	27.6	± 0.67
Room CO_2 concentration (ppm)	395	410	468	± 7.75
Temperature before LTES – T5 (ºC)	19.8	26.4	30.2	± 2.70
Relative room Humidity	21	32	43	± 3
Temperature after LTES – T7 (ºC)	22.2	26.0	30.1	± 2.33
Outside air temperature	16.3	23.8	28.0	± 3.08

4.3 Spring and autumn period (March–April and October–November)

During spring and autumn, Cool-phase® operation mode and set-points are the same and due to that a week with more fluctuations in temperature and CO_2 during this period was chosen (16/11/2013 – 22/11/2013).

Figure 4.8 shows the room CO_2 concentration (ppm), room temperature and outside ambient air temperature (downloaded from Weather Underground ('Weather Underground', n.d.)). During this season, there is no need to charge the PCM which means that the drop in room temperature was probably caused by outside air infiltration and heat transfer from surroundings. To avoid more infiltration, the outside damper was closed during the night but open during almost the whole cooling period.
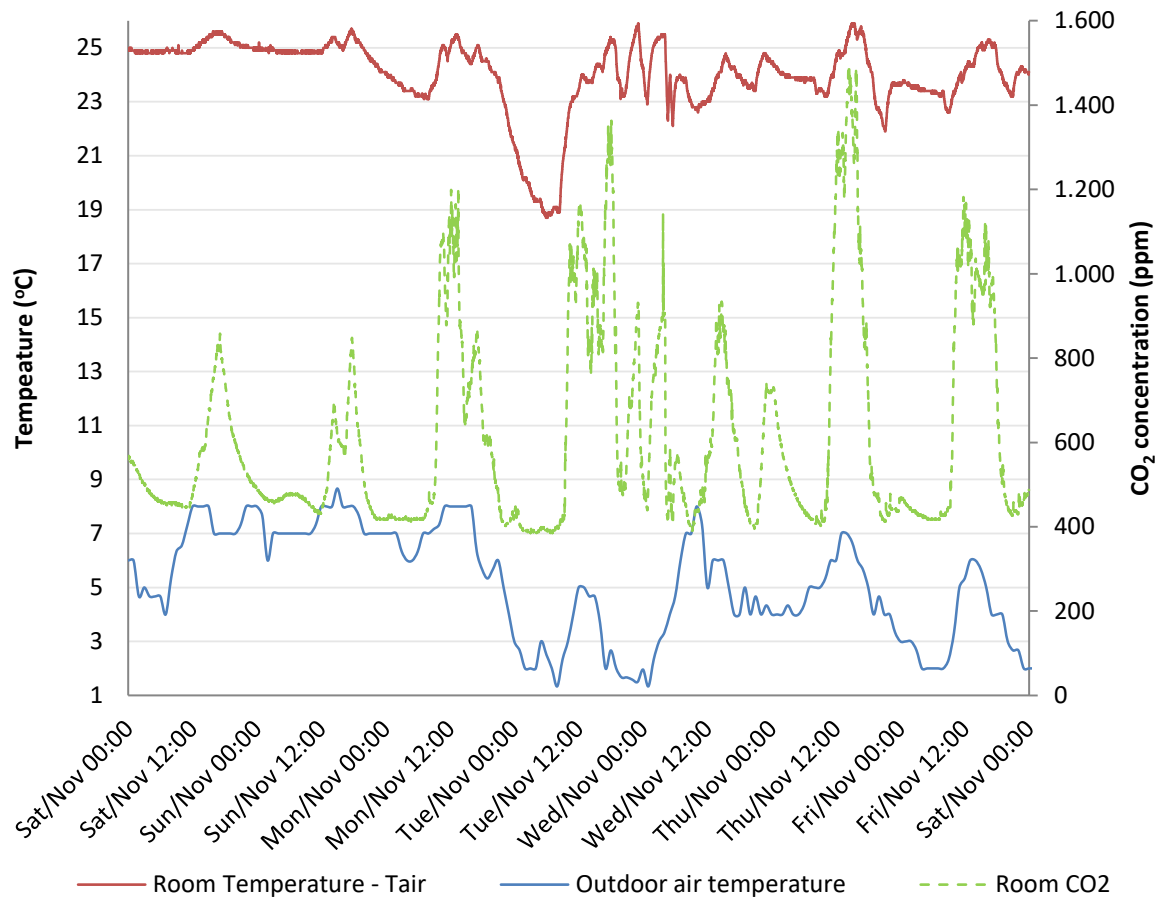
Figure 4.8 – Room temperature, CO_2 and outside ambient air temperature of a 2013 autumn week (16/11 – 22/11/2013).

Figure 4.9 shows the inside damper opening and closing to keep the room close to the set-point temperature for this season (23 °C). From Figure 4.8 it is possible to see the CO_2 varying during the day due to the presence of occupants. This is confirmed by Figure 4.9 where the fan varied the airflow to keep CO_2 within the set-point. This

figure also shows the volume flow reaching the maximum of 300 l/s due to a quick CO_2 increase on days 19/Nov/2013 and 21/Nov/2013 (Tuesday and Thursday respectively). These levels were rapidly reduced by the MVS as can be seen in Figure 4.8.
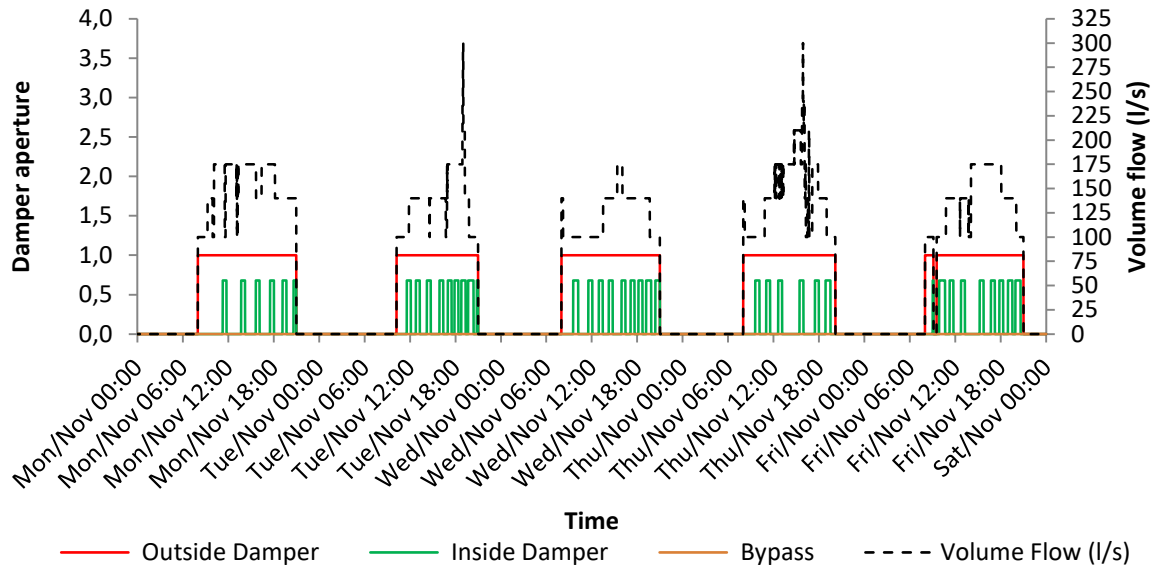
Figure 4.9 - **Damper operation and volume flow during the week (16/11 – 22/11/2013).**

Figure 4.10 shows relative humidity as well as the temperatures before and after the LTES and room temperature during a week. The temperature before the LTES (T5) varied in a wide range several times during the day because the damper was opening and closing to control room temperature and CO_2. This can be seen more closely in Figure 4.11, where one day (19/11/2013) is presented. The levels of CO_2 clearly show some activity in the room. It can also be seen that the thermal batteries reduced the fluctuations from T5 and provide a more stable cooling temperature for the occupants.
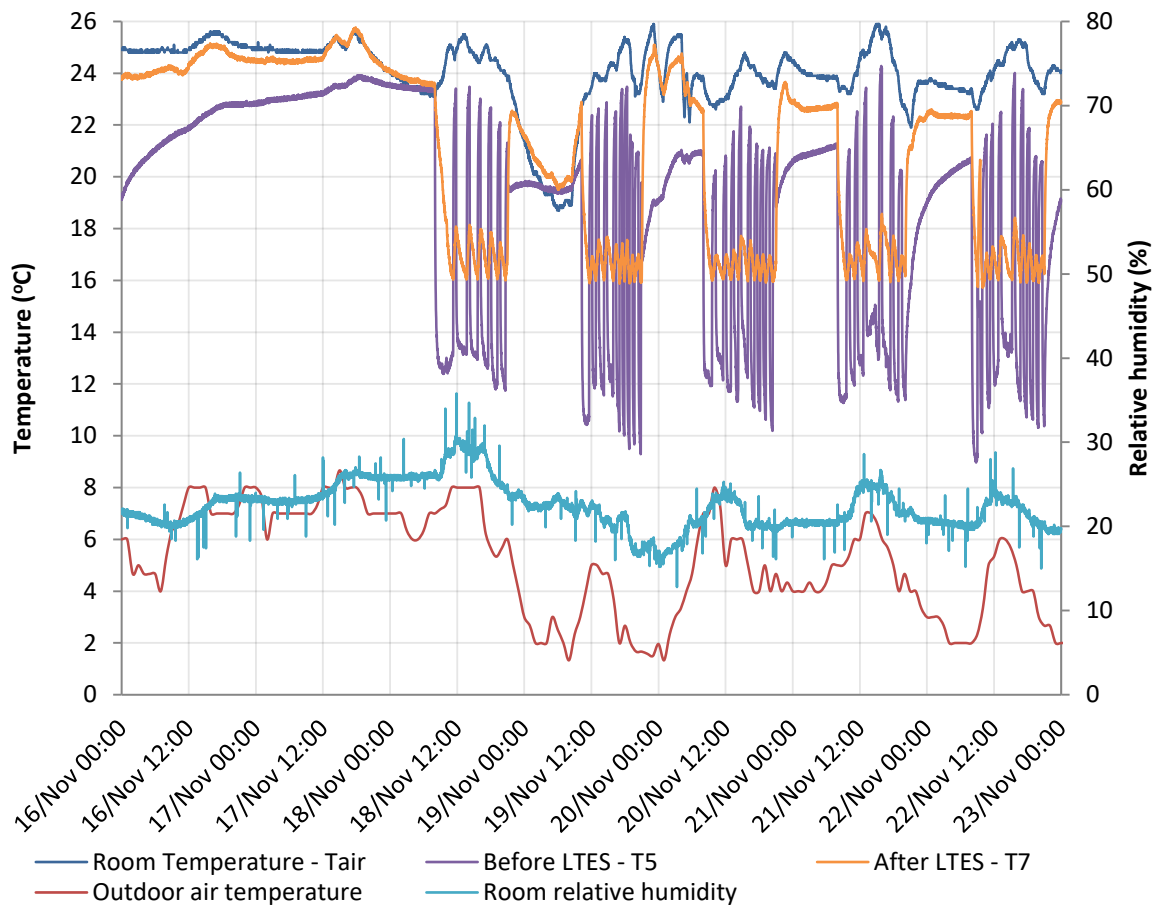
Figure 4.10 – Relative humidity and room temperature, T5 and T7 average of a 2013 autumn week (16/11 – 22/11/2013).
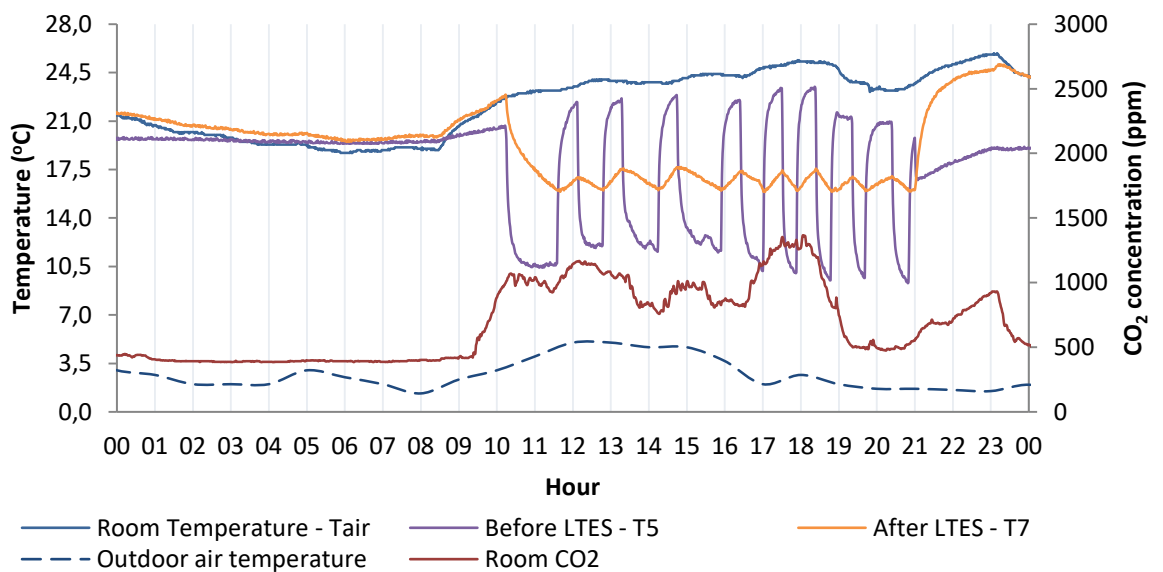
Figure 4.11 – Humidity and room temperature, T5 and T7 of one autumn

Table 4.7 shows minimum, average and maximum room temperature values, temperatures before and after the thermal battery (T5 and T7), outside air temperature, humidity and CO_2 concentration during the occupied hours of a 2013 autumn period (16/nov – 22/nov). It can be seen that the average temperature was 1 °C above the set-point during occupied hours. The system provided an average of 17.2 °C and the CO_2 average was below the set-point. The maximum outside temperature of 8 °C also confirmed that is not necessary to charge the PCM.

Table 4.7 – Minimum, average and maximum values from Room temperature, Cool-Phase® T5 and T7, outside air temperature, humidity and CO_2 concentration during the occupied hours of a 2013 autumn period (18/nov – 22/nov).

	Minimum	Average	Maximum	Standard deviation (σ)
Room Temperature (°C)	18.9	24.0	25.9	± 1.0
Room CO_2 concentration (ppm)	390	774	1495	± 290
Temperature before LTES – T5 (°C)	9.0	15.6	24.3	± 4.1
Relative room Humidity	15	23	36	± 3
Temperature after LTES – T7 (°C)	15.7	17.2	23.6	± 1.3
Outside air temperature	1.3	5.2	8.0	± 1.7

As a conclusion, the period analysed in autumn presented room temperatures and CO_2 concentration above the equipment set point. This can show inefficiency in the system but did not mean that the room is considered overheated or with CO_2 above the regulations. To evaluate that, sensors were installed in the room and monitored over a year and analysed. The next chapter (chapter 5) is dedicated to this analysis.

4.4 Winter season (December – February)

Figure 4.12 presents room temperature, outside air temperature and CO_2 concentration (ppm) from 22/02/2014 to 28/02/2014. The room temperature had an average of 24.1 °C during occupied hours (Monday to Friday from 08:00 to 21:00) and was very close to the setpoint temperature for this season (24 °C). For the same reason of the autumn/spring season, there is no need to charge the PCM and due to that, the fan was off during the charging period (00:00 to 07:00). Outside and inside dampers were responsible to control temperature and CO_2 concentration inside the room.
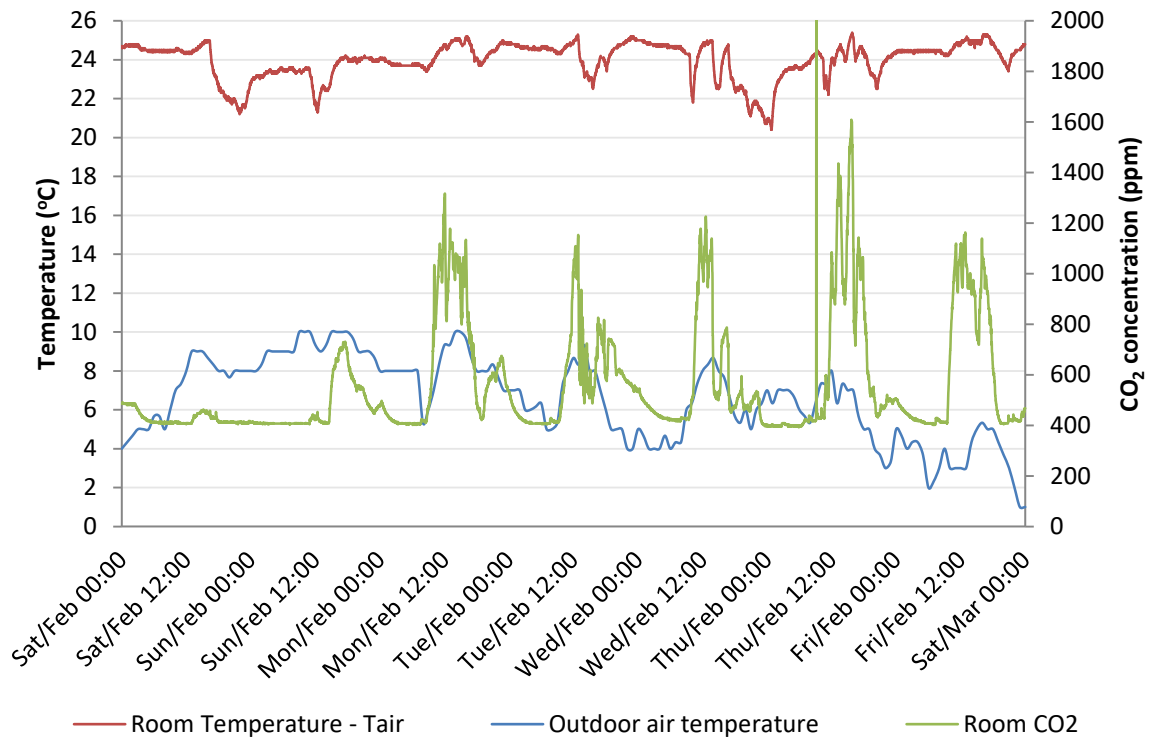
Figure 4.12 – Room temperature, CO₂ and outside ambient air temperature a winter week (22/02/2014 to 28/02/2014).

Figure 4.13 shows the temperature before and after the LTES, room humidity and room temperature in the seminar room. On Saturday and Sunday, when the system is not working and no one is occupying the room, the temperature varies from 21.5 to 24.5 °C approximately.
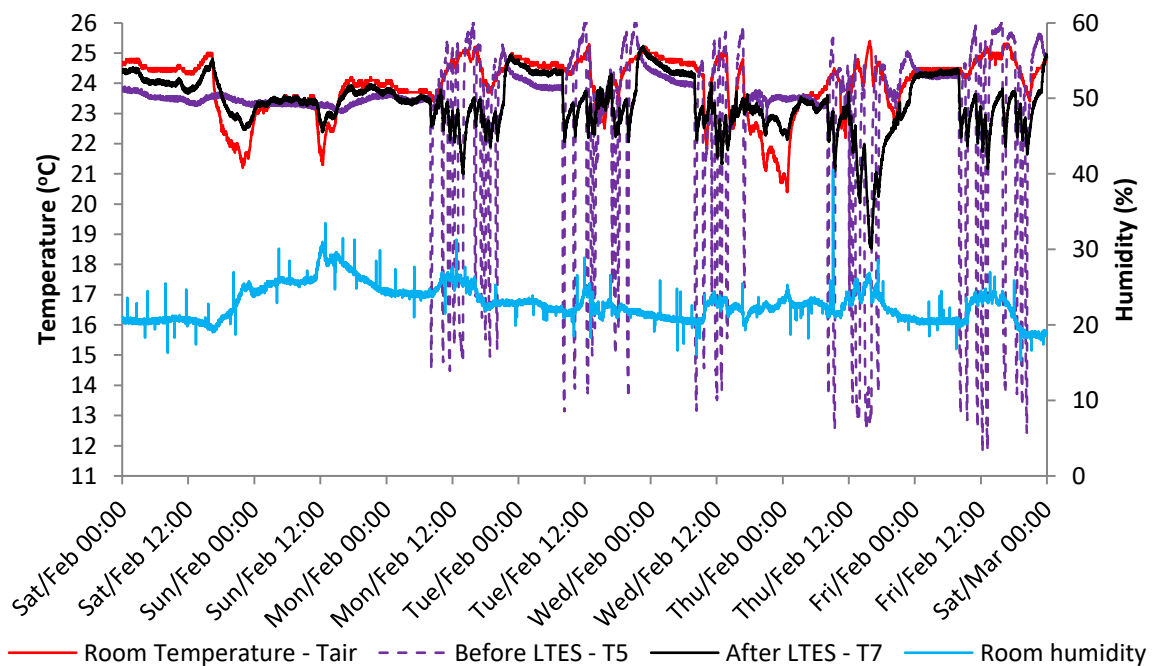
Figure 4.13 – Room temperature, CO₂ and outside ambient air temperature of a 2014 winter week (22- 28/02/2014).

Similar to the autumn, volume flow and dampers varied considerably during the day to keep temperature and CO_2 concentration close to the setpoint. This can be seen in Figure 4.14 and more closely in Figure 4.15 where one day (28/02/2014) was selected. The temperature quickly dropped before thermal batteries (T5) and because they were not charged, the PCM absorbed this high fluctuation and delivered a more stable air temperature into the room.
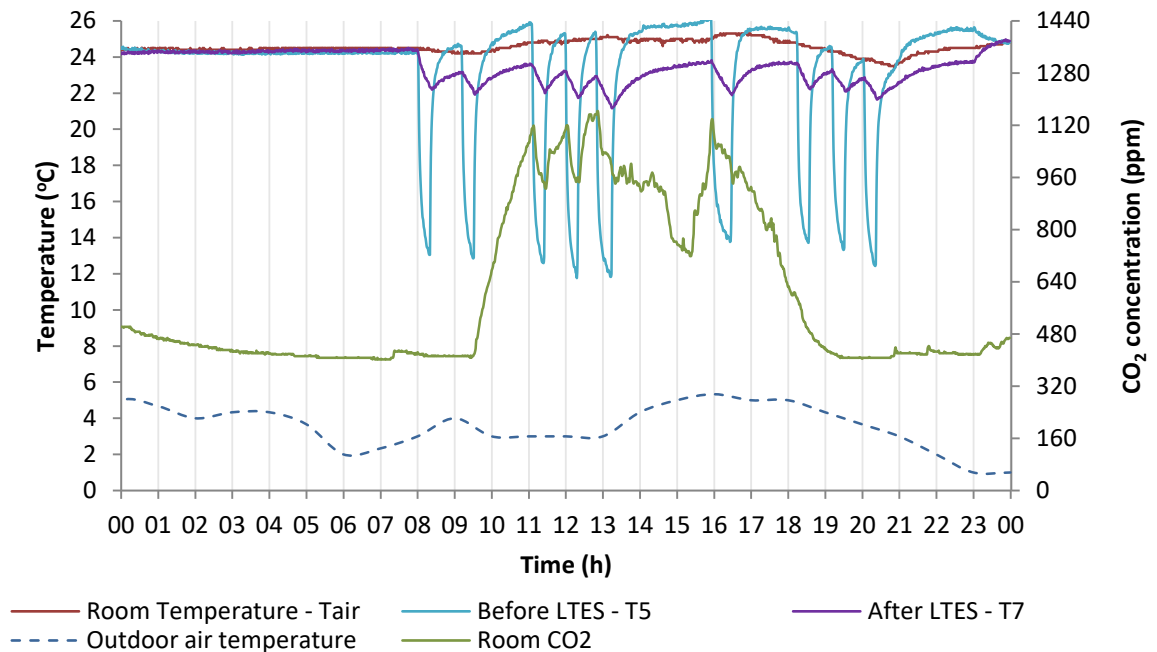
Figure 4.14 – Room temperature, outside temperature, CO_2 and temperature before and after the batteries 28/02/2014.

Figure 4.14 also shows that even with a lower outside air temperature, the system was capable to provide fresh air to control CO_2 and kept the temperature of the room stable (23.4 to 25.3 °C). These fluctuations on T5 and T7 are due to opening and closing of the dampers as it can be seen Figure 4.15 and in Figure 4.16 with more details. Figure 4.15 shows the damper operation from Monday to Wednesday (24-28/02/2014)) while Figure 4.16 presents a particular day (Friday, 28/02/2014). Different from autumn where outside damper was open 100 % and the inside damper changed between open and close during the operational time: the winter period close outside damper and open inside damper or open the outside damper and close the inside. This is to avoid cold drafts. From the same Figure 4.15, it can also be seen that during the night, the fan was off.
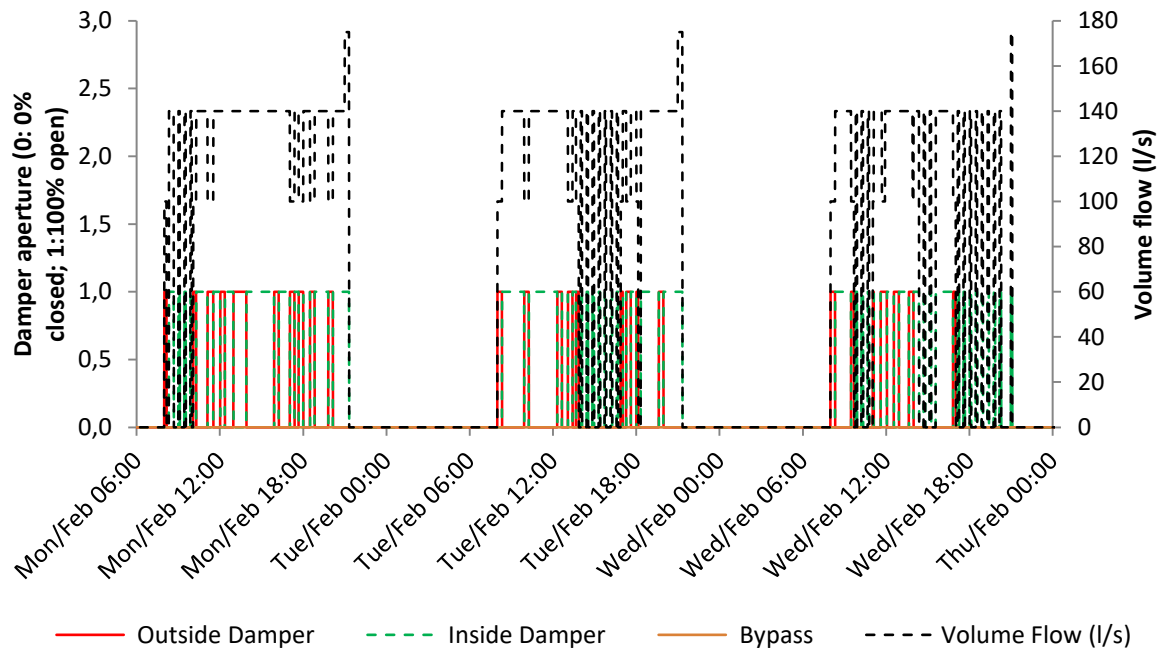
Figure 4.15 – Dampers and volume flow operation from 24 to 26/02/2014
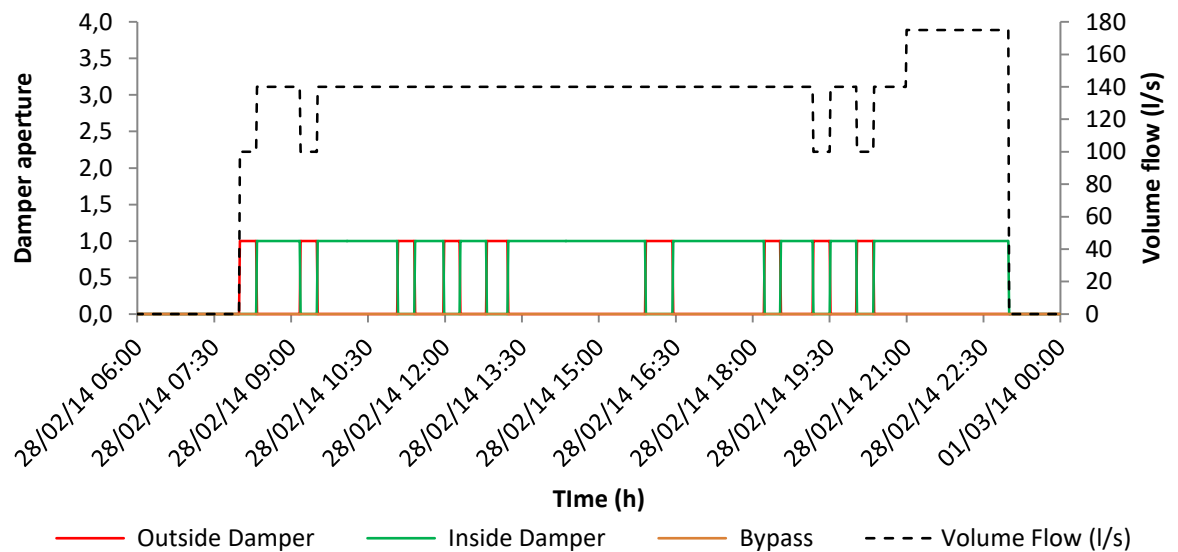
Figure 4.16 – Dampers and volume flow operation on 28/02/2014

Table 4.8 summarises the winter period by presenting minimum, average and maximum values from the room temperature, the Cool-Phase® T5 and T7, outside air temperature, humidity and CO_2 concentration. The maximum temperature of 10 ºC during this period confirmed that charging the thermal battery was not necessary.

The relative humidity achieved low limits during this period and the average of 23 % is not acceptable according to BB 101 (Regulations Standards Design Guidance, 2006). This occurred during all periods analysed and shows that the MVS is not

capable to provide humid air to the occupants. As a solution, a humidifier might be necessary during cold periods in winter.

Table 4.8 – Minimum, average and maximum values from the room temperature, Cool-Phase® T5 and T7, outside air temperature, humidity and CO_2 concentration during the occupied hours of a 2014 winter period (22/feb – 28/feb).

	Minimum	Average	Maximum	Standard deviation (σ)
Room Temperature (ºC)	21.1	24.1	25.4	± 0.81
Room CO_2 concentration (ppm)	404	722	2019	± 264
Temperature before LTES – T5 (ºC)	11.8	22.0	26.2	± 3.8
Relative room Humidity (%)	15	22	40	± 2
Temperature after LTES – T7 (ºC)	18.5	22.7	24.4	± 0.81
Outside air temperature	3.0	6.4	10.0	± 1.9

4.5 Chapter's summary

This chapter described the MVS operation and used system data to explain how the system works over the year. It started by describing the system control, set points and operational modes; key features to control temperature and CO_2 concentrations. After that, data logged by the system was used to explain how the MVS works according to the season (summer, spring/autumn, winter). A week from each period was used and one day was explained in more details.

It was found that the MVS performs well during the analysed period. However, a study analysing the thermal comfort according to the adaptive thermal comfort criteria will judge if the system is performing according to current regulations. This will be detailed in chapter 5 where results from a field monitoring over one year was used.

CHAPTER 5 - CONDITIONED SPACE FIELD MONITORING AND ANALYSIS

Introduction to the chapter

This chapter presents the results of field monitoring of an operational Cool-Phase® system installed in a seminar room located at the University of West England (Bristol/UK). The chapter starts by presenting the results of field monitoring over one year (19/08/2015 - 18/08/2016) described in chapter 3. The monitored data was then divided into Cooling and Heating season and analysed in terms of thermal comfort and overheating according to the adaptive thermal comfort approach. Indoor air quality was assessed by system data and two CO_2 sensors were installed for two days and compared with Cool-phase® data. After that, a CFD simulation analysed the MVS performance over the seasons. Moreover, the monitored data was used to calibrate the model in IESVE, the heat gains were extracted analysed in a CFD simulation. It is followed by a CFD simulation for summer, autumn and winter and a calibrated day with heat gains extracted from a DTM model. The chapter concludes by presenting energy consumption and the equipment performance.

5.1 Analysis of field measurements within the conditioned space

Table 5.1 presents seminar room monthly daily mean minimum, average and maximum temperature and relative humidity of sensors H1, H2, H3 and H4 (sensors at 0.70m from the floor) from occupational hours (8:00 to 21:00) as well as the standard deviation. It can be seen that the temperatures slightly vary during the measured period and the room presents a uniform temperature with a maximum mean standard deviation of ± 1.5 K for January. Furthermore, the annual average of 22.1 °C (± 1.3 K) shows that the MVS is capable to maintain the room within a stable condition during occupied hours.

Figure 5.1 shows the temperature distribution over the year during occupied hours as well as the MVS set point. With the exception of the winter period, where the set point of 24 °C was barely achieved, the MVS maintained well the temperature along the set point. The University was closed during the first week of January and due to that, an accentuated decrease in temperature is identified.

Table 5.1 – Minimum, mean, maximum and standard deviation of the temperature at 0.70m for sensors H1, H2, H3 and H4 from 8:00 to 21:00 from Aug/2015 – Aug/2016

Month	Mean min Temp at 0.70 m (ºC)	Mean average Temp at 0.70 m (ºC)	Mean max Temp at 0.70 m (ºC)	Mean standard deviation (K)
Aug-15	20.1	21.1	21.8	± 0.4
Sep-15	18.1	21.0	23.2	± 0.9
Oct-15	19.3	22.9	24.9	± 0.9
Nov-15	19.9	22.3	24.4	± 0.9
Dec-15	18.8	21.5	23.9	± 1.1
Jan-16	18.3	21.3	23.8	± 1.5
Feb-16	18.3	22.6	24.1	± 1.1
Mar-16	17.7	22.5	25.2	± 1.1
Apr-16	18.0	23.1	25.7	± 1.2
May-16	18.7	21.6	24.5	± 1.3
Jun-16	20.1	21.5	23.5	± 0.7
Jul-16	20.4	22.2	25.3	± 1.0
Aug-16	21.2	23.1	25.4	± 1.2
Average	**17.7**	**22.1**	**25.7**	**± 1.3**
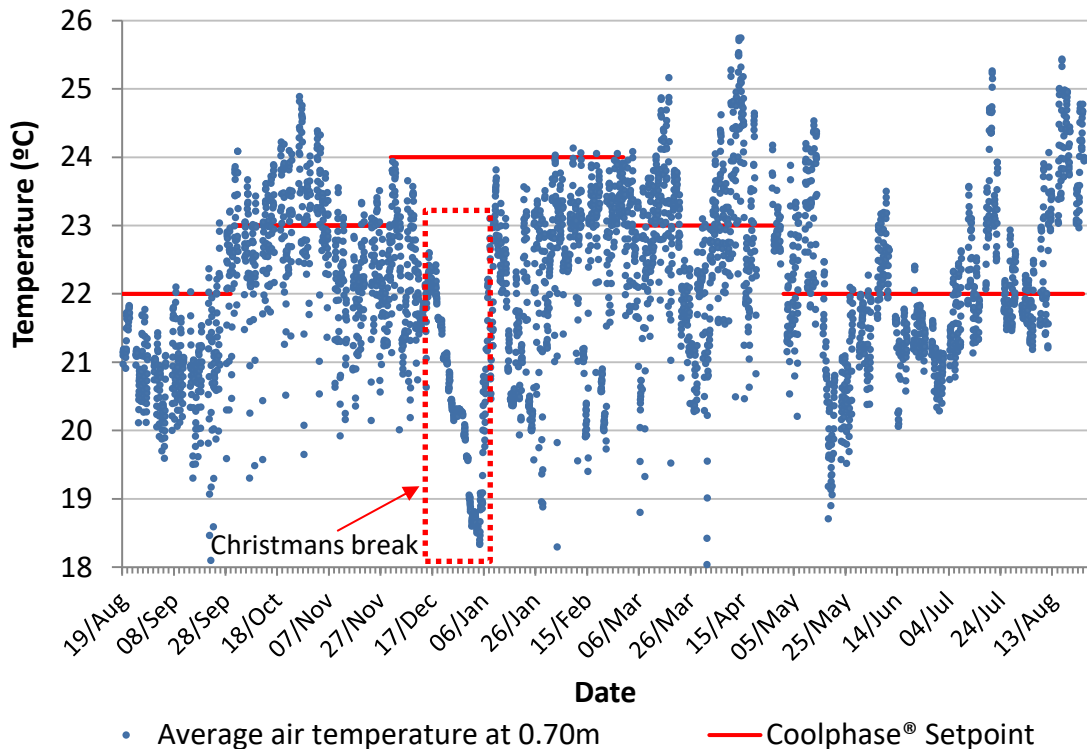
Figure 5.1 – Daily mean temperature and relative humidity from 8 AM to 8:59 PM from 19/08/2015 to 25/11/2015

A closer analysis was done in Figure 5.2 where five days in August (07-12/09/2015) were chosen. Temperature from sensors H1, H2, H3, H4, H8 are plotted as well as the

thermal comfort temperature and its lower limit according to adaptive thermal comfort criteria (CIBSE, 2013). It can be seen a uniform temperature at 0.70m (sensors H1, H2, H3, H4) and the difference between them are inside the logger accuracy range (±0.21 °C) with an exception of H1, probably caused by its location (close to the window). Sensor i1 (located at the supply diffuser) has a similar behaviour compared to the system sensor presented in the previous chapter.
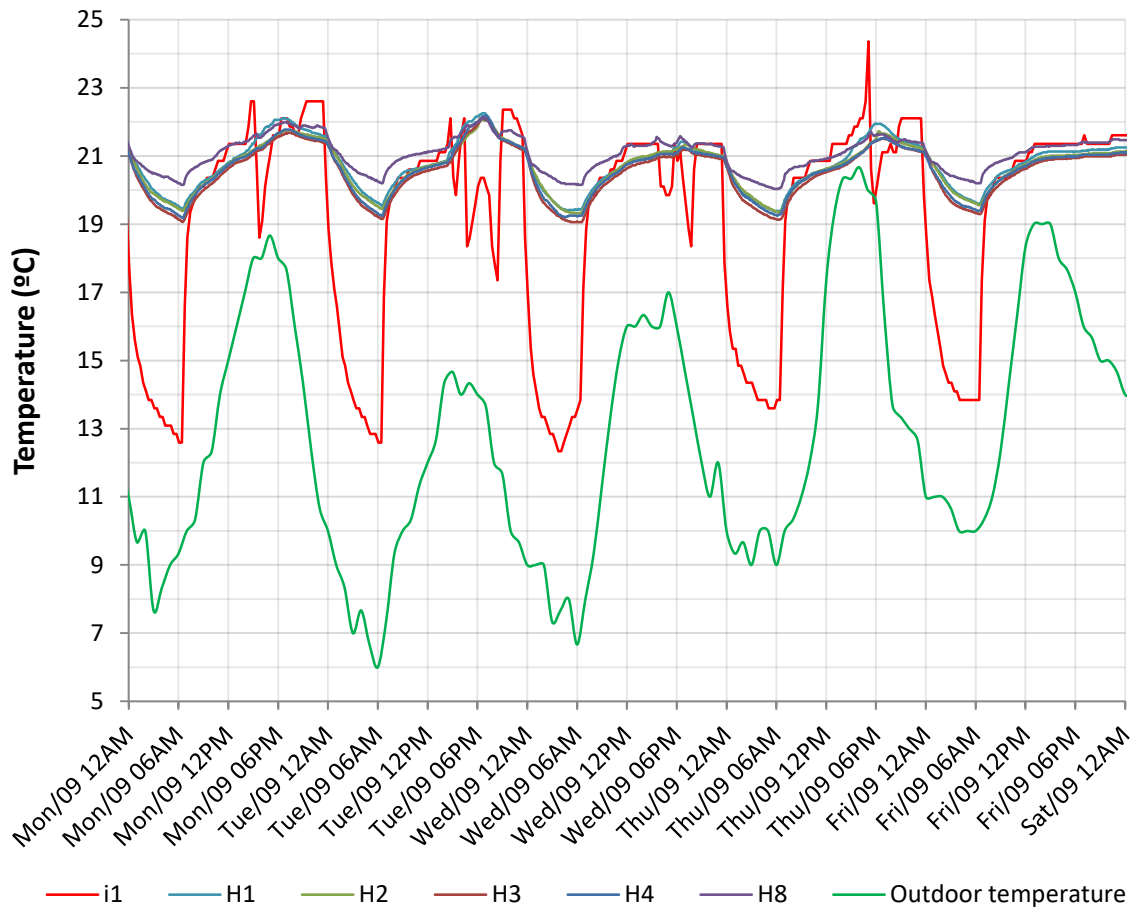
Figure 5.2 – Monitored sensors at 0.70m, exhaust, diffuser and thermal comfort and lower thermal comfort limit from 07/09/2015 to 12/09/2015

When all sensors in the room are grouped together (H1 – H7) and compared with the sensor located at the exhaust grille and at the seating level (Figure 5.3), a small difference is noticed between 0.70m and all sensor averaged. The air is exhausted from the MVS exhaust grille and due to that, it is noticeable the difference between all sensor average and exhaust temperature (H8). During weekends where the seminar room is non-occupied, Figure 5.3 also shows a smaller stratification when compared to weekdays.
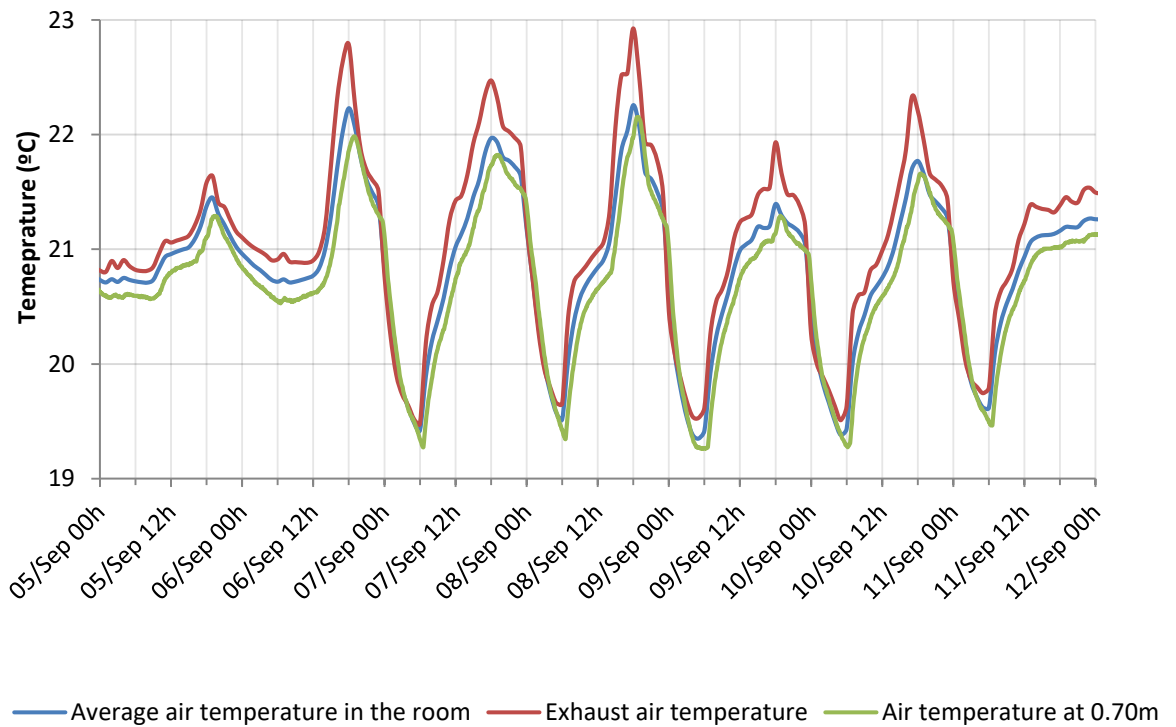
Figure 5.3 – Exhaust temperature, average of all sensors and temperature average at 0.70m from 05/09/2015 to 12/09/2015

5.2 Thermal comfort analysis

5.2.1 **Cooling season**

Adaptive thermal comfort approach was used for evaluation during the cooling season (Ds/En, 2007) as these are current guidelines for school buildings in the UK (Education Funding Agency, 2014b) and followed for non-AC office buildings (CIBSE, 2013). The upper and lower limits of adaptive thermal comfort are based on category II ($T_{min} = T_{comf} - 3$ and $T_{max} = T_{comf} + 3$) with T$_{min}$ and T$_{max}$ calculated by: $T_{comf} = 0.33T_{rm} + 18.8$ where T_{rm} is the running mean external temperature. This was explained in the literature review in more details (section 2.2).

Figure 5.4 and Figure 5.5 shows the results during weekdays (8:00 to 21:00) for the seminar room for two cooling periods (May until September); temperature and relative humidity were averaged by all sensors at 0.7m. Relative humidity is within a good range between 30 (apart from 3 hrs on one day in May) and 70 % (apart from one day in August), the temperature did not exceed the upper thermal limit. In general, the seminar room has low solar gains because of the small area of windows and ground floor position. This favour the maintenance of the temperature in comfortable conditions during summer periods with full occupancy; for example during examination times in mid-May and mid-August 2016. However, some overcooling occurs for some hours (116 hours (3 %)) indicating that night purging

might need more detailed control than relying on a timer. Conversely, this discomfort can be solved simply by enhancing clo (e.g. wearing heavier clothes like a sweater or jacket) [14].
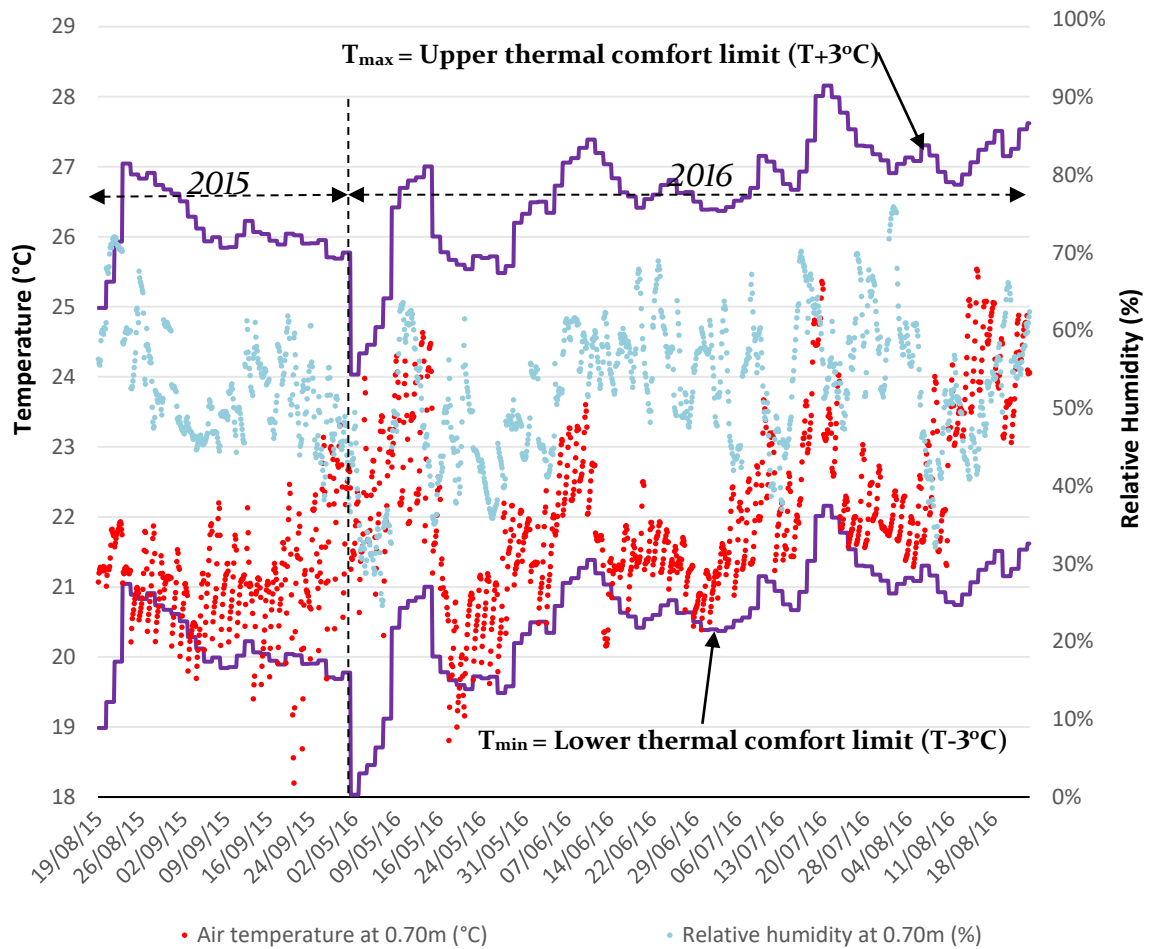
Figure 5.4 – Average temperature and relative humidity at 0.70m for the cooling season and upper and lower thermal comfort limits bands.

Figure 5.5 presents the outdoor running mean temperature versus the indoor temperature over the summer period. It can be seen that temperatures are well distributed but are predominantly below the thermal comfort temperature curve. The majority of the period where temperatures above the thermal comfort occur is when the running mean temperature is below 12.5 °C. This can lead students to increase their clo but again, it can be overcome simply by reducing clo (eg. removing heavier clothes like a sweater or jacket).
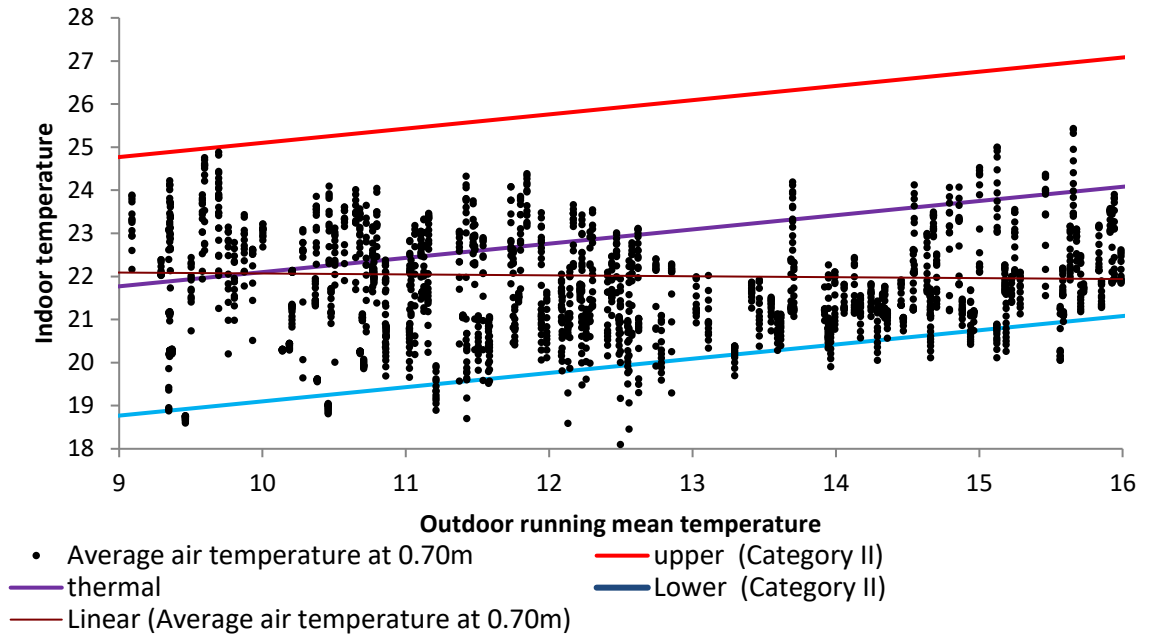
Figure 5.5 – Design values for indoor temperature for buildings without mechanical cooling systems for cooling season. T_{min} and T_{max} are the bands of comfort based on category II ($T \pm 3\,K$)

5.2.2 Heating season

During the heating period (October until April), heating is provided by perimeter radiators but is controlled by Cool-Phase®. Figure 5.6 and Table 5.2 show the PMV and PPD results for this period.

When the outside running mean temperature is below 10 °C, the occupants felt uncomfortable when PMV > 0.5 or PPD <10 and this represent 43 and 142 hours respectively (2.6 and 8.5 %). When outside running mean temperatures are between 10 and 15 °C, occupants felt uncomfortable in 8 and 22 hours when PMV < -0.5 and PPD <10 (or 1.8 and 4.8 %), respectively. This corresponds to a total of occupants dissatisfied of 13.3 % (PPD) and 4.4 % for PMV.

When T_{rm} is below 10 °C, PMV presents an average temperature of 25 °C which occupants might feel uncomfortable due to heavy clothes they are wearing. As a solution, occupants are free to reduce their own clo or increase the airflow by activating the boost mode on Cool-Phase®. When PMV is 15 °C > T_{rm} >10 °C, the lower temperature average (19 °C) shows that students might feel uncomfortable but they are free to adapt themselves by increasing clo.
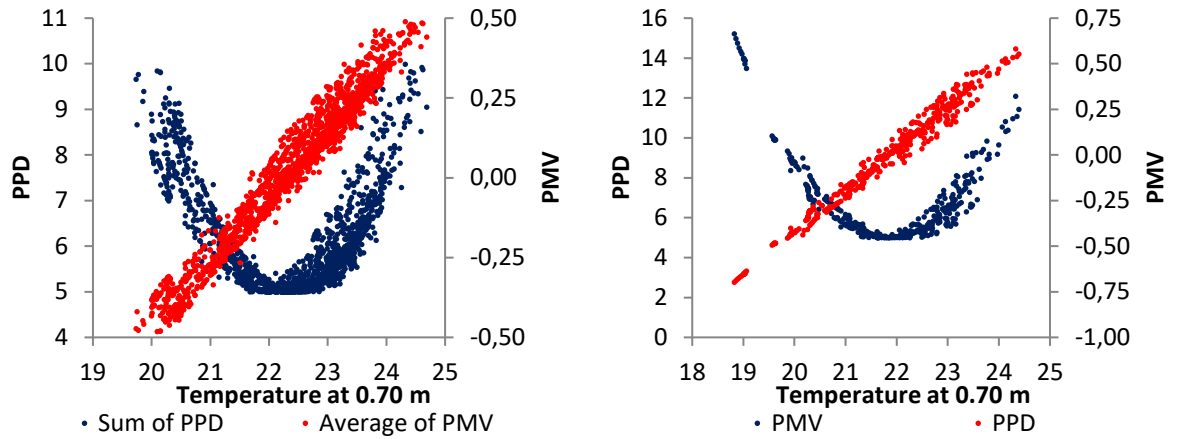
Figure 5.6 – PPD and PMV during heating season for T_{rm} <10 ºC (left) and 15 ºC > T_{rm} >10 ºC (right)

Table 5.2 – Overheating during the heating season

	For Trm <10 ºC		For 15 ºC > Trm >10 ºC	
	PMV > 0.5	PPD > 10	PMV < -0.5	PPD > 10
Hours	43	142	8	22
Percentage of total	2.60 %	8.50 %	1.80 %	4.80 %
Min Temperature	24.42	17.74	18.82	18.82
Avg. Temperature	24.97	20.99	18.96	20.90
Max. Temperature	25.75	25.75	19.06	24.39
Standard deviation (σ)	± 0.36	± 2.86	± 0.07	± 2.52

5.2.3 Relative humidity

System data

Integrated School design TM57 (CIBSE, 2015c) recommends that relative humidity in teaching spaces should be between 30 and 70 %. From Table 5.3, it can be seen that the relative humidity acquired by the system data never goes higher than 70 % inside the classroom. High humidity levels should be avoided because it can impact IAQ by collaborating on mould growth and propagating dust mites and fungal spores (CIBSE, 2015b). When temperatures are not above 26-28 ºC, little effect on feelings of warmth, apart from the wetness of the skin, is noticed. However, system data shows that relative humidity reached critical values during the months of January to April in 2014 and January to March in 2015. During this period, the values higher than 30 % occurs only for a short period of time (Table 5.3). Relative humidity below 30 % could be acceptable but precautions should be taken to limit dust generation and airborne irritants as well as when materials should be correctly specified to prevent

build-up static electricity (Nevins et al., 1966). However, dry air cause discomfort to students by enhancing chances to become ill, inflame the respiratory tract mucous membrane and dry skin and eyes (ASHRAE, 2013a).

Temperatures in the seminar room above the set point during two months of 2014 (November and December). This forced Cool-Phase® to cool the environment by blowing fresh air inside the room and due to this, relative humidity remained above 30 % for a short period of time (respectively 10 and 20.4 %). Charging thermal batteries during winter period could prevent air with low relative humidity being introduced into the room.

Table 5.3 – Daily mean relative humidity for 2014 and 2015 from 8:00 to 21:00 (system data)

		Jan	Feb	Mar	Apr	May	Jun	Jul	Aug	Sep	Oct	Nov	Dec
2014	Mean min Humidity (%)	19	18	19	21	25	29	30	29	30	27	21	20
	Average Humidity (%)	24	23	24	26	30	35	36	34	36	32	26	25
	Mean max Humidity (%)	28	29	29	32	35	41	42	41	42	39	31	30
	Percentile above 30 %	9.2	0.9	0.5	1.3	10.9	60.9	68.1	94.5	97.1	61.7	77.3	67.7
2015	Mean min Humidity (%)	17	14	15	18	19	25	26	33	29	27	28	27
	Average Humidity (%)	22	20	20	23	25	31	33	39	35	33	33	31
	Mean max Humidity (%)	27	24	25	28	32	37	40	46	40	38	40	38
	Percentile above 30 %	4.0	0.6	1.9	22.4	47.0	91.7	97.1	77.1	92.6	72.3	10.0	20.4

Room data

Figure 5.7 shows the hourly average relative humidity levels for occupied period at seating level. Similar to the system data presented in Table 5.3, lower humidity levels occur mainly during the heating season where outside air needs to be supplied for cooling purposes or to reduce CO_2 concentration. During almost one year of measurements, the room data presented a relative humidity below 30 % for 653 hours, corresponding to 16.52 % of the time with an average of 28.06 %. Above 70 % of RH, it happens only 35 hours (or 0.89 %). This becomes clear in Figure 5.8 where the frequency of the relative humidity of the room data at 0.70m is presented. The PCM-Air heat exchanger tends to maintain RH between 40 and 55 % of the time, corresponding to nearly 45 % of frequency for all monitored period.
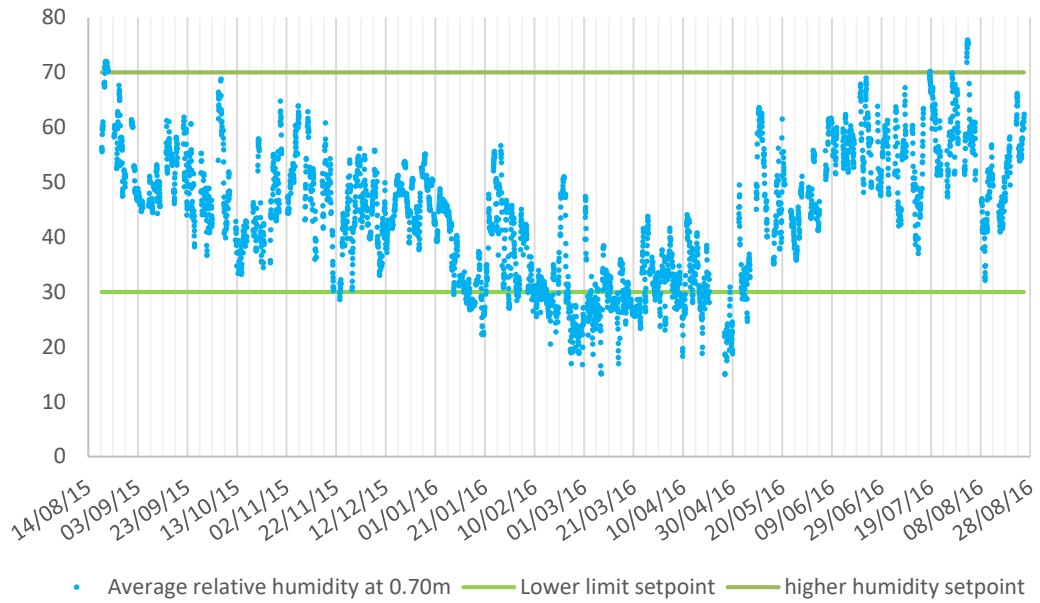
Figure 5.7 – Hourly average relative humidity at 0.70m for the heating season and the lower
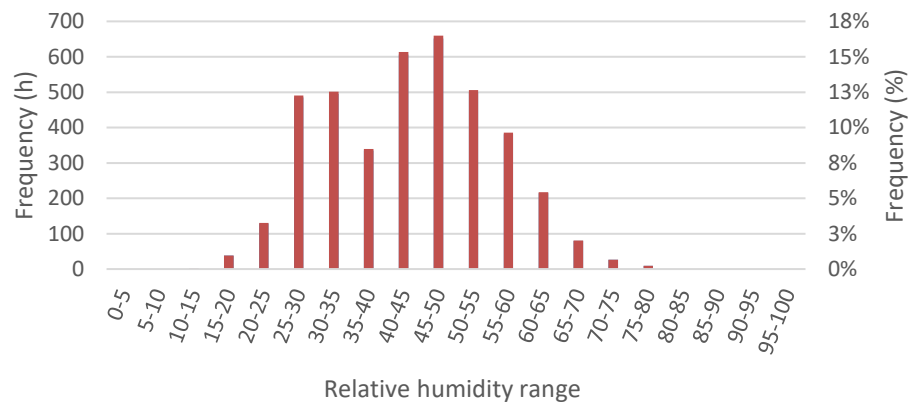
Figure 5.8 – RH frequency from room data for the occupied hours

When RH is analysed monthly, Table 5.4 shows that RH was above 70 % for a short period of time. Reaching the maximum of 17 % during August 2015. Conversely, from January until April, RH remained below 30 % in the class for about 43 % of the time on average. A humidifier can be included in the MVS in order to provide an environment with a higher RH.

Table 5.4 – Minimum, mean, maximum and standard deviation (σ) of the mean average relative humidity at 0.70m from 8:00 to 21:00 from Aug/2015 – Aug/2016

Month	Mean min RH at 0.70 m (%)	Mean average RH at 0.70 m (%)	Mean max RH at 0.70 m (%)	Mean σ (%)	Percentile above 70%	Percentile below 30%
Aug-15	47	60	72	± 6.8	17 %	0 %
Sep-15	37	50	62	± 4.8	0 %	0 %
Oct-15	33	46	69	± 8.6	0 %	0 %
Nov-15	29	47	64	± 7.9	0 %	1 %
Dec-15	33	46	56	± 4.9	0 %	0 %
Jan-16	22	38	57	± 8.1	0 %	20 %
Feb-16	17	31	51	± 7.5	0 %	50 %
Mar-16	15	30	47	± 5.1	0 %	59 %
Apr-16	15	31	44	± 6.0	0 %	46 %
May-16	25	44	64	± 8.7	0 %	4 %
Jun-16	41	56	69	± 5.7	0 %	0 %
Jul-16	37	55	70	± 8.0	1 %	0 %
Aug-16	32	53	76	± 8.9	5 %	0 %
Average	**15**	**43**	**76**	**± 11.8**	-	-

5.3 Indoor air quality (CO_2 analysis)

Table 5.5 presents CO_2 concentration monitored by the system during the occupied hours of 2014 and 2015 in the seminar room. Average CO_2 is below the limit of 1000 ppm for any month and 1500 ppm is exceeded by more than 20 minutes (Education Funding Agency, 2013) only once (29 minutes in 2014) which shows a good performance in terms of IAQ.

Table 5.5 – CO_2 concentration (ppm) by system data in the seminar room from 8:00 to 21:00.

Month	2014			2015			> 1500 ppm for more than 20 min
	Avg. CO_2	Max. CO_2	Standard deviation	Avg. CO_2	Max. CO_2	Standard deviation	
Jan	601	1963	± 212	563	1312	± 181	0
Feb	719	2019	± 253	671	1358	± 203	1
Mar	695	2019	± 229	645	1204	± 181	0
Apr	559	2019	± 182	549	1236	± 124	0
May	469	885	± 87	443	978	± 57	0
Jun	412	607	± 25	420	531	± 23	0
Jul	409	663	± 22	420	575	± 25	0
Aug	423	580	± 30	418	826	± 24	0
Sep	493	1199	± 141	541	1326	± 212	0
Oct	599	1229	± 184	689	1268	± 242	0
Nov	701	1317	± 217	752	1480	± 242	0
Dec	551	1463	± 221	586	1551	± 274	0
Avg.	553	-	± 202	558	-	± 206	-

Additional CO_2 monitoring was carried out in the seminar room space. Figure 5.9 shows the CO_2 distribution during two days (25-26/11/2015). It can be seen that the values were always below 1500, apart from one minute on 25/11/2015 where CO_2 concentration reaches 1923 ppm. Because this value cannot be observed on the second sensor, it is possible that one occupant blew directly on the sensor or an unexpected error occurred.

In addition, Figure 5.9 shows that the CO_2 system sensor has a similar trend when compared to the room data but a response delay was noticed. This will delay Cool-Phase® reaction and will provide unnecessary air flow. A faster response CO_2 sensor on the system or a better location of it might improve equipment performance.
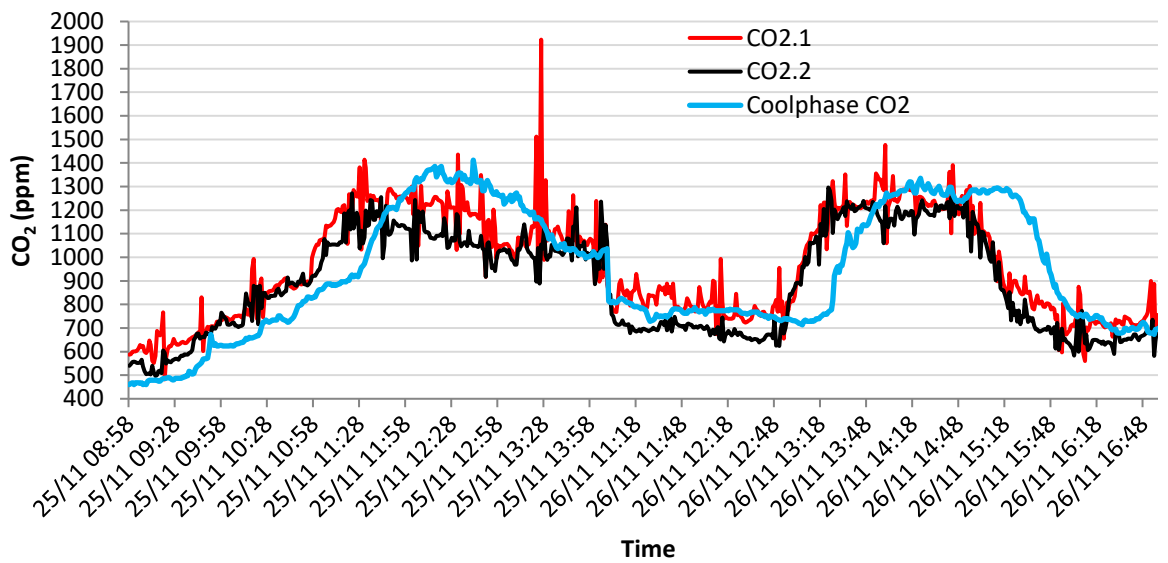
Figure 5.9 – CO_2 measurements taken in 25 and 26 of November at UWE.

When the daily average is taken, they present average concentration inside the accuracy range (Table 5.6) which means that Cool-phase® is performing well and the CO_2 sensor is well located.

Table 5.6 – CO_2 system data and room data from 25 and 26 of November of 2015.

	CO_2 - 1	CO_2 - 2	Cool-phase® CO_2
Average 25/11/2015	963	935	952
Average 26/11/2015	895	895	913

Figure 5.10 shows CO_2 concentration frequency by minute from 8:00 to 21:00 of 2014 and 2015; levels are below 1000 ppm for approximately 95 % of the period showing that CO_2 concentration are well controlled by Cool-Phase®.
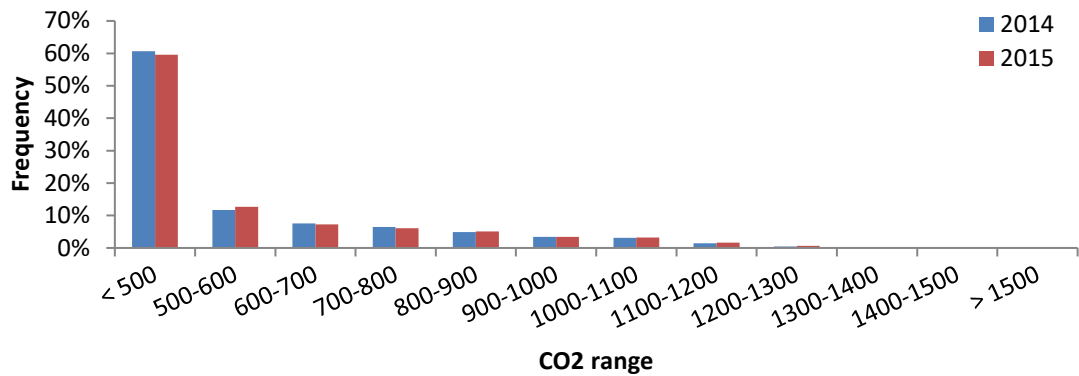
Figure 5.10 – CO2 Frequency for the occupied hours in 2014 and 2015.

5.4 CFD study of the conditioned space

As discussed in the previous sections (4.2 to 4.4), Cool-Phase® has three main operational systems that work according to the season (summer, autumn/spring, and winter). To understand if the system distributes air temperature and air flow uniformly within the conditioned space for each season, the seminar room was modelled following the procedure described in section 3.4.

A particular day and time was selected and presented in Table 5.7. For the selected cases, the outside damper was open for the summer and autumn and closed for the winter. In all three cases, the air was crossing the thermal batteries and weather conditions were taken from Wunderground ('Weather Underground', n.d.).

The seminar room was considered fully occupied (26 students and 26 computers turned on). The purpose is to model airflow and air temperature distribution within the room over the seasons instead of representing the MVS in real operation. A further study will use calibrated data to analyse the MVS performance.

Table 5.7 – CFD cases implemented on ANSYS Fluent.

	Case 1 (summer)	Case 2 (Autumn)	Case 3 (Winter)
Day and Time	16/07/2013 12:00	19/11/2013 15:00	28/02/2014 14:00
Outdoor wind velocity (m/s)	1.5	4.1	6.7
Outdoor temperature (ºC)	23	5	5
Outdoor relative humidity	60 %	72 %	24 %
Air density considered in the room (23 ºC)	1.176	1.176	1.176
Air thermal expansion coefficient (23 ºC)	0.003386	0.003386	0.003386
CO_2 (ppm)	421	1004	931
Mass flow rate (l/s)	210	140	140
MVS supplied air temperature (ºC)	23.47	17.46	22.83
Internal walls heat flux (W)	0	0	0
Ceiling heat flux (W)	0	0	0
Floor heat flux (W)	0	0	0
Tables heat flux (W)	0	0	0
Lamp temperature (ºC) (Lei et al., 2014)	40	40	40
Window and wall heat transfer coefficient (W/mK)	11.4892	21.6604	41.0666
Wall free stream temperature (ºC)	23	4.6667	5
Students (skin temperature) (ºC)	33.7	33.7	33.7
Number of students	26	26	26
Number of PC's (in use)	26 (26)	26 (26)	26 (26)
PC temperature (ºC) (Lei et al., 2014)	40	40	40

5.4.1 Temperature distribution

Aimed to understand the temperature and airflow distribution in the seminar room, six planes were generated along axis x and y to show temperature stratification and air velocity. A plane normal to the z-axis represents the height from the floor to the head of a seated person (1.2 m). Figure 5.11 shows where each plane is located and Table 5.8 shows the point and normal plane direction.
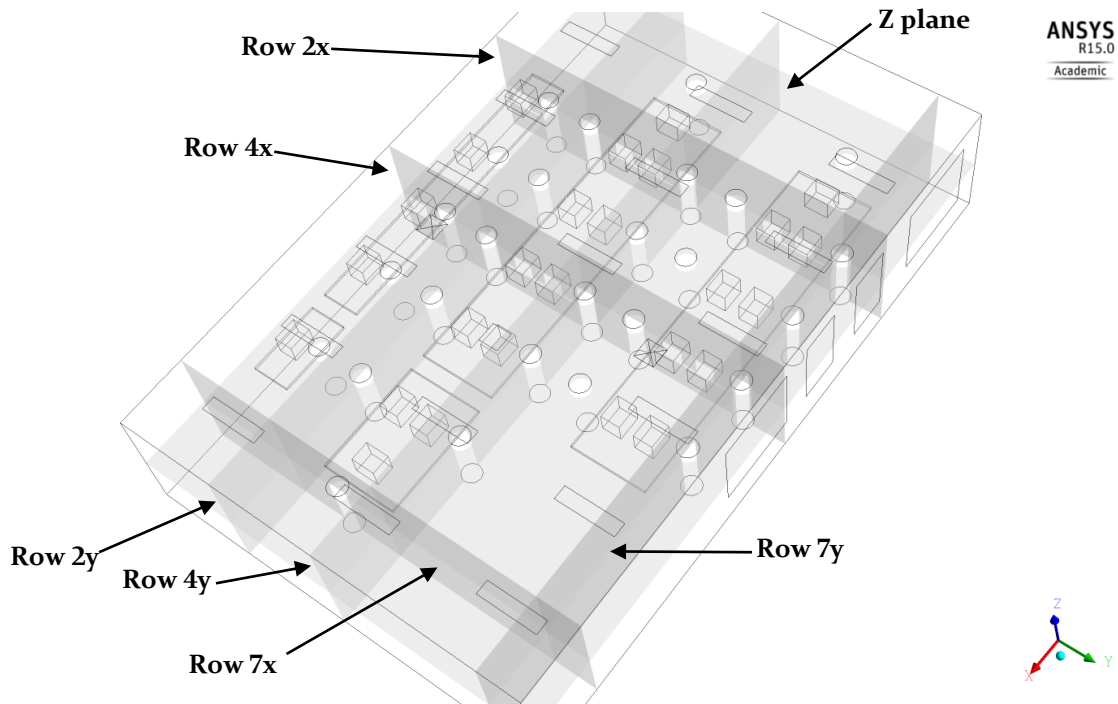
Figure 5.11 – Seminar Room model with section planes.

Table 5.8 – Location of each plane

Plane	Point	Direction normal to the plane
Row 2x	x=3.14m	[1,0,0]
Row 4x	x= 6.33m	[1,0,0]
Row 7x	x= 11.9m	[1,0,0]
Row 2y	y= 2.08m	[0,1,0]
Row 4y	y= 4.4m	[0,1,0]
Row 7y	y=7.8m	[0,1,0]

Figure 5.12 presents the temperature distribution at 1.2 meters above the floor for the three studied cases. At this height, summer, autumn and winter have an average temperature of 28.5, 26.7 and 28.8°C respectively. Volume flow and cooling temperature provided by Cool-Phase® were 210, 140 and 140 l/s and 23.5, 17.5 and 22.8°C for summer, autumn and winter respectively. For the summer period, the simulation is in agreement with BB101 which recommends that the temperature of the room should never exceed 32°C at any time during the occupied hours. Temperatures above 28°C are acceptable at the maximum of 120 hours during the summer.

However, and as previously discussed, a better approach to analyse if buildings with free cooling are suffering overheating or not is to use the adaptive thermal comfort criteria. An upper limit of 28.41 $^{\circ}$C was calculated for the summer period, which

means in a temperature slightly below the average obtained from simulation (28.5 ^{o}C). This analysis was presented in section 5.2 where data acquired by sensors installed along the room were used to evaluate if the space overheats or not.

Figure 5.13 shows the temperature distribution on plane 2x, 4x and 7x. It can be seen that the temperature varies from 23.5 to 28°C from the floor up to the students. This difference of 4.5 K is above the difference of 3 K recommended by ISO 7730 (ISO, 2005). According to this ISO, approximately 20 % of the occupants will feel dissatisfied if this situation happened in a real case. This is discussed in section 5.4.3 where a simulation with calibrated data is used.

Independent of the plan location, Figure 5.13 shows that temperature is equally distributed at the same height. Temperatures are higher ($\geq 30^{o}$C) close to the ceiling and hot air is extracted by the exhaust grille. This is motivated by the buoyancy effect where the heat generated by the occupants and computers warm the air and reduces its density, resulting in a upward movement while the cold and dense air move downwards. Moreover, Figure 5.12 and Figure 5.13 also show that the temperature distribution is uniform and there are no hot spots in the room.

Moreover, Figure 5.14 shows the row 2y, 4y and 7y. This figure presents a different temperature range compared to Figure 5.13 because the air temperature supplied by Cool-Phase® is 17.5 ^{o}C. These planes show uniformity in temperature distribution which indicates that the MVS is distributing well the temperature. It also shows that most of the cooling air provided by the MVS is directed downwards which might affect occupants' thermal comfort. This is more pronounced for the winter and autumn case studies where simulations with an airflow of 100 l/s were performed. Due to a higher airflow during the summer (210 l/s), the temperature is better distributed and less stratification was identified. This is also confirmed by Figure 5.12 where a cross with temperatures lower than the room average surface shows that the air is dispersing more easily.

5.4.2 Air flow distribution

Figure 5.15 and Figure 5.16 presents the velocity vectors of rows 5x and 2y. These planes are the nearest to the Cool-Phase® exhaust grille and include positions with students. Velocities higher than 0.3 m/s were found on row 2y in autumn and winter at approximately 0.15m from the student, while in the summer case study, velocities higher than 0.3 m/s reach the students. This difference is due to the higher airflow during the analysed period (210 l/s). Row 2y in the summer study (Figure 5.16) shows air velocities of about 0.18 m/s reaching student's head and row 5x (Figure 5.15) shows an air velocity of about 0.4 m/s close to students ankles at any studied case. CIBSE (CIBSE, 2015b) points that air velocities greater than about 0.3 m/s are probably

unacceptable with the exception of naturally ventilated buildings during the summer period, when higher airspeeds are desired due to their cooling effect.

The summer case has approximately double the airflow when compared to autumn and winter cases (respectively 210 and 100 l/s). This analysis shows the importance of how air distribution in the room can affect occupants comfort and temperature distribution. Higher velocities will cause discomfort to occupants close to the diffuser but provide an environment with less stratification at seating level. However, a supplied airflow above 210 l/s is not common during occupied hours. During 2014 and 2015, it occurred during 12 and 10 % of the occupied hours, respectively.

Figure 5.12 — Temperature distribution at z=1.2m
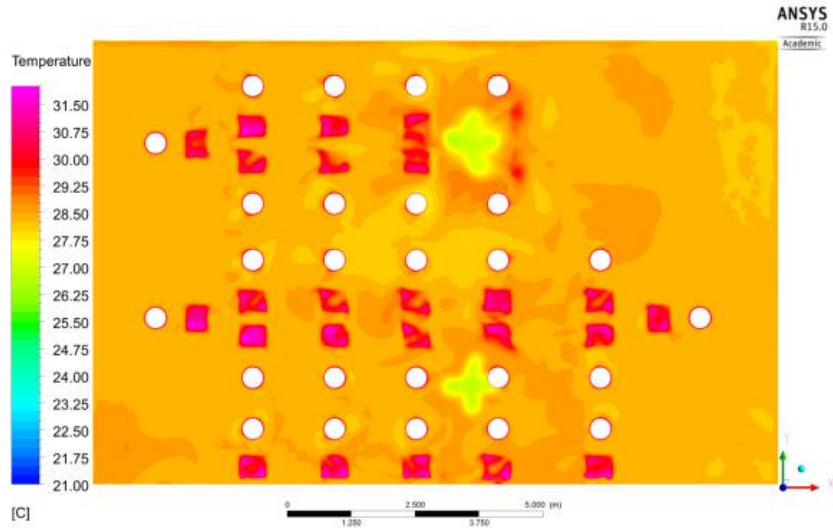
Summer
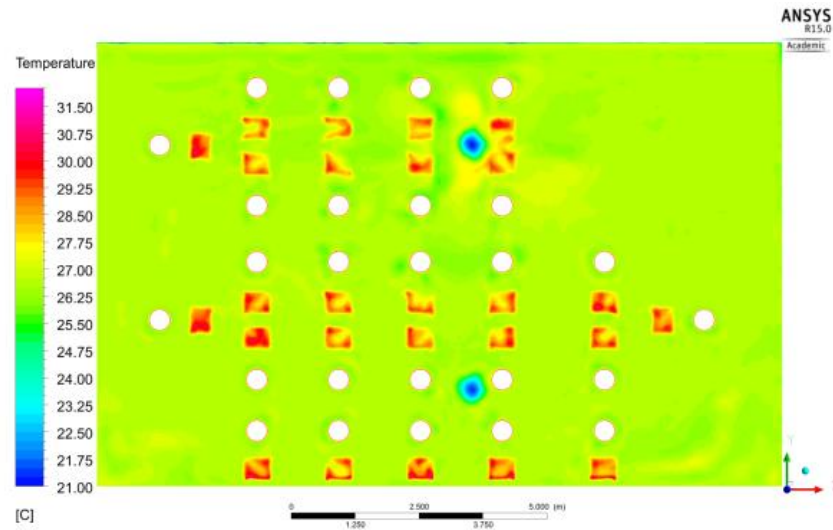
Autumn
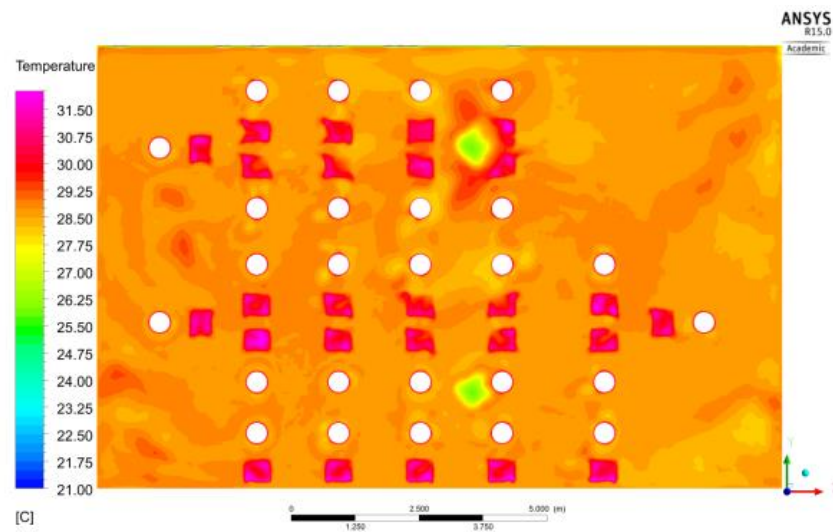
Winter
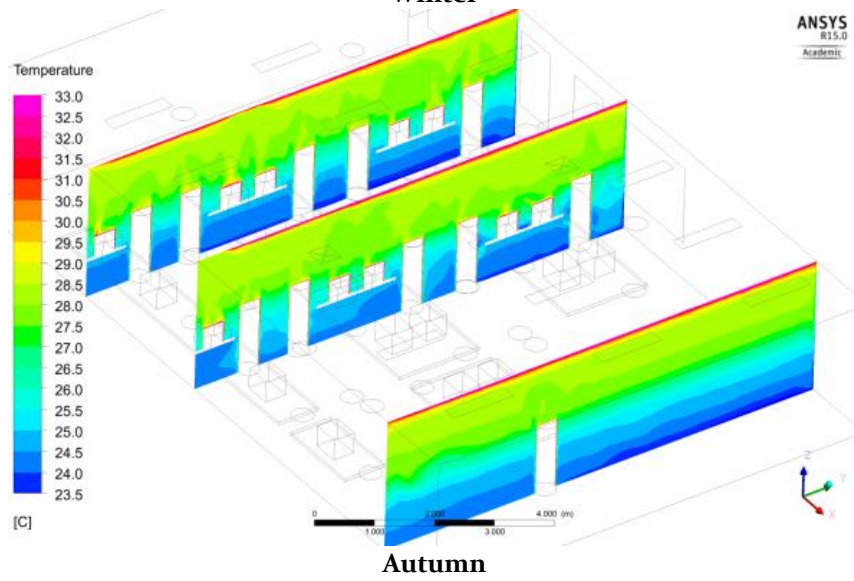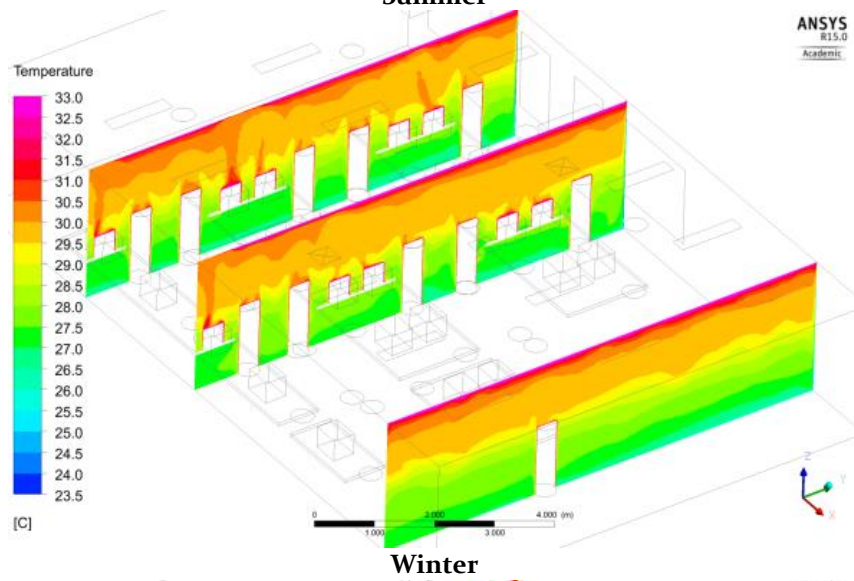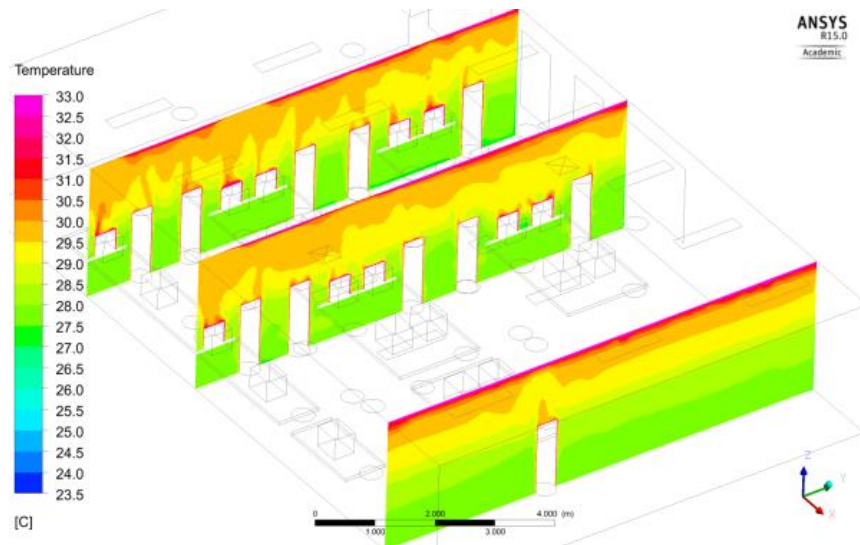
Figure 5.13 – Temperature distribution of rows 2x, 4x and 7x
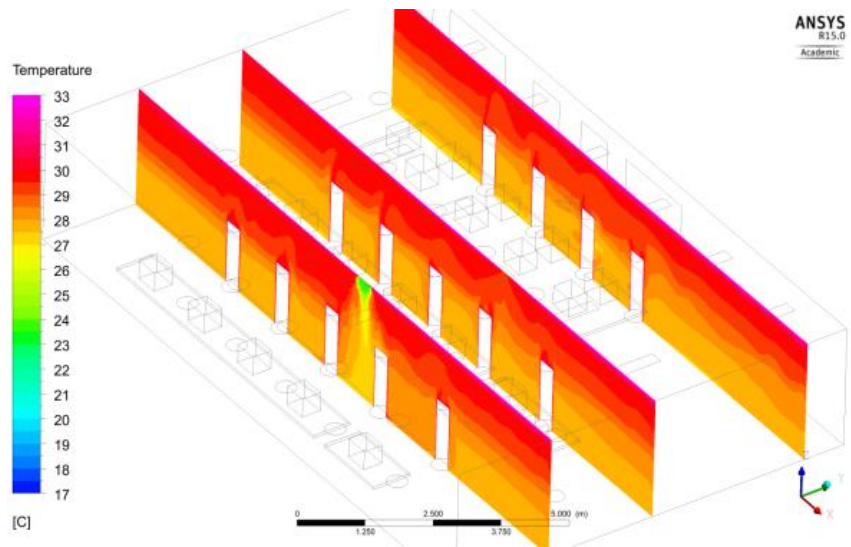
Summer
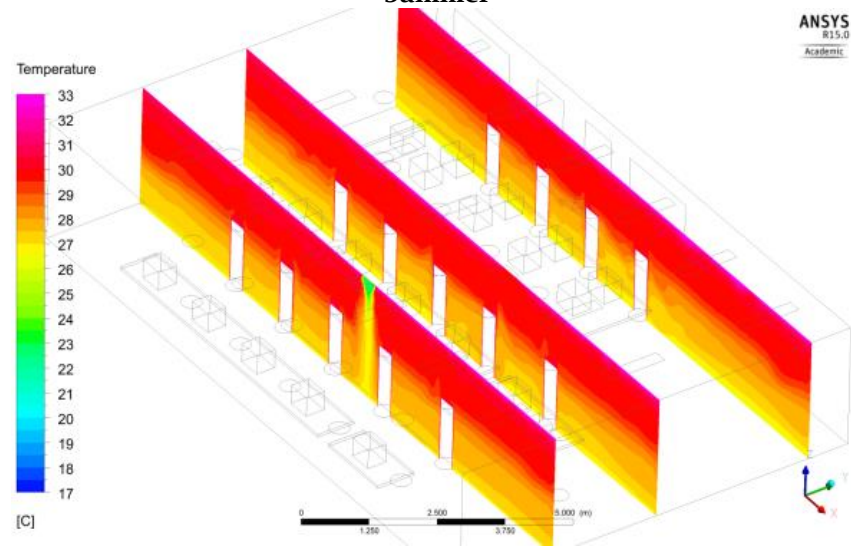
Winter
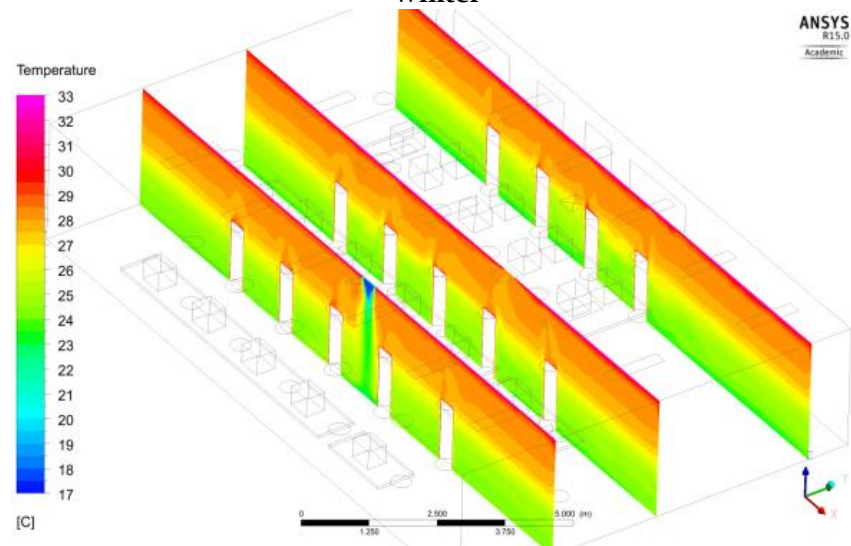
Autumn

Figure 5.14 – Temperature distribution of rows 2y, 4y and 7y
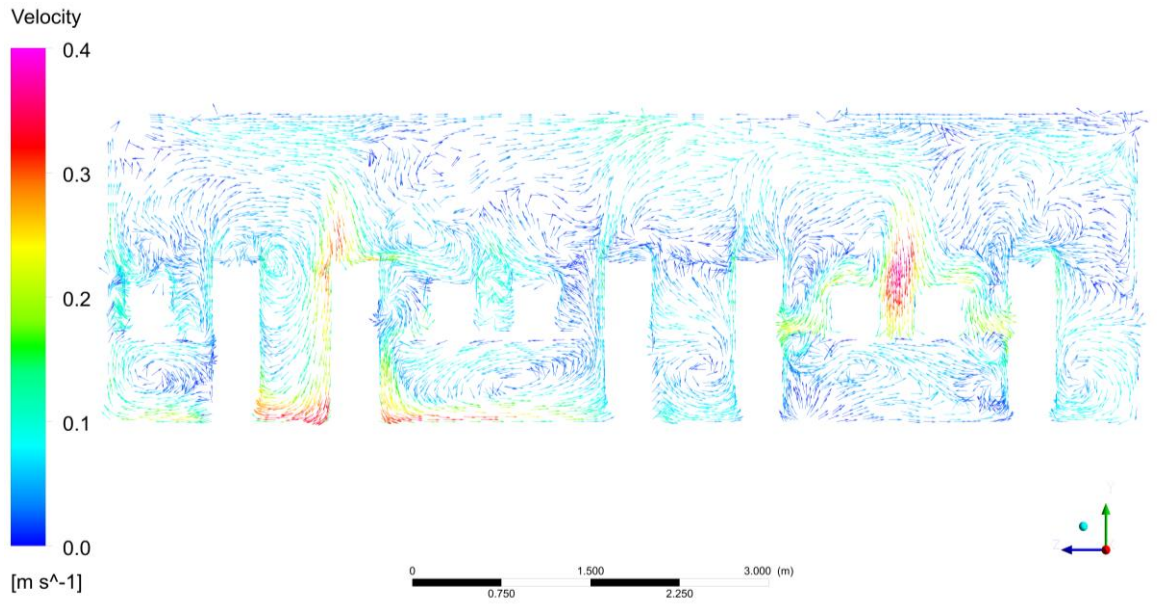
Summer
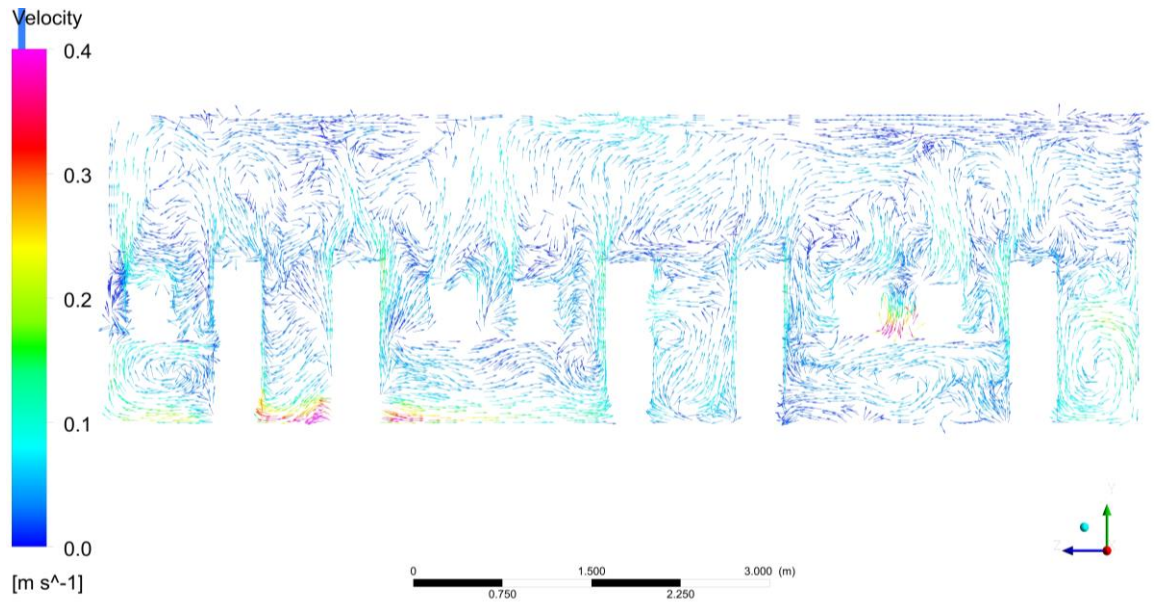
Winter
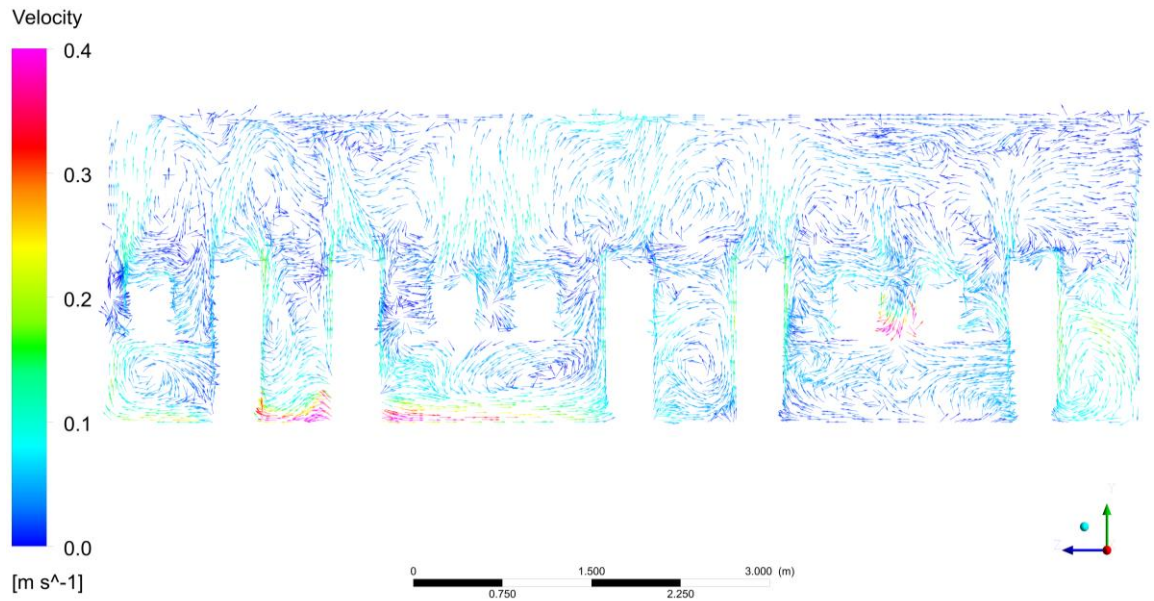
Autumn
Figure 5.15 – Velocity vector on row 5x

Summer

Winter

Autumn
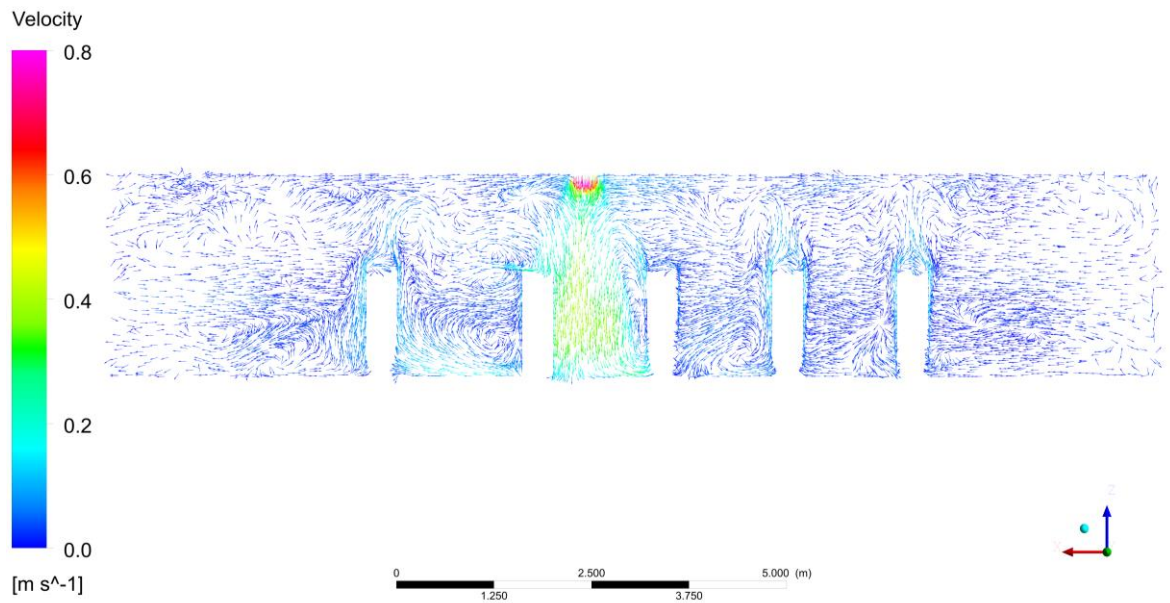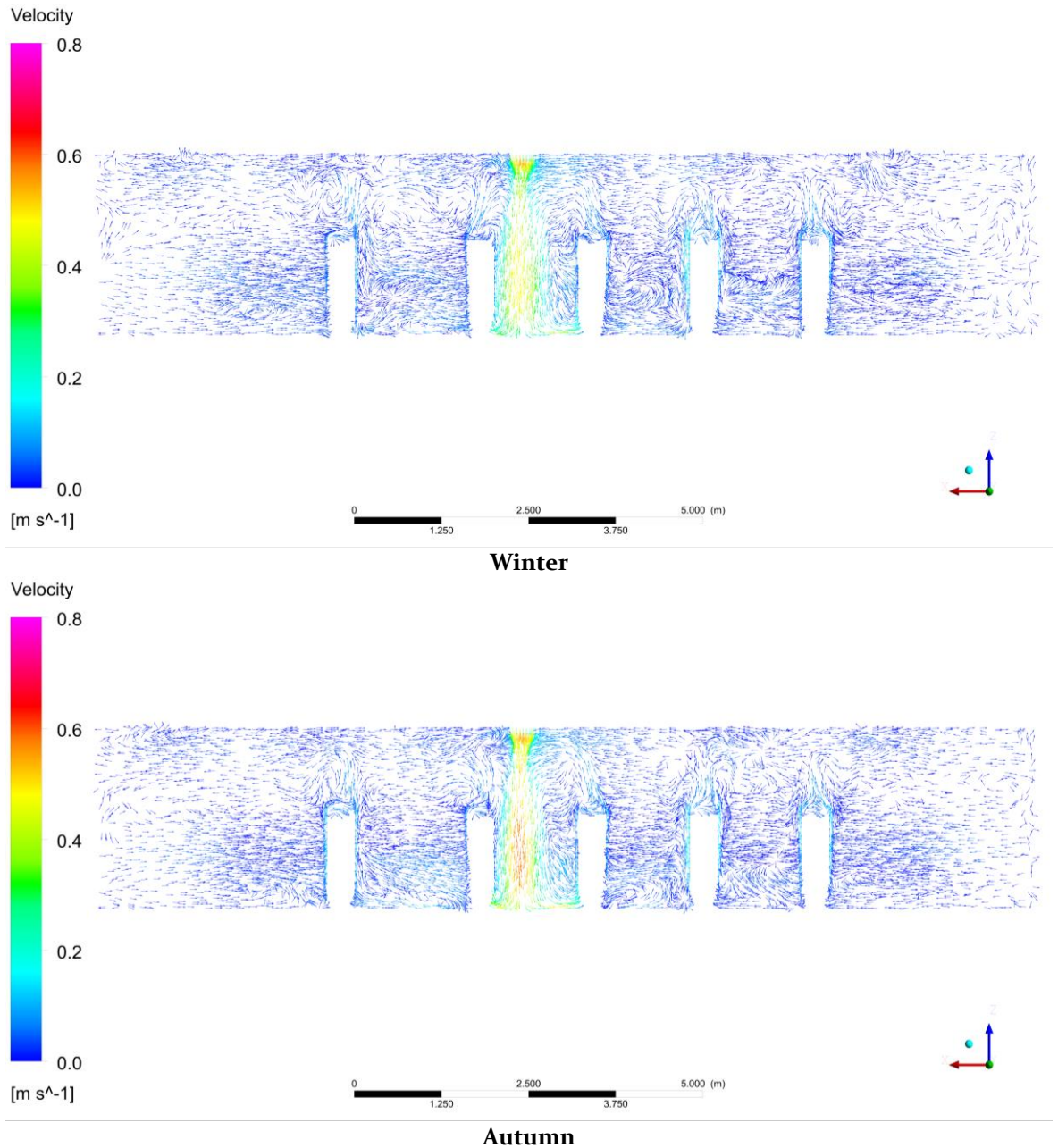
Figure 5.16 – Velocity vector on row 2y

5.4.3   MVS performance analysis

To analyse if space conditions are within the thermal comfort range throughout the room, a CFD modelling was carried out. A 3D model of the seminar room was made and the day of 24/09/2015 was chosen for investigation due to the better match between room data, system data and IESVE temperature profiles (Figure 5.17, right).
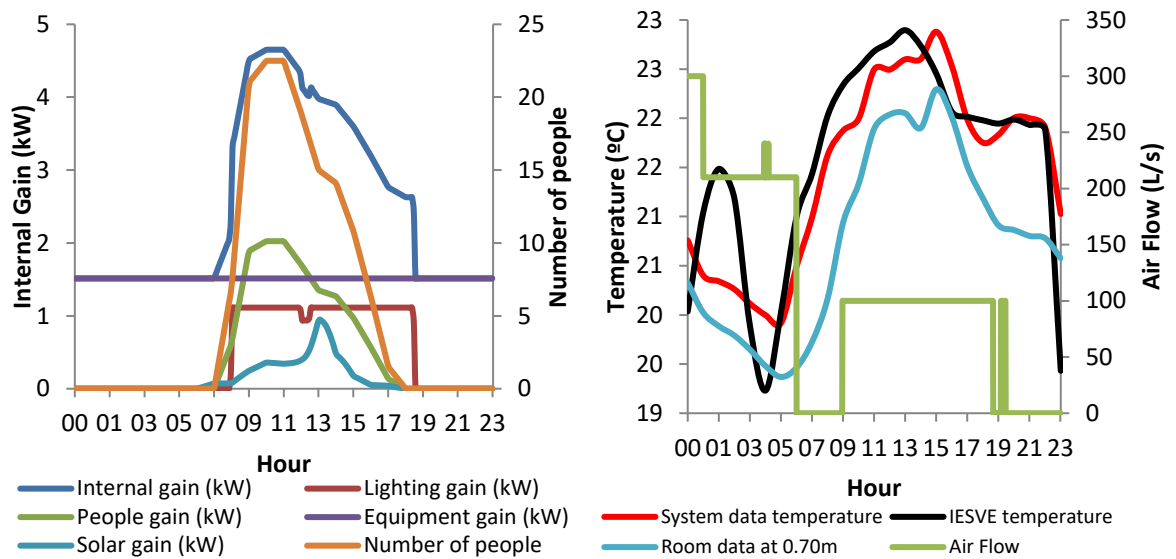
Figure 5.17 – Internal gains (left) and temperature from IESVE calibrated model and system data (right) of 24/09/2015

A constant air flow of 100 l/s supplied by the system was also important to secure a uniform air distribution and consistent CFD simulation. 100 l/s is the design air flow to operate for most of the cooling period and when occupants are accommodated (for this particular case, when students are seated). 100 l/s occur in 26.8 % and 44.3 % of the cooling time in 2014 and 2015 respectively. Airflows between 100-140 l/s in 2014 and 2015 occurred in 63 % and 78 % of the cooling time.

To simulate this particular day, the procedure to generate the mesh from the first CFD simulation presented in section 4.5 was used. It was noticed during the visit at UWE that the seminar room now accommodates 29 students instead of 26. Due to that, the CFD drawing was updated. Heat gains from computers (11) and students (14) at 15:00 were extracted from IESVE (Figure 5.17, left) and introduced in ANSYS Fluent as a boundary condition. The rest of the input variables were taken from system data and Wunderground ('Weather Underground', n.d.).

For this particular case, the same procedure to generate the mesh presented in Chapter 3 was used with more refined meshes (1,103,501 and 2,789,988 nodes). The planes of interest were analysed to understand if significant changes were found plus a comparison with the monitoring data at 0.70m. Figure 5.18 presents these results. It can be seen that no significant difference in the results was found when the two meshes are compared. This is confirmed when the simulation is compared with monitoring data where a difference of 7.55 and 7.23 % (or 1.707 and 1.635 °C) was found for 1,103,501 and 2,789,988 nodes, respectively. The finest mesh was chosen as no extra simulation needs to be performed. This is a reasonable result as the indoor environmental modelling chapter of ASHRAE fundamentals (ASHRAE, 2013b)

indicates that a difference of 20 % could be considered excellent for complex flow problems.
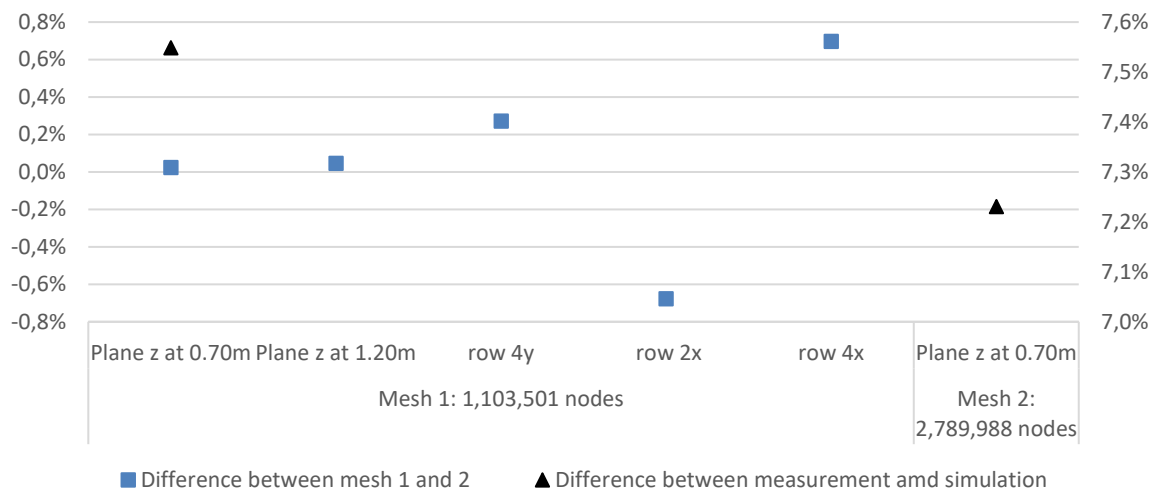
Figure 5.18 – Grid independence analysis for seminar room with 29 occupants.

Results from this simulation are presented in Figure 5.19 where a plane at seated level (0.70m) shows that the temperature is well distributed with an average of 24.2 °C, 8.5 % higher than the field monitoring. It also shows that at 0.70m, no thermal discomfort is expected based on the adaptive thermal comfort limits. However, section B-B shows a stratification of 23 - 25 °C from the ankles to the head of the occupants, below the 3 K recommended by ISO 7730 (ISO, 2005). Air velocity contours show a range of 0.1 – 0.2 m/s within the space apart from a small area near or directly under the air supplier. Occupants located close to the diffuser might feel uncomfortable as air velocity reached a maximum of 0.6 m/s. Changing the diffuser angle or its geometry might reduce this effect. Another solution is to relocate the occupants so they are not directly hit by the air jet.
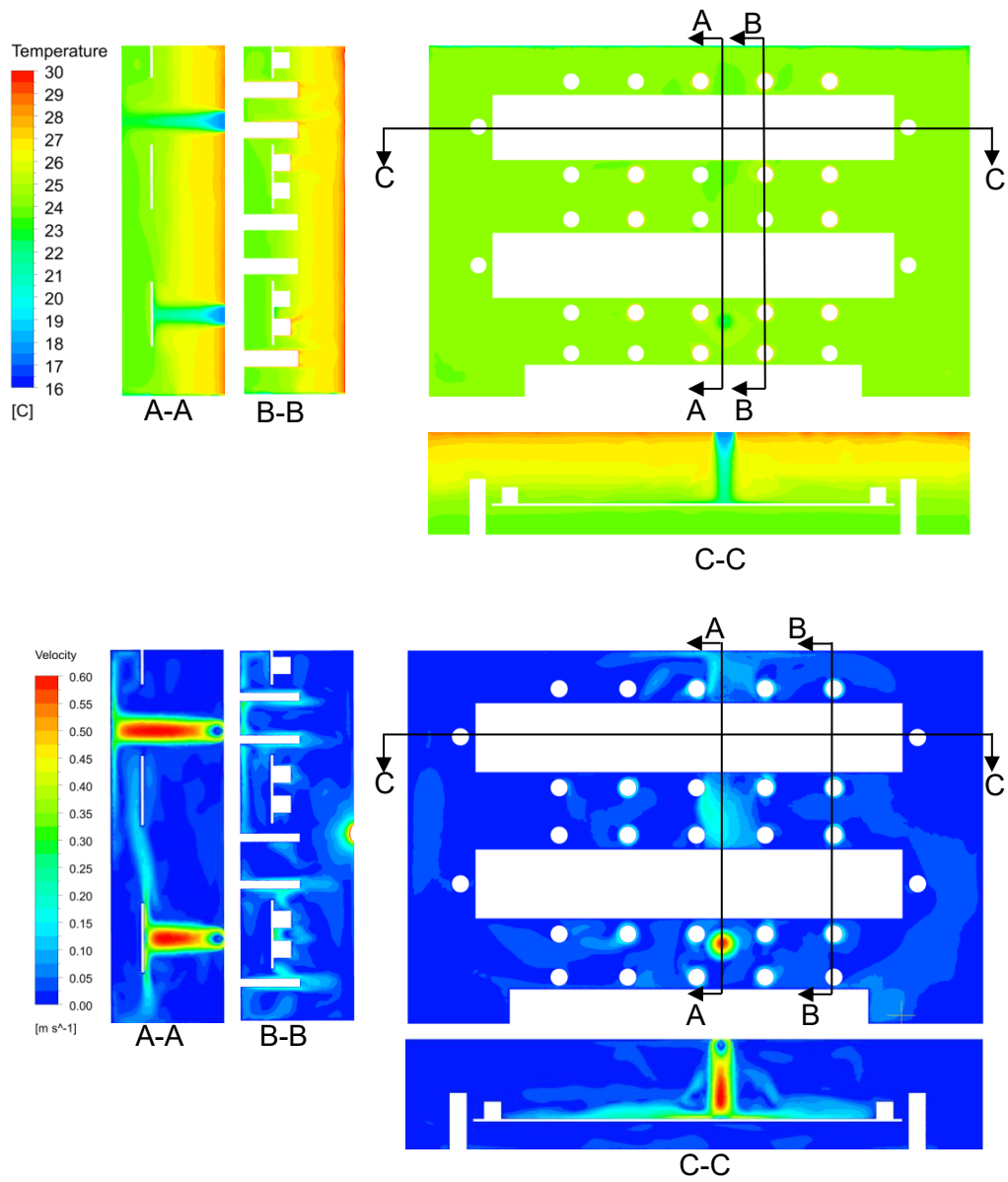
Figure 5.19 - CFD predictions of Temperature and air velocity at 0.70m at 15:00 on 24/09/2015

5.5 Energy consumption and MVS performance

The system includes a variable speed fan and motors to control the dampers resulting in low overall energy consumption. Electrical energy consumption in the seminar room was 91.7 kWh (0.78 kWh/m²/annum) in 2014 and 78 kWh (0.67 kWh/m²/annum) in 2015. In monetary terms, this will cost less than £ 10 per year (based on 2015 cost average of £0.104 per kWh for a medium size building (Department of Energy & Climate Change, 2013)). Simulations with IESVE (discussed in more detail in section 5.4.3) show an energy demand of 8.83 MWh (75.5 kWh/m²/annum) to maintain the same internal conditions. Therefore, the energy used by the system is a small fraction of the energy required by an AC system (the exact saving is dependent on the AC system and its COP). Annual electricity energy use intensity for secondary schools in the UK has a median of 51 kWh/m² (CIBSE, 2015c) including electricity used for lighting and office equipment. This increases by 5kWh/m² when moving from 'heating and natural ventilation' to 'heating and mechanical ventilation' buildings, indicating the typical magnitude of energy use by mechanical ventilation. CIBSE TM57 (CIBSE, 2015c) presents good case-studies with cooling energy intensity of 12.5kWh and 3.5 kWh/m². Therefore, the energy needed to operate the system is small compared to available benchmarks.

Figure 5.20 presents Monodraught Cool-Phase® weekday indoor temperature frequency in percentage from 8:00 until 21:00 in 2014 (left) and 2015 (right). In 2014, temperatures of 24 ± 0.5 °C were more frequent for winter and summer (25.77 and 28.65 % respectively) and 35.39 % for 25 ± 0.5 °C for Autumn/Spring. In 2015, Cool-phase® maintained the seminar room in the set-point temperature more frequently during summer (35.16 %) and winter (42.15 %). During Spring/Autumn, the room was slightly warmer than the Cool-Phase® set-point (37.02 % for 24 ± 0.5 °C). Figure 5.20 also shows that Cool-phase® maintained the room temperature between 21.5 and 26.5 °C for most of the time in 2014 (93 %) and between 21.5 and 25.5 for 88.76 % in 2015. In this case, occupants can easily adapt by increasing or decreasing clothing.
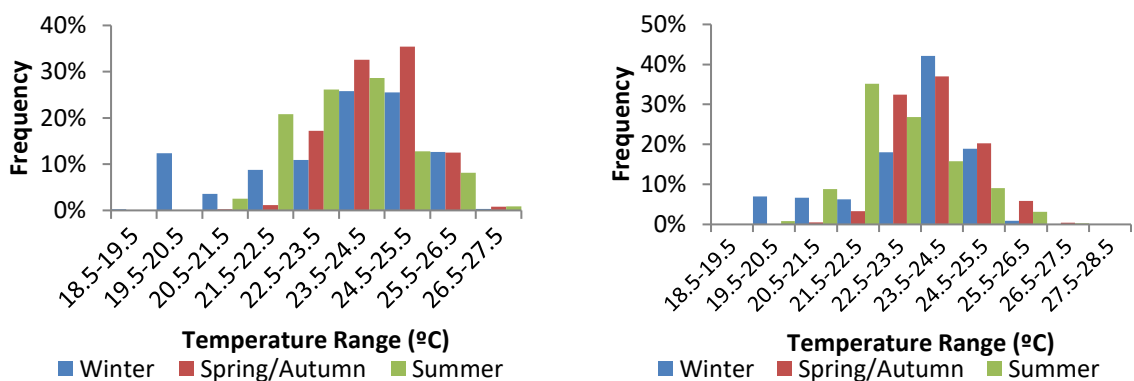
Figure 5.20 – Percent range of indoor temperature system data for weekdays of 2014 (left) and 2015 (right) from 8:00 to 21:00.

5.6 Chapter's summary

This chapter presented the case study of a seminar room containing a PCM-Air heat exchanger located in the West of England that is suitable for newly built and retrofit applications. The seminar computer room (with internal heat gains of $60W/m^2$) has the system installed in the existing plenum of the space with access to outside. Detailed monitoring of the spaces and thermal/CFD analysis indicated that the system can provide acceptable thermal comfort throughout at seating occupant level (0.7 m from the floor) in the moderate summer weather conditions of southwest England using adaptive thermal comfort limits. Furthermore, the heating season was also studied following BS EN 15251. According to that, occupants might feel dissatisfied for 13.3 % of the time according to PPD and uncomfortable for about 4.4 % according to PMV.

In order to understand the MVS performance over the seasons, a CFD analysis was carried out considering full occupancy and analysed temperature and air velocity distribution. Moreover, data from the monitoring was used to calibrate a DTM model and the heat gains introduced as a boundary condition in the CFD simulation in order to study the MVS performance.

The chapter concludes by presenting the energy consumption and MVS performance during 2014 and 2015. These results show that improvements in the system control can increase the MVS performance and raised the question if other strategies to improve the MVS can be used. Chapter 6 approached this by performing a parametric analysis of the system control and proposing a new design for the panel where the PCM is encapsulated.

CHAPTER 6 - IMPROVEMENTS OF THE MVS AND PCM PANEL THROUGH DTM AND CFD MODELLING

Introduction to the chapter

This chapter presents the results obtained of the analysis to improve the control system and the design of the panel to substitute the existing one. Divided into two main sections with methods described in Chapter 3, the first part includes the improvements in the plugin and in the performance of the system by introducing more control components and increasing the airflow. The second part of the chapter is dedicated to present the results related to the panel design. It shows the results from the 3D simulations and explains why the following simulations are performed in 2D. Refinements with changes in the thickness of the panel and number of panels per thermal battery are presented together with the results of pressure drop. These are plotted in the fan curve and the capability to be able to provide the required airflow is analysed.

6.1 Improvements of the MVS through DTM

6.1.1 Step control introduction in modelling

Described in chapter 2, IESVE is a DTM software which includes a Cool-phase® plugin with a simplified control system. As mentioned in chapter 4 (MVS operation), cool-phase® has a step control for the airflow while the plugin has a proportional controller. To represent more realistically the equipment, a step control was introduced in the plugin by adding more components (Figure 6.1 (right)).
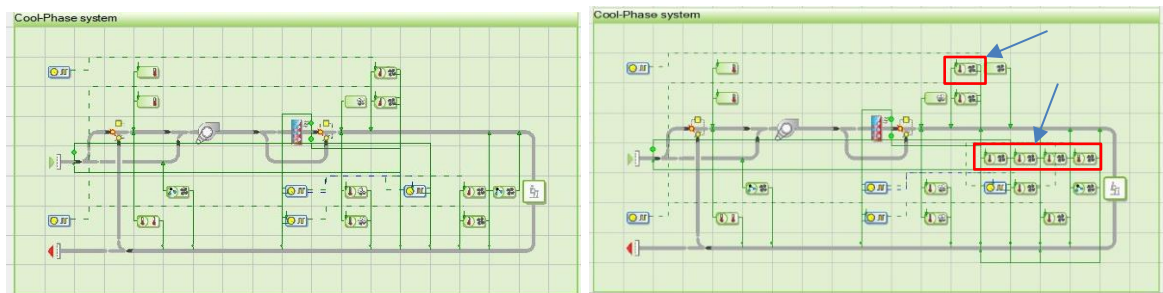
Figure 6.1 – Improvement in the plugin control system (left: initial, right: step control introduced)

The results presented in Figure 6.2 show the difference in the room temperature and in the fan behaviour when the simplified component (Figure 6.1 (left)) is compared with the step control component Figure 6.1 (right). This reveals the importance to have a plugin that represents the reality as much as possible to correctly design the MVS.
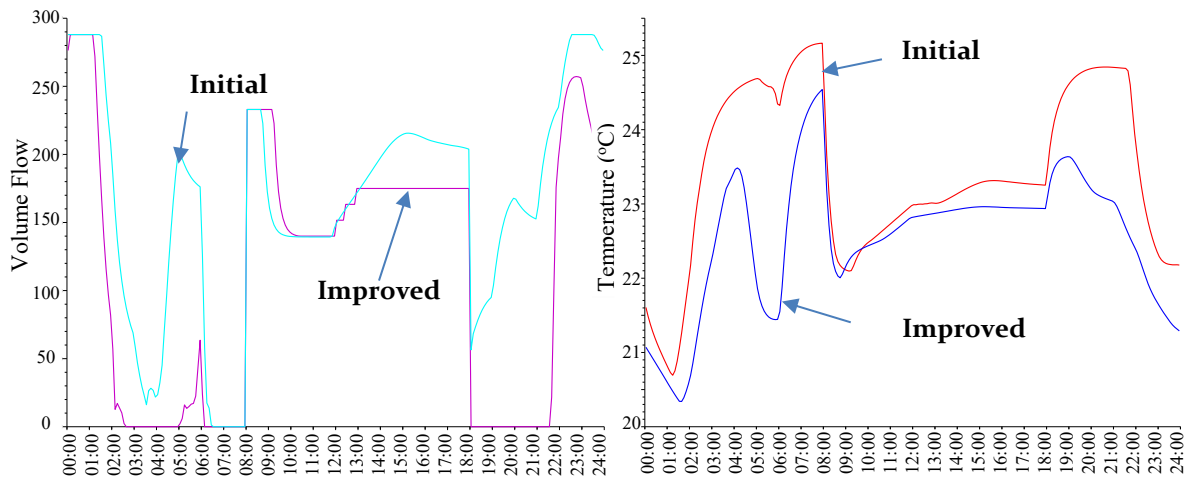
Figure 6.2 – Improvement in the plugin control system (left: initial, right: step control introduced)

6.1.2 Calibration of the improved plugin and MVS improvement

To calibrate the MVS and propose improvements in the control system, same weather conditions need to be represented. To achieve that, weather data for the prediction period was sourced from Weather Underground ('Weather Underground', n.d.) and introduced in simulations by updating the EWY weather file with air temperature and relative humidity data of the monitored period (2015). IESVE plug-in standard control system was improved using CO_2 data (Labeodan et al., 2015) to calculate the number of students and computers during operation until the simulation results for each month achieved values of MBE and CVRSME below 10 % and 30 % respectively when compared to measurements (Table 6.1). Figure 6.3 presents the simulations performed until the levels of MBE and CVRMSE were achieved. Furthermore, Figure 6.4 shows the air temperature after calibration and temperature measured by the Cool-phase® for the months of June and July. As a result, IESVE can provide information such as the main heat gains for a particular day (Figure 5.17, left). On the right, a similar trend can be seen between system data, room data at 0.70m and IESVE calibrated model.

Table 6.1 – MBE and CVRSME for 2015 calibration (in %)

	Jan	Feb	Mar	Apr	May	Jun	Jul	Aug	Sep	Oct	Nov	Dec
MBE	-0.59	0.68	0.09	-0.37	-0.81	-0.81	-0.29	-0.37	-0.20	-1.15	-1.21	-0.32
CVRMSE	12.93	14.84	2.10	8.49	18.27	18.28	6.76	8.38	4.67	26.33	27.15	5.81
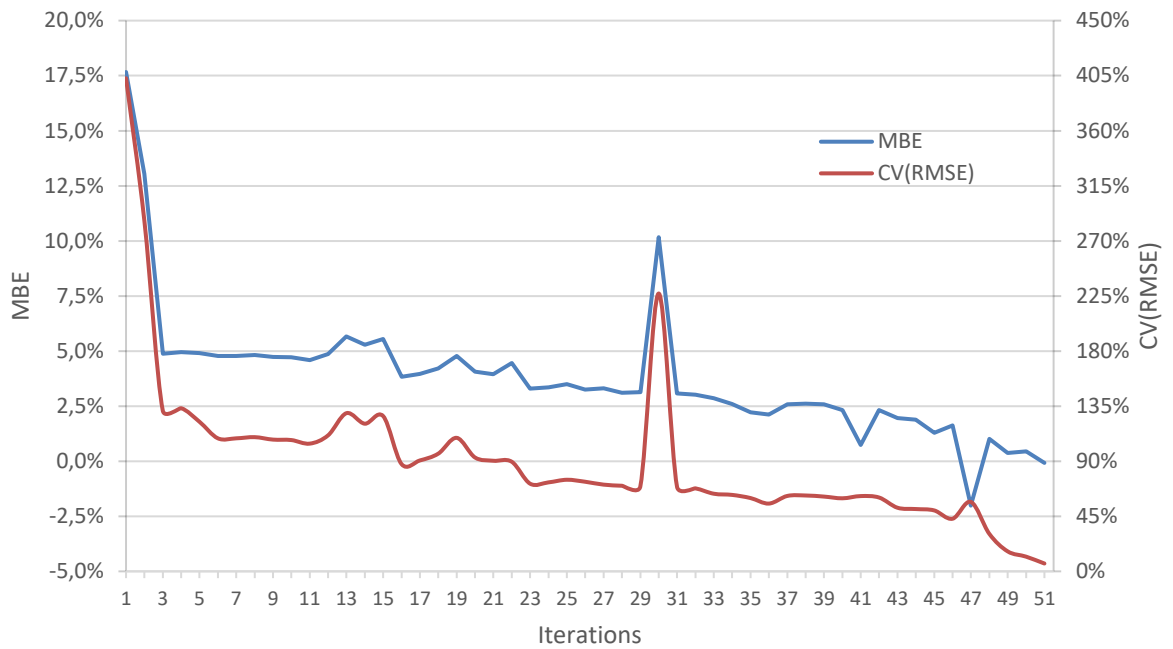
Figure 6.3 – Iterations on IESVE to achieve MBE and CV(RMSE) below 10 and 30 %, respectively.
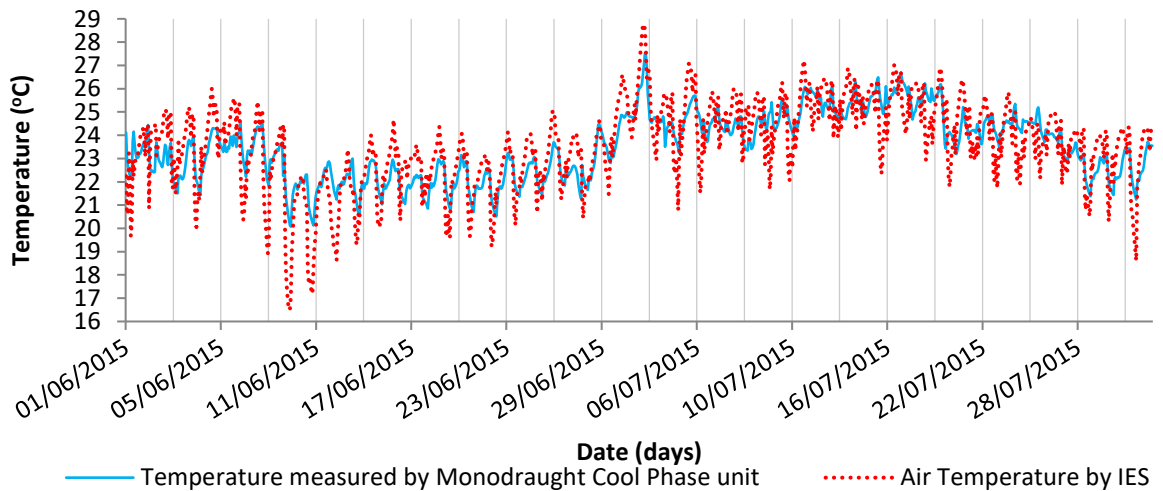
Figure 6.4 – Calibrated result obtained on IESVE and temperature measured by Monodraught Cool-Phase® unit.

With the calibrated models, parameters in IESVE were adjusted and improvements on system performance can be tested with confidence.

The question studied is whether airflow rate increases will improve the equipment performance. This was investigated by increasing the airflow at each temperature set-point (Table 5.8) by downgrading the set-point airflow in 2 degrees (e.g. set-point of 24 °C now will be the set-point of 22 °C, 25 °C will be the set-point of 23 and so on).

Table 6.2 – Set points for Cool-Phase® and improved IESVE model

Set-point (°C)	Cool-Phase® Air flow (l/s)	Improved Air flow (l/s)
22	100	175
23	140	210
24	175	240
25	210	260
26	240	300
>26	260	300
Purge	300	300

The results presented in Figure 6.5 indicate an increased percentage of air temperature in the summer, autumn/spring and winter set-points. For the summer period, 43.6 % of hourly temperatures are inside the set-point range (22 °C± 0.5 °C) an increase of 14.2 %. During the autumn there was also an increase of 12.3 % of hourly temperatures inside the setpoint temperature (23 °C ± 0.5 °C) while temperatures above 24.5 °C had a significant reduction of 27.7 %. During winter, temperatures were close to the set-point of 24 °C (± 0.5 °C) for 69.6 % of the time, an increase of 3.7 %. These differences in percentage between improved and calibrated model are break-down in Table 6.3 where temperatures ranging from 18 °C (± 0.5 °C) and 27 °C (± 0.5 °C) are presented.
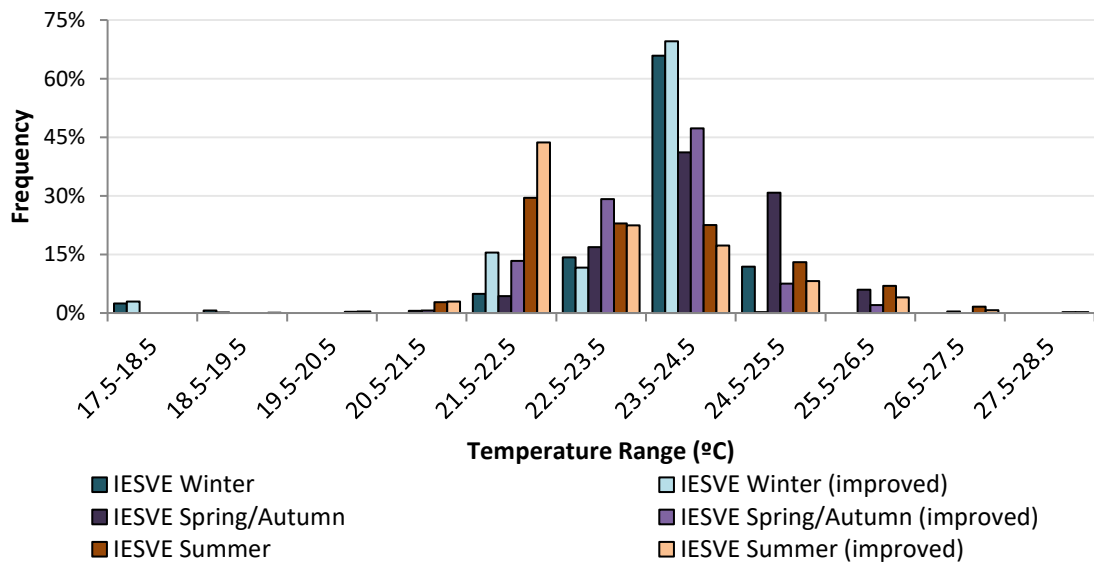
Figure 6.5 – Frequencies of improved and calibrated model on IESVE for each season from 8:00 to 21:00

Table 6.3 – Difference (in percentage) from the Improved model and calibrated model for each temperature range.

Temperature (°C)	IESVE winter	IESVE spring/autumn	IESVE summer
17.5-18.5	0.5 %	0.0 %	0.0 %
18.5-19.5	-0.5 %	0.0 %	0.0 %
19.5-20.5	0.0 %	0.0 %	0.0 %
20.5-21.5	0.0 %	0.1 %	0.2 %
21.5-22.5	10.6 %	9.1 %	14.2 %
22.5-23.5	-2.6 %	12.3 %	-0.5 %
23.5-24.5	3.7 %	6.2 %	-5.2 %
24.5-25.5	-11.6 %	-23.3 %	-4.8 %
25.5-26.5	0.0 %	-4.0 %	-3.0 %
26.5-27.5	0.0 %	-0.4 %	-0.9 %

For the entire year, the base-case model present temperatures inside the season set-point range for 37.4 % and the model with enhanced airflow rates 47.4 %. This increase in frequency of approximately 10 % will consume additionally 44 kWh per year (or 51.4 %) which is a small penalty despite the high increase in percentage value. (Table 6.4).

Table 6.4 – Energy consumed and difference from Cool-Phase®.

	Energy consumed (kWh)	Difference from Cool-Phase®
Cool-phase®	78.74	
Calibrated model	85.52	108.6 %
Improved model	129.52	164.5 %

6.2 Encapsulation panel design

6.2.1 3D simulations

As described in chapter 3, a number of shapes for the encapsulation panel were investigated. The different shapes were presented in Table 3.14 and is included in this section for easiness of reference.

Table 3.13 – Modelled geometrical variations of the panel (included in this section for easiness of reference)

3D Simulations				
Shape	Ridge height/ Air gap (e/h)	Ridge pitch length/ Panel length (s/l)	Ridge width / Panel width (w_r/w)	Ridge Radius (r) (mm)
Basecase	0.125	0.033	0.033	-
Teardrop	0.313	0.039	0.029	5
Dimpled	0.250	0.058	0.033	6
Shape 1	0.188	0.039	0.077	1.5
Shape 2	0.188	0.039	0.083	1.5
Shape 3	0.313	0.039	0.083	2.5
Shape 4	0.125	0.039	0.077	1.5
Shape 5	0.313	0.078	0.183	2.5
Shape 6	0.250	0.039	0.093	5
Shape 7	0.250	0.062	0.867	5
Shape 9	0.219	0.044	0.867	2.5
Shape 10	0.313	0.056	0.867	2.5

2D simulation of Shape 9				2D simulation refinement			
Shape 9 variations	Ridge Height / Air gap (e/h)	Ridge Pitch / Panel length (s/l)	Ridge Radius (r) (mm)	Shape 9 in module	Gap between panels / Duct height (h/H)	Panel thickness / Duct height (T_t/H)	Number of panels (p)
Shape 11	0.219	0.044	2.5				
Shape 12	0.063	0.022	7.5				
Shape 13	0.063	0.022	7.5	Shape 24	0.042	0.069	9
Shape 14	0.188	0.044	2.5	Shape 25	0.042	0.079	8
Shape 15	0.250	0.044	2.5	Shape 26	0.042	0.124	6
Shape 17	0.188	0.033	2.5	Shape 27	0.048	0.101	6
Shape 18	0.188	0.022	2.5	Shape 28	0.053	0.101	6
Shape 19	0.219	0.044	2.5	Shape 29	0.051	0.121	5
Shape 20	0.219	0.056	2.5	Shape 30	0.063	0.151	4
Shape 21	0.281	0.044	3.0	Shape 31	0.034	0.080	8
Shape 22	0.219	0.044	2.5	Shape 32	0.030	0.070	9
Shape 23	0.281	0.044	2.5				

The results of Nusselt number, pressure drop and the ratio between the existing panel and smooth panels are presented in Figure 6.6. All panels present a Nusselt number higher than the existing panel; the highest is for the dimpled panel with a three fold increase in pressure drop. Shapes 6 and 3 present the higher pressure drop (approximately 10 times higher than the existing panel) which makes them unsuitable. Shapes 1 and 2 have good heat transfer but the lozenges (as seen in Figure

3.13 and in Appendix III) along its width doubles the cost of production and makes it unfeasible; for the same reason, the dimpled and the teardrop panel was discarded. Shape 9 is the panel with the simplest design (ridges along its width through the whole panel) and capable of increasing the Nusselt number three fold, with the cost of a pressure drop five times higher compared to the existing panel. These ratios can be seen in Figure 6.6 where Nusselt number and pressure drop over existing and smooth panel are presented. Figure 6.6 also shows that shape 2, teardrop and dimpled panel, has an efficiency (thermal enhancement factor, see section 3.4.2) higher than 1.0 which means that gains in heat transfer are higher than gains in pressure drop, while for shapes 6, 1, 9 and 3 the pressure drop increased more than the heat transfer.

Based on the results and due to the simplicity of its design and manufacturing cost, shape 9 was chosen for additional refinements. Moreover, as this panel is uniform along its width, it gives rigidity to the panel and avoids the need of having both surfaces attached as in the existing panel (Figure 6.11 (left)).
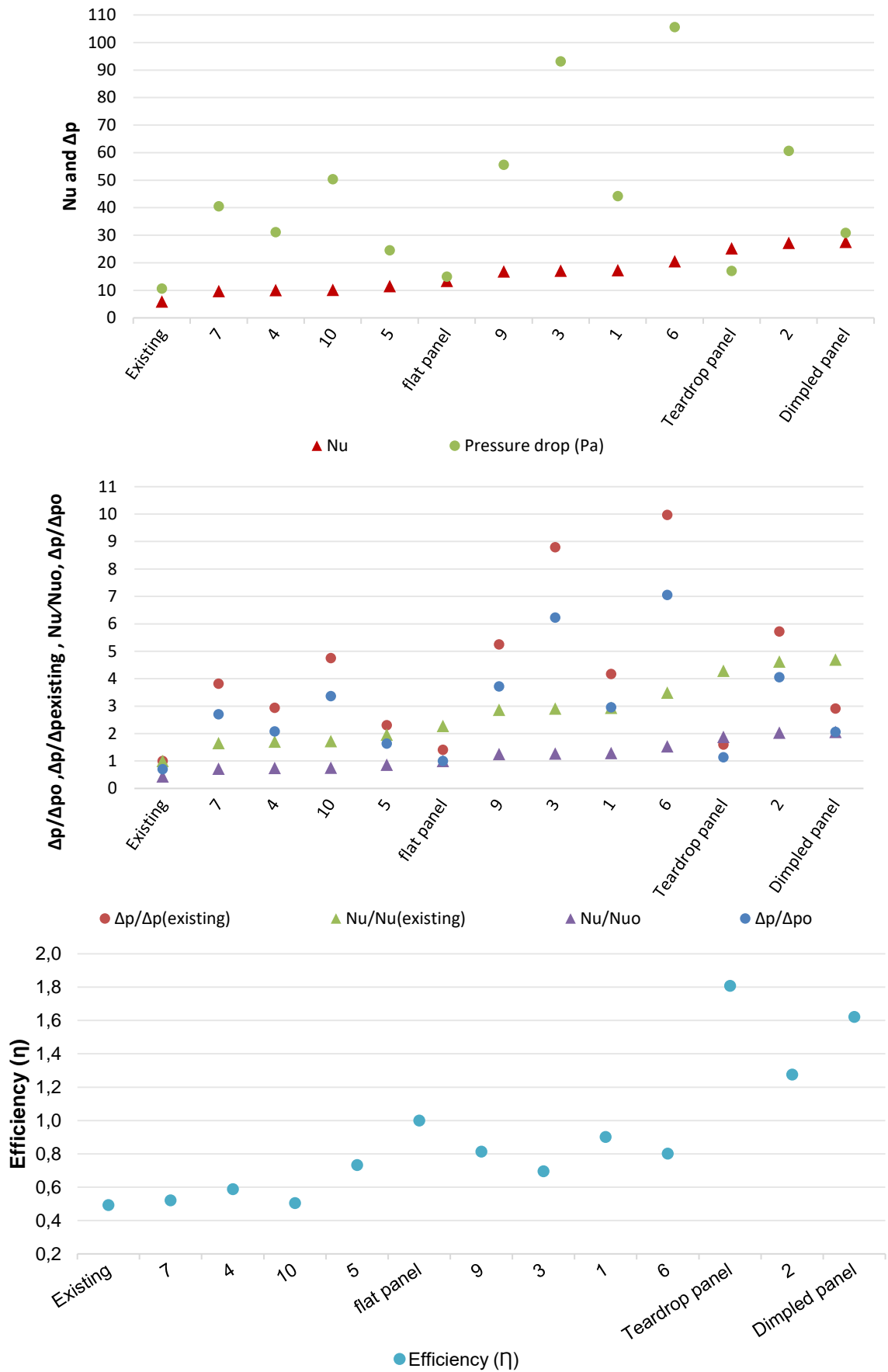
Figure 6.6 –Nusselt number and pressure drop ratio for existing and smooth panel (left) and Nusselt and pressure drop (right) at *Re* = 18736 for 3D simulations.

6.2.2 2D simulations

The design of Shape 9 (uniform along its width) allows the simulations to be conducted in 2D. 13 variations (Shapes 11 to 23) were generated and stacked in 7 panels per module to perform a parametric analysis of the spacing between ridges, ridge height and radius for Reynolds number varying from 7200 to 21600. Figure 6.7 shows the temperature distribution of Shape 11. The outlet temperature and inlet pressure were averaged and used to calculate the Nusselt number and pressure drop presented in Figure 6.8 for all shapes examined.
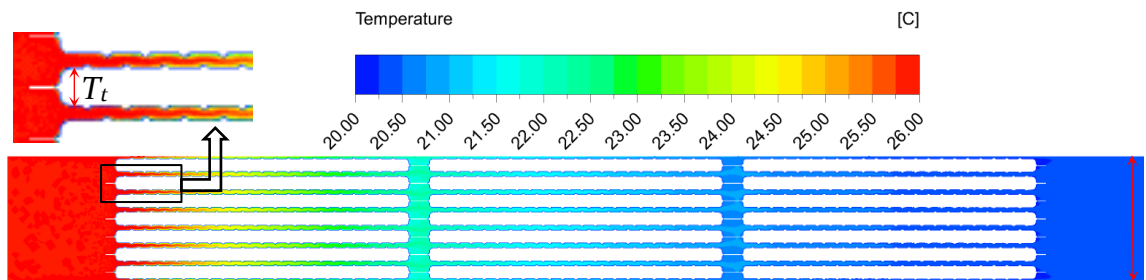
Figure 6.7 – Temperature distribution of Shape 11 at $Re = 18736$

Figure 6.8 shows that shape 11 has, at most Reynolds numbers, the highest heat transfer representing 75 % more heat transfer on average when compared to a smooth panel. It also shows that shape 11 has an efficiency close to 1.0 on average, which reflects that the heat transfer increased in a similar rate as the pressure drop while other shapes have a higher increase in pressure drop when compared to heat transfer.

Figure 6.8 – Nusselt number and Nusselt number ratio from a smooth panel.
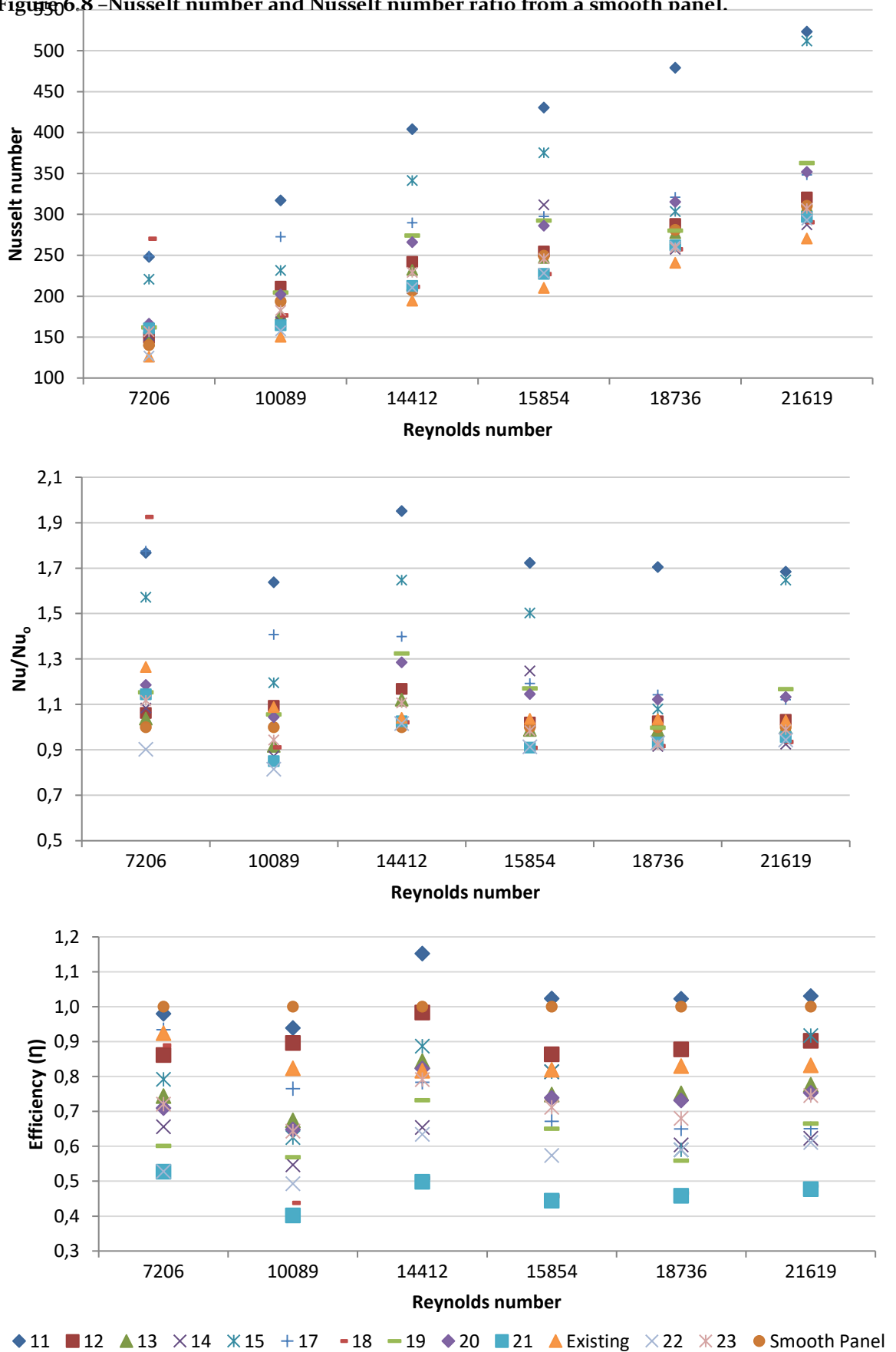
As Shape 11 was the most effective in terms of heat transfer and pressure drop, the same gap distance and surface geometry was used to generate 9 more cases (Shapes 24 to 32) by varying panel thickness, spacing between panels and total of panels per module, with results presented in Figure 6.9.

Figure 6.9 shows that shape 29 had the worst performance when compared to other shapes. Conversely, shapes 26, 11 and 24 have the best performance at any Reynolds number, evaluated by showing an average increase of 2.2 times for shape 26, 2.02 for shape 11 and 2.03 for shape 24 for Reynolds between 7,200 and 22,000 when compared to the existing panel. This increase allows a fast response by the PCM-Air heat exchanger when the heat load increases suddenly. Furthermore, when no air is crossing the thermal batteries, shapes 26 and 11 lose less energy through free convection due to a lower surface area when compared to the existing panel.

When the Nusselt number is compared to a smooth surface (Nu/Nu_o), shapes 24, 26 and 11 present the best results, showing an average increase of 2, 1.8 and 1.75 as it can be seen in Figure 6.9 where the ratio is shown for all cases. The inclusion of ridges favoured heat transfer by the increase of turbulence at lower Reynolds number, allowing a reduction in PCM-Air heat exchanger airflow, saving energy and reducing noise. The result also shows that the existing panel performs better than a smooth surface only at low Reynolds numbers (1.27 and 1.09 for 7,200 and 10,089 respectively). For Reynolds numbers above 10,089, the existing panel have a performance similar to a smooth panel as Nu/Nu_o is lower or equal to 1.

Figure 6.9 also shows that the efficiency of shapes 11, 24, 25, 27, 28 and 30 have values above 1; this means that the inclusion of ridges enhanced the heat transfer at a lower cost in terms of pressure drop when compared to a smooth surface. Values below 1 mean that the pressure drop increases in a proportion higher than the Nusselt number, leading to an increase in noise and energy cost with a small benefit on heat transfer. Shape 26 has the best performance in terms of Nusselt number but the higher pressure drop lowers its efficiency (0.86 on average).
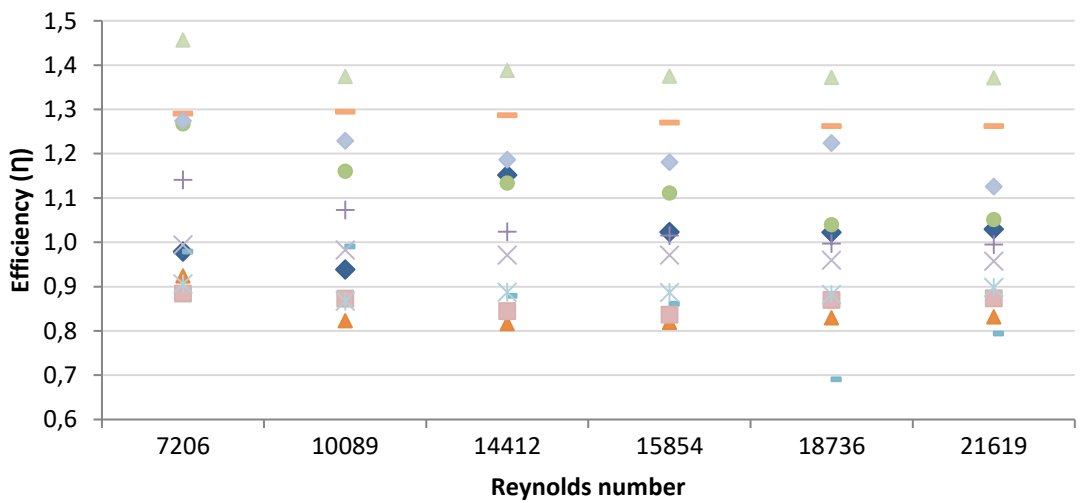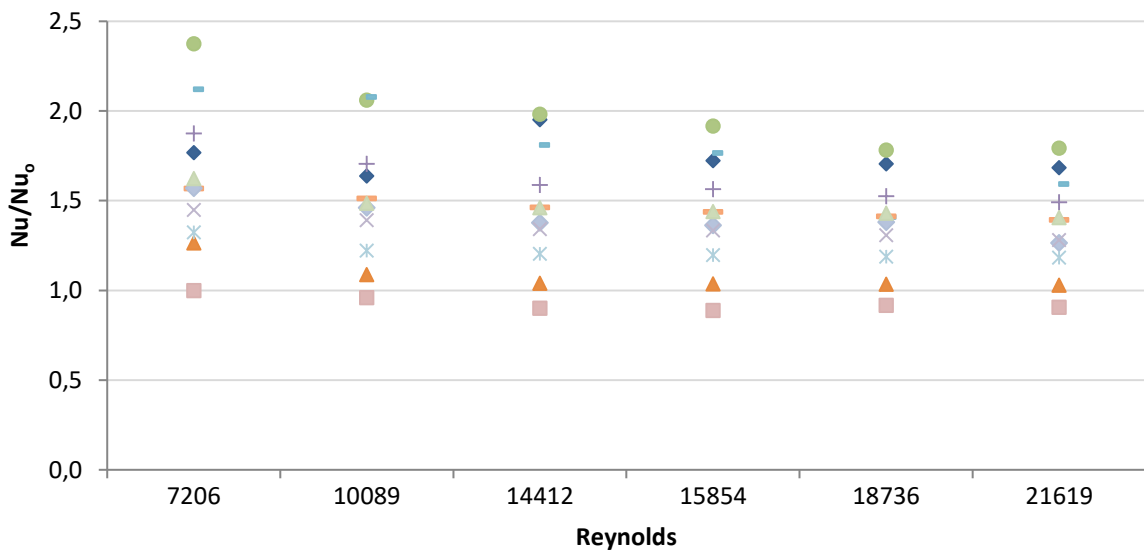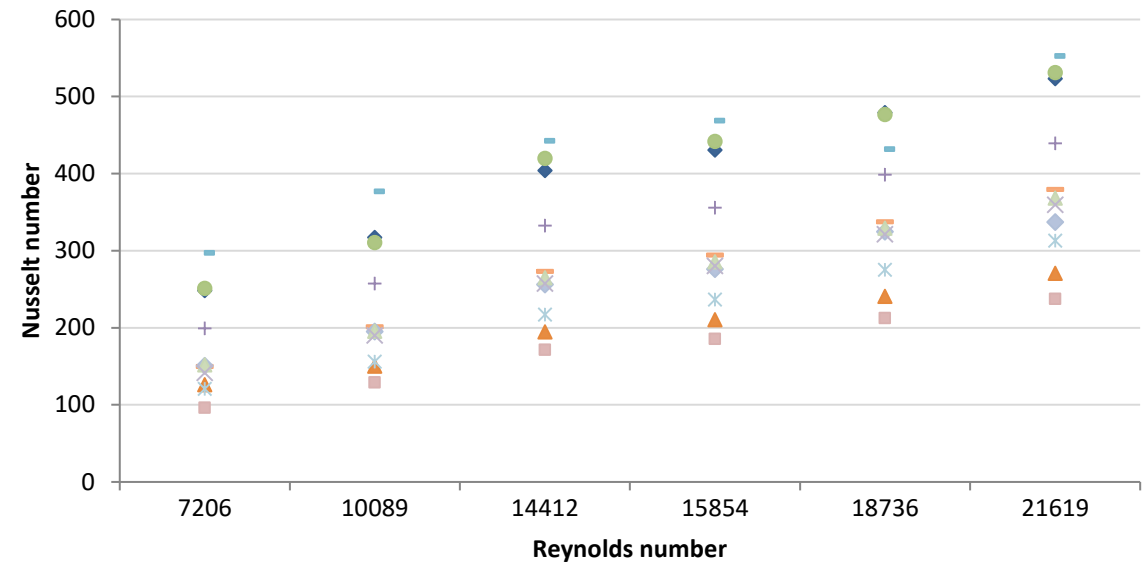
Figure 6.9 – Ratio between the Nusselt number and a smooth panel and Nusselt number for refined panels

When the volume of PCM held per thermal battery is analysed (Table 6.5), it can be seen that shape 26 holds 20.51 % more PCM per TB when compared to the existing panel while shapes 11 and 24 are able to hold 13.68 and 0.08 % more, respectively.

Table 6.5 – Volume change in comparison with existing panel

	11	24	25	26	27	28	29	30	31	32
Volume Change (in %)	13.68	0.08	2.63	20.51	-2.56	-2.56	-2.56	-2.56	3.93	2.31
Panels per module	7	9	8	6	6	6	5	4	8	9

Table 6.5 also shows that shapes 27, 28, 29 and 30 reduce PCM volume even if different amounts of panels per module are used due to the increase in panel thickness. Conversely, shape 26 has the highest increase in volume but the higher pressure drop (323.34 Pa at *Re* = 18,736), which makes shape 11 the most suitable in terms of increase in volume change, pressure drop and heat transfer. Furthermore, due to the increase in energy transfer, less airflow is required over the panels and, consequently, less electric energy is demanded.

6.2.3 Panel selection

To ensure that a small fan can provide the required airflow for the selected shapes, the pressure drop of the panels against the fan head curve was plotted. As it can be seen in Figure 6.10, the air handling unit can provide sufficient pressure at the required airflow to overcome this drop for shapes 11, 24 and 25.
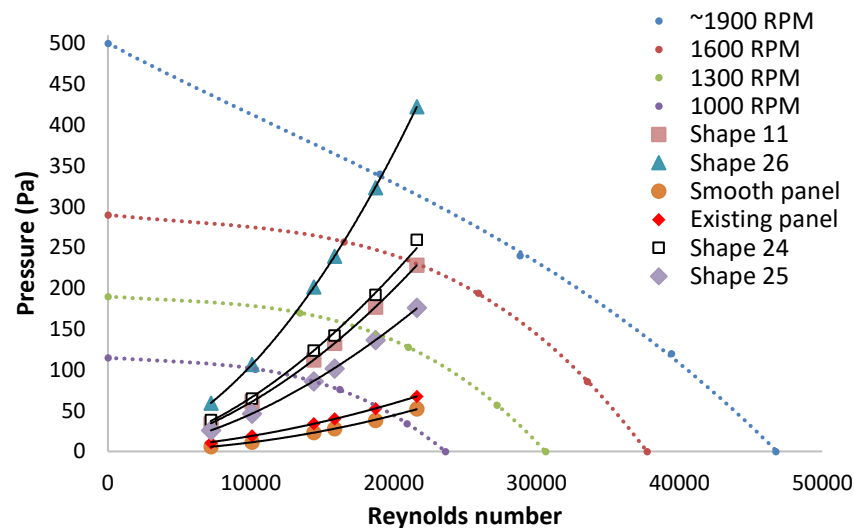
Figure 6.10 – Head curve of panels 11, 24, 25, 26 as well as the smooth and the existing panel with fan curves at different rotation speeds.

Based on the ease to manufacture, cost of production, increase in heat transfer and volume of PCM per panel, Shape 11 ($e/h = 0.219, s/l = 0.044, r = 0.0025\ m, E/H = 0.296, w_r/w = 0.867, T_t/H = 0.101, p = 7$) was chosen to be fabricated. Figure 6.11

shows the existing and fabricated new panel with dimensions being presented in Figure 6.12.
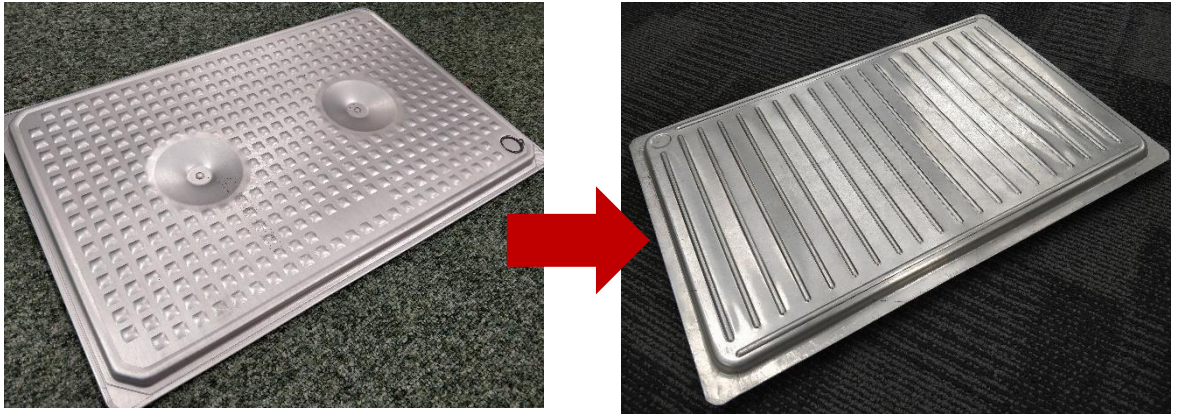
Figure 6.11 – Existing and new panel
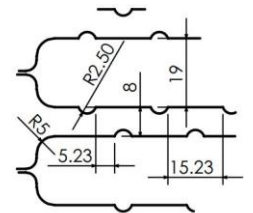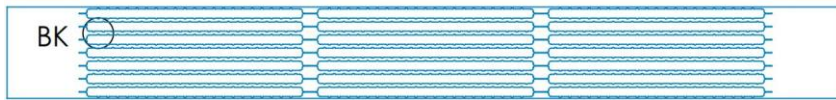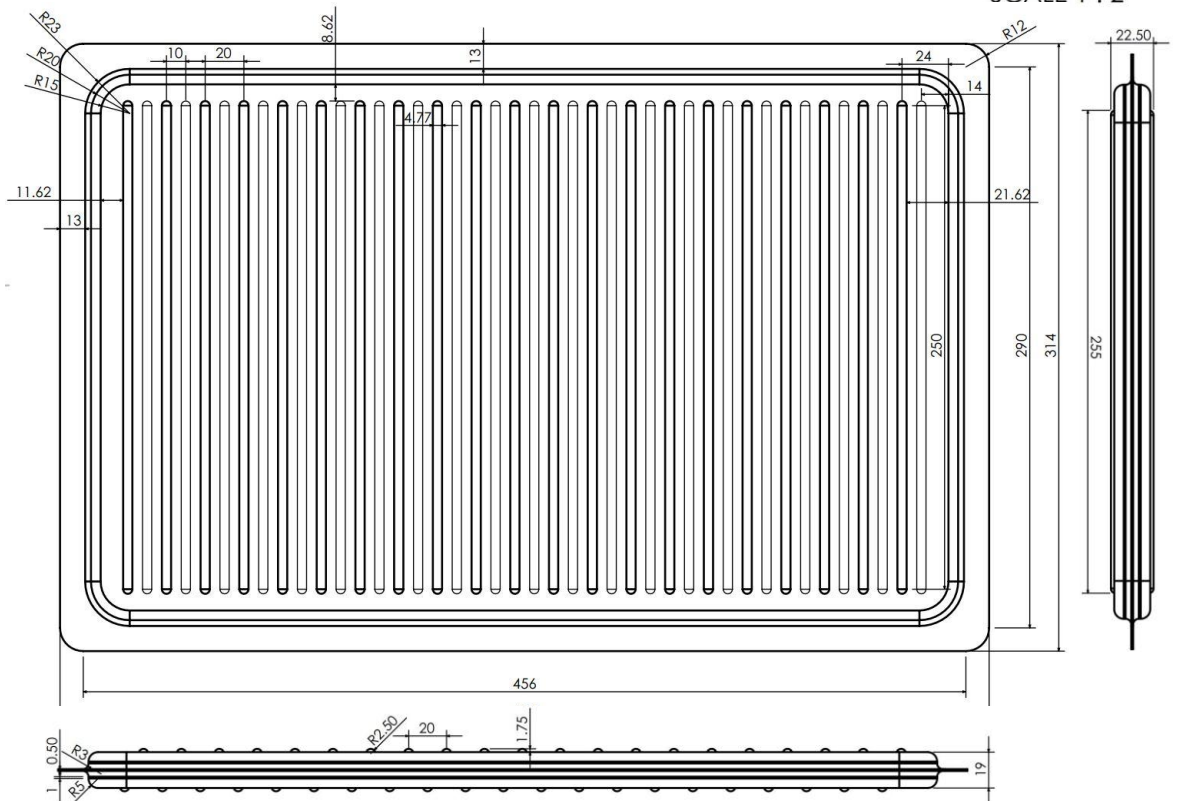
6.3 Chapter's summary

This chapter presented the improvements of the MVS by (a) presenting a more realistic system control in IESVE plug-in, (b) modifying the airflow set points in the plug-in in order to improve MVS performance and (c) designing a new encapsulation panel.

A parametric analysis was carried out to investigate possible improvements in performance. An optimised control strategy found through simulations indicated that an increase in air flow will keep internal temperatures more frequently within the set-point range without compromising thermal comfort and indoor air quality with a small penalty in electricity increase. The analysis indicated that changes in the control strategy improve the performance of the system. However, this is limited by the cooling capacity of the PCM. One solution is to increase the PCM material but this will result in a larger space requirement. Another solution is to increase the heat transfer rate of the existing configuration. This was achieved by proposing a new encapsulation design where the air-side heat exchange for a set of 32 different geometries were analysed via CFD.

Focusing on the ease to manufacture, cost of production, increase in heat transfer and volume of PCM per panel, one shape (shape 11, Figure 6.11 (right)) was selected which doubles the heat transfer and holds 13.7 % more PCM material when compared to the existing panel. The pressure drop increased 3.3 times but a 200 W fan is capable to provide the required airflow. However, heat transfer increase may require less airflow for the same cooling demand.

Based on that, shape 11 was selected to be manufactured and the experiments in chapter 7 will validate its performance.

CHAPTER 7 - LABORATORY RESULTS

Introduction to the chapter

This chapter presents the laboratory tests' results of the fabricated panel and comparison with the existing panel. Three tests were carried out as described in Chapter 3.

7.1 First laboratory test: Investigation of heat transfer of one panel with different gaps between panels

7.1.1 Test rig validation

Section 3.5.1 presented the reasons why the test rig with thermocouples was selected. To validate the rig, Gnielinski's correlation (Eq. (3.8)) for a smooth panel was used. Gnielinski's equation was used instead of Dittus-Boelter due to the range of Reynolds number ($3000 \leq Re \leq 5000$) and Prandtl (0.707) performed in this laboratory test. Gnielinski's correlation is applicable for $3 \times 10^3 \leq Re \leq 5 \times 10^6$ and $0.5 \leq Pr \leq 2000$ while Dittus-Boelter requires a minimum Reynolds number of 10,000.

Gnielinski's correlation presented a good estimation when compared to experiments (see Table 7.1). Only when Re=3054, a considerable difference of -19.09 % was found. However, this can be explained because the Reynolds number is close to the edge of Gnielinski's correlation (Re=3000). In addition, this percentage is reduced when the Nusselt number uncertainty of 5.6 % (as show in Table 3.19) is considered.

Table 7.1 – Experiment Nusselt numbers for a flat panel for each gap tested and values found through Gnielinski's Correlation with the respective difference in percentage

Reynolds number	3054	3165	3276	4580	4748	4914
Panel gap	8 mm	9 mm	10 mm	8 mm	9 mm	10 mm
Experiment Nusselt Number	13.4	16.2	16.8	19,5	21,7	20,8
Correlation Nusselt Number	16.54	16.93	17.31	21.21	21.72	22.23
Difference	-19.09 %	-4.13 %	-3.15 %	-8.25 %	-0.02 %	-6.40 %

With results validated, it is now possible to test the existing and the new panel with confidence. Note that the smooth panel results were also used to estimate the Thermal Enhancement Factor (TEF).

This first laboratory test was aimed to compare the heat transfer efficiency between the existing and the new panel at three different gaps (8, 9 and 10 mm) and air velocities (0.5, 1.0 and 1.5 m/s). The different gaps alter the inlet area and as a consequence, the Reynolds number for the same air velocity. To facilitate the result

discussion, the Reynolds number is averaged. In this case 0.5 m/s refers $Re = 1954$, 1.0 m/s to $Re = 4067$ and 1.5 m/s to $Re = 6061$.

To ensure consistency within results, the experiment was repeated two times at 0.5 and 1.5 m/s (or $Re = 1954$ and 6061) with the results presented in Figure 7.1. The thermocouples attached on the surface of the panels have their temperature averaged and are presented in the figure as bottom average and top average. After achieving stable conditions, the temperature difference between inlet and outlet from both cases were taken by averaging more than 1h of data. The results show consistency where a difference of 0.11 ºC (or 3.32 %) for 0.5 m/s test and 0.04 ºC (or 1.87 %) for 1.5 m/s test was found. A reasonable result considering the uncertainty of 0.51 % (Table 3.19)

Figure 7.1 – Repeatability test for 0.5 (above) and 1.5 m/s (bottom) with existing panel 10mm gap
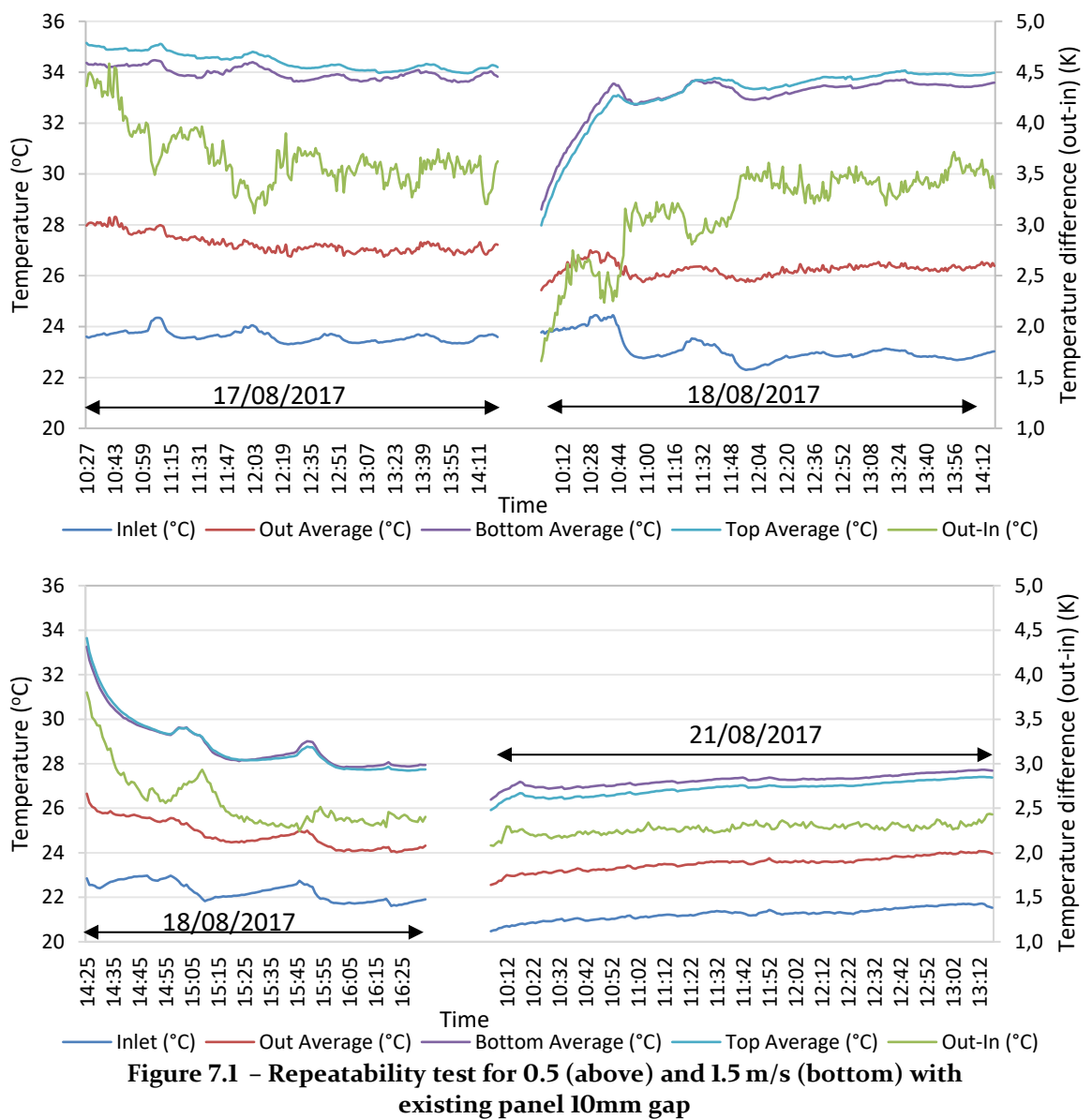
Figure 7.2 shows one day of test (29/08/2017) with all thermocouples per minute. Fluctuations during the test were mainly caused by inlet temperature instability and turbulent outlet airflow.
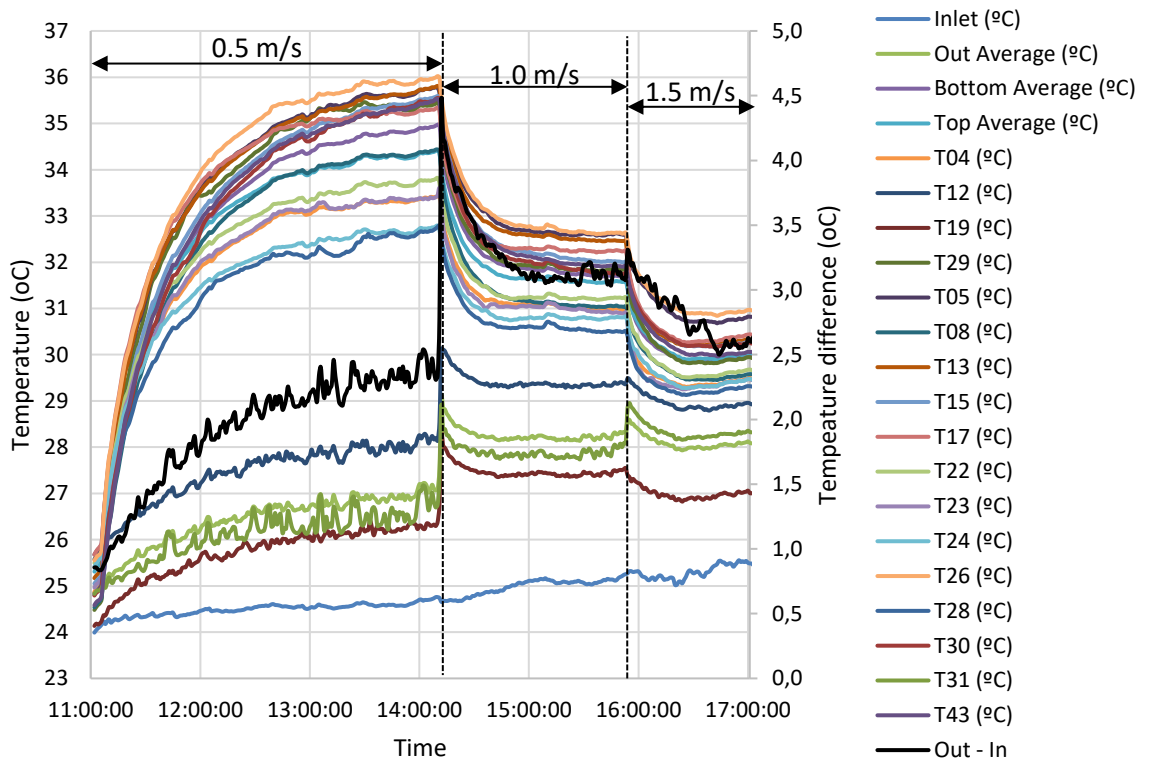
Figure 7.2 – Panel test for the new panel, 10mm gap

The panel surface temperature measurement was needed to ensure stable conditions. The temperature difference between inlet and outlet confirms that energy was transferred from the panels to the air. After the system achieved stable conditions, outlet and surface temperature remained stable if the inlet temperature remained constant. The results of all experiments can be seen in Figure 7.3 where top and bottom panel surface temperatures, inlet, outlet average and the difference between outlet and inlet are presented. As it can be seen, each test ceased when the air temperature difference between outlet and inlet were stable (±0.25 °C) for at least 30 min. They are indicated by blue arrows.
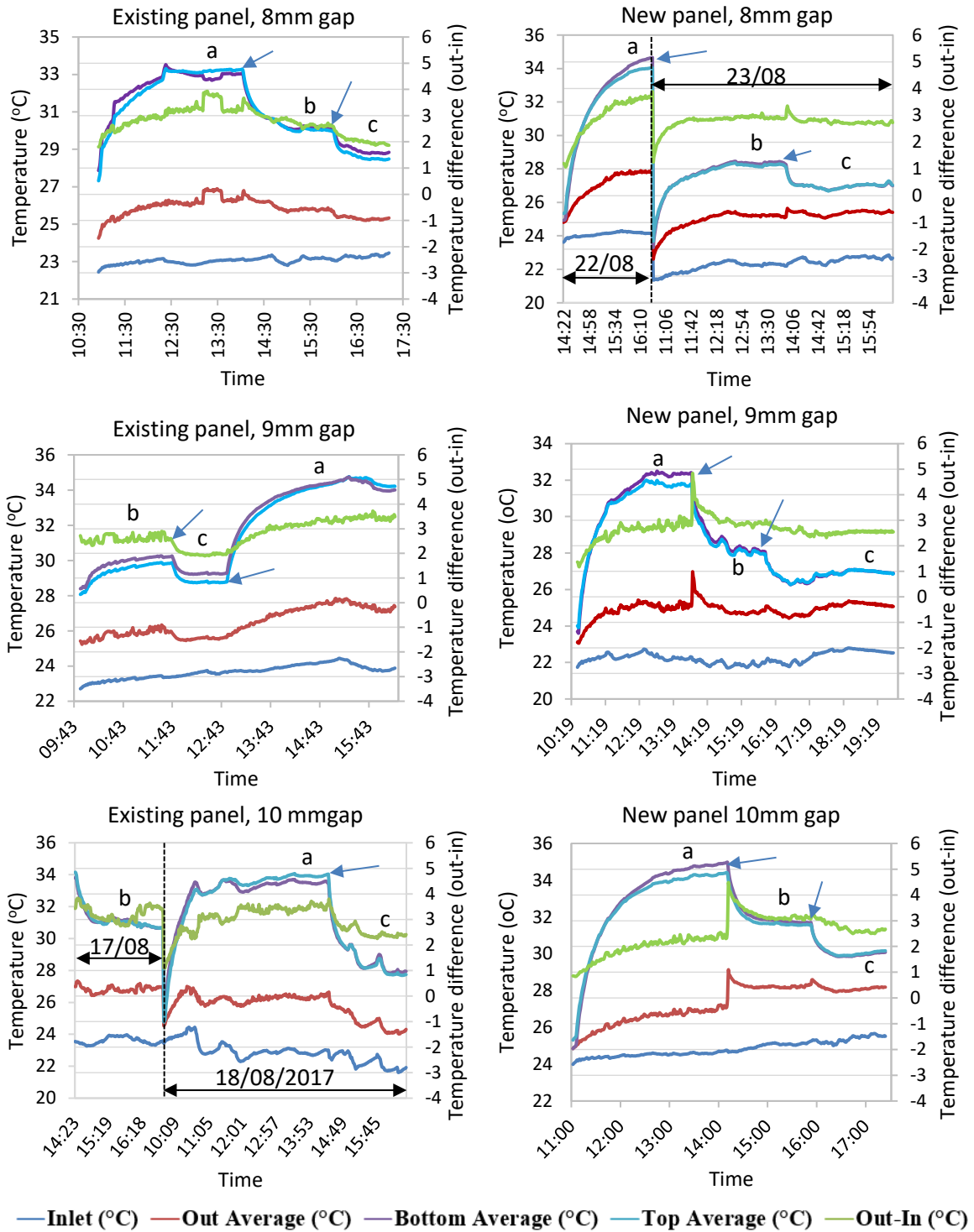
Figure 7.3 – Tests performed for 8, 9 and 10mm gap for existing and new panel at different airspeeds ((a) 0.5 m/s, (b) 1.0 m/s and (c) 1.5 m/s).

7.1.2 Temperature and Nusselt number analysis

The inclusion of ridges in the new panel increased, when compared to the existing panel, the Nusselt number. This can be seen in Figure 7.4 where the temperature difference between inlet and outlet is presented. With 8mm gap, the new panel had the highest temperature difference ($T_{out} - T_{in}$ = 3.64 K), 7 % more than the existing panel (Figure 7.5). Figure 7.4 and Figure 7.5 also shows that the new panel performs worse than the existing panel at lower Reynold numbers and high panel gaps (-9 % and -34 % respectively for 9 and 10mm gap). Conversely, the increase in the Reynolds number shows the benefit of the new panel design reaching the maximum of 38 % for an 8mm gap.
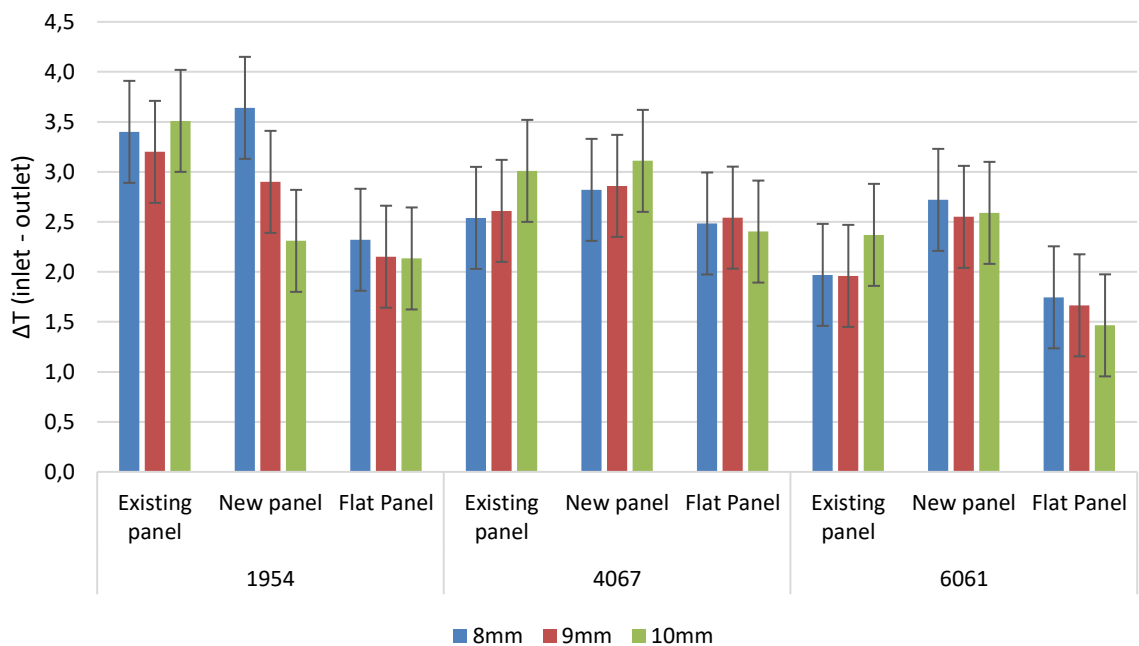
Figure 7.4 – Temperature difference (Outlet – Inlet) at three different Reynold numbers and three gaps for existing and new panel and the uncertainty of ± 0.56 ºC.
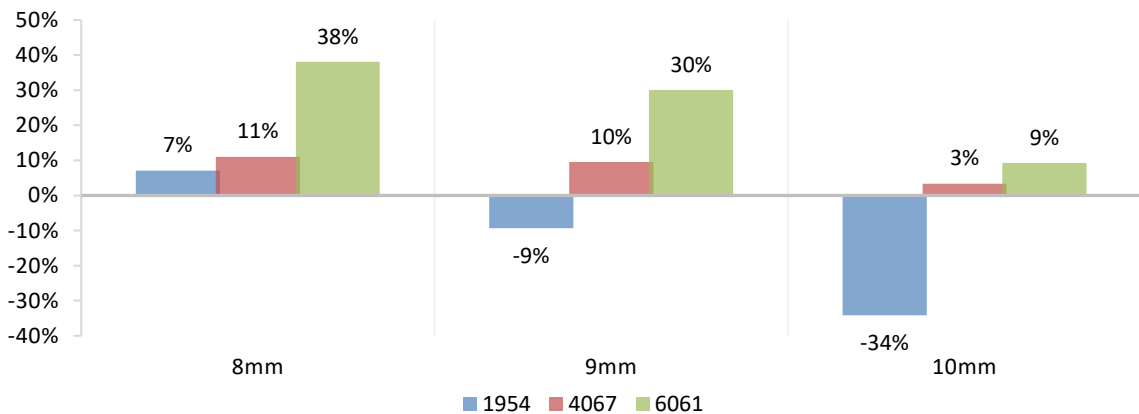
Figure 7.5 – Percentage of temperature difference between new and existing panel for a Reynolds number of 1954, 4067 and 6061.

When heat transfer is analysed, the Nusselt number should be used. As the resistance wire provide a uniform heat flux along its length, the method of the differences was used to calculate the coefficient of convection presented in the literature review (2.6.1). Thus, the coefficient of convection was used to evaluate the Nusselt number. During the experiment, air temperature had an average of 299.4 (±2.0) K and air properties were assumed constant and equal to 300K.

As observed through the ΔT difference (Figure 7.4) at low Reynold numbers, the new panel performed better than the existing panel only at 8 mm gap (Table 7.2).

Table 7.2 – Nusselt number improvement from existing to new panel

Reynolds Number	8 mm gap	9mm gap	10 mm gap
1954	20 %	-5 %	-26 %
4067	94 %	36 %	5 %
6061	124 %	72 %	77 %

Conversely, at higher Reynolds numbers (Re=4067 and 6061), the new panel increased the heat transfer at significant values for 8 and 9 mm gap. For 10 mm gap, the same happens only when the Nusselt number was equal to Re=6061 where high airflows are needed to generate attachments and detachments on the panel surface.

For Re=6061 (airflow used during PCM-Air heat exchanger charging period), 8 mm gap increased the heat transfer by 124 %. This is important to notice as the charging period occurs during a short period of time and the heat transfer needs to be as efficient as possible. When Nusselt number between the new and the existing panel is compared, 8 mm gap was shown to be the most effective.

When the gaps between the new panel are compared, 10mm gap turns the most effective at Re=6061. The values can be seen in Figure 7.6 and the percentages in Table 7.3. Higher rates of heat transfer are important to ensure fast charge and response. The gap of 10mm will also lead to a smaller pressure drop and noise. However, fewer panels can be fitted in the thermal battery as its dimensions are limited. At low Reynolds number, the opposite occurs: 8 mm gap turns the most effective. This is probably due to the attachments and detachments of the boundary layer, which is easier for small for low airflows and gaps.

Table 7.3 – Nusselt number increase between gaps of the new panel (NP: new panel)

Reynolds Number	NP 10mm / NP 8mm	NP 10mm / NP 9mm	NP 9mm / NP 8mm
1954	-22 %	-11 %	-12 %
4067	-9 %	21 %	-25 %
6061	15 %	11 %	3 %
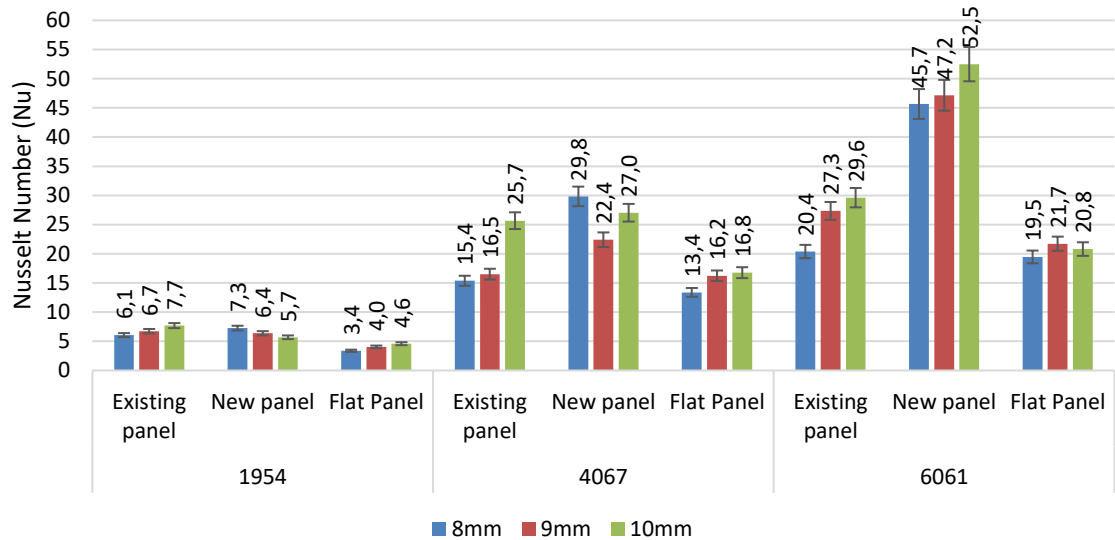
Figure 7.6 – Nusselt number for existing, new and flat panels with error bar showing the uncertainty of 5.6 %.

Figure 7.6 also shows the Nusselt number for the flat panel. At Re= 4067 and 6061 for 9 and 10mm gap, the existing panel performs similar to the flat panel and shows inefficiency in terms of heat transfer. This increases the charging period, reduce chances to fully charge the thermal battery as well as require a lower outdoor temperature during the charging period when compared to the new panel. This information can also be found in Figure 7.7 where the Nusselt number ratio (Nu/Nu_o) is presented. From this figure, it can be seen that the performance is similar at any gap when Re=6061 and the ratio remain the same for 8 and 9mm. At Re=1954, gaps of 9 and 10mm perform worse than the existing panel.
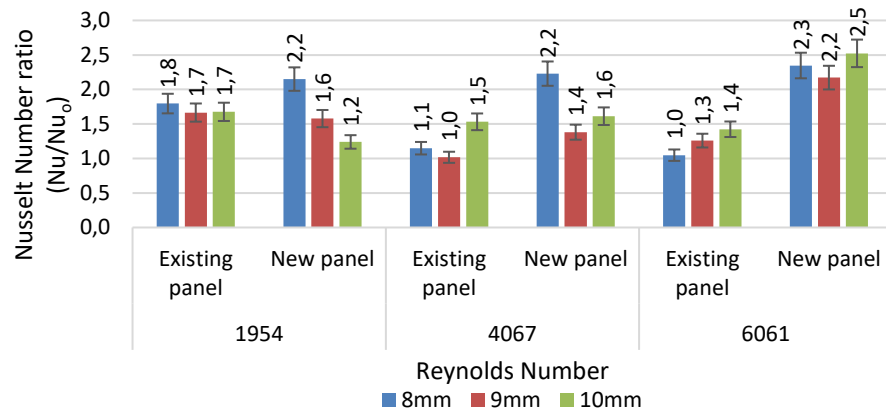
Figure 7.7 – Nusselt number ratio between existing and new panel with flat panel with error bar showing the uncertainty of 7.9 %.

7.1.3 Pressure drop analysis

When improvements in heat transfer are caused by turbulators, the pressure drop increase due to restrictions in the flow area. In the case of a PCM-Air heat exchanger, a high-pressure drop leads to an oversized fan and an increase of noise. Commercial PCM-Air heat exchanger is primarily installed in offices and schools where noise is an important factor for a cooling equipment. This could be overcome by noise insulation improvement but this will lead to an increase in cost. Thus, a compromising between heat transfer and pressure drop needs attention and this was achieved by estimating the efficiency and pressure drop ratio between panel and flat panel. Figure 7.8 presents the pressure drop for the existing, new and flat panel for 8, 9 and 10mm gap.

	Flat Panel	Existing panel	New Panel	Flat panel	Existing panel	New panel	Flat Panel	Existing panel	New panel
		1954			4067			6061	
8mm	2,1	1,9	9,9	2,75	10,4	16,4	22,6	24,6	44,1
9mm	1,9	1,9	7,6	2,5	8,5	11,7	18,3	20,6	32
10mm	1,5	1,45	6,50	1,7	7,05	10,9	16,30	17,7	29,3
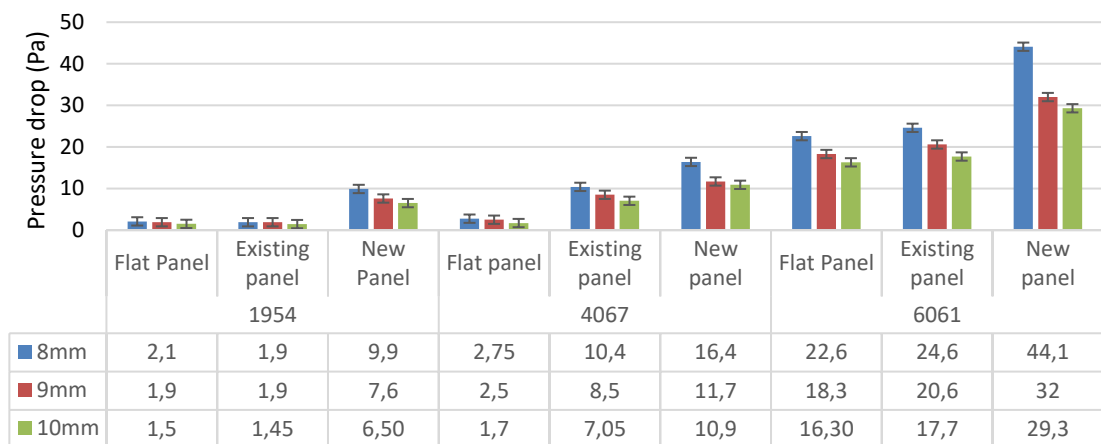
Figure 7.8 – Panel pressure drop at different Reynolds number and three gaps for existing, new and flat panel with error bar showing the uncertainty ± 1 Pa.

At low Reynolds number (Re=1954), the pressure drop increase varies from 0.85 to 0.25 Pa, representing 45 to 17 % (Table 7.4). As it can be seen, the gap increase results in a lower pressure drop compared to the existing panel. Due to a higher restriction, 8 mm gap presented the highest pressure drop compared with the existing panel and

equivalent of 45, 58 and 79 % for Reynolds numbers of 1954, 4067 and 6061, respectively.

Pressure drop is also notable when the new panel with 9mm gap is compared with the existing panel with 8mm gap. As presented in Table 7.4, a maximum increase of 32 % was found. The new panel also present a pressure drop increase at Reynolds 4067 and 6061 (5 and 19 % respectively). This analysis presents the influence of ridges in the pressure drop but also the increase between gaps where a maximum of 40 % and 62 % were found respectively when the pressure drop with a gap of 8 mm is compared with 9 and 10mm respectively.

Table 7.4 – Pressure drop increase

Average Reynolds number	NP 8mm EP 8mm	NP 9mm EP 9mm	NP 10mm EP 10mm	NP 9mm EP 8mm	NP 10mm EP 8mm	NP 8mm NP 9mm	NP 8mm NP 10mm
1954	45 %	32 %	17 %	32 %	-11 %	10 %	62 %
4067	58 %	38 %	55 %	13 %	5 %	40 %	50 %
6061	79 %	55 %	66 %	30 %	19 %	38 %	51 %

The pressure drop is also compared with the flat panel tested and the results are presented in Table 7.5. It can be seen the increase in the ratio for both existing and new panel when the Reynolds number increase for each gap. The difference between the existing and the flat panel has an increase averaged of 7 % with the maximum of 13 % (Re=6061) showing that the existing surface behaves similarly to a flat panel. When the new panel is compared with the flat panel, an increase of average in 60 % was found with a maximum of 95 % at 4067 and 8mm gap.

Table 7.5 – Pressure drop increase of existing and new panel against flat panel

Average Reynolds number	Existing /Flat panel			New / Flat Panel		
	8 mm gap	9mm gap	10 mm gap	8 mm gap	9mm gap	10 mm gap
1954	0.0 %	0.0 %	3.6 %	44.7 %	38.9 %	21.4 %
4067	5.1 %	11.8 %	8.5 %	65.7 %	53.9 %	67.7 %
6061	8.8 %	12.6 %	8.6 %	95.1 %	74.9 %	79.8 %

7.1.4 Thermal Enhancement Factor (TEF)

The pressure drop increase presented in the previous section was expected due to the introduction of ridges. However, to evaluate if the pressure drop increases effectively or in other words, if the pressure drop increased in a lower rate than the heat transfer, both existing and new panel were compared with the flat panel using Eq. (2.19). These results are presented in Figure 7.9. As it can be seen, the new panel with 8mm gap

presented the best performance with a TEF higher above 1.8 for the three Reynolds numbers tested and have an average of 1.89.

At low Reynolds number, (Re=1954) the existing panel performed better than at higher airflows (Re=4067 and 6061). However, the higher TEF is not higher than the new panel with 8 mm gap. The effectiveness of the new panel is exposed more clearly according to the increase of the Reynolds number while the existing panel reduces to an average of 1.20.
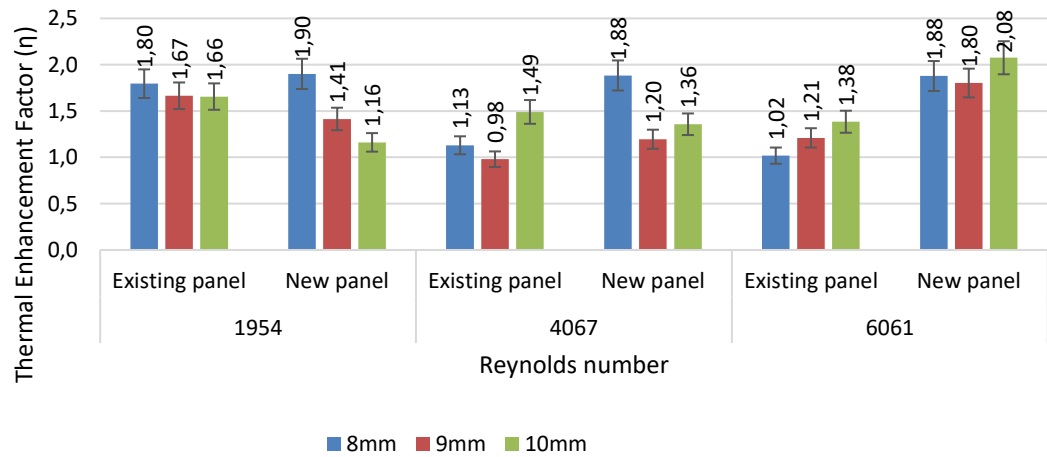
Figure 7.9 – Thermal Enhancement Factor of the existing and new panel with error bar showing the uncertainty of 8.6 %.

It is interesting to notice that the existing panel has a lower TEF (1.08 on average) when Re= 4067 and 6061 at 8 and 9mm gap. This result indicates the inefficiency of the existing panel at higher airflows where the introduction of bulges in the flat panel results in an increase of heat transfer at the same cost of an increase in pressure drop.

Conversely, the highest TEF was found at Re=6061 with 10mm gap and represented an increase of 49.9 % when compared to the existing panel (Table 7.6). This table also shows that the highest increase in percentile when compared to the existing panel occurred at 8mm gap and Re=6061 and represented an increase of 84.4 %. Furthermore, Table 7.6 also shows that improvements at any Reynolds number was found with a gap of 8mm.

Table 7.6 – Percentile increase in TEF from the existing to the new panel

Averaged Reynolds number	8 mm	9 mm	10 mm
1954	5.9 %	-15.1 %	-29.8 %
4067	66.7 %	22.0 %	-8.9 %
6061	84.4 %	48.9 %	49.9 %

As a result, after heat transfer, pressure drop and TEF analysis, the new panel with a gap of 8mm presented the best choice as it has the highest TEF on average (1.88) and the highest increase in heat transfer (20, 94 and 124 % respectively for Re=1954, 4067 and 6061). The increase in pressure drop was expected due to ridges inclusions and corresponded to 44.7, 65.7, and 95.1 % respectively for Re=1954, 4067 and 6061.

7.2 Second laboratory test: Investigation of pressure drop for 1, 2 and 3 thermal batteries

The design process presented in chapter 6 highlighted the importance of the pressure drop on the PCM-Air heat exchangers and the design selection considered the capability of the existing fan to provide the necessary airflow when the new panels are stacked in one, two or three thermal batteries (TB). With panels manufactured and its efficiency in terms of heat transfer proven in section 7.1, this section assesses the pressure drop to evaluate the capacity of the fan to provide the required airflow.

The test was carried out to analyse the pressure drop of one, two and three thermal batteries for the existing and new panel. The experimental procedure is presented in the section 3.5.2 and the results are presented below (Figure 7.10)
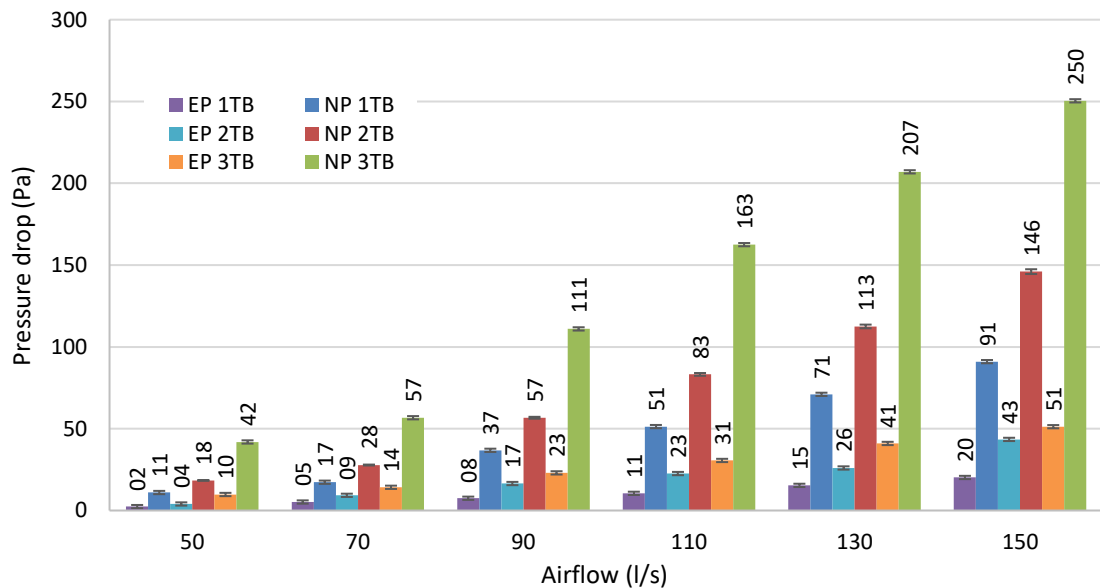
Figure 7.10 – Thermal battery pressure drop test for existing panel (EP) and new panel (NP) with error bar showing the uncertainty of ±1 Pa.

The results show a considerable increase in pressure drop. Table 7.7 shows an average increase of 345, 258 and 380 % when the pressure drop of the new and existing thermal batteries are compared. However, the higher heat transfer of the new panel will reduce the MVS operation time at higher airflows.

Table 7.7 – Pressure drop increase between existing and New thermal batteries

	Pressure drop increase		
Airflow	1 TB	2 TB	3 TB
50	230 %	200 %	300 %
70	390 %	240 %	380 %
90	390 %	270 %	430 %
110	360 %	330 %	410 %
130	350 %	240 %	390 %
150	350 %	270 %	370 %
Average	345 %	258 %	380 %

The results can also be seen in Figure 7.11 where the head curve of the fan is plotted with the results obtained from the laboratory tests and the simulations of shape 11, 24 and 26. Figure 7.11 shows that the fan is capable to provide the airflow required when one, two or three thermal batteries are used.
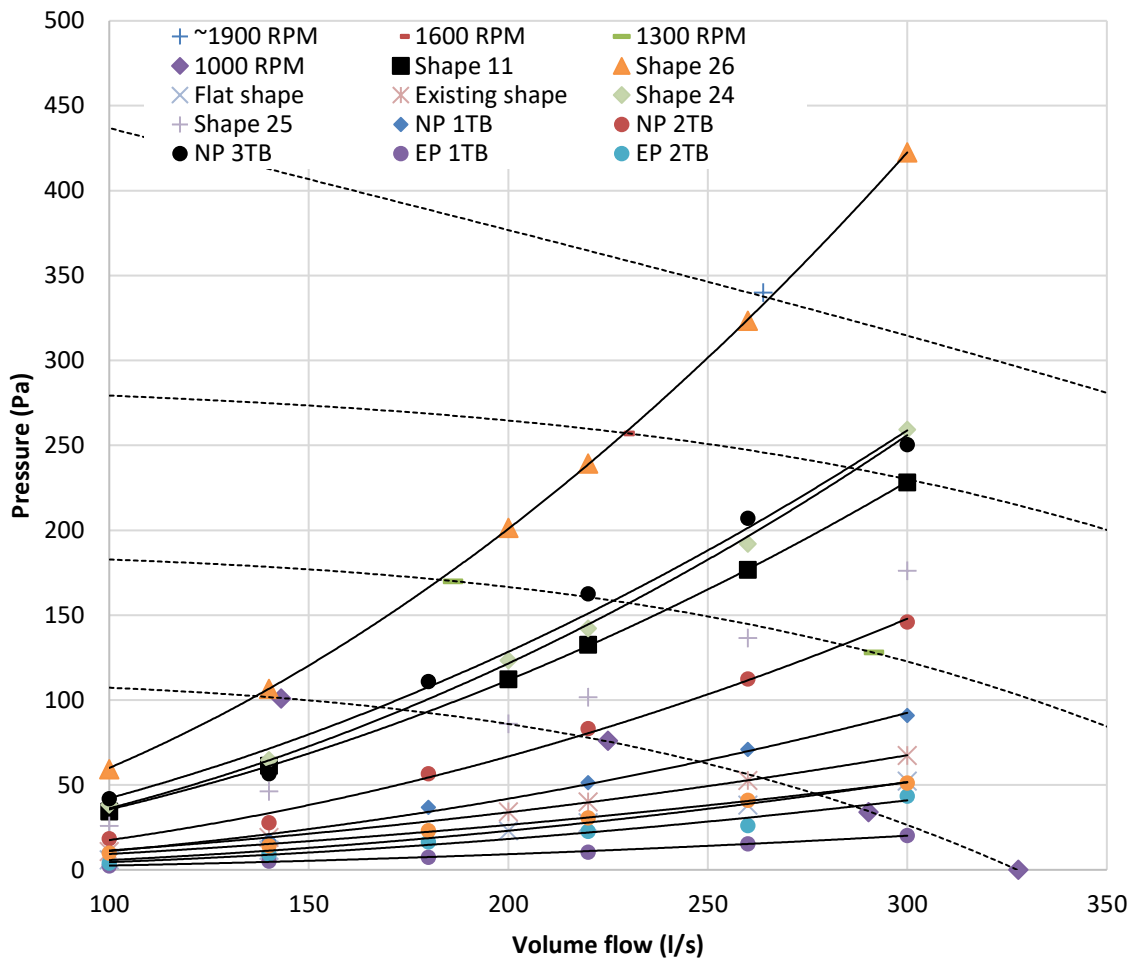
Figure 7.11 – Melting and solidifying temperature for existing and new panel with two thermal battery.

When the results of the design process are compared with the laboratory tests, reasonable agreement is found, considering that assumptions were made during the design process and possible errors obtained during the experiment such as air leakage, reading errors and even the differences between the actual model and the one designed during the manufacturing process. As it can be seen from Table 7.8, an average difference of 14 Pa (± 14.15 Pa) pressure drop between the laboratory tests and in the design process was found. In percentage, this represents an average of 10.5 % (± 11.4 %). A good result according to Zhang et al. (Zhang et al., 2007).

Table 7.8 – Pressure drop increase between existing and New thermal batteries

Airflow (l/s)	Shape 11	NP 3TB	% (experiment/design)	Difference (Pa)
100	34.31	41.9	22.1 %	7.6
140	61.28	56.7	-7.5 %	-4.6
180	112.27	111.0	-1.1 %	-1.3
220	132.60	162.5	22.6 %	29.9
260	176.80	207.0	17.1 %	30.2
300	228.24	250.4	9.7 %	22.2
Average			10.5 %	14.00
Standard Deviation (σ)			± 11.4 %	± 14.15

7.3 Third laboratory test: Melting and solidifying analysis between the existing and new panel

With the laboratory procedure described in chapter 3, the third test is intended to analyse the thermal load and response of the existing and new panel as well as the charging and discharging time for one, two and three TB. However, the test for the third TB was not possible. This was due to the climate conditions as the charging period uses outside air and the test of the third TB reached the summer period. To overcome this, a heat pump was used in conjunction with an air conditioner unit. Even though, the system was not able to provide a stable temperature of 15 °C. The laboratory test with one and two thermal battery was well performed with results being compared with the laboratory tests (3LC) provided by the PCM manufacturer and presented in Appendix VII.

7.3.1 Charging and discharging time

Figure 7.12 presents the results for one thermal battery; more time is needed to charge and discharge the new TB. This is due to the capability of the new TB to hold 17.5 kg (total latent heat of 3202.5 kJ) against 13.5 kg (total latent heat of 2470.5 kJ) of the existing TB. This 30 % extra PCM made the surface temperature of the new TB solidify and melt gradually while the phase change in the existing TB (which has a thinner panel) is more pronounced. Due to that, Figure 7.12 clearly shows the onset and endset for both melting and solidifying (20-18 °C and 24-26 °C, respectively) for the existing TB. When two thermal batteries are used (Figure 7.12), a similar behaviour was found.

In terms of time required to melt and solidify, the TB is considered fully charged or discharged when the surface temperature achieve stable. Figure 7.12, it is clear that the new TB needs more time to complete the cycle and this is explained by the capacity that the new TB can hold. However, the time required to solidify is lower than the time to melt the PCM properties. This is an interesting result as the MVS needs less time to charge the TB. For one TB, 4h is necessary to solidify the existing TB while 5h30min is needed for the new TB, an increase of 38 %. For two TB, 8h30min is needed to charge the new TB and while 5h is needed for the existing TB, representing 66 % more time.
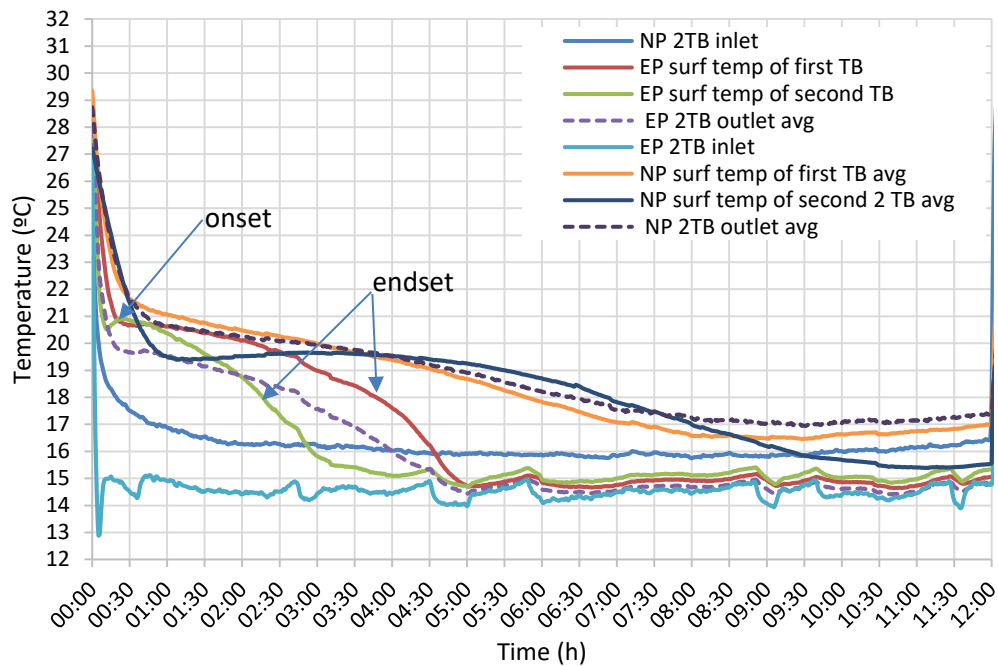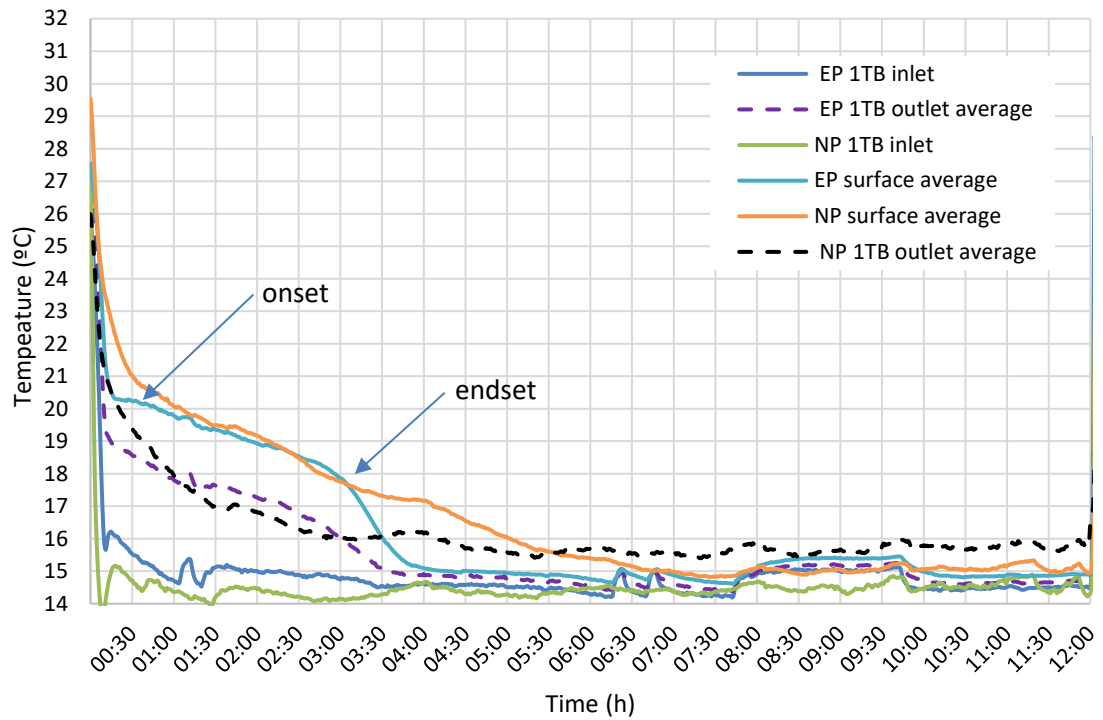
Figure 7.12 –Solidifying temperature for the existing and new panel with one and two thermal batteries.

When the discharging period is analysed, the new TB is capable to provide cooling for a longer period of time. This is explained by the additional PCM it can hold. As it can be seen in Figure 7.13, the outlet temperature gradually increases to reach the inlet temperature. For 1 TB with the existing panel, the TB is completely discharged after 3h30min while the new TB need approximately 6h30min to completely

discharge, an increase of 86 %. When a MVS with 2 TB is analysed, the existing TB is fully discharged after 4h30 min while the new TB needs the double of the time.

The first laboratory test presented in section 7.1 proved that the new panel is more efficient in terms of heat transfer than the existing panel, an important feature when a faster thermal response is needed. However, Figure 7.13 shows that the temperature for the existing and new TB increase at the same rate until the PCM starts to melt. This could be explained by number of panels the existing TB have. With two panels more when compared to the new TB, it has 28 % more surface area and reflects in an outlet temperature similar to the new TB. For the same reason, the outlet temperature during the solidifying period in Figure 7.12 shows a similar pattern.
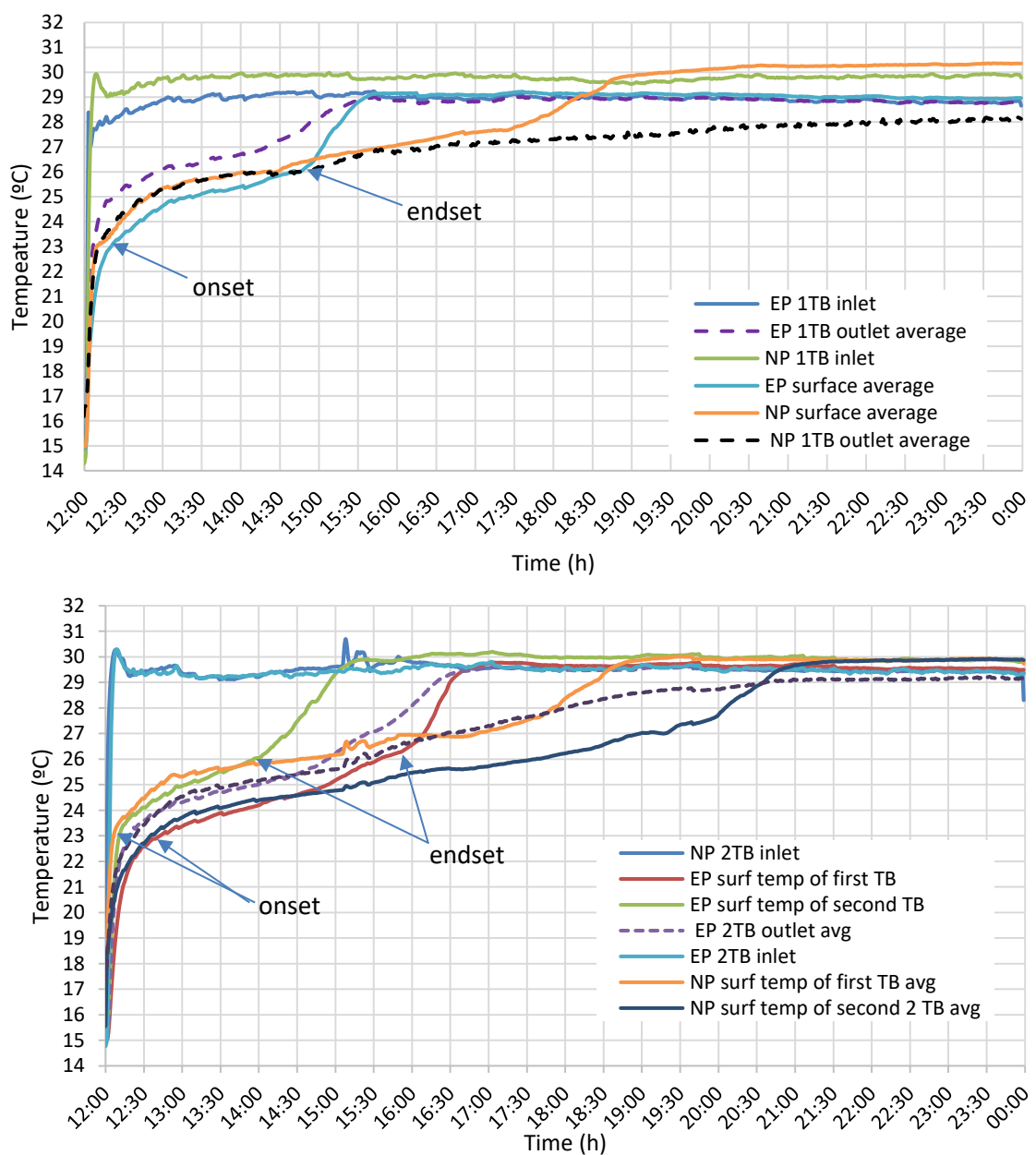
Figure 7.13 – Melting temperature for existing and new panel with one and two thermal batteries.

7.3.2 Thermal load

During the melting and solidifying process, the air was cooled down or heated up to a correspondent cooling (Q_c) or heating load (Q_h). To estimate those values, equations (3.10) and (3.11) were used. The heating and cooling cycle ceased when outlet temperature stabilise and achieve values close to the inlet temperature. These results are presented in Figure 7.14 and Figure 7.15. Interestingly, when one thermal battery is used the new panel provides a faster response when compared to the existing panel for the melting period and the opposite occurs for two TB. This is probably caused by fluctuations in temperature during the transition from charge to discharge mode and vice-versa.
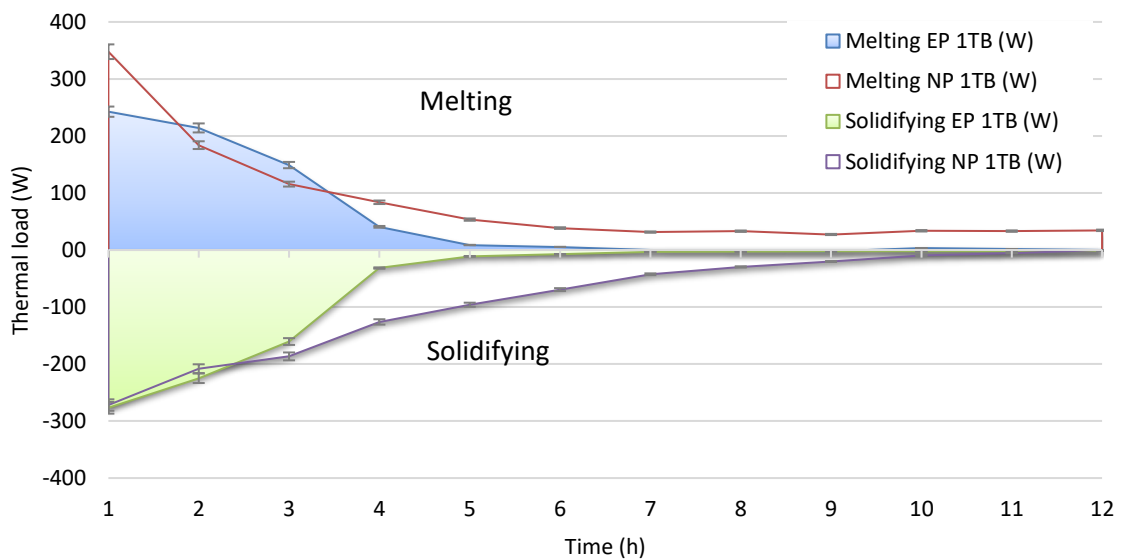
Figure 7.14 – Thermal load for existing and new panel with one thermal battery with error bar showing the uncertainty of 3.7 %.
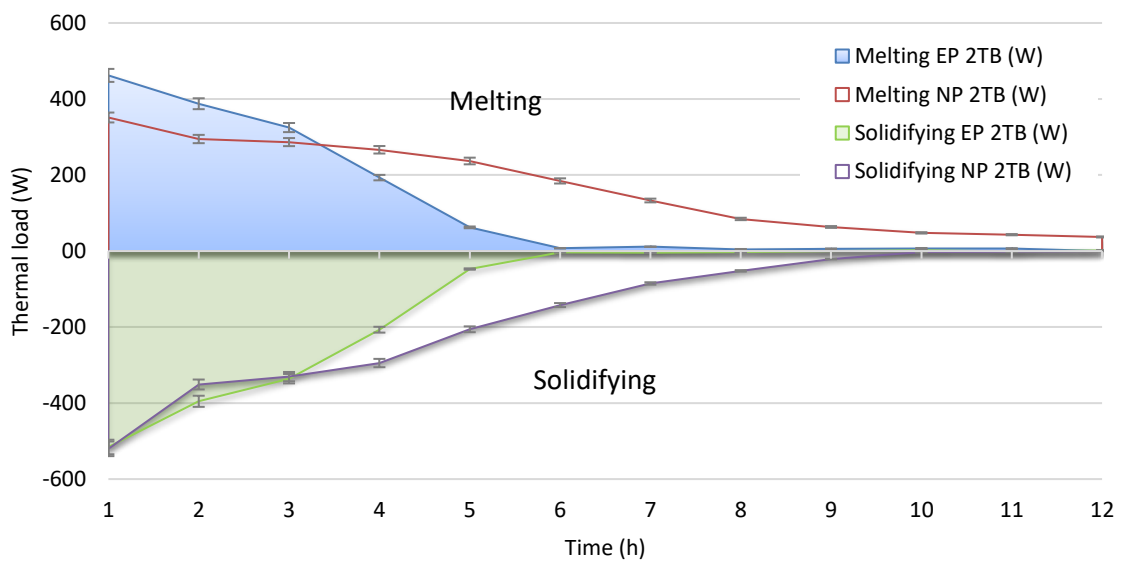
Figure 7.15 – Thermal load for existing and new panel with two thermal battery with error bar showing the uncertainty of 3.7 %.

It can be seen that after 4h for 1 TB, the TB is fully melted or solidified as a small amount of energy is released or absorbed by the TB. For the new TB, 6h30min is needed to complete the cycle and after this time, the energy released or absorbed by the TB remains stable. A similar pattern occurs with 2 TB (Figure 7.15) where more time for solidification was needed. This is explained by 8kg of extra PCM the two TB are holding, however, the extra PCM reflects in more energy stored.

The PCM used for this present study (CrodaTherm 24™) was subjected to a 3LC (three-layer-calorimeter) test in order to assess heat storage properties. The results of this test are presented in the PCM datasheet (Appendix VII). In the 3LC, the energy stored during a heat up from 15 to 30 °C and cooling from 30 to 15°C are in agreement to the laboratory tests as it can be seen in Table 7.9. The results present an average of 105.4 Wh (± 44.5 Wh) or 4.4 % (± 6.9 %).

Table 7.9 – Thermal load for melting and solidifying

| | 1 Thermal Battery | | | | 2 Thermal Batteries | | | | |
| | Melting | | Solidifying | | Melting | | Solidifying | | |
	EP	NP	EP	NP	EP	NP	EP	NP	Average (σ)
Laboratory test (Wh)	831.8	1015.8	-725.6	-1066.0	1472.3	2029.1	-1508.6	-2336.0	
3LC (Wh)	817.5	1059.7	828.8	1074.3	1635.0	2119.4	1657.5	2148.6	
Difference (Wh)	-14.3	43.9	103.2	8.4	162.7	90.4	148.9	-187.4	105.4 (± 44.5)
Difference	-1.7 %	4.3 %	14.2 %	0.8 %	11.1 %	4.5 %	9.9 %	-8.0 %	9.4 % (± 6.7 %)

7.4 Chapter's summary

PCM's commonly have a lower thermal conductivity. This reduces the heat transfer between panel and air as the PCM increase the thermal resistance. Strategies to diminish this effect and increase the heat transfer are important to improve the feasibility of this technology. The literature review pointed out that few studies focused their attention on the heat transfer between the encapsulation and the air.

This chapter is focused on the laboratory tests of the panel and presented the results of three laboratory tests performed to assess the performance of the designed PCM panel and compare this with the existing panel. Each test provided the following output:

1. Heat transfer evaluation of one panel at different gaps:

    Using a test rig with the new and existing panels filled with a heating compound and heated by a resistance wire, three different gaps and Reynolds numbers evaluate the heat transfer and TEF. With data validated by Gnielinski's correlation, satisfactory results in terms of Nusselt number were found when compared to the existing panel. The increase is more pronounced as the gap is smaller and Reynolds number higher. For the highest Reynolds number tested (6061), the Nusselt number increased by 124, 72 and 77 % when compared to the existing panel. For Re=4067, 94, 36 and 5 % were found and the most interesting was at a lower Reynolds number (1954). This lower number made the existing panel more efficient when a gap of 9 and 10 mm was used. A reasonable explanation is that at lower airflows, the protrusions now contribute to increase the heat transfer.

    The pressure drop was also analysed and compared between the panels and the flat panel. The increase varied from 79 % to 17 % when panels were compared; 95.1 % to 21.4 % when new and flat panel were compared and 8.6 % to 0 % when the existing panel was compared. These values were expected since similar results were found during the panel design.

    The thermal enhancement factor takes into consideration the heat transfer and pressure drop when compared to a flat panel. It was found that the existing panel performs better at lower Reynolds number while at higher numbers, the increase in heat transfer comes nearly with the same cost of an increase in pressure drop. When the new and existing panel are compared, an increase of 84.4 % was found for 8 mm gap and a Reynolds number of 6061 while at 10 mm and a Reynolds number equals to 1954, the existing panel performs 29.8 % better than the new panel.

2. Pressure drop investigation for 1, 2 and 3 thermal batteries

    To evaluate if the small fan will be able to provide the same airflow from the existing panel, the pressure drop of 1, 2 and three TB were evaluated. The results were positive and with the fan being able to provide the same airflow as the existing panel. In addition, the results agreed with the simulations during the design process. An average difference of 14 Pa (or 10.5 %) was found for airflows varying from 100 – 300 l/s.

3. Melting and solidifying analysis between existing and new panel

    Holding 30 % more material, the new panel needs more time to solidify and melt when compared to the existing panel this is confirmed by Table 7.10, which summarizes the time required and the increase in percentage from new to existing thermal battery.

Table 7.10 – Melting and solidifying times for one and two thermal batteries

			Time (h)	Increase (in %)
1TB	Melting	EP 1TB	3.5	86 %
		NP 1TB	6.5	
	Solidifying	EP 1TB	4.0	38 %
		NP 1TB	5.5	
2TB	Melting	EP 2TB	4.5	100 %
		NP 2TB	9.0	
	Solidifying	EP 2TB	5.0	70 %
		NP 2TB	8.5	

These results can also be seen from the cooling and heating load. It was compared with a 3LC test and the results presented a good agreement, indicating an average difference of 105.4 Wh ($\pm$ 44.5 Wh) or 4.4 % ($\pm$ 6.9 %).

CHAPTER 8 - CONCLUSIONS AND RECOMMENDATIONS FOR FUTURE WORK

8.1 Overview

The aim of the thesis was to investigate and improve the performance of PCM-Air heat exchangers used in small mechanical ventilation systems to provide cooling. This was achieved by analysis of a MVS installed in a case-study seminar room in the UK using data from the system, in-situ monitoring within the conditioned space and CFD simulation. Improvements in the system control and system performance were achieved through a calibrated model in a DTM software. Improvements in the heat exchange between the PCM and air were achieved by designing, fabricating and validating through laboratory tests a new panel to encapsulate the PCM. This has also achieved reduced costs of production because fewer panels are needed in the thermal battery to provide the same cooling capacity. .

The objectives set in the beginning of this thesis were achieved as follows:

<u>Objective 1:</u> *Conduct a literature review on (a) thermal comfort in non-domestic buildings, (b) use of PCMs as thermal storage in small (room size) ventilation systems (MVS) storage, and (c) strategies to improve the ventilation system (MVS) cooling efficiency.*

A comprehensive literature review was carried out on ventilation systems integrated with latent thermal energy storage to provide cooling. It was revealed that although extensive research has been carried out computationally and using laboratory tests, the penetration to the market is limited and data on operational performance are lacking. As the purpose of such systems is to provide cooling and improve thermal comfort, a review on thermal comfort focused to assess free-running buildings was performed. The characteristics of the MVS plugin in DTM modelling (IESVE) used to evaluate the MVS performance were explained and strategies on how the system can be improved through the control system were pointed out. However, improvements in control system tuning are restricted as the PCM-Air heat exchanger performance is limited by the cooling capacity of the PCM. The literature review revealed that a critical component in the PCM-Air heat exchanger is the design of the encapsulation panel and in particular, the heat transfer channels. One solution is to increase the PCM material but this will require an increase in weight and required area for installation. Developing a material with higher conductivity is one option but this will increase the final cost of the MVS. Another solution is to increase the heat transfer rate of the existing encapsulation as PCM materials have a lower thermal conductivity. This generates two thermal boundary layers (one in the panel and one in the PCM material). The boundary layer

To achieve that, the literature review indicated that the inclusion of ridges over a channel is an efficient solution to enhance the heat transfer and rounded ridges are

more cost effective as it has a small increase in pressure drop when compared to other ridges as well as a reduced cost of production.

To support the study of the MVS performance and the development of the new panel, a literature review on the governing equations and main models used in CFD simulation was covered. Once the panel was fabricated, it should be tested. A review on laboratory tests commonly used to assess heat transfer augmentation in channels pointed out the most suitable for this study.

<u>Objective 2:</u> *Understand and describe in detail the operational performance of a PCM-Air heat exchanger integrated into a MVS together with an analysis of indicators of thermal comfort provision.*

Chapter 4 was dedicated to explain in detail the operational performance of a PCM-Air heat exchanger integrated with a MVS. The equipment uses fan and dampers to control temperature and CO_2 concentration in the room by adjusting the airflow that pass through the thermal batteries or by supplying outside air. It has different operational modes and set points which are designed according to season, regulation and client needs. To explain the MVS in operation, system data was used. The system operates in a different way depending on the season, so three periods were analysed: (a) summer, (b) spring and autumn and (c) winter. This understanding of the system was the key to propose improvements to the MVS.

Chapter 5 evaluated thermal comfort and indoor air quality of the MVS through field monitoring and CFD analysis. Sensors were installed within the conditioned space to log temperature and relative humidity at different heights. After one year of measurement, the data from the seating level was used to evaluate thermal comfort according to BS EN 15251. Moreover, CFD analysis was carried out to predict air temperature and air velocity distribution.

<u>Objective 3:</u> *Improve the cooling efficiency of the MVS by focussing on (a) control strategies and (b) the design of the PCM panel to increase heat transfer without additional (or even reduced) costs.*

Chapter 6 presented the improvements in the cooling efficiency of the MVS. To represent the MVS more realistically and design the system in IESVE with more confidence, the MVS plugin was updated with more control components. Moreover, the performance of the equipment was improved by changes in the airflow set points. This was achieved using a model calibrated by one year of field monitoring. However, this improvement in tuning is restricted as the LTES performance is limited by the cooling capacity of the PCM. The cost-effective solution was to develop a new panel surface to increase the heat transfer as PCM material have a lower thermal

conductivity when compared to other thermal storage materials (e.g. water). Using the literature review as a starting point, a parametric study via CFD modelling evaluated 32 panel designs. Starting with 9 designs in 3D, the results were compared with the existing, dimpled and teardrop panels. It was followed by a 2D analysis followed by refinements until the final design was reached. At each stage of the design, the following parameters were the key for the panel selection:

- Heat transfer in terms of Nusselt number;
- Rigidity;
- Pressure drop;
- Cost of production;
- Ease of manufacture.

<u>Objective 4</u>: *Fabricate and validate the performance of the new design.*

With the panel fabricated, three laboratory tests were evaluated to assess the performance of the new design and compare with the existing panel. With results presented in chapter 7, the tests were performed as follows:

1. Heat transfer evaluation of one panel at different gaps:

   The new, existing and flat panel were split in half and filled with a heating compound and a resistance wire. The test measured the temperature and the pressure drop of three different gaps (8, 9 and 10 mm) at three different Reynolds number (1954, 4067 and 6061) with a supplied power of 17 W. Each test ceased when temperatures achieved stable conditions. A flat panel was used to validate the test rig by comparing the results with Gnielinski's correlation. Furthermore, it was used to estimate the thermal enhancement factor. Outlet and inlet temperatures were logged and used to evaluate the heat transfer in terms of Nusselt number. The results were compared within new, existing and flat panels.

2. Investigation of pressure drop for 1, 2 and 3 thermal batteries

   A test rig was mounted using components from the MVS to assess the pressure drop of 1, 2 and 3 TB. With panels manufactured, this test evaluated capability of the MVS fan to provide the required airflow for the new TB as this new configuration increased the pressure drop of the system. With the use of an airflow meter, 6 airflows (50, 70, 90, 110, 130, 150 l/s) evaluated and compared the pressure drop of the existing and the new TB.

3. Melting and solidifying analysis between the existing and new panel

The third test analysed the thermal load and response of the existing and new panel as well as the charging and discharging time for one and two TB. Thermocouples were attached to the panels' surface located at the middle of each TB as well as placed in the outlet and inlet of the test rig. With a cycle of charging and discharging lasting 24h, the night period was dedicated to charge and the discharge was performed during day time. The analysis of the charging time was performed by analysing the inlet and outlet temperature as well as the surface temperature of the panel. The thermal load and response were evaluated using equations (3.10) and (3.11).

8.2 Key findings of the research

The key findings of the research can be divided to those (a) operational performance, thermal comfort and IAQ provision and (b) proposed improvements.

8.2.1 Evaluation of the MVS in terms of operational performance, thermal comfort and IAQ

Key findings from the MVS operational performance and thermal comfort

- The MVS and its control system was capable to provide a fast response to control the CO_2 concentration in the room and can maintain a thermally comfortable environment.
- Results from field monitoring indicated that the MVS was capable to maintain the temperature within comfort range according to BS EN 15251. Average temperatures of 26.2 ^{o}C (± 0.67 K), 24 ^{o}C (± 1.0 K) and 24.1 ^{o}C (± 0.81 K) were found during the occupied hours of summer, spring/autumn and winter of the analysed period of 2014-2015 at seating level.
- Category II for the adaptive thermal comfort was used in this study. No overheating was found but some overcooling occurs for some hours (116 hours (3 %)) indicating that night purging might need more detailed control. However, this discomfort can be solved simply by enhancing clo (e.g. wearing heavier clothes like a sweater or jacket).
- System data indicated that the MVS has no control on relative humidity. Critical results (RH < 30 %) were found during January to April in 2014 and January to March in 2015.
- The CFD simulation considering full occupancy for summer, winter and autumn and the field monitoring within the space predicted a uniform temperature distribution at seating level.
- The CFD simulation using data calibrated from a DTM software indicated that the temperature is uniformly distributed at seating level with an average of 24.2 ^{o}C,

8.5% more than the field monitoring. A stratification from 23 to 25 °C was found between occupants head and ankles. This value is agreement with ISO 7730 which recommends values below the 3 K (ISO, 2005).

- The CFD simulation indicated that occupants located close to the diffuser might feel uncomfortable as air velocity reached the maximum of 0.6 m/s. Changing the diffuser angle or its geometry might reduce this and effect. Another solution is to relocate the occupants so they are not directly hit by the air jet.

Key findings from the MVS on IAQ

- Additional CO_2 monitoring shows good agreement with the system data but a response delay was noticed. This will delay Cool-Phase® reaction and will provide unnecessary airflow. A faster response CO_2 sensor on the system or a better location of it might improve equipment performance.
- CO_2 concentration remained below 1000 ppm during all the months of the analysed period (2014-2015).

Key findings from the MVS energy consumption

- Electrical energy consumption of the MVS in the seminar room was 0.78 kWh/m^2/annum in 2014 and 0.67 kWh/m^2/annum in 2015. Secondary schools in the UK has a median of 51 kWh/m^2 including electricity used for lighting and office equipment. In monetary terms, this will cost less than £10 per year (based on 2015 cost average of £0.104 per kWh for a medium size building.
- Simulations in IESVE show an energy demand of 75.5 kWh/m^2/annum to maintain the same internal conditions (the exact saving is dependent on the AC system and its COP).

8.2.2 Improvements of the MVS through DTM software

Designers who use IESVE to design HVAC systems have the option to select low energy efficient solutions such as Cool-phase®. The correct design is essential to not overprice and avoid client dissatisfaction as the initial cost of this equipment is elevated when compared to a conventional cooling system. Due to that, an update in the plugin was proposed as the actual component do not entirely represent the real equipment. To represent more realistically, a step control was introduced in the plugin by adding more components. With this, the MVS can be designed with more confidence. Furthermore, changes in airflow at each set point were performed and the key finding is:

- Changes in the airflow at each temperature set-point increase the frequency of temperatures inside the set-point range. It represents an increase of 14.2% for

summer, 3.7% for the winter and 12.3% for spring/autumn. This denotes an annual increase of approximately 10% but will consume additionally 44 kWh per year (or 51.4 %). This is a small penalty despite the high increase in percentage value (129.5 kWh per year).

8.2.3 Improvements of the MVS through the development of an encapsulation panel

The air-side heat exchange for a set of 32 different geometries were analysed via CFD simulation to design an encapsulation panel for a PCM-Air heat exchanger. The key findings are:

- Based on the ease to manufacture, cost of production, increase in heat transfer and volume of PCM per panel, one shape which has rounded ridges and is uniform along its width was chosen as the most suitable for fabrication. This was fabricated as shown in Figure 8.1.

Figure 8.1 – New panel

- The selected design has the geometrical details of ($e/h = 0.219, s/l = 0.044, r = 0.0025\ m, w_r/w = 0.867,\ T_t/H = 0.101, p = 7$)
- The panel chosen is uniform along its width. This gives simplicity to the design, rigidity, let the air be driven uniformly along its width and avoids the need of having both surfaces attached as in the existing panel.
  - The parametric analysis via CFD simulation indicated that the panel chosen is capable to double the heat transfer when compared to the existing panel.
  - The chosen design is capable to hold 13.7 % more PCM when compared to the existing panel.
- The number of panels were reduced from 9 to 7 per thermal battery.
- The pressure drop of 3 thermal batteries with the new panel increased 3.3 times but a small fan is capable to provide the required airflow.

- More power will be necessary to provide the same airflow but the heat transfer increase leads to a reduction in airflow for the same cooling demand.
- The tool responsible to fabricate the encapsulation is capable to produce panels with different thicknesses.

8.2.4 Thermal battery evaluation

The evaluation of fabricated panel is essential to prove its enhanced performance. This was performed over 3 laboratory tests. The key findings of each are presented below:

Key findings from the investigation of heat transfer of one panel with different gaps between panels

- With 8 mm gap, the new panel had the highest temperature difference ($T_{out} - T_{in}$ = 3.64 K), 7 % more than the existing panel.
- The increase in heat transfer is more pronounced as the gap is smaller and Reynolds number higher. For the highest Reynolds number tested (6061), the Nusselt number increased by 124, 72 and 77 % when compared to the existing panel. For Re=4067, 94, 36 and 5 % were found and the most interesting was at a lower Reynolds number (1954). This lower number made the existing panel more efficient when a gap of 9 and 10 mm was tested.
- The Nusselt number ratio performed better with a gap of 8mm and a Reynolds of 1954 and 5067 (2.2 and 2.2, respectively). For Re=6061, the air gap of 10mm performed better against 8 mm air gap (2.5 against 2.3).
- The pressure drop increase varied from 79 % to 17 % when panels were compared; 95.1 % to 21.4 % when new and flat panel were compared and 8.6 % to 0 % when the existing panel was compared.
- The TEF increased in 84.4 % when the new and existing panel are compared for 8 mm gap and Reynolds number of 6061.
- The TEF decreased in 29.8 % when existing and new panels are compared for an air gap of 10 mm and Reynolds number of 1954.

Key findings from the investigation of pressure drop for 1, 2 and 3 thermal batteries

- The existing fan was capable to overcome the increase in pressure drop of the new thermal battery and provide the same airflow in the existing thermal battery.
- The pressure drop increase in 345, 258 and 380 % for 1, 2 and 3 thermal batteries when compared to the existing thermal battery.

- The results of pressure drop between the laboratory test and the design presented a good agreement. A difference of 14 Pa (± 14.15 Pa) was noticed. In percentage, it represents 10.5 % (± 11.4%).

Melting and solidifying analysis between the existing and the new panel

- The new panel fabricated was capable to hold 30 % more material than the existing panel. This represents an increase of 118% when compared to the panel designed during CFD simulation.
- The new thermal battery needs 86% more time to melt and 38% time to solidify for 1 TB. For two TB, 100 % is necessary to melt and 70% to solidify. This can be explained by the 30% more material each panel can hold. Furthermore, the existing thermal battery has 9 instead of 7 panels, representing a heat exchange area 28% bigger than the new thermal battery.

8.3   Impact on the research field and industry

The findings of the research can be summarized in three main contributions to the academia and industry.

Contribution 1: *Monitoring and data analysis of a MVS in real operation*

Few studies exist on the performance of commercially installed MVS with PCM heat exchangers during real operation. Monitoring, analysing and publishing studies of such systems in real operation will help researchers to understand their operation in detail and use it as a guide for future studies. It will also help designers to understand the benefits of this technology and opt for this low energy cooling system in new designs.

Contribution 2: *Improvement of the MVS through DTM*

A correct representation of the MVS with PCM heat exchangers is important to correctly design the system and essential to decide what cooling system is appropriate. This will essentially help designers. Furthermore, simulations showing more reliable results can avoid future claims about system performance.

Minor alterations in the MVS set points presented positive effects in MVS performance. This will give another strategy for designers to better design the system.

Contribution 3: *Improvement in the MVS through PCM encapsulation design*

Researchers have focused their attention to develop new PCM's or assess existing PCM encapsulations in different climates and environmental conditions. However, few of them focused their attention on the heat transfer between panel and air. This

is essential to provide a more responsive ventilation system. The development of a new encapsulation panel for MVS opens a field of investigation where researchers are able to develop new tools to improve the MVS.

The new PCM panel will also contribute to the industry as it provides a new option of encapsulation for cooling purposes. The flexibility of providing different thicknesses is also positive characteristic of this panel.

8.4 Suggestions for future work

- Evaluate side-by-side the new and the existing system and compare the results over one year of tests.

All the tests performed in this study are laboratory tests and the results of the new thermal battery were satisfactory. However, it is important to analyse the efficiency of the system in real operation. To reach that, the new thermal battery can be installed at one side of the MVS while the other side remains the existing thermal battery. The data over one year will be logged and the performance of the existing and new thermal battery evaluated.

- Study the impact of outside temperature and airflow to charge the TB.

MVS in real operation do not have stable outdoor temperatures and airflow during the charging period. The study of this two parameters will evaluate the equipment performance and propose alterations in control system can be proposed in order to promote enough airflow to charge the TB. This study is important as the results presented in this thesis showed that longer times are needed to charge the new thermal battery when compared to the existing one. Even if the reason for that is the additional material that the new TB can hold and less area to transfer the heat due to the use of less panels per TB.

- Use IESVE to analyse the feasibility in continental countries such as Brazil and China.

This thesis showed the feasibility of this low energy cooling system in UKBy using IESVE and a calibrated model, studies can be performed to analyse the feasibility in different countries and climates. Furthermore, continental contries such as Brazil and China have different climates within the country and such study will analyse in each location of the country the MVS is suitable or not. This will create a guidance for designers and help polititians to create incentives to install such systems.

In addition, where MVS with PCM heat exchangers are not able tp provide all cooling requirements, hybrid systems can be tested.

REFERENCES

Aneke, M. & Wang, M. (2016) Energy storage technologies and real life applications – A state of the art review. *Applied Energy*. [Online] 179350–377. [online]. Available from: http://dx.doi.org/10.1016/j.apenergy.2016.06.097.

Anon (n.d.) *Airflow Instruments Micromanometer PVM610* [online]. Available from: http://www.tsi.com/Airflow-Instruments-Micromanometer-PVM610/ (Accessed 3 April 2018).

Anon (n.d.) *Europe 2020 indicators - climate change and energy - Statistics Explained* [online]. Available from: http://ec.europa.eu/eurostat/statistics-explained/index.php?title=Europe_2020_indicators_-_climate_change_and_energy (Accessed 8 July 2018).

Anon (n.d.) *HTM F Hybrid Ventilation* [online]. Available from: https://www.monodraught.com/products/hybrid-ventilation/htm-f (Accessed 16 June 2018).

Anon (n.d.) *Inventables* [online]. Available from: https://www.inventables.com/ (Accessed 4 June 2018).

Anon (2016) *Meteonorm* [online]. Available from: http://www.meteonorm.com (Accessed 20 February 2017).

Anon (n.d.) *Monodraught; Natural Ventilation, Cooling and Lighting Specialists* [online]. Available from: https://www.monodraught.com/ (Accessed 9 April 2018).

Anon (n.d.) *RD 100/0,6 | Block Resistance Wire, 0.01 mm^2 CSA 39m | Block* [online]. Available from: http://uk.rs-online.com/web/p/multicore-industrial-cable/7496341/?searchTerm=749-6341&relevancy-data=636F3D3126696E3D4931384E525353746F636B4E756D626572266C753D656E266D6D3D6D61746368686C6C26706D3D5E285C647B362C377D5B4161426250705D297C285C647B337D5B5C732D2F (Accessed 28 September 2017).

Anon (n.d.) *RS Pro White Chemical Resistance, Water Resistance Epoxy Potting Compound* [online]. Available from: https://uk.rs-online.com/web/p/products/0552668/?grossPrice=Y&cm_mmc=UK-PLA-DS3A-_-google-_-PLA_UK_EN_Adhesives_And_Sealants_And_Tapes-_-Adhesives_And_Glues%7CPotting_Compounds-_-PRODUCT+GROUP&matchtype=&gclid=Cj0KCQjwzIzWBRDnARIsAAkc8hH0nZxFyF35fZzAqHFJb (Accessed 3 April 2018).

Anon (n.d.) *SMART GEMS project* [online]. Available from: http://www.smartgems.tuc.gr/index.php?id=smart_gems.

Anon (2018) *Venticool, http://venticool.eu/. Acessed in* [online]. Available from: http://venticool.eu/venticool-home/.

Anon (n.d.) *Weather Underground* [online]. Available from: www.wunderground.com (Accessed 1 May 2016).

ANSI/ASHRAE (2002) 'Measurement of Energy and Demand Savings', in *ASHRAE Guideline 14-2002*. p. 170.

ANSYS (2017) *ANSYS Fluent Theory guide*.

Antony Aroul Raj, V. & Velraj, R. (2011) Heat transfer and pressure drop studies on a PCM-heat exchanger module for free cooling applications. *International Journal of Thermal Sciences*. [Online] 50 (8), 1573–1582. [online]. Available from: http://dx.doi.org/10.1016/j.ijthermalsci.2011.01.025.

ASHRAE (2013a) *2013 Ashrae handbook fundamentals*. SI Edition. Mark S. Owen (ed.). Atlanta, GA: ASHRAE. [online]. Available from: www.ashrae.org.

ASHRAE (2013b) Page 285 talks about comparison of results with data. "for example, 20% could be satisfactory"page 494 have an example of cooling and heating load calculations. also 483appliances - page 466page 469ASHRAE research project RP-1055 (Hosni et al. 1999) found that, for general office equipment with nameplate power con- sumption of less than 1000 W, the actual ratio of total heat gain to nameplate ranged from 25% to 50%, but when all tested equipment is considered, the range is broader.Page 470have a table with avarage computer power (heat gain)page. *ASHRAE Fundamentals*. SI edition. Vol. 1. Atlanta, GA: ASHRAE.

ASHRAE (2017) *ASHRAE HANDBOOK FUNDAMENTALS*. ASHRAE.

ASHRAE (2013c) Thermal Environmental Conditions for Human Occupancy - ANSI/ASHRAE Standard 55-2013. ASHRAE

Bardina, J. E. et al. (1997) *Turbulence Modeling Validation, Testing, and Development*. [online]. Available from: https://ntrs.nasa.gov/search.jsp?R=19970017828 (Accessed 4 January 2018).

Bhuiya, M. M. K. et al. (2012) Heat transfer enhancement and development of correlation for turbulent flow through a tube with triple helical tape inserts. *International Communications in Heat and Mass Transfer*. [Online] 39 (1), 94–101. [online]. Available from: http://dx.doi.org/10.1016/j.icheatmasstransfer.2011.09.007.

Bilen, K. et al. (2009) The investigation of groove geometry effect on heat transfer for internally grooved tubes. *Applied Thermal Engineering*. [Online] 29 (4), 753–761. [online]. Available from: http://dx.doi.org/10.1016/j.applthermaleng.2008.04.008.

Blazek, J. (2005) *Computational fluid dynamics : principles and applications*. Elsevier.

Borderon, J. et al. (2015) Modeling and simulation of a phase change material system for improving summer comfort in domestic residence. *Applied Energy*. [Online] 140288–296. [online]. Available from: https://www.sciencedirect.com/science/article/pii/S0306261914012318?via%3Dihub (Accessed 20 June 2018).

Boussinesq, J. (2016) *Essai sue la theorie des eaux courantes*. Hachette Livre - BNF.

Butala, V. & Stritih, U. (2009) Experimental investigation of PCM cold storage. *Energy and Buildings*. [Online] 41 (3), 354–359.

CCC (2018) *Reducing UK emissions - 2018 Progress Report to Parliament - Committee on Climate Change* [online]. Available from: https://www.theccc.org.uk/publication/reducing-uk-emissions-2018-progress-report-to-parliament/ (Accessed 11 July 2018).

Chang, S. W. et al. (2008) Heat transfer and pressure drop in rectangular channel with compound roughness of V-shaped ribs and deepened scales. *International Journal of Heat and Mass Transfer*. [Online] 51 (3–4), 457–468.

Chen, Y. et al. (2012) Enhancement of heat transfer in turbulent channel flow over dimpled surface. *International Journal of Heat and Mass Transfer*. [Online] 55 (25–26), 8100–8121. [online]. Available from: http://dx.doi.org/10.1016/j.ijheatmasstransfer.2012.08.043.

Choi, E. Y. et al. (2013) Heat transfer augmentation using a rib-dimple compound cooling technique. *Applied Thermal Engineering*. [Online] 51 (1–2), 435–441. [online]. Available from: http://dx.doi.org/10.1016/j.applthermaleng.2012.09.041.

CIBSE (2015a) *Building Performance Modelling Tools. AM11: 2015*.

CIBSE (2015b) page 32:seminar rooms temperature limitsSection 1.3.1.3; chapter 8, section 8.3.1. *CIBSE Guide A: Environmental Design*. Vol. 30. [Online]. The Lavenham Press. [online]. Available from: http://www.amazon.co.uk/dp/1903287669.

CIBSE (2010) *CIBSE KS16 - How to manage overheating in buildings*. CIBSE.

CIBSE (2015c) *Integrated school design TM 57*. London: CIBSE.

CIBSE (2013) *The limits of thermal comfort : avoiding overheating in European buildings TM52: 2013*.

Committee on Climate Change (2018) *Reducing UK emissions – 2018 Progress Report to Parliament*. [online]. Available from: www.theccc.org.uk/publications (Accessed 8 July 2018). [online]. Available from: www.theccc.org.uk/publications (Accessed 8 July 2018).

COMSOL (2018) *Boussinesq Approximation Definition* [online]. Available from: https://www.comsol.com/multiphysics/boussinesq-approximation (Accessed 3 January 2018).

de Dear, R. & Brager, G. (1998) Developing an adaptive model of thermal comfort and preference. *ASHRAE Transactions*. 104 (March), 1–18. [online]. Available from: http://repositories.cdlib.org/cedr/cbe/ieq/deDear1998_ThermComPref.

de Dear, R. & Schiller Brager, G. (2001) The adaptive model of thermal comfort and energy conservation in the built environment. *International Journal of Biometeorology*. [Online] 45 (2), 100–108. [online]. Available from: http://link.springer.com/10.1007/s004840100093.

Deardorff, J. W. (1970) A numerical study of three-dimensional turbulent channel flow at large Reynolds numbers. *Journal of Fluid Mechanics*. [Online] 41 (2), 453. [online]. Available from: http://www.journals.cambridge.org/abstract_S0022112070000691 (Accessed 4 January 2018).

Department of Energy & Climate Change (2013) *Gas and electricity prices in the non-domestic sector* [online]. Available from: https://www.gov.uk/government/statistical-data-sets/gas-and-electricity-prices-in-the-non-domestic-sector (Accessed 21 June 2015).

Dhainaut, J.-F. et al. (2004) Unprecedented heat-related deaths during the 2003 heat wave in Paris: consequences on emergency departments. *Critical care*. [Online] 8 (1), 1–2. [online]. Available from: http://www.pubmedcentral.nih.gov/articlerender.fcgi?artid=420061&tool=p

mcentrez&rendertype=abstract (Accessed 13 April 2014).

Dolado, P. et al. (2011) Characterization of melting and solidification in a real-scale PCM-air heat exchanger: Experimental results and empirical model. *Renewable Energy*. [Online] 36 (11), 2906–2917. [online]. Available from: http://www.sciencedirect.com/science/article/pii/S0960148111001807 (Accessed 18 October 2014).

Domaschke, N. et al. (2012) Heat Transfer and Pressure Drop Measurements in a Rib Roughened Leading Edge Cooling Channel. *Journal of Turbomachinery*. [Online] 134 (6), 61006. [online]. Available from: http://link.aip.org/link/abstract/ASMECP/v2009/i48845/p337/s1.

Ds/En (2007) *BS EN 15251: Indoor environmental input parameters for design and assessment of energy performance of buildings addressing indoor air quality, thermal environment, lighting and acoustics*. 3.

Education Funding Agency (2014a) *Acoustics, lighting and ventilation in schools* [online]. Available from: https://www.gov.uk/government/publications/acoustics-lighting-and-ventilation-in-schools/acoustics-lighting-and-ventilation-in-schools (Accessed 19 March 2015).

Education Funding Agency (2014b) *Baseline Designs for Schools, 'Environmental Services Strategy' and 'Ventilation Strategy'*. [online]. Available from: https://www.gov.uk/government/publications/psbp-baseline-designs (Accessed 7 August 2015). [online]. Available from: https://www.gov.uk/government/publications/psbp-baseline-designs (Accessed 7 August 2015).

Education Funding Agency (2013) *Priority School Building Programme: Services Output Specification*. (June).

Eiamsa-ard, S. & Promvonge, P. (2009) Thermal characteristics of turbulent rib-grooved channel flows. *International Communications in Heat and Mass Transfer*. [Online] 36 (7), 705–711. [online]. Available from: http://dx.doi.org/10.1016/j.icheatmasstransfer.2009.03.025.

Fanger, P. O. (1972) *Thermal comfort: analysis and applications in environmental engineering*. McGraw-Hill. [online]. Available from: https://books.google.co.uk/books/about/Thermal_comfort_analysis_and_application.html?id=mUFSAAAAMAAJ&redir_esc=y (Accessed 22 January 2018).

Farnel (n.d.) *PPC186 - Epoxy Encapsulant, Flame Retardant, Packet, Black, 1 kg* [online]. Available from: http://uk.farnell.com/pro-power/ppc186/encapsulant-epoxy-flame-retard/dp/1784624 (Accessed 3 April 2018).

Fouillet, A. et al. (2008) Has the impact of heat waves on mortality changed in France since the European heat wave of summer 2003? A study of the 2006 heat wave. *International Journal of Epidemiology*. [Online] 37 (2), 309–317.

Gnielinski & V. (1976) New equations for heat and mass transfer in turbulent pipe and channel flow. *International Chemical Engineering*. 16 (2), 359–368.

HANDBOOK, A. (2012) chapter 12Gas Input Rate (page 500) - have an expression to calculate the gas heat gain.Commercial systems with significant variation in airflow for cooling, heating, and large internal loads (e.g., kitchens, theaters) should be designed in accordance with Chapters 20 and 21 of the 2009

ASHRAE Handbook—Fundamentals, Chapters 5 and 33 in the 2011 ASHRAE Handbook—HVAC Applications, and Chapters 19 (duct construction) to 21 (Fans) of this volume. *HVAC Systems and Equipment*. Vol. 1. ASHRAE.

Heiselberg, P. (2018) *Ventilative Cooling Design Guide Energy in Buildings and Communities Programme*. [online]. Available from: http://iea-ebc.org/Data/publications/EBC_Annex_62_Design_Guide.pdf. (March). [online]. Available from: http://iea-ebc.org/Data/publications/EBC_Annex_62_Design_Guide.pdf.

Holzer, P. & Psomas, T. (2018) *Ventilative Cooling Sourcebook Energy in Buildings and Communities Programme*. [online]. Available from: http://venticool.eu/wp-content/uploads/2016/11/VC-Sourcebook-EBC-Annex-62-March-2018.pdf. (March). [online]. Available from: http://venticool.eu/wp-content/uploads/2016/11/VC-Sourcebook-EBC-Annex-62-March-2018.pdf.

Hwang, S. D. et al. (2008) Heat transfer with dimple/protrusion arrays in a rectangular duct with a low Reynolds number range. *International Journal of Heat and Fluid Flow*. [Online] 29 (4), 916–926.

Hwang, S. D. et al. (2010) Local heat transfer and thermal performance on periodically dimple-protrusion patterned walls for compact heat exchangers. *Energy*. [Online] 35 (12), 5357–5364. [online]. Available from: http://dx.doi.org/10.1016/j.energy.2010.07.022.

IESVE (2016) *Integrated Environmental Solutions* [online]. Available from: https://www.iesve.com/ (Accessed 20 February 2017).

Incropera, F. P. (2007) *Fundamentals of heat and mass transfer.* John Wiley.

ISO (2005) ISO 7730: Ergonomics of the thermal environment Analytical determination and interpretation of thermal comfort using calculation of the PMV and PPD indices and local thermal comfort criteria. *Management*. [Online] 3605–615. [online]. Available from: http://linkinghub.elsevier.com/retrieve/pii/S0267726105000503.

Iten, M. et al. (2016) Experimental study on the thermal performance of air-PCM unit. *Building and Environment*. [Online] 105128–139. [online]. Available from: http://dx.doi.org/10.1016/j.buildenv.2016.05.035.

Iten, M. & Liu, S. (2015) Experimental Study on the Performance of RT 25 to be Used as Ambient Energy Storage. *Energy Procedia*. [Online] 70229–240. [online]. Available from: http://dx.doi.org/10.1016/j.egypro.2015.02.119.

Jaber, S. & Ajib, S. (2012) Novel cooling unit using PCM for residential application. *International Journal of Refrigeration*. [Online] 35 (5), 1292–1303. [online]. Available from: https://www.sciencedirect.com/science/article/pii/S0140700712000813?via%3Dihub#fig3 (Accessed 20 June 2018).

Kasaeian, A. et al. (2017) Experimental studies on the applications of PCMs and nano-PCMs in buildings: A critical review. *Energy and Buildings*. [Online] 15496–112. [online]. Available from: https://www.sciencedirect.com/science/article/pii/S0378778817321564 (Accessed 5 January 2018).

Kim, K. M. et al. (2009) Optimal design of angled rib turbulators in a cooling channel. *Heat and Mass Transfer/Waerme- und Stoffuebertragung*. [Online] 45

(12), 1617–1625.

Kolokotroni, M. & Heiselberg, P. (2015) *Ventilative Cooling (State-of-the-art review)*. Vol. Annex 62. Department of Civil Engineering. Aalborg University. [online]. Available from: http://venticool.eu/wp-content/uploads/2013/09/SOTAR-Annex-62-FINAL.pdf.

Labat, M. et al. (2014) Experimental assessment of a PCM to air heat exchanger storage system for building ventilation application. *Applied Thermal Engineering*. [Online] 66 (1–2), 375–382. [online]. Available from: http://www.sciencedirect.com/science/article/pii/S135943111400115X (Accessed 5 November 2014).

Labeodan, T. et al. (2015) Occupancy measurement in commercial office buildings for demand-driven control applications - A survey and detection system evaluation. *Energy and Buildings*. [Online] 93303–314. [online]. Available from: http://dx.doi.org/10.1016/j.enbuild.2015.02.028.

Launder, B. E. et al. (1975) Progress in the development of a Reynolds-stress turbulence closure. *Journal of Fluid Mechanics*. [Online] 68 (3), 537. [online]. Available from: http://www.journals.cambridge.org/abstract_S0022112075001814 (Accessed 4 January 2018).

Launder, B. E. & Spalding, D. B. (1973) Mathematical Models of Turbulence. *Academic Press*. [Online] 53 (6), 424–424. [online]. Available from: http://doi.wiley.com/10.1002/zamm.19730530619 (Accessed 4 January 2018).

Lazaro, A., Dolado, P., Marin, J. M., et al. (2009) PCM-air heat exchangers for free-cooling applications in buildings: Empirical model and application to design. *Energy Conversion and Management*. [Online] 50 (3), 444–449. [online]. Available from: http://www.sciencedirect.com/science/article/pii/S0196890408004561 (Accessed 3 November 2014).

Lazaro, A., Dolado, P., Marín, J. M., et al. (2009) PCM–air heat exchangers for free-cooling applications in buildings: Experimental results of two real-scale prototypes. *Energy Conversion and Management*. [Online] 50 (3), 439–443. [online]. Available from: http://www.sciencedirect.com/science/article/pii/S0196890408004500 (Accessed 20 October 2014).

Lei, L. et al. (2014) Inverse determination of wall boundary convective heat fluxes in indoor environments based on CFD. *Energy and Buildings*. [Online] 73130–136. [online]. Available from: http://www.sciencedirect.com/science/article/pii/S037877881400005X.

Ligrani, P. M. et al. (2001) Flow structure and local Nusselt number variations in a channel with dimples and protrusions on opposite walls. *International Journal of Heat and Mass Transfer*. [Online] 44 (23), 4413–4425.

Liou, T. M. et al. (2016) Particle image velocimetry and infrared thermography measurements in a two-pass 90-deg ribbed parallelogram channel. *International Journal of Heat and Mass Transfer*. [Online] 931175–1189. [online]. Available from: http://dx.doi.org/10.1016/j.ijheatmasstransfer.2015.11.016.

Liou, T.-M. et al. (2014) Thermal Performance of a Radially Rotating Twin-Pass Smooth-Walled Parallelogram Channel. *Journal of Turbomachinery*. [Online]

136 (12), 121007. [online]. Available from: http://turbomachinery.asmedigitalcollection.asme.org/article.aspx?doi=10.1115/1.4028239.

Liu, J. et al. (2015) Numerical modeling flow and heat transfer in dimpled cooling channels with secondary hemispherical protrusions. *Energy*. [Online] 79 (C), 1–19. [online]. Available from: http://dx.doi.org/10.1016/j.energy.2014.05.075.

Lomax, H. et al. (2001) *Fundamentals of Computational Fluid Dynamics*. Springer Berlin Heidelberg.

Lorenz, E. N. (1963) Deterministic Nonperiodic Flow. *Journal of the Atmospheric Sciences*. [Online] 20 (2), 130–141. [online]. Available from: http://journals.ametsoc.org/doi/abs/10.1175/1520-0469%281963%29020%3C0130%3ADNF%3E2.0.CO%3B2 (Accessed 4 January 2018).

Macias, M. et al. (2006) Application of night cooling concept to social housing design in dry hot climate. *Energy and Buildings*. [Online] 38 (9), 1104–1110. [online]. Available from: http://www.sciencedirect.com/science/article/pii/S0378778806000181 (Accessed 13 November 2014).

McAdams, W. H. (1954) *Heat Transmission (McGraw-Hill Series in Chemical Engineering)*. McGraw-Hill. [online]. Available from: http://www.amazon.com/Transmission-McGraw-Hill-Series-Chemical-Engineering/dp/B0006ATKWI (Accessed 6 March 2013).

Medved, S. & Arkar, C. (2008) Correlation between the local climate and the free-cooling potential of latent heat storage. *Energy and Buildings*. [Online] 40 (4), 429–437. [online]. Available from: http://www.sciencedirect.com/science/article/pii/S0378778807001120 (Accessed 5 November 2014).

Menter, F. R. (1994) Two-equation eddy-viscosity turbulence models for engineering applications. *AIAA Journal*. [Online] 32 (8), 1598–1605. [online]. Available from: http://arc.aiaa.org/doi/10.2514/3.12149 (Accessed 5 January 2018).

Ministry of Housing, C. & L. G. (2010) *Approved Documents* [online]. Available from: https://www.gov.uk/government/collections/approved-documents#contents (Accessed 10 August 2015).

Moffat, R. J. (1988) Describing the uncertainties in experimental results. *Experimental Thermal and Fluid Science*. [Online] 1 (1), 3–17. [online]. Available from: https://www.sciencedirect.com/science/article/pii/089417778890043X (Accessed 15 July 2018).

Moon, M. A. et al. (2014) Evaluation of heat transfer performances of various rib shapes. *International Journal of Heat and Mass Transfer*. [Online] 71275–284. [online]. Available from: http://dx.doi.org/10.1016/j.ijheatmasstransfer.2013.12.026.

Nagano, K. et al. (2006) Study of a floor supply air conditioning system using granular phase change material to augment building mass thermal storage—Heat response in small scale experiments. *Energy and Buildings*. [Online] 38 (5), 436–446. [online]. Available from: https://www.sciencedirect.com/science/article/pii/S037877880500143X?via

%3Dihub#fig4 (Accessed 20 June 2018).

Nagano, K. et al. (2004) Thermal characteristics of a direct heat exchange system between granules with phase change material and air. *Applied Thermal Engineering*. [Online] 24 (14–15), 2131–2144. [online]. Available from: https://www.sciencedirect.com/science/article/pii/S1359431104000560?via% 3Dihub (Accessed 19 June 2018).

Nevins, R. G. et al. (1966) A temperature-humidity chart for thermal comfort of seated persons. *ASHRAE transactions*. 72 (1), 283–291.

Nicol, J. F. & Humphreys, M. A. (2002) Adaptive thermal comfort and sustainable thermal standards for buildings. *Energy and Buildings*. [Online] 34 (6), 563–572. [online]. Available from: http://www.sciencedirect.com/science/article/pii/S0378778802000063 (Accessed 11 January 2015).

O'Sullivan, P. & Adam O'Donovan (2018) *Ventilative Cooling Case Studies Energy in Buildings and Communities Programme*. [online]. Available from: http://venticool.eu/wp-content/uploads/2016/11/VC-Case-Studies-EBC-Annex-62-May-2018-Final.pdf. (May). [online]. Available from: http://venticool.eu/wp-content/uploads/2016/11/VC-Case-Studies-EBC-Annex-62-May-2018-Final.pdf.

Oliveira Santos T.V. (2011) *Efeito da emissividade no infravermelho e da refletividade no espectro da radiação solar sobre o desempenho térmico de cobertas metálicas de construções situadas em regiões de clima subtropical e equatorial*. Universidade Federal de Pernambuco.

Orszag, S. A. & Patterson, G. S. (1972) Numerical simulation of turbulence: statistical models and turbulence. Lecture Notes in Physics p.127–147.

Osterman, E. et al. (2015) Parametrical analysis of latent heat and cold storage for heating and cooling of rooms. *Applied Thermal Engineering*. [Online] 84138–149. [online]. Available from: http://linkinghub.elsevier.com/retrieve/pii/S1359431115002240.

Park, J. et al. (2004) Numerical Predictions of Flow Structure Above a Dimpled Surface in a Channel. *Numerical Heat Transfer, Part A: Applications*. [Online] 45 (1), 1–20. [online]. Available from: http://www.tandfonline.com/doi/abs/10.1080/10407780490026740.

Patel, V. C. et al. (1985) Turbulence models for near-wall and low Reynolds number flows - A review. *AIAA Journal*. [Online] 23 (9), 1308–1319. [online]. Available from: http://arc.aiaa.org/doi/10.2514/3.9086 (Accessed 4 January 2018).

Precision, S. (n.d.) *Sensing Precision Balance Master* [online]. Available from: http://sensing-precision.com/wp-content/uploads/2014/12/BALANCE-MASTER-Data-Sheet.pdf (Accessed 15 June 2017).

Prieto, A. et al. (2017) 25 Years of cooling research in office buildings: Review for the integration of cooling strategies into the building façade (1990–2014). *Renewable and Sustainable Energy Reviews*. [Online] 71 (January), 89–102. [online]. Available from: http://dx.doi.org/10.1016/j.rser.2017.01.012.

Promvonge, P. et al. (2010) Enhanced heat transfer in a triangular ribbed channel with longitudinal vortex generators. *Energy Conversion and Management*. [Online] 51 (6), 1242–1249. [online]. Available from: http://dx.doi.org/10.1016/j.enconman.2009.12.035.

Promvonge, P. (2010) Heat transfer and pressure drop in a channel with multiple 60º V-baffles. *International Communications in Heat and Mass Transfer*. [Online] 37 (7), 835–840. [online]. Available from: http://dx.doi.org/10.1016/j.icheatmasstransfer.2010.04.003.

Promvonge, P. & Thianpong, C. (2008) Thermal performance assessment of turbulent channel flows over different shaped ribs. *International Communications in Heat and Mass Transfer*. [Online] 35 (10), 1327–1334. [online]. Available from: http://dx.doi.org/10.1016/j.icheatmasstransfer.2008.07.016.

Raj, V. A. A. & Velraj, R. (2010) Review on free cooling of buildings using phase change materials. *Renewable and Sustainable Energy Reviews*. [Online] 14 (9), 2819–2829. [online]. Available from: http://www.sciencedirect.com/science/article/pii/S136403211000184X (Accessed 31 August 2014).

Regulations Standards Design Guidance (2006) Building Bulletin 101 Ventilation of School Buildings. Department for Education (July).

Reynolds, O. (1895) On the Dynamical Theory of Incompressible Viscous Fluids and the Determination of the Criterion. *Philosophical Transactions of the Royal Society A: Mathematical, Physical and Engineering Sciences*. [Online] 186 (0), 123–164. [online]. Available from: http://rsta.royalsocietypublishing.org/cgi/doi/10.1098/rsta.1895.0004 (Accessed 4 January 2018).

Robine, J. M. et al. (2008) Death toll exceeded 70,000 in Europe during the summer of 2003. *Comptes Rendus - Biologies*. [Online] 331 (2), 171–178.

Rohles, F. H. J. & Nevins, R. G. (1971) The nature of thermal comfort for sedentary man. *ASHRAE Transactions*. 77 (1), 239.

Rosenzweig, C. et al. (2005) Characterizing the urban heat island in current and future climates in New Jersey. *Environmental Hazards*. [Online] 6 (1), 51–62. [online]. Available from: http://linkinghub.elsevier.com/retrieve/pii/S1464286705000057 (Accessed 23 July 2011).

Rouault, F. et al. (2013) Numerical modelling of tube bundle thermal energy storage for free-cooling of buildings. *Applied Energy*. [Online] 1111099–1106. [online]. Available from: https://www.sciencedirect.com/science/article/pii/S0306261913004686?via%3Dihub (Accessed 20 June 2018).

Rubitherm GmbH (n.d.) *Rubitherm* [online]. Available from: https://www.rubitherm.eu/en/index.php/productcategory/makroverkaspelung-csm (Accessed 2 May 2017).

Santamouris, M. & Asimakopoulos, D. N. (1996) *Passive cooling of buildings*. James & James.

Santamouris, M. & Kolokotsa, D. (2013) Passive cooling dissipation techniques for buildings and other structures: The state of the art. *Energy and Buildings*. [Online] 5774–94. [online]. Available from: http://www.sciencedirect.com/science/article/pii/S0378778812005762 (Accessed 3 March 2013).

Santos, T. et al. (2016) 'Performance in practice of a ventilation system with thermal

storage in a computer seminar room', in *CLIMA 2016, 12th CLIMA REHVA World Congress*. May 2016 Aalborg, Denmark: . p. [online]. Available from: http://vbn.aau.dk/files/233719310/paper_142.pdf.

Sharma, A. et al. (2009) Review on thermal energy storage with phase change materials and applications. *Renewable and Sustainable Energy Reviews*. [Online] 13 (2), 318–345. [online]. Available from: http://www.sciencedirect.com/science/article/pii/S1364032107001402 (Accessed 10 July 2014).

Singh, P. et al. (2017) Characterization of heat transfer enhancement and frictional losses in a two-pass square duct featuring unique combinations of rib turbulators and cylindrical dimples. *International Journal of Heat and Mass Transfer*. [Online] 106629–647. [online]. Available from: http://dx.doi.org/10.1016/j.ijheatmasstransfer.2016.09.037.

Souayfane, F. et al. (2016) Phase change materials (PCM) for cooling applications in buildings: A review. *Energy and Buildings*. [Online] 129396–431. [online]. Available from: http://dx.doi.org/10.1016/j.enbuild.2016.04.006 (Accessed 5 January 2018).

SriHarsha, V. et al. (2009) Influence of rib height on the local heat transfer distribution and pressure drop in a square channel with 90° continuous and 60° V-broken ribs. *Applied Thermal Engineering*. [Online] 29 (11–12), 2444–2459. [online]. Available from: http://linkinghub.elsevier.com/retrieve/pii/S1359431108004882 (Accessed 6 January 2017).

Stritih, U. & Butala, V. (2010) Experimental investigation of energy saving in buildings with PCM cold storage. *International Journal of Refrigeration*. [Online] 33 (8), 1676–1683. [online]. Available from: https://www.sciencedirect.com/science/article/pii/S0140700710001635 (Accessed 28 October 2014).

Takeda, S. et al. (2004) Development of a ventilation system utilizing thermal energy storage for granules containing phase change material. *Solar Energy*. [Online] 77 (3), 329–338. [online]. Available from: http://linkinghub.elsevier.com/retrieve/pii/S0038092X04001057.

Tanda, G. (2004) Heat transfer in rectangular channels with transverse and V-shaped broken ribs. *International Journal of Heat and Mass Transfer*. [Online] 47 (2), 229–243. [online]. Available from: http://linkinghub.elsevier.com/retrieve/pii/S0017931003004149.

Taylor, G. I. (1935) Statistical Theory of Turbulence. *Proceedings of the Royal Society A: Mathematical, Physical and Engineering Sciences*. [Online] 151 (873), 421–444. [online]. Available from: http://rspa.royalsocietypublishing.org/cgi/doi/10.1098/rspa.1935.0158 (Accessed 4 January 2018).

Testo (n.d.) *Testo 410i - Bluetooth Vane Anemometer Smart Probe | Air outlets | Velocity measurement | Operations, maintenance and service - Air-conditioning systems maintenance | Operations, maintenance and service | Applications | Testo Ltd* [online]. Available from: https://www.testo.com/en-UK/testo-410-i/p/0560-1410 (Accessed 11 April 2018).

Thianpong, C. et al. (2009) Thermal characterization of turbulent flow in a channel

with isosceles triangular ribs. *International Communications in Heat and Mass Transfer*. [Online] 36 (7), 712–717. [online]. Available from: http://dx.doi.org/10.1016/j.icheatmasstransfer.2009.03.027.

Turnpenny, J. R. et al. (2000) Novel ventilation cooling system for reducing air conditioning in buildings. Part I: Testing and theoretical modelling. *Applied Thermal Engineering*. [Online] 20 (11), 1019–1037. [online]. Available from: http://www.sciencedirect.com/science/article/pii/S135943119900068X (Accessed 13 November 2014).

Turnpenny, J. R. R. et al. (2001) Novel ventilation system for reducing air conditioning in buildings. Part II: testing of prototype. *Applied Thermal Engineering*. [Online] 21 (12), 1203–1217. [online]. Available from: http://www.sciencedirect.com/science/article/pii/S1359431101000035 (Accessed 13 November 2014).

Tyagi, K. et al. (2015) 'Experimental study of heat transfer augmentation in high aspect-ratio channels featuring different dimple configurations', in *ASME Turbo Expo 2015: Turbine Technical Conference and Exposition*. 2015 ASME. pp. 1–11.

U.S. Energy Information Administration (2016) International Energy Outlook 2016. International Energy Outlook 2016 0484(2016).

Vesma (2014) *Vesma* [online]. Available from: http://vesma.com/ (Accessed 3 March 2017).

Waqas, A. et al. (2017) Performance analysis of phase-change material storage unit for both heating and cooling of buildings. *International Journal of Sustainable Energy*. [Online] 36 (4), 379–397. [online]. Available from: http://dx.doi.org/10.1080/14786451.2015.1018832 (Accessed 20 June 2018).

Waqas, A. & Kumar, S. (2011) Thermal performance of latent heat storage for free cooling of buildings in a dry and hot climate: An experimental study. *Energy and Buildings*. [Online] 43 (10), 2621–2630. [online]. Available from: http://www.sciencedirect.com/science/article/pii/S0378778811002647 (Accessed 5 November 2014).

Wilcox, D. C. (2006) *Turbulence modeling for CFD*. DCW Industries.

Yanbing, K. et al. (2003) Modeling and experimental study on an innovative passive cooling system—NVP system. *Energy and Buildings*. [Online] 35 (4), 417–425. [online]. Available from: http://www.sciencedirect.com/science/article/pii/S037877880200141X (Accessed 3 November 2014).

Yang, W. et al. (2017) Experimental study on the heat transfer characteristics of high blockage ribs channel. *Experimental Thermal and Fluid Science*. [Online] 83248–259. [online]. Available from: http://linkinghub.elsevier.com/retrieve/pii/S089417771730016X.

Zalba, B. et al. (2004) Free-cooling of buildings with phase change materials. *International Journal of Refrigeration*. [Online] 27 (8), 839–849. [online]. Available from: http://www.sciencedirect.com/science/article/pii/S0140700704000623 (Accessed 20 October 2014).

Zeinelabdein, R. et al. (2018) Critical review of latent heat storage systems for free cooling in buildings. *Renewable and Sustainable Energy Reviews*. [Online] 82

(October), 2843–2868. [online]. Available from: https://www.sciencedirect.com/science/article/pii/S1364032117314223?via%3Dihub (Accessed 8 March 2018).

Zhang, F. et al. (2017) Flow and heat transfer characteristics in rectangular channels using combination of convex-dimples with grooves. *Applied Thermal Engineering*. [Online] 113926–936. [online]. Available from: http://dx.doi.org/10.1016/j.applthermaleng.2016.11.047.

Zhang, Y. (2005) *Indoor air quality engineering*. CRC Press.

Zhang, Z. et al. (2007) Evaluation of Various Turbulence Models in Predicting Airflow and Turbulence in Enclosed Environments by CFD: Part 2—Comparison with Experimental Data from Literature. *HVAC&R Research*. [Online] 13 (March 2015), 871–886.

Zolfaghari, A. & Maerefat, M. (2010) A new simplified thermoregulatory bioheat model for evaluating thermal response of the human body to transient environments. *Building and Environment*. [Online] 45 (10), 2068–2076. [online]. Available from: http://dx.doi.org/10.1016/j.buildenv.2010.03.002.

APPENDIX I – BUILDING AND CLIMATIC INFORMATION

Table I.1 – Key Information about building

|	
Location	Bristol, UK
Building Type	School
Retrofit (Y/N)	Y
Surroundings (Urban / Rural)	Rural
Ventilative Cooling Strategy	Mechanical
Year of Completion	2013
Floor Area (m^2)	117
Openable Area to Floor Area Ratio (%)	4
Window to Ext Wall Ratio (%)	50
Sensible Internal Load (W/m^2)	54
Climate Zone (KG)	(Cfb)
No. of Days with T_e max > 25	17
Cooling Season Humidity	Medium
Heating Degree days (Kd)	2684
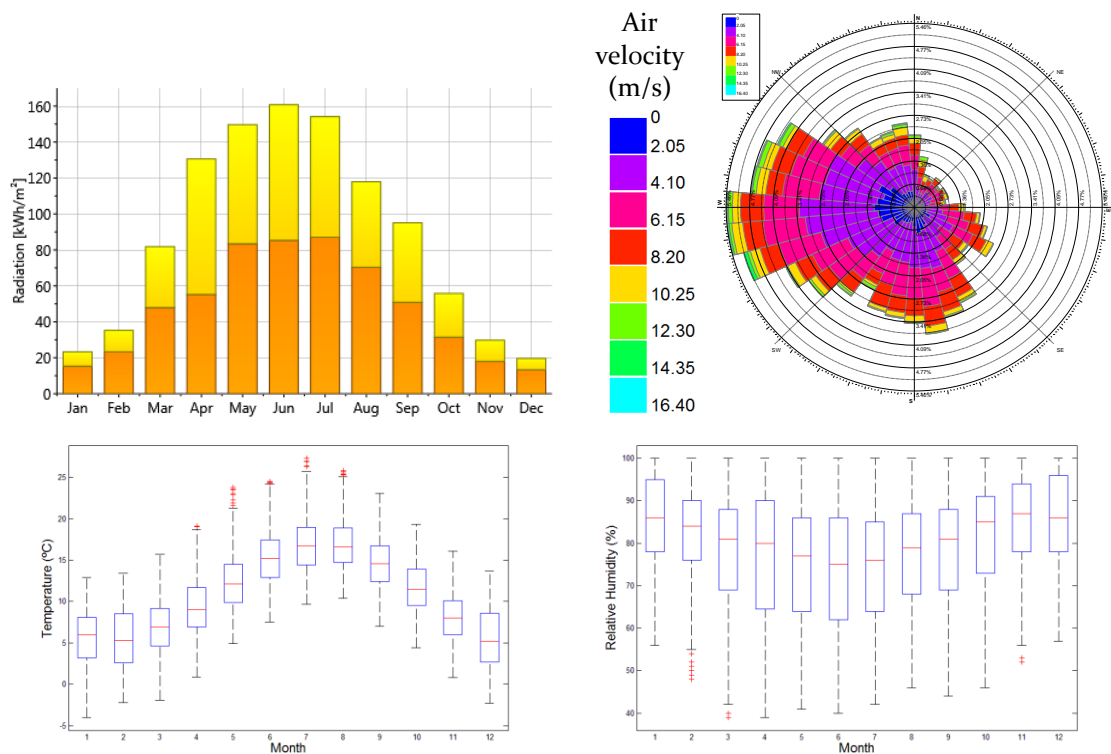
Figure I.1 – Mean, maximum and minimum external conditions in Bristol using TMY3 from Meteonorm 7 ('Meteonorm', 2016) and wind rose for Bristol (TMY3) (IESVE, 2016)

Table I.2 – Building Properties and Design influences

Property	Unit	Value
Occupant density	m^2/p	4
Hours of occupancy	h/week	60
Sensible Internal Load	(W/m^2)	54
Window U-value	W/m^2K	1.82
Window g-value	(-)	0.43
Wall U-value	W/m^2K	0.56
Roof U-value	W/m^2K	NA
Floor U-value	W/m^2K	2.11
Thermal Mass (ISO 13790)	-	Medium
Window to Wall Ratio	%	50
Air-tightness (@50 Pa)	m^3/hm^2	< 10

APPENDIX II – LOGGERS SPECIFICATION AND FIELD SENSOR LOCATIONS

Table II.1 – Loggers specification

	HOBO UX100-003	ibutton DS1922L
Dimensions	3.66 x 8.48 x 1.52 cm	Ø 1.735 x 0.589 cm
Range	-20° to 70°C	-40°C to +85°C
Temperature Accuracy	±0.21°C from 0° to 50°C	±0.5°C from -10°C to +65°C
Resolution	0.024°C at 25°C	8-Bit (0.5°C) or 11-Bit (0.0625°C)
Response Time (airflow of 1 m/s (2.2mph))	4 minutes to 90 %	
Range	15 % to 95 %	
Humidity Accuracy	±3.5 % from 25 % to 85 %	
Resolution	0.07 % at 25°C	
Response Time (airflow of 1 m/s (2.2mph))	43 seconds to 90 %	

Table II.2 – CO₂ Loggers specification

		Telaire 7001
CO₂	Range	0 to 2500 ppm
	Accuracy	±50 ppm or 5 % of reading, whichever is greater
	Resolution	±1 ppm
	Temperature Dependence:	±0.1 % of reading per °C or ±2 ppm per °C, whichever is greater, referenced at 25°C.
	Pressure Dependence:	0.13 % of reading per mmHg (corrected via user input for elevation)
Temperature	Range	0°C to 40°C
	Resolution	0.1°C
	Accuracy	±1°C

Figure II.1 – Seminar Room view with the location of two sensors, wall mounted control and H7 and HOBO (H8) placed at the exhausting griddle.

APPENDIX III – DESIGN OF THE PANEL: 3D DRAWINGS

SHAPE 0

SECTION A-A

SHAPE 1

SECTION B-B

SHAPE 2

SECTION C-C

TITLE:
3D Shapes

SCALE:1:5

205

SHAPE 3

SHAPE 4

SHAPE 5

SECTION D-D

SECTION E-E

SECTION F-F

E

D

C

B

A

E

D

C

B

A

2

1

2

1

D

D

E

E

F

F

TITLE:

3D Shapes

SCALE:1:5

SHAPE 6

G

SECTION G-G

SHAPE 7

H

SECTION H-H

SHAPE 8

I

SECTION I-I

TITLE:	
3D Shapes	
SCALE:1:5	

207

SHAPE 9

SECTION J-J

SHAPE 10

SECTION K-K

EXISTING

SECTION L-L

TITLE:	
	3D Shapes
	SCALE:1:5
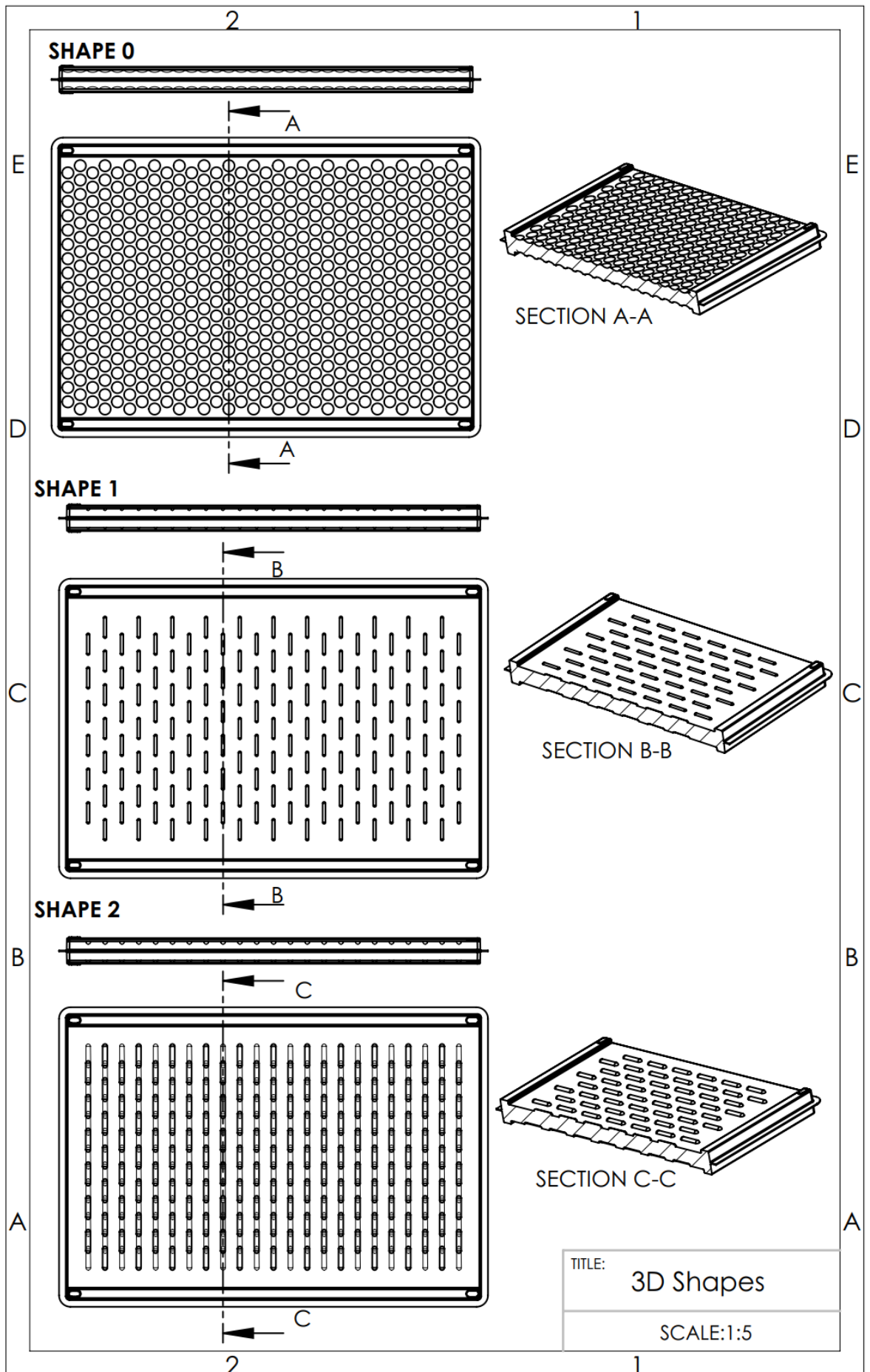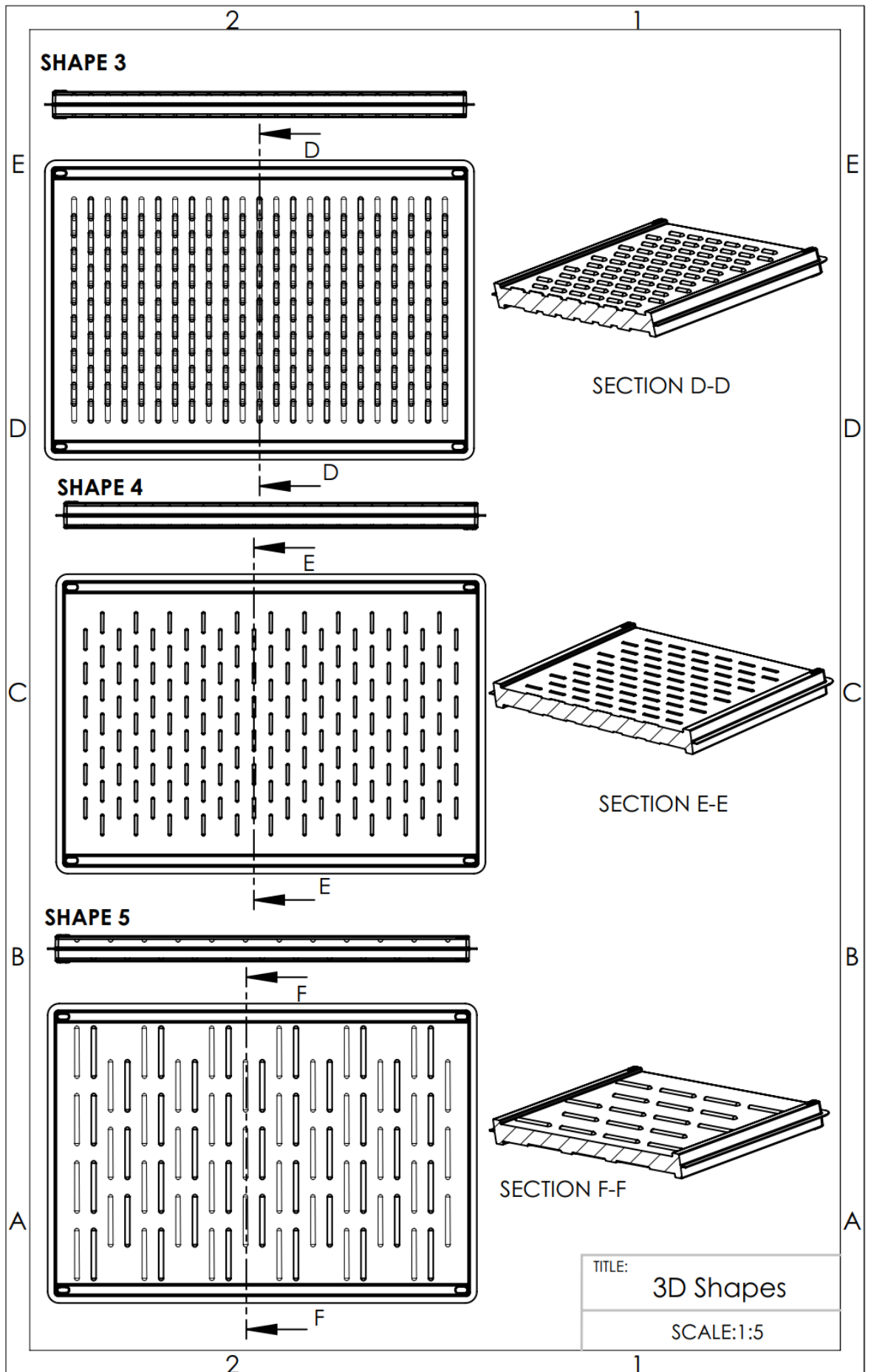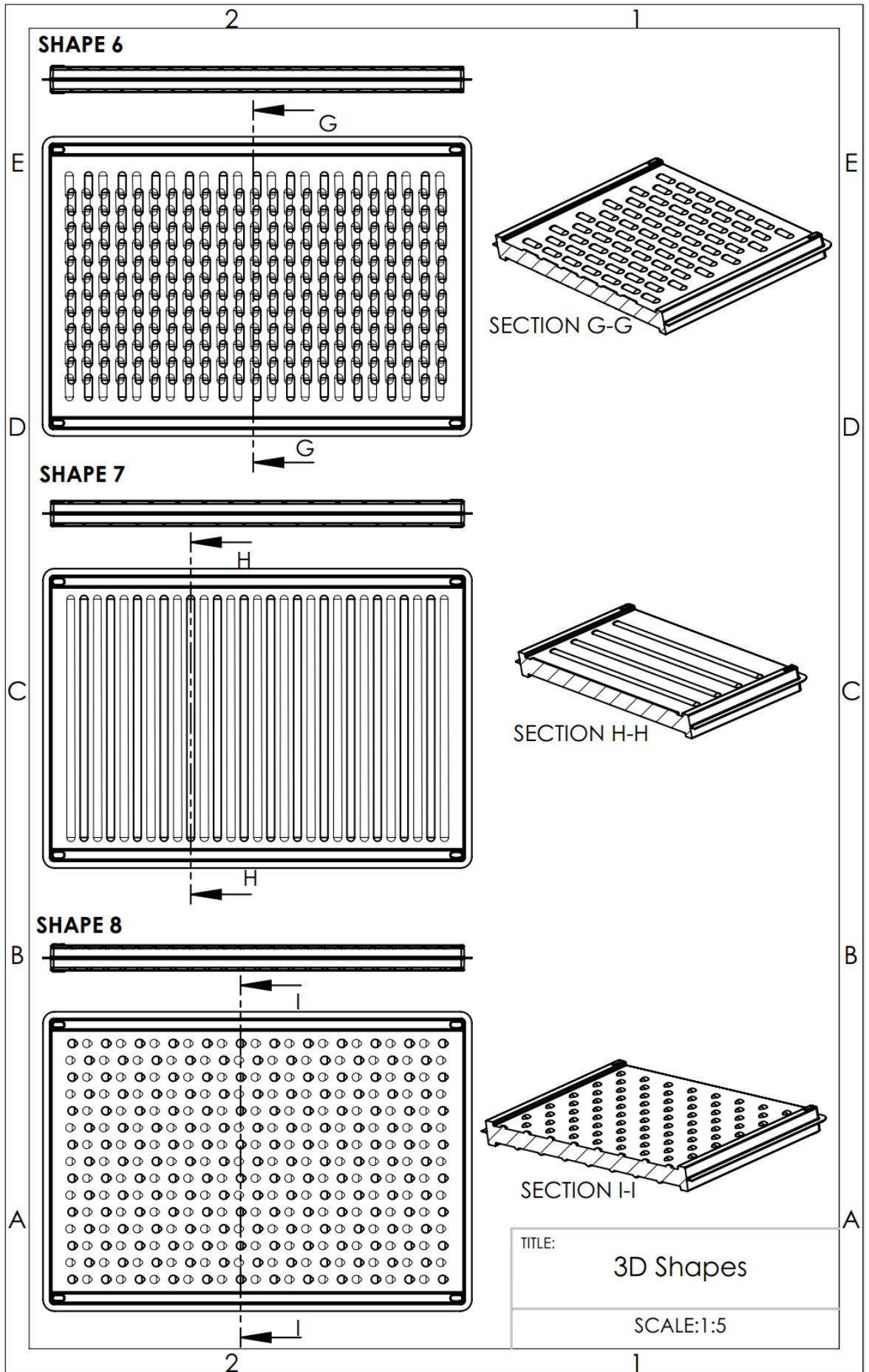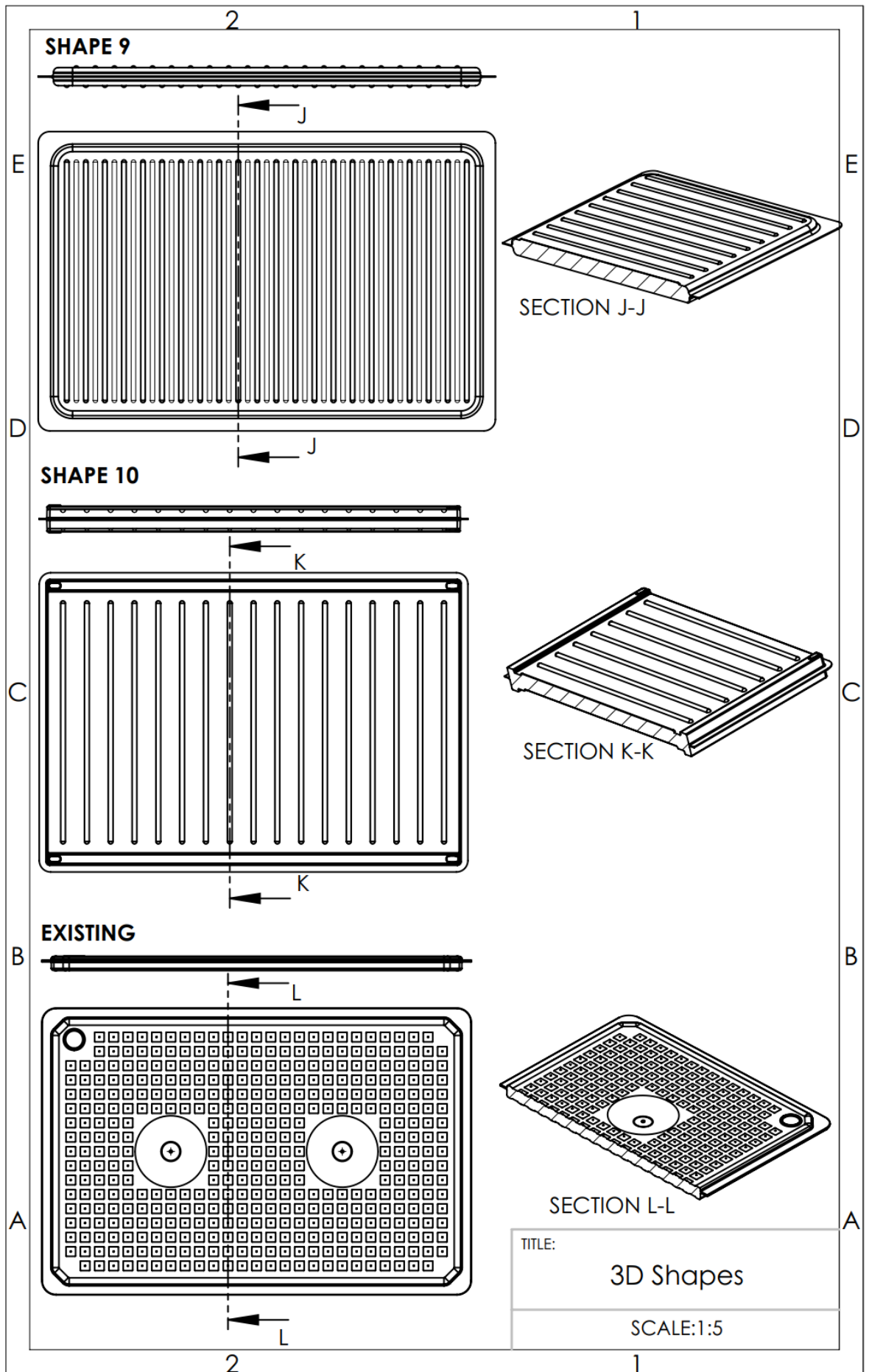
APPENDIX IV - DESIGN OF THE PANEL: 2D DRAWINGS

SHAPE 11

DETAIL G
SCALE 1 : 1

SHAPE 12

DETAIL H
SCALE 1 : 1

SHAPE 13

DETAIL I
SCALE 1 : 1

SHAPE 14

DETAIL J
SCALE 1 : 1

SHAPE 15

DETAIL K
SCALE 1 : 1

SHAPE 16

SHAPE 17

DETAIL L
SCALE 1 : 1

SHAPE 18

DETAIL M
SCALE 1 : 1

TITLE:

2D Shapes

SCALE:1:5

210

SHAPE 19

DETAIL N
SCALE 1 : 1

R2.50 4.77
4.50 20 1.75

N

SHAPE 20

DETAIL O
SCALE 1 : 1

12.50 R2.50
4.50 25 4.77
1.75

O

SHAPE 21

DETAIL B
SCALE 1 : 1

R3 10 5.81
3.50 20 2.25

B

SHAPE 22

DETAIL P
SCALE 1 : 1

10 R2.50
8.75 Ø5 4.77 1.75
20

P

SHAPE 23

DETAIL Q
SCALE 1 : 1

Ø5
10 13
20
R2.50 20

Q

TITLE:

2D Shapes

SCALE:1:5

211

APPENDIX V – REFINEMENT AND SHAPE 11 DIMENSIONS

Shape 11

BK

DETAIL BK
SCALE 1 : 2

R2.50
R5
8
19
5.23
15.23

Shape 24

BB

DETAIL BB
SCALE 1 : 2

8
13.01
R2.50
15.23
5.23

Shape 25

BC

DETAIL BC
SCALE 1 : 2

15
8
R2.50
15.23
5.23

TITLE:

3 Thermal Batteries

SCALE:1:15

213

Shape 26

BD

23.50
8
R2.50
R2.50
15.23
5.67

DETAIL BD
SCALE 1 : 2

Shape 27

BE

19
9
R2.50
R5
15.23
5.23

DETAIL BE
SCALE 1 : 2

Shape 28

BF

19
10
R5
R2.50
15.23
5.23

DETAIL BF
SCALE 1 : 2

TITLE:

3 Thermal Batteries

SCALE:1:15

214

Shape 29

BG

DETAIL BG
SCALE 1 : 2

9.60
14.28
R5
R3
22.80
4.28

Shape 30

BH

DETAIL BH
SCALE 1 : 2

28.50
12.85
R5
12
2.85
R3.58

Shape 31

BI

DETAIL BI
SCALE 1 : 2

6.41
R3
6.18
15.20
R5.37
16.18

Shape 32

BJ

DETAIL BJ
SCALE 1 : 2

6.66
5.60
R1.75
13.30
R3
16.66

TITLE:

3 Thermal Batteries

SCALE:1:15

215

APPENDIX VI –THERMOCOUPLE CALIBRATION AND SPECIFICATION OF MEASURING EQUIPMENT USED FOR THE LABORATORY TESTS

Thermocouple Calibration

The calibration takes place at CSEF where a thermal bath (CTB9500) and a 0.001 °C resolution Hand-held thermometer (CTH7000) were used. Thermocouples type K were joined with the Thermocouple Welder L60+ (Figure VI.1) and DataTaker DT80 with the extension (CEM20) logged the temperature (Figure VI.2).

Figure VI.1 – Thermocouple Welder L60+

Five points evenly distributed from 8 to 50 °C were used to calibrate the thermocouples. More than one hundred thermocouples were used in this study. Values were logged and a regression analysis found an average error of 0.36 °C with a standard deviation of ± 0.52 °C.

Figure VI.2 – Thermocouple calibration performed at CSEF with equipment used presented in detail.

i.   Sensing Balance Master

Figure VI.3 – Sensing Balance Master 4250

Table VI.1 – Conditions of volume flow through Cool-Phase®

Airflow Measuring Range	40 to 4250 m³/h
Accuracy	± 3 % of reading, ±10 m³/h
Resolution	1 m³/h
Temperature Measuring Range	± 0 to 50 ºC
Accuracy	± 0.5 ºC
Resolution	0.1 ºC
Humidity Measuring Range	0 - 100 % RH
Accuracy	± 3.0 % RH
Resolution	RH
Standard Hood Dimensions	610x610 mm
Power Supply	4xAA batteries or AC adapter
Weight	3.6 kg

ii.   Testo 410i Vane anemometer

Figure VI.4 – Testo 410i Vane anemometer

Table VI.2 – Testo vane anemometer

Measuring range	0.4 to 30 m/s
Accuracy ± 1 digit	± (0.2 m/s + 2 % of mv) (0.4 to 20 m/s)
Resolution	0.1 m/s

iii.   Power Supply

Figure VI.5 – Power supply

Table VI.3 – Power supply main specifications

Voltage Range	0-30 V
Current Range	0-5 A
Load Regulation	
Voltage Current	≤ 0.01 % +2mV / ≤ 0.1 % +5mV
Line Regulation	
Voltage Current	≤ 0.01 % +3mV / ≤ 0.1 % +3mV
Setup Resolution	
Voltage Current	10 mV / 1 mA

iv.   PVM610 from TSI

Figure VI.6 – PVM610 from TSI

Table VI.4 – PVM610 from TSI specifications

Static/Differential Pressure	-3735 to + 3735 Pa
Accuracy	±0.01 mm Hg, ±1 Pa
Velocity from a Pitot Tube	1.27 to 78.7 m/s
Accuracy	10.16 m/s
Resolution	0.1 m/s

v. Cool-phase®
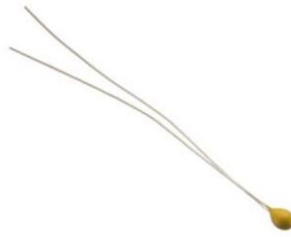
Figure VI.7 – 10K3A1B Series 1 Thermistor

Table VI.5 – 10K3A1B Series 1 Thermistor specification

Parameters	Value	Units
Resistance @ +25°C	10,000	Ohms
Resistance tolerance from 0°C to +70°C	0.2	°C
Alpha Value @ 25°C	4.39	%/°C
Beta Value 25/85	3976	K

APPENDIX VII – CRODATHERM^{TM} 24 DATA SHEET

CrodaTherm™ 24

Ambient temperature phase change material

CrodaTherm 24 is a water insoluble organic phase change material (PCM) derived from plant-based feedstocks and has the form of a crystalline wax or oily liquid (depending on temperature).

CrodaTherm 24 is ideal for use in temperature controlled packaging as well as building, construction and HVAC applications. CrodaTherm 24 has low flammability and has a high renewable carbon content.

Typical properties

Thermal properties by *differential scanning calorimetry* (DSC)

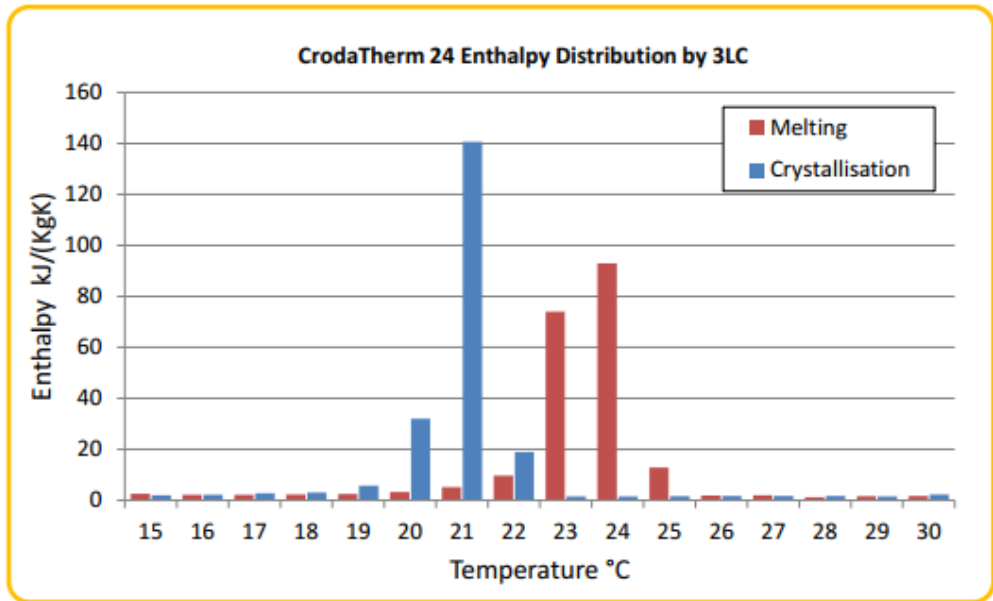| Property	Typical Value	Units
Peak melting temperature	24.1 *(75.4)*	°C *(°F)*
Latent heat, melting	183	kJ/kg
Peak crystallisation temperature	20.1 *(68.2)*	°C *(°F)*
Latent heat, crystallisation	-183	kJ/kg

DSC scanning rate: 1°C/ minute

DSC is an analytical technique used for the thermal characterisation of phase change materials. Croda applies the peak melting temperature obtained by DSC in the suffix of the CrodaTherm product name. See appendix for more information on the calorimetry techniques used by Croda.

Thermal Properties by *three-layer calorimetry* (3LC)

Property	Typical Value	Units
Peak melting temperature	24 *(75.2)*	°C *(°F)*
Total stored heat, 15°C to 30°C (melting)[1]	218	kJ/kg
Peak crystallisation temperature	21 *(69.8)*	°C *(°F)*
Total stored heat, 30°C to 15°C (crystallisation)[1]	221	kJ/kg

[1] Heat stored comprises latent heat and sensible heat

Three-layer calorimetry is a technique used to assess heat storage properties under conditions that are often closer to those encountered in use. See appendix for more information on the calorimetry techniques used by Croda.

CRODA

CrodaTherm 24 Enthalpy Distribution by 3LC

Other Properties

Property	Typical Value	Units
Bio-based content	100	%
Density at 15ºC (solid)	949	kg/m³
Density at 40ºC (liquid)	842	kg/m³
Flash point	228	ºC
Specific heat capacity (solid)	2.4	kJ/(kg·ºC)
Specific heat capacity (liquid)	1.7	kJ/(kg·ºC)
Volume expansion 15ºC – 40 ºC[2]	12.7	%
Thermal conductivity (solid)	0.29	W/(m·ºC)
Thermal conductivity (liquid)	0.16	W/(m·ºC)
Thermal cycles without change in properties[3]	10000	Cycles

[2]Expansion due to normal decrease in density with increasing temperature, including solid to liquid phase change, between the stated temperature limits

[3]Cycles completed at the issue date of this document. Testing is ended at 10,000 cycles.

Handling

For ease of handling and optimum performance, please ensure CrodaTherm 24 is completely molten and homogenous before transferring from the container. If stored at below 22°C for an extended period of time, CrodaTherm 24 may need to be heated before use, to ensure that the product has completely melted. Avoid excessive temperatures (>80°C) and prolonged exposure to open air.

Appendix

About our testing methods

Differential Scanning Calorimetry (DSC)
DSC is an industry standard technique for determining heat capacity using a small sample (in the order of milligrams) of the PCM to be tested. DSC works by comparing the amount of heat that flows into the PCM against a blank control. A temperature program is run to heat or cool the sample, which results in a (calculated) heat flow. During phase change of the sample, the temperature remains constant while the reference still follows the programmed temperature. In the case of PCMs, generally the phase change is solid - liquid (melting) or liquid - solid (crystallisation). The difference in heat flow reflects the absorbed or released amount of heat of the sample. Based upon this, the latent heat during melting and crystallisation and the peak melting and crystallisation temperatures are determined.

Three-layer calorimetry (3LC)
3LC is an industry standard technique for determining the heat capacity of a PCM that uses a much larger amount of sample (~100ml). With 3LC, the thermal response of the PCM within an insulated compartment is measured as the ambient temperature is cycled between temperature limits chosen to ensure full melting and crystallisation of the PCM (normally over a 30°C range). Depending on the application, 3LC can give a much better representation of the "real world" behaviour of a PCM, because of the larger sample quantity, compared to DSC. The rate of temperature change of the PCM during measurement is also lower than is often possible by DSC (the average temperature change rate is 0.3°C/minute). The output from 3LC is the total heat capacity (latent heat and sensible heat) within the temperature range reported. In addition, the heat capacity as a function of temperature, reported in 1°C intervals, is also provided.

Differences in the results
You will find that the peak melting and crystallisation temperature is reported differently by the two methods. Croda reports the results from both DSC and 3LC methods so you can make an informed decision about the right phase change material for you. The results given in this datasheet are typical, and we recommend completing your own testing to validate our products in your applications.